Nanoscale Degradation of Metal-on-Metal Implants

Mohamed A. M. Koronfel

December 2018

A thesis submitted to Imperial College London in fulfilment of the requirements for the degree of Doctor of Philosophy (PhD)

Department of Materials

Imperial College London

Abstract

CoCrMo-based hip implants experienced high failure rates despite the high wear and corrosion resistance of the bulk material. Although they exhibit a lower volumetric wear compared to other implant materials, CoCrMo-based implants produced a significantly larger *number* of smaller wear particles. Simulation studies show that up to *one trillion* wear particles could be produced in one patient annually.[1] Implant wear particles can trigger an immune system inflammatory response[2,3] which is associated with eventual failure of the implants. In light of these failures, many devices have been retracted from the market, and class-action lawsuits were filed in the US. Additionally, one of the largest product liability hearings is currently ongoing in the UK as patients sue implant manufacturers.

CoCrMo is nominally an extremely stable material with high Cr content providing passivity. However, despite the Co:Cr ratio in the original alloy being 2:1, chemical analyses of wear particles from periprosthetic tissue have found the particles to be composed predominately of Cr species, with only trace amounts of Co remaining.[4] The immune system's inflammatory response leads to a rise in local electrochemical potential *via* the production of reactive oxygen/nitrogen species by activated macrophages as well as local acidification. However, the mechanism eliciting the inflammatory response is uncertain.

In this work, the dissolution of CoCrMo in bulk, thin film and nanoparticle form was studied in a simulated biological environment. Electrochemical potentials were applied to simulate the increasingly oxidising environment found within the macrophage cells. A multimodal *in situ* spectroscopy and microscopy approach was used, at high chemical and spatial resolution, to elucidate the dissolution mechanism. The results reveal that CoCrMo dissolution occurs *via* a non-stoichiometric, geometrically inhomogeneous mechanism similar to de-alloying, and previously unreported for this material. Taken together, the results suggest that the *in vivo* dissolution of CoCrMo wear debris can be understood in terms of the local environment and specific corrosion mechanisms that come into play under these conditions: not observed in conventional testing for implant safety.

Declaration of Originality

I declare that this work is my own and that any references to other work are appropriately referenced. Some of the work presented in this thesis has been published in the following journal articles:

M. A. Koronfel, A. E. Goode, J. Nelson Weker, S. E. R. Tay, C. A. Stitt, T. A. Simoes, J. F. W. Mosselmans, P. Quinn, R. Brydson, A. Hart, M. F. Toney, A. E. Porter and M. P. Ryan, "Understanding the reactivity of CoCrMo-implant wear particles," *npj Mater. Degrad.,* **2**, 8 (2018)

M. A. Koronfel, A. E. Goode, M. A. Gomez-Gonzalez, J. Nelson Weker, T. A. Simoes, R. Brydson, P. Quinn, M. F. Toney, A. Hart, A. E. Porter and M. P. Ryan, "In-situ speciation of Co and Cr from CoCrMo-implant wear particles," *submitted to Acta Materialia.,* (2018)

Copyright Declaration

The copyright of this thesis rests with the author and is made available under the Creative Commons Attribution Non-Commercial No Derivatives license. Researchers are free to copy, distribute or transmit the thesis on the condition that they attribute it, that they do not use it for commercial purposes and that they do not alter, transform or build upon it. For any reuse or redistribution, researchers must make it clear to others the license terms of this work.

Acknowledgements

I would like to express my gratitude to my supervisor Prof Mary Ryan for her guidance throughout this work, her patient support, and all the knowledge I gained from her expertise. I am thankful to my second supervisor Prof Alexandra Porter who was always available and provided me with insightful comments on all my presented and written work. I am also lucky to have had the support and mentorship of Dr Angela Goode who expanded my knowledge and inspired my development as a researcher.

I owe a debt of gratitude to the CDT in Advanced Characterisation of Materials who not only funded my studentship, but also made this journey an enriching and enjoyable experience. Thank you Prof Stephen Skinner, Dr Neil Curson, and the rest of the CDT committee for all the activities, events, and pastoral care. I believe my PhD experience was made much more comprehensive and fulfilling by being part of this CDT, and for that I will be forever grateful. Special thanks to Ms Hafiza Bibi who organised numerous seminars, social events, and who took care of my finances, consumable purchases, and travel arrangements.

This work involved many synchrotron beamtime experiments, and I would like to give a special thanks to my beamtime partners Angela, Miguel, and Milly. Not only did I learn a lot from you but you made all of our beamtimes enjoyable and something I will greatly miss. I am thankful to Dr Mahmoud Ardakani, Dr Ecaterina Ware, and Dr Catriona McGilvery for the training and kind support on electron microscopes.

I would not be where I am if it was not for my parents Dr Ashraf Koronfel and Dr Nahla Elgarf. I will forever be indebted and grateful for your constant care, love, and inspiration. I dedicate this to you and I hope it makes you proud. I am also truly lucky to have had the support of two inspirational sisters Mennah and Mariam.

I am grateful for my wonderful wife and best friend Noha Shohayeb who fills my life with happiness, stands by me through the good and tough times, and brings the best out of me. I am also grateful for my beautiful daughter Noor whose smile makes my day.

As my first language, Arabic is the language of my thoughts, feelings and emotions. I am therefore grateful for all my friends who I shared a common-language relationship with. Thank you Ahmed, Karim, Amir, Omar, M. Bahnasawi and Motaz. I savoured the last four years of football, swimming and “Coup” that we shared together.

I would like to thank all my friends and lab colleagues who, over the last four years, have each taught me something new and made this a rewarding experience: Thank you to the first person I met when I began this degree, my office neighbour for the last four years Tim Ellis. Thank you Eleonora and Gabri for the special dinner and game nights. Thank you Rosalia, Jiahui, Jing, Aigerim, Maryam, Noora, Miguel, Liya, Milly, Shengda, and my sputtering partner Emma who spent with me many days and hours on troubleshooting and maintaining the thin film deposition equipment. Thank you Sofia, Lizzie, Shiny, Tim, Jon, Nadir, Josh, and Martin – the brilliant CDT “Cohort 1”.

Contents

Abstract 3
Declaration of Originality 4
Copyright Declaration 5
Acknowledgements 6
Contents 7
List of Abbreviations 11
List of Figures 13
List of Tables 21
1 Introduction 22
2 Literature Review 25
2.1 The CoCrMo Alloy 25
2.1.1 CoCrMo Composition 25
2.1.2 CoCrMo Phases 26
2.1.3 CoCrMo Microstructure 26
2.1.4 CoCrMo Precipitates/Inclusions 26
2.2 CoCrMo Mechanical Wear 27
2.2.1 Mechanisms of Wear 27
2.2.2 Effect of Microstructure on CoCrMo Wearsubs 28
2.2.3 Effect of Protein on CoCrMo Wear 30
2.3 CoCrMo Electrochemical and Corrosion Behaviour 31
2.3.1 The Passive Film on CoCrMo Alloys 32
2.3.2 CoCrMo Polarisation 34
2.3.3 CoCrMo Dissolution 35
2.3.4 CoCrMo Tribocorrosion 36
2.3.5 Effect of Electrolyte Chemistry on CoCrMo Corrosion 38
2.3.5.1 Effect of Phosphate 38
2.3.5.2 Effect of Proteins 39
2.3.5.3 Effect of Simulated Inflammatory Conditions 41
2.3.6 Effect of Microstructure on CoCrMo Corrosion 41
2.4 CoCrMo Biological Impact 43
2.4.1 Particle-Induced Inflammation 44
2.4.2 CoCrMo *in vivo* Distribution 45
2.4.3 CoCrMo Toxicity 45
2.5 CoCrMo Wear Particles 48

2.5.1 Characterisation of *in vitro* Wear Particles 48
2.5.2 Chemical Characterisation of *in vivo* Produced Wear Particles 49
2.6 *In situ* Spectromicroscopy 50
2.7 Summary and Aims 51
3 Experimental Techniques 54
3.1 Electrochemical Measurements of Corrosion 54
3.1.1 Electrochemical Kinetics 54
3.1.2 Electrochemical Polarisation 55
3.2 Introduction to Particle-Matter Interactions 57
3.2.1 Interactions of Incident Electrons 58
3.2.1.1 Elastic Scattering 59
3.2.1.2 Inelastic Scattering: Atomic Excitation/Ionisation 59
3.2.1.3 Inelastic Scattering: Bremsstrahlung 60
3.2.2 Interactions of Incident Photons 60
3.2.2.1 Photoabsorption 60
3.3 Electron Characterisation Techniques 61
3.3.1 Electron Techniques Instrumentation 62
3.3.1.1 Electron Sources (Guns) 62
3.3.1.2 Electromagnetic Lenses 63
3.3.2 Transmission Electron Microscopy 64
3.3.2.1 TEM Image Contrast (Mass-thickness contrast) 65
3.3.3 Scanning Electron Microscopy 65
3.3.4 Scanning Transmission Electron Microscopy 66
3.3.5 Energy Dispersive X-ray Spectroscopy 66
3.4 X-ray Characterisation Techniques 68
3.4.1 X-ray Techniques Instrumentation 68
3.4.1.1 X-ray Sources: Synchrotron Radiation 68
3.4.1.2 X-ray Beamlines 69
3.4.1.2.1 Slits 70
3.4.1.2.2 Monochromator 70
3.4.1.2.3 Harmonic Rejection 71
3.4.1.2.4 Detectors 71
3.4.1.3 X-ray Lenses 73
3.4.2 X-ray Absorption Spectroscopy 74
3.4.2.1 X-ray Absorption Coefficient 74
3.4.2.2 X-ray Absorption Edges 75
3.4.2.3 XAS Scan Parameters and Data Collection 77
3.4.2.4 XAS Data Analysis 79

3.4.2.4.1 Normalisation 79
3.4.2.4.2 Linear Combination Fitting 80
3.4.3 Transmission X-ray Microscopy 80
3.4.3.1 Data Collection and Interpretation 81
3.5 Magnetron Sputtering 82
3.6 General Experimental Procedures 84
3.6.1 Simulated Biological Environment 84
3.6.2 Electrochemistry Methods 85
3.6.3 Electron Microscopy 85
3.6.4 CoCrMo Particles 85
3.6.5 3-D Printed Electrochemical Cells 85
4 Dissolution of Multiscale CoCrMo 86
4.1 Introduction 86
4.2 Methods 86
4.3 Results and Discussion 87
4.3.1 Thin Film Growth 87
4.3.2 Potentiodynamic Polarisation 88
4.3.3 Potentiostatic Polarisation 91
4.3.4 Surface Morphology 93
4.3.4.1 Effect of Applied Potential 93
4.3.4.2 Effect of Protein 93
4.3.4.3 Effect of Microstructure (Inclusions) 96
4.3.5 Relative Elemental Concentrations 100
4.3.6 Spatial Elemental Distribution 103
4.3.7 Dealloying Mechanisms 106
4.4 Summary 107
5 Dissolution Mechanism of CoCrMo Particles 108
5.1 Introduction 108
5.2 Methods 108
5.2.1 *Ex situ* Studies 108
5.2.2 *In situ* Spectroscopy at Diamond Beamline I20 109
5.2.3 *In situ* Microscopy at SSRL Beamline 6-2 109
5.3 Results and Discussion 110
5.3.1 *Ex situ* Spectroscopy 111
5.3.2 *In situ* Spectroscopy 112
5.3.3 *In situ* Microscopy 116
5.3.4 *Ex situ* High-Resolution Microscopy 119

5.4 Summary 122
6 Chemical Speciation Studies 124
6.1 Introduction 124
6.2 Methods 124
6.2.1 Co Speciation: Spectromicroscopy of CoCrMo Particles 125
6.2.2 Cr Speciation: Conventional XAS at SSRL Beamline 4-3 126
6.3 Results and Discussion 127
6.3.1 Spatial Co Speciation Mapping 127
6.3.1.1 Illustration of Mapping Procedure 127
6.3.1.1.1 Data Collection 127
6.3.1.1.2 Noise Reduction 130
6.3.1.1.3 Spectral Background Removal and Normalisation 131
6.3.1.1.4 Identifying Spatial Background 133
6.3.1.1.5 Linear Combination Fitting and Mapping 134
6.3.1.1.6 Reducing Energy Data Points 137
6.3.1.2 Co Speciation as a Function of Applied Potential 137
6.3.2 Tracing the Transient Cr(VI) 142
6.3.2.1 Detecting Cr Dissolution by TXM-XAS 142
6.3.2.2 Detecting Cr Dissolution by Population-Averaged XAS 144
6.3.3 *Ex situ* Co and Cr Speciation 149
6.4 Summary 153
7 Conclusions and Future Work 154
8 Appendix A: TXM-XAS Simulation 157
8.1 Introduction 157
8.2 Simulated Structure Design 157
8.3 Speciation Mapping 159
9 References 162

List of Abbreviations

AFM	Atomic force microscopy
AR	As received
BSA	Bovine serum albumin
BSE	Backscattered electrons
CAD	Computer-aided design
CE	Counter electrode
EDX	Energy dispersive X-rays
EELS	Electron energy loss spectroscopy
EIS	Electrochemical impedance spectroscopy
EXAFS	Extended X-ray absorption fine structure
FCC	Face-centred-cubic
FEG	Field emission gun
FIB	Focused ion beam
HAADF	High-angle annular dark field
HCP	Hexagonal close-packed
HIP	Hot isostatic pressing
LCF	Linear combination fitting
MOM	Metal on metal
MOP	Metal on polyethylene
NC	Nanocrystalline

OCP	Open circuit potential
PBS	Phosphate-buffered saline
RE	Reference electrode
SBF	Simulated body fluid
SCE	Saturated calomel electrode
SE	Secondary electron
SEM	Scanning electron microscopy
SHE	Standard hydrogen electrode
STEM	Scanning transmission electron microscopy
TEG	Thermionic emission gun
TEM	Transmission electron microscopy
TF	Thin film
THR	Total hip replacement
TXM	Transmission X-ray microscopy
WE	Working electrode
XANES	X-ray absorption near edge structure
XAS	X-ray absorption spectroscopy
XFM	X-ray fluorescence microscopy
XPS	X-ray photoelectron spectroscopy

List of Figures

Fig. 1.1 The components of hip implants prostheses. The acetabulum-head combination forms the articulating junction providing mobility. In MOM implants (left) this junction is made of CoCrMo alloys. In MOP implants (right) an UHMWPE on Ti alloy is used. MOM models are also available as “hip resurfacing” implants with a shorter femoral stem component preserving more femoral bone during implantation. The “hip resurfacing’ model was introduced particularly for younger patients. 23

Fig. 2.1 Polarisation curves of CoCrMo alloy and its constituting metals in 0.14 M NaCl (pH 7.4). The passive and transpassive behaviour of the alloy is similar to Cr (reproduced with permission from[89]). 35

Fig. 2.2 Potentiodynamic polarisation curves of CoCrMo in NaCl and PBS with and without protein (reproduced with permission from [81]). 39

Fig. 2.3 Light microscopy image showing wear particles (black spots) in macrophage cell from periprosthetic tissue (adapted and reproduced with permission from [4]). 45

Fig. 2.4 Model for the process leading to inflammatory tissue reaction. The relatively bigger wear particles, which are metallic and of the bulk alloy composition, are phagocytised by macrophages and transported to the acidic environment in the lysosomes where they corrode releasing metal ions. (adapted and reproduced with permission from [27]) 47

Fig. 2.5 Schematic illustrating the mechanisms of cellular uptake of wear products, their intracellular metabolism, and effects (reproduced with permission from [27]). 48

Fig. 3.1 Simplified illustration of the circuit required for performing electrochemical polarisation measurements . 57

Fig. 3.2 Schematic of X-ray photoabsorption followed by fluorescence. An incident photon of energy hv_i is absorbed by the atom, ejecting an electron from an inner shell of the atom. The atom relaxes by filling the vacancy by emitting an X-ray photon with a characteristic energy hv_f. (adapted and reproduced with permission from [241]). 61

Fig. 3.3 Schematic of the structure of an electromagnetic lens (left), and an illustration of the difference in ray path between electromagnetic lenses and optical lenses (from [242] licensed under CC BY-SA 2.5). 63

Fig. 3.4 Schematic illustrating (a) a perfect lens imaging a point object as a point, (b) spherical aberration where a point object is focused as a disc called the disc of uncertainty, due to over-focusing of the rays which are further away from the optical axis, and (c) chromatic aberration where beams of different energies (indicated by the different colours) are focused at a different strength by the lens. 64

Fig. 3.5 Simplified schematics of the instrumentation for (a) SEM, (b) TEM, and (c) STEM. CL stands for condenser lens, while OL stands for objective lens (reproduced with permission from [248]) 67

Fig. 3.6 Schematic illustrating the X-ray spectra emitted from (a) a bending magnet, (b) wiggler, and (c) undulator. (adapted from [250]). 69

Fig. 3.7 Schematic of the main structure of a synchrotron facility. 69

Fig. 3.8 Beamline configuration and typical apparatus for XAS measurements in (a) transmission geometry and (b) fluorescence geometry. 72
Fig. 3.9 Structure and parameters of the Fresnel Zone Plate (adapted and reproduced with permission from[255]). 74
Fig. 3.10 Schematics of four common X-ray microscopy optics. (a) A Fresnel zone plate lens is a circular diffractive grating that can be used for focusing or imaging X-ray. (b) A multilayer-coated two-bounce Schwarzschild reflective objective for focusing or imaging. (c) A KB glancing incidence mirror pair for focusing hard X-rays. (d) A multilayer Laue lens for focusing X-rays (adapted and reproduced with permission from [253]). 74
Fig. 3.11 An example of an X-ray absorption spectrum, with the main spectrum regions (XANES and EXAFS) indicated (from[251]). 76
Fig. 3.12 Example of an XAS data illustrating the raw data acquired and after normalisation to the edge step (adapted and reproduced with permission from [252]). 80
Fig. 3.13 (a) Schematic illustrating the set-up of a TXM. (b) Illustration of spectromicroscopy performed through obtaining a stack of multiple images at different photon energies and thus image intensities can be translated to absorption spectra. (Adapted and reproduced with permission from [262]). 82
Fig. 3.14 Schematic showing the principle of operation of a magnetron sputtering system. Ar ions are accelerated by an electric field towards the target, leading to the ejection of target atoms which condense on the substrate. The magnetic field is used to trap secondary electrons emitted from the sputtering collision which are then used to increase the ionisation rate of Ar atoms. 84
Fig. 4.1 The effect of three sputtering parameters on the deposited film thickness. While no obvious trend could be concluded between film thickness and argon pressure, a linear relationship between thickness and both growth time and power was observed. 88
Fig. 4.2 Potentiodynamic polarisation curves of CoCrMo as (a) 80 nm thin films, (b) 160 nm thin films, and (c) bulk discs; in simulated body fluids. Three repetitions were measured for each sample in SBF (solid lines) and in Serum SBF (dashed lines).The main chemical reactions associated with the different domains are annotated in (c). While the passive and transpassive domains (regions 3 and 4) will be dominated by the stated Cr reactions, the measured current densities will also include contributions from Co and Mo. (37° C and pH 5.2). 90
Fig. 4.3 Polarisation curves of CoCrMo alloy, as well as pure metals Co and Cr (polarised in SBF). 91
Fig. 4.4 Potentiostatic polarisation measurements of CoCrMo as (a) 80 nm thin films, (b) 160 nm thin films, and (c) bulk discs; recorded when switching the applied potential from -500 mV in the cathodic domain, to either 400 mV (passive domain) or 800 mV (transpassive domain). (d-f) show the same data rearranged per potential/electrolyte. 92
Fig. 4.5 Optical images recorded at different times during the polarisation of CoCrMo 80 nm TF at 800 mV in SBF. The images reveal the geometrically inhomogeneous dissolution of the film. The red colour in the 1800 s and 2400

s images is the background colour behind the glass substrate (upon which the TF was grown); hence the appearance of the red background colour is indicative of regions where the TF dissolved. Scale bars = 1 mm. .. 92
Fig. 4.6 Secondary electron SEM images of CoCrMo 80 nm TFs (a) as received, (b) after 30 min polarisation at 400 mV in SBF, (c) after 30 min polarisation at 800 mV in SBF, and (d) after 30 min polarisation at 800 mV in Serum-SBF. Scale bars = 100 nm. 94
Fig. 4.7 Secondary electron SEM images of CoCrMo 160 nm TFs (a) as received, (b) after 30 min polarisation at 400 mV in SBF, (c) after 30 min polarisation at 800 mV in SBF, and (d) after 30 min polarisation at 800 mV in Serum-SBF. Scale bars = 100 nm. 95
Fig. 4.8 Secondary electron SEM images of CoCrMo bulk discs (a) as received, (b) after 30 min polarisation at 400 mV in SBF, (c) after 30 min polarisation at 800 mV in SBF, and (d) after 30 min polarisation at 800 mV in Serum-SBF. Scale bars = 100 nm. 95
Fig. 4.9 Dark-field STEM images from two regions of CoCrMo TF polarised at 800 mV for 5 minutes in SBF. Scale bars = 100 nm. 96
Fig. 4.10 Secondary electron SEM images of CoCrMo bulk discs surfaces showing the randomly shaped inclusions across the alloy matrix. (a-b) as received, (c-d) after 30 min polarisation at 800 mV in SBF. Scale bars = 1 μm. 97
Fig. 4.11 Secondary electron SEM images at the matrix/inclusions interface of CoCrMo bulk discs (a) as received, (b) after 30 min polarisation at 400 mV in SBF, (c) after 30 min polarisation at 800 mV in SBF, and (d) after 30 min polarisation at 800 mV in Serum-SBF. Scale bars = 100 nm. 98
Fig. 4.12 Secondary electron SEM images of CoCrMo bulk samples after using FIB to expose the cross-section at inclusion sites revealing that the developed morphology extends to approximately 500 nm below the surface. Scale bar = 500 nm 99
Fig. 4.13 Secondary electron SEM images and EDX elemental maps at inclusion sites showing a lack of Co and enrichment of Cr and Mo in inclusions. (a) Top view SEM and EDX with scale bars = 5 μm. (b) Cross-sectional view (at a different site) with scale bars = 1 μm. 100
Fig. 4.14 Bar charts of the mean Co:Cr at.% ratio, obtained by EDX, from TFs and bulk samples under four different polarisation conditions. Each bar represents the average of ten different measurements. Error bars represent standard deviation. ('ns' indicates 'non-significant', and asterisks indicate 'significant' as follows: 2 asterisks = $p<0.01$, 3 asterisks = $p<0.001$, 4 asterisks = $p<0.0001$). 102
Fig. 4.15 (a-f) Dark field STEM images from six different regions of a CoCrMo TF polarised at 800 mV for 5 minutes in SBF. Nanoporosity is more prevalent in some regions compared to others. Scale bars = 100 nm. (g) Bar chart showing the Co:Cr (at. %) ratio across the six regions. 102
Fig. 4.16 XRF maps revealing the distribution of Co and Cr in (a) as grown TF, and (b-c) two different sites of the TF polarised at 0.8 V in SBF. Colour bars indicate absorbance intensity (a.u.). 104

Fig. 4.17 (a-b) XRF maps of Co and Cr distribution at two different sites of a TF polarised at 0.8 V in SBF (Colour bars indicate the absorbance intensity (a.u.)). (c) SEM images of the same polarised TF revealing that surface morphology is consistent with the Cr distribution (Scale bars = 1μm). 105
Fig. 5.1 Schematic of the electrochemical cell set up used during in situ spectroscopy by XAS..... 109
Fig. 5.2 Schematic of the 3D-printed electrochemical cell used for in situ imaging by TXM (adapted and reproduced with permission from[271]) 110
Fig. 5.3 TEM images of AR CoCrMo particles. The particles had a range of sizes and shapes (red arrows point to examples of smaller particles). 111
Fig. 5.4 Histograms of Co:Cr atomic ratios calculated from EDX analysis of CoCrMo particles in four conditions: As Received (AR), after exposure to SBF at OCP, after exposure to SBF at 1 V polarisation, and after exposure to serum-containing SBF at 1V polarisation (54 particles in each condition). 112
Fig. 5.5 (a) Fluorescence intensity of Co (at 7757 eV) and Cr (at 6009 eV) over time. The particles were at OCP for the first five minutes before the potential (dashed line) was stepped from 0.4 to 0.8 V. Drops in the Co and Cr amounts are observed after the 0.7 V and 0.8 V steps. The drop in the amount of Co is noticeably larger compared to Cr, particularly after 0.8 V polarisation. (b) A bar chart illustrating the levels of Co and Cr at the end of the 0.7 V and 0.8 V potential steps in (a), where 100% Co and Cr amounts were taken to be the average fluorescence intensity before the first potential step was applied. Error bars represent the standard deviation over three scans recorded for each case. (reproduced from[272] licensed under CC BY 4.0). 113
Fig. 5.6 Co (a-b) and Cr (c-d) K-edge XANES spectra collected before and after polarisation in SBF and serum-SBF. The difference in the edge steps between unnormalised pre- and post-polarisation spectra is proportional to the amount of elemental dissolution. The vertical dashed lines in (a) & (c) illustrate the energies at which time-scans reported in figure 5.5(a) were collected. 115
Fig. 5.7 A series of in situ TXM images of CoCrMo particle in Agar-SBF recorded during the potential scan, revealing the onset of release of diffuse material which corresponded to 0.56 V. Scale bars = 3 μm. 116
Fig. 5.8 (a) TEM image of a macrophage cell from periprosthetic tissue recovered from a patient showing CoCrMo wear debris marked by the red (solid particles) and green (diffuse, less electron dense material) arrows. (Legend: C= collagen, V= vesicles, dotted line = plasma membrane). (b-d) Higher magnification TEM images of CoCrMo wear debris from within the cell in (a), Scale bars = 200 nm. (e-g) A series of in situ TXM images of CoCrMo particle in Agar-SBF recorded during the potential scan, revealing the onset of release of diffuse material, Scale bars = 3 μm. Images (a-d) were provided by Dr Angela Goode. (reproduced from[272] licensed under CC BY 4.0). 118
Fig. 5.9 Secondary electron SEM images of (a) AR particle, (b) a particle after immersion in SBF at OCP, (c) a particle after polarisation in SBF at 0.8 V showing the development of a nanoporous surface, (d) a particle after polarisation in serum-SBF at 0.8 V, with little porosity observed (red arrows). Scale bars = 200 nm. (reproduced from[272] licensed under CC BY 4.0). 119

Fig. 5.10 (a-f) Secondary electron SEM images showing the development of nanopores on the surface of CoCrMo particles after polarisation at 0.8 V in SBF. The image pairs (a-b) and (c-d) show different magnification images of the same particles. Gold particles (labelled Au in (f)) were formed from the Au film during polarisation. Scale bars = 100 nm. 120

Fig. 5.11 (a) High angle annular dark field (HAADF) STEM image of the complete layered structure of the FIB-section including the Pt layer deposited to protect the particle's top surface during the lift-out procedure, the CoCrMo cross-section, the sputtered gold film, and the glass substrate, scale bar = 1µm. (b-d) higher magnification HAADF STEM images of the area marked by the green box in (a) revealing the nanoporosity network across particle surface, examples of porosity are indicated with the red arrows, scale bar = 50 nm. 121

Fig. 5.12 (a) Dark field STEM image of CoCrMo particle (biased in SBF at 1 V), (b-e) Cross-sections through tomographic reconstructions, 8 nm apart, taken from a 370 x 360 x 40 nm section outlined by the white box in (a). Gold particles (labelled Au) were formed from the TEM grid during polarisation. Scale bar = 200 nm. Images were provided by Dr Angela Goode. (reproduced from[272] licensed under CC BY 4.0). 122

Fig. 6.1 Schematic illustrating the XAS measurement setup and the source of the detected signal. This set up was employed for XAS measurements at Beamline 4-3, SSRL for Cr speciation studies. 127

Fig. 6.2 Standard XAS spectra for Co metal and Co(II) as obtained from Co foil and CoO powder respectively 129

Fig. 6.3 TXM images of CoCrMo particles at four selected energies. The selected energy points here are indicated on the XAS spectra in figure 6.2. Colour bars indicate absorbance (a.u.). 130

Fig. 6.4 A scree plot ranking the TXM dataset principal components by their eigenvalues in descending order. The data was reconstructed using the first six components (as marked by the red arrow at the inflexion point) which represented 99.5 % variance of the original dataset. 131

Fig. 6.5 Examples of three XAS spectra from three different locations in a CoCrMo particle extracted from the TXM-XAS images dataset. (a) raw spectra, (b) Reconstructed spectra after PCA, (c) Spectra after background removal, (d) Normalised spectra. 132

Fig. 6.6 Illustration of TXM images before and after background removal at both a pre-edge energy point 7700 eV, and a post-edge energy point 7788 eV. Colour bars indicate absorbance (a.u.). 133

Fig. 6.7 Demonstration of spatial background filtering procedure. (a) TXM image at the isosbestic energy point 7788 eV, a line profile across the image is selected (indicated by the red dashed line). (b) a plot of absorbance across the line selected in (a). A threshold/cut-off absorbance value is selected to separate the spatial background regions from particles' (sample) regions. A cut-off value of 0.025 was selected, which equals 3.1σ of the absorbance values outlined by the white rectangle in (a). 134

Fig. 6.8 Speciation map representing the distribution of the Co(II) composition fraction as constructed by LCF of individual region/pixel spectra. 135

Fig. 6.9 A histogram of the frequency of R-factor values from all sample spectra fits. Bin size is 0.01. More than 95 % of the fits had an R-factor value of less than 0.05. 136
Fig. 6.10 The spatial distribution map of the R-factor values (a), compared to the speciation composition map (b). The regions with higher R-factors correlated with dynamically evolving regions such as those of higher Co(II):Co ratio, at the edges of particles, and diffuse material around the particles (marked by the white arrow in (a)). 137
Fig. 6.11 (a) A stack of TXM absorbance images of a CoCrMo particle recorded at six different energies illustrating the TXM data collection procedure. (b) The recorded standard X-ray absorption spectra for Co metal and Co(II). The black vertical lines illustrate the three post-edge incident X-ray energy points selected for TXM imaging (in addition to three pre-edge energies). (c) Examples of the six-energy spectra of two different sample regions, resembling Co metal absorption (blue) and Co(II) absorption (red). 139
Fig. 6.12 (a) Raw six-energy spectra of two example sample regions. (b) The same spectra after normalisation. 140
Fig. 6.13 Speciation maps representing the Co(II) composition fraction of every 30 nm pixel/region in the CoCrMo particle at different applied electrochemical potential. The total Co(II)% (displayed above each corresponding map) were calculated per equation (6.4) and was found to increase as the applied potential increased, with a noticeable rise at the 0.8 V step. 140
Fig. 6.14 Histograms of the frequency of Co(II) composition fraction (fitting weight) after the LCF of all sample spectra at the different applied potential. Bin size = 0.1. The increase in the frequency of high Co(II) fraction values is noted as potential increases, particularly at 0.8 V. 141
Fig. 6.15 Histograms of the frequency of R-factor values of all sample spectra fits at each applied potential. Bin size = 0.01. In each case, 95 % of values remained less than 0.05. 141
Fig. 6.16 TXM images (at isosbestic X-ray energy 7788 eV) (a) before and (b) during the 0.8 V applied potential step, showing the egress of diffuse material from the particle. 142
Fig. 6.17 Standard XAS spectra of Cr metal, obtained from a Cr foil, Cr(III), and Cr(VI), as obtained from boron nitride pellets containing 10 wt.% of $CrCl_3$ and $Na_2Cr_2O_7$ respectively. 143
Fig. 6.18 In situ absorbance intensity from CoCrMo TF as a function of time and potential recorded at Cr(VI) pre-edge energy (E1) at the SSRL TXM beamline 6-2. (a) Scatter plot of absorbance intensity of CoCrMo thin-film at the Cr(VI) pre-edge peak energy (E1) while electrical potential (red plot) was applied in steps from 0.4 V to 0.8 V. A small increase in the absorbance intensity is observed at the 0.7 V and 0.8 V steps. (b) The average absorbance intensity from (a) at each potential step. Error bars represent standard deviation. The differences in intensity between 0.6 V and 0.7 V, as well as 0.7 V and 0.8 V, are statistically significant with $p<0.0001$ (indicated by 4 asterisks) and $p<0.001$ (indicated by 3 asterisks) respectively. 144
Fig. 6.19 In situ absorbance intensity as a function of time and potential recorded at the Cr(VI) pre-edge energy point (E1) at the SSRL conventional XAS beamline 4-3. An onset of absorbance intensity increase is observed at

0.7 V and continuous increase during 0.8 V. After the end of 0.8 V, when the system is at OCP, the absorbance intensity remains constant for the 20 minutes of recording. 145
Fig. 6.20 In situ absorbance intensity as a function of time and potential at both the Cr(VI) pre-edge energy point 5993.25 eV (E1) and 6009 eV (E2) showing greater increase in the absorbance intensity signal at E2 suggesting that the detected signal is likely Cr(III) species rather than Cr(VI). The system was at OCP at the end of the 0.8 V step. 145
Fig. 6.21 Standard Cr metal, Cr(III), and Cr(VI) X-ray absorption spectra with a magnified view of the pre-edge region showing the pre-edge shoulder characteristic of Cr(III). 146
Fig. 6.22 In situ absorbance intensity (at E2) as a function of time and potential. A comparison of detected dissolution in SBF and Serum SBF from CoCrMo TF samples (a), and CoCrMo particles samples (b). The results indicate less detected dissolution in the presence of serum. The system was at OCP at the end of the 0.8 V step. 147
Fig. 6.23 XAS spectra of TF and electrolyte before and after potential application in both the SBF (blue) and Serum SBF (red). 148
Fig. 6.24 XAS spectra of TF biased in SBF (a) and serum SBF (b) overlaid with fit results obtained by a linear combination of the TF pre-bias (original TF state, Weighted 1) and electrolyte post-bias (oxidised species, Weighted 2) spectra. The data shows a greater ratio of oxidised Cr (Weighted 2) on the surface of the TF biased in SBF compared to Serum SBF. 149
Fig. 6.25 XFM images of Co from (a) polarised, and (b) AR, CoCrMo TFs at the three selected energy points for speciation analysis. Colour bars indicate absorbance intensity (a.u.). 150
Fig. 6.26 Speciation maps representing the distribution of Co(II) composition fraction in (a-b) polarised, and (c-d) AR CoCrMo TFs. The overall Co(II) % was (a) 17.7 %, (b) 5.8 %, (c) 1.6 %, and (d) 1.7 %. 150
Fig. 6.27 Standard XAS spectra of Cr metal, obtained from a Cr foil, Cr(III), and Cr(VI), as obtained from boron nitride pellets containing 10 wt.% of $CrCl_3$ and $Na_2Cr_2O_7$ respectively. The vertical dotted lines indicate the energy points selected for speciation analysis 151
Fig. 6.28 XFM images of Cr from (a) polarised, and (b) AR, CoCrMo TFs at three of the selected energy points for speciation analysis. Colour bars indicate absorbance intensity (a.u.).Colour bars indicate absorbance intensity (a.u.) 152
Fig. 6.29 Speciation maps representing the distribution of Cr(III) composition fraction in (a-b) polarised, and (c-d) AR CoCrMo TFs. The overall Cr(III) % was (a) 78.6 %, (b) 83.8 %, (c) 30.3 %, and (d) 28.8 %. 152
Fig. 8.1 Simulated TXM images of the two simulated designs, at energy 7727 eV (peak of absorption edge). (a-b) are the simulated images before addition of noise. (c-d) the images after the addition of random Gaussian noise. Colour bars indicate absorbance intensity (a.u.). 158

Fig. 8.2 Examples of simulated XAS spectra before (blue) and after (red) addition of noise. (a & c) spectra from the core and outer most squares of design A respectively. (b & d) spectra from the core and outer most squares of design B respectively. 158
Fig. 8.3 Simulated TXM images of the two simulated designs, at energy 7788 eV (isosbestic point). (a-b) are the simulated images before addition of noise. (c-d) the images after the addition of random Gaussian noise. Colour bars indicate absorbance intensity (a.u.). 159
Fig. 8.4 Constructed speciation maps representing the distribution of the Co(II) composition fraction for both design A (a, c) and design B (b, d). (a-b) represent the speciation map of originally intended designs (i.e. before addition of noise). (c-d) represent the maps after the addition of random noise. Colour bars represent the Co(II):Co composition ratio. 160

List of Tables

Table 2.1 The chemical composition of the biomedical ASTM F75 alloy (from [31]) 25

Table 3.1 Comparison between the TXM and TEM techniques (adapted from[245]) 81

Table 6.1 The energy steps at which the TXM images were recorded 128

Table 6.2 LCF parameters for both TF biased in SBF and Serum SBF 149

Table 8.1 The calculated % Co(II) for both design A and B using different sets of energy points 161

1 Introduction

Total hip replacement (THR) is a surgical intervention for the treatment of osteoarthritis in the hip joint, whereby the head of the femur is sectioned off, the femoral canal is reamed, and the acetabulum is shaved to make way for an artificial hip prosthesis. THR is one of the most common and highly successful orthopaedic procedures.[5] THR operations are predicted to double over the next 20 years due to a growing number of younger THR patients, as well as an increasingly ageing population.[6,7] While the first THR operation was performed in 1934, implants at the time were limited by design and choice of materials.[8] The modern design of a THR implant consists of three main parts: the stem, femoral head, and the acetabular cup (figure 1.1). The stem is fixed, usually cemented, in the femur bone while the femoral head and acetabulum form the articulating junction which provides the degrees of movement. Wear debris generated at this junction, from mechanical and chemical processes, have been a root cause of many complications since the inception of these implants. Thus, considerable research was conducted in pursuit of a more wear resistant material combination. First implants of this design were introduced in the 1960s and were made of metallic cup and head (metal-on-metal, MOM). Although some of these early MOM implants survived for 25 years, in some cases metallic debris was observed in patients' tissue raising concerns on the safety of these implants.[9] In the mid-1970s MOM implants were mostly abandoned especially after Charnley introduced metal-on-polyethylene (MOP) implants, utilising ultra-high molecular weight polyethylene (UHMWPE) as an acetabular cup material, to achieve lower friction at the articulating junction.[10] Nonetheless, polyethylene wear debris limited the life of MOP implants to only ten years. A number of studies have shown that polyethylene wear particles trigger an inflammatory immune response which causes osteolysis (resorption of bone tissue).[11–13] The breakdown of bone tissue, in turn, leads to the aseptic loosening of the implant and the need for revision surgery. Towards the turn of the century, MOM implants received a revived interest in efforts to avoid the production of polyethylene wear particles. Advances in tribological understanding led to the introduction of second-generation MOM implants based on CoCrMo alloys. Pre-clinical testing delivered promising results with MOM implants exhibiting lower wear rates and smaller particle size distributions compared to MOP implants in simulation studies.[14–17] This superior wear resistance, as well as theoretical mechanical advantages, were used to demonstrate the suitability of these second-generation MOM implants for younger and more active patients. However, the encouraging performance in hip simulators did not translate into clinical success and these CoCrMo-based implants suffered an excessively high failure rate.[18] MOM devices have been removed prematurely in up to 10 % of patients within only five years of impanation.[19,20] Although the unsatisfactory clinical performance has led to a decline in the use of MOM implants over the last decade, more than one thousand MOM operations were still performed in the UK in 2014.[21] Considerable attention in the literature has been given to understanding and explaining the reasons behind this unexpected failure. Additionally, debate continues over the safety of these

implants which are currently the subject of one of the largest product liability hearings in the UK.[22] Furthermore, many devices have been retracted from the market, and class-action lawsuits were filed in the US.[23]

Despite the lower volumetric wear exhibited by CoCrMo implants, compared to MOP implants, it was found that CoCrMo alloys lead to the release of smaller, but a significantly larger *number,* of wear particles; up to *one trillion* particles may be released in one patient annually.[24] While osteolysis is the main clinical concern and mechanism of failure of MOP implants, it is less prevalent in the case of MOM implants. Instead, MOM wear-particles trigger an adverse inflammatory response with characteristic pseudo-tumours which lead to severe pain warranting the need for a revision surgery.[25,26] A major clinical concern from CoCrMo wear particles is the potential release of the cytotoxic and genotoxic cations (Co(II) and Cr(VI)) due to particle dissolution.[27] CoCrMo is nominally an extremely stable material with high Cr content providing strong corrosion resistance: the alloy is passive under a large range of conditions. However, despite the Co:Cr ratio in the original alloy being 2:1; chemical analyses of wear particles from periprosthetic tissue, explanted from patients, have found the particles to be composed predominately of Cr species, with only trace amounts of Co remaining.[4] From a materials science perspective, this high level of dissolution was previously unexpected from CoCrMo alloys and the mechanism behind it is not understood. Understanding the mechanism of *in vivo* dissolution of CoCrMo particles will provide further insights on the overall failure mechanism of MOM implants, and is vital to identify the clinical risks faced by the tens of thousands of patients who currently have such an implant.[28] In addition, the findings will be essential for developing new implant materials, as well as updating the testing and regulatory criteria to be required from future biomedical implants.

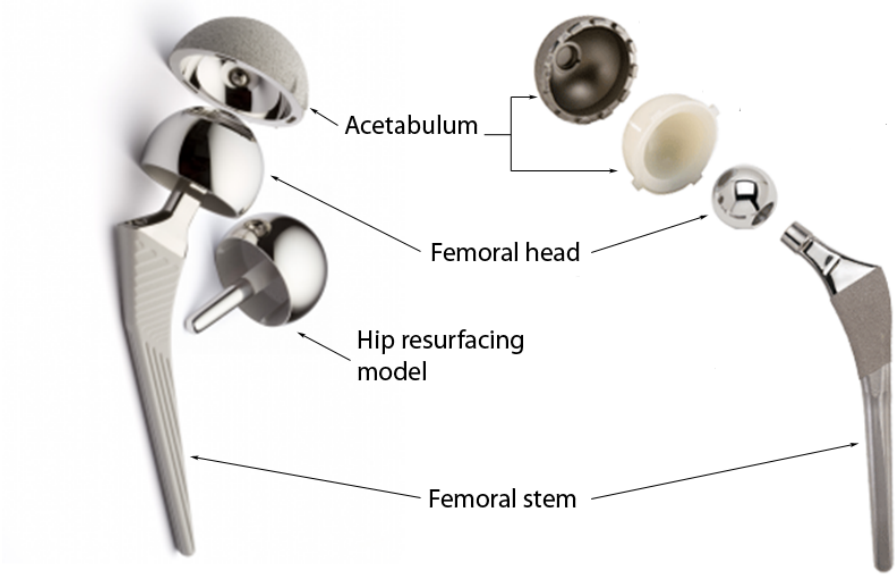


Fig. 1.1 The components of hip implants prostheses. The acetabulum-head combination forms the articulating junction providing mobility. In MOM implants (left) this junction is made of CoCrMo alloys. In MOP implants (right) an UHMWPE on Ti alloy is used. MOM models are also available as "hip resurfacing" implants with a shorter femoral stem component preserving more femoral bone during implantation. The "hip resurfacing' model was introduced particularly for younger patients.

The aim of this work was to elucidate the dissolution mechanism of CoCrMo wear particles as it occurs *in vivo*, by designing appropriately sensitive and representative *in vitro/in situ* experiments. A complementary spectroscopy and microscopy approach was used to develop an understanding of the dissolution of these particles based on chemical and morphological changes. These changes were studied, by a range of techniques, both *ex situ* and *in situ* under a simulated biological environment. The simulated environment encompassed: firstly a simulated biological fluid (SBF) which mimicked the lysosomal environment inside macrophages (immune system cells where wear particles are typically found *in vivo*). Additionally, an applied electrochemical potential was used to simulate the increasingly oxidising environment characteristic of the human inflammatory response.

Chapter two of this thesis presents a review of the relevant literature providing a further understanding of the structure of biomedical CoCrMo alloys and their electrochemical behaviour. Additionally, the characteristics of the produced wear debris are presented from both simulation and clinical studies. The potential clinical risks imposed by the dissolution of CoCrMo wear is reported. Furthermore, the previous work towards understanding the *in vivo* behaviour of CoCrMo wear are discussed. Finally, the use of synchrotrons for *in situ* studies of corrosion is reviewed.

Chapter three presents the theoretical background behind the main methods and characterisation techniques utilised in this work.

The results of this work are presented in chapters four, five and six; firstly, in chapter four, the electrochemical behaviour, and surface morphology, of *bulk* CoCrMo is compared to that of CoCrMo thin films to determine any difference in the alloy's behaviour at different size scales. CoCrMo wear particles are studied in chapter five; a complementary spectroscopy and microscopy approach is used to study the chemical and morphological changes of the particles both *ex situ* and *in situ*. Chapter six presents a simultaneous spectromicroscopy approach for chemical speciation analysis of CoCrMo. This approach aimed to achieve spatially resolved chemical information, determine the onset of dissolution, and to identify the release of transient species such as the carcinogenic Cr(VI) ions.

2 Literature Review

2.1 The CoCrMo Alloy

In this section, the standard composition and structure of biomedical CoCrMo alloys are discussed.

2.1.1 CoCrMo Composition

CoCr alloys are produced by reducing cobalt and chromium ores followed by combining the pure metals by an electric arc or through induction melting, under vacuum conditions. Most of the CoCr alloys currently used in industrial and biomedical fields evolved from the work of Elwood Haynes at the turn of the previous century. Haynes demonstrated that the binary CoCr alloy possesses high strength and resists stain as they became one of the first superalloys (alloys with a superior combination of mechanical strength and corrosion resistance). Subsequently, Haynes found that the alloy's mechanical properties could be improved by the addition of molybdenum and tungsten.[29] Chromium is the element which gives the alloy its corrosion resistance characteristics (more details in section 2.3.1). In a more recent work, Lee *et al.*[30] reported that the addition of nitrogen to a 0.61 wt. % (facilitated by increasing the Cr content) could result in significant improvement in the alloy's mechanical properties such as yield stress, tensile strength, and fracture elongation.

The chemical composition and mechanical properties of CoCrMo alloys currently used in biomedical implants follow the American Society for Testing and Materials (ASTM) standards. ASTM F75[31] and ASTM F1537[32] are the standards for cast and wrought alloys respectively. While cast manufacturing is suitable for more complex designs, unequal cooling rates may cause micropores which reduce the strength of as-cast alloys. Therefore cast alloys are usually subjected to heat treatments: solution annealing (isothermal ageing) and hot isostatic pressing (HIP), which reduce subsurface microporosity and improve alloy homogeneity and ductility.[33,34] The ASTM F75 as-cast alloy is the commonly used alloy for orthopaedic implants and have the composition shown in table 2.1.

Table 2.1 The chemical composition of the biomedical ASTM F75 alloy (from [31])

Element	Chemical Composition wt. %	
	min	max
Chromium	27.00	30.00
Molybdenum	5.00	7.00
Nickel	-	0.50
Iron	-	0.75
Carbon	-	0.35
Silicon	-	1.00
Manganese	-	1.00
Tungsten	-	0.20
Phosphorous	-	0.020
Sulfur	-	0.010
Nitrogen	-	0.25
Aluminium	-	0.10
Titanium	-	0.10
Boron	-	0.010

Cobalt	balance	balance

2.1.2 CoCrMo Phases

Pure Co is liquid above 1495 °C and forms a face-centred-cubic (FCC) crystal structure below this temperature. The metastable FCC structure transforms to the thermodynamically stable hexagonal close-packed (HCP) crystal structure by a displacive martensitic transformation at 417 °C.[35] This transformation temperature is higher in CoCrMo alloys as both Cr and Mo increase the stability of the HCP phase.[36] However, although HCP is the expected thermodynamically stable phase, most Co-based alloys retain the FCC structure at room temperature.[33] This is attributed to a slow kinetics of the FCC to HCP transformation under normal cooling conditions. Nonetheless, the HCP phase, known as ε–martensite, can be induced from the metastable FCC phase by strain/plastic deformation,[37–39] quenching,[40] and heat treatments (isothermal ageing).[36,40,41]

2.1.3 CoCrMo Microstructure

The microstructure of the alloy plays an important role in determining its mechanical properties. A smaller grain size leads to a higher yield strength for the material, according to the Hall-Petch equation. Smaller grain sizes indicate the presence of more grain boundaries per unit area. These grain boundaries act as impeding points to dislocation propagation; hence a higher applied stress is required for dislocations to propagate in materials with smaller grain sizes. The microstructure of as-cast CoCrMo alloys is composed of a cobalt-based FCC dendritic matrix with interdendritic and grain boundary precipitates.[42]

The solidification of the alloy during casting results in large dendritic grains in addition to casting defects, such as micropores, which may induce stress. Therefore, heat treatments have been employed to reduce the microporosity with the aim of improving the mechanical properties of cast alloys. These heat treatments can have other effects on the alloy microstructure. They lead to a heterogeneous alloy (multi-phase) by inducing the formation of the HCP phase (see section 2.1.2). The mechanical properties of the heterogeneous alloy would be dependent on the size and distribution of the different phases. In addition, heat treatments also affect the shape and constituent phases of the precipitates, causing the partial or complete dissolution of the precipitates depending on the treatment temperature, treatment time, and carbon content in the alloy.[43]

2.1.4 CoCrMo Precipitates/Inclusions

Inclusions are chemical compounds, of metal or non-metal components, that form in metal alloy matrices during melting and pouring processes. Inclusions may be endogenous that form as a result of chemical reactions within the metal in the molten state and precipitate during cooling. They may also be exogenous which are caused by the entrapment of external particles (e.g. mold powder). The word precipitates also refers to particles of a second phase within the original phase matrix. The formation of precipitates, as well as their size and distribution, are

accomplished by appropriate heat treatments. These precipitates are used to enhance the hardness and strength of metal alloys (this process is termed precipitation hardening). Certain endogenous inclusions (carbides, nitrides and carbonitrides) are classified as precipitates because they can have strong influences on alloy properties *via* mechanisms like grain refinement and precipitation hardening.

The precipitates formed in CoCrMo alloys may be a mixture of metal carbides, intermetallic sigma σ-phase (Co(Cr, Mo)) and FCC phase.[44,45] Additionally, more recently Mineta *et al.*[43] reported the presence of a phase mixture, including π and η metal carbide phases, in the precipitates of as-cast alloys. Liao *et al.*[46] reported the presence of mixed phase inclusions in cast alloys but homogeneous (single phase) carbide inclusions in the wrought alloys. This was attributed to the repeated heating and deformation steps experienced by wrought alloys, as well as the slower cooling rates used during casting.

Carbon content plays an important role in CoCrMo alloys. Wrought alloys are classified as either low carbon (LC) alloys, with less than 0.15 wt. % carbon content or high carbon (HC) alloys with a carbon content between 0.15 and 0.35 wt. %. ASTM F75 as-cast alloys may also contain up to 0.35 wt. % carbon content. The cooling process during eutectic solidification of the alloy, or after heat treatments, promote the formation of metal carbide precipitates at the grain boundaries.[47] These metal carbides have the formula of $M_{23}C_6$, where M tends to be Cr or Mo[48–52] although Co-rich grains may also be present in these carbide phases.[46]

Heat treatments may cause the dissolution of the metal carbides precipitates into the matrix. It has been shown that metal carbides transform from $M_{23}C_6$ to M_6C when CoCrMo alloys are annealed between 1230 ^oC and 1250 ^oC, while the complete dissolution of carbides occurs between 1250 ^oC and 1270 ^oC.[53] These temperature values would be dependent on the carbon content of the alloy.[43] Although Caudillo *et al.*[45] did not observe a phase transformation in the carbides (from $M_{23}C_6$ to M_6C) they also reported their dissolution into the matrix after thermal treatments at three different heating rates.

2.2 CoCrMo Mechanical Wear

Volumetric wear of CoCrMo alloys was assessed in tribology studies, comparing different alloy characteristics such as carbon content, as well as the effect of different environments (lubricating solution) such as the effect of proteins. These studies typically employ pin-on-disc reciprocating wear machines where a pin (usually an alumina ball) is rubbing against a flat alloy disc. Hip simulators have also been used, as a more realistic geometry for hip implants, and it has been suggested that they result in less wear compared to pin-on-disc tribometers.[54]

2.2.1 Mechanisms of Wear

In general, there are four key mechanisms of mechanical wear: adhesive, abrasive, third-body, and fatigue wear.

Adhesive wear occurs when the atomic forces between two surfaces, under relative load, are stronger than the inherent material properties of either surface. The continued motion of the surfaces requires breaking the bond junctions where every time a bond junction is broken, a wear particle is created.

Abrasive wear occurs between surfaces of different relative hardness. In an abrasive wear mechanism, micro-roughened regions and small asperities on the harder surface locally plough through the softer surfaces. Abrasive wear results in the softer material being removed from the track traced by the asperity during the motion of the harder surface.

Third-body wear is a form of abrasive wear that occurs when hard particles become embedded in a soft surface. The embedded particle acts like the asperity of a harder material in abrasive wear, removing material in its path.

Fatigue wear occurs when surface and subsurface cyclic shear stresses or strains in the softer material of an articulation exceed the fatigue limit for that materials.

2.2.2 Effect of Microstructure on CoCrMo Wear

The microstructure of the alloy plays an important role in its mechanical and tribological behaviour. Additionally, the microstructure may change under tribological contact, and this in turn changes/affects the tribological process such as wear rate, and wear-particles' properties and numbers.

Carbide inclusions are one of the main aspects that play a role in CoCrMo wear. In general, as carbide inclusions are much harder than the surrounding metal matrix, the precipitates are a strengthening mechanism for CoCrMo alloys and therefore a better wear resistance is naturally expected from HC alloys. Therefore, while thermal treatments offer many benefits and are advised by international standards, there has been a concern regarding the carbide dissolution caused by these heat treatments (as discussed in section 2.1.4). The effect of carbon content and heat treatments on the wear resistance behaviour of the alloy have been subjects of unresolved debate in tribology studies.

A number of studies reported the negative effect of heat treatments on the volume fraction of carbide precipitates and the subsequent negative effect of this on wear rates. Cawley *et al.*[50] found that as-cast alloys contained the highest volume fraction of carbides and exhibited lower wear rates compared to solution annealed (1200 ^{o}C for four hours) and hot isostatically pressed alloys. Similar conclusions were drawn by other studies[55–58] including Kinbrum *et al.*[57] who observed abrasive wear on as-cast surfaces compared to adhesive wear on double heat treated surfaces. This could be attributed to a higher fraction of carbide precipitates on the as-cast surfaces, which are harder than the alloy matrix and hence cause grooves on opposing surface and overall higher surface roughness. The reported volumetric wear for as-cast alloys was approximately 0.05 mm^3 per 10^6 cycles and 0.25 mm^3 per 10^6 cycles for double heat treated alloys.[56,57]Furthermore, some studies reported that carbides play a

positive role on wear resistance in the presence of protein. Yan *et al.*[59] reported that carbides increased the surface energy and hence promoted bovine serum albumin (BSA) adsorption on the surfaces leading to a decrease in frictional losses. Additionally, Julián *et al.*[58] found that BSA leads to agglomeration of wear debris. They concluded that carbides could indirectly lead to lower wear volume by facilitating this agglomeration into grooves resulting in a smoother surface.

On the other hand, Bowsher *et al.*[60] found no statistical difference in volumetric wear between as-cast and double heat treated (1200 ^{o}C for four hours solution annealing and hot isostatic pressing) alloys concluding that carbide inclusions did not influence the alloy's wear resistance. Other studies reported the detrimental effect of carbide precipitates on wear rates. Synergistic effect of the sigma σ-phase and the metal carbides in the precipitates were reported as an underlying mechanism that enhanced alloy wear.[38] Carbides were found to be torn off and σ-phase uprooted leading to micro-cracks in the surface of the alloy. Additionally, torn-off carbides confined between the two articulating surfaces enhance wear (third-body wear).[61] Similar conclusion was reported by Chiba *et al.,*[62] who found that large carbides were prone to fragmentation and partial pull-out resulting in more abrasive wear. Furthermore, Wang *et al.*[52] reported that the phase boundaries between the matrix and the precipitates became stress concentration zones during tribological contact (due to the accumulation of stacking faults at these boundaries); this, in turn, led to surface fatigue in the form of micro-cracks. The main mechanisms leading to plastic deformation and microstructural refinement in CoCrMo alloys are the formation of stacking faults, grain subdivision, and martensitic transformation.[63] While carbide precipitates may reduce the formation or propagation of the stacking faults, their accumulation at the carbide/matrix boundaries could lead to increased fatigue.

The effect of carbide precipitates on the alloy's wear resistance may, therefore, appear to be a subject of controversy, however various reasons could explain the varying results. Balagna *et al.*[41] demonstrated one order of magnitude less volumetric wear on HC cast alloys compared to HC wrought alloys. This was attributed to the difference in carbide distribution between the two alloys. In fact, previous studies had suggested that not only volume fraction but size, distribution, and morphology of carbide precipitates may play a role in wear resistance of the alloy.[50,61] Furthermore, Mo-rich carbides were found to be more detrimental to the wear resistance of HC alloys, compared to Cr-rich ones, by causing discontinuities at the precipitate-matrix interface.[51] Therefore, exclusively increasing carbon content in the alloy does not necessarily result in increased wear resistance. A careful heat treatment to optimize the size, distribution as well the composition of carbide precipitates is as important as increasing the carbon content.[51]

Other microstructure aspects affecting wear include the initial surface deformation. Zeng *et al.*[64] compared the wear rate of mechanically polished and electro-polished HC CoCrMo plates in a reciprocating pin-on-disc wear machine at different loads. The two surfaces exhibited a substantial difference in the initial surface microstructure: while the mechanically polished surface had significant deformation compromising of ε-martensite plates,

mechanical twins and high dislocation density, the electro-polished surface showed no signs of deformation. The wear rate of the mechanically polished surface was significantly higher than the electro-polished surface at all applied loads, which was attributed to the increased surface strain in the mechanically polished surfaces.

Furthermore, the alloy's microstructure is adjusted in response to mechanical load, which in turn affects the wear behaviour. Several authors reported the development of a nanocrystalline (NC) layer on worn surfaces.[63–69] For instance, Wang *et al.*[66] observed an inhomogeneous NC layer, forming the top 200 nm within a total of a 500 nm deep wear-affected zone. Stacking faults were found under the NC layer and many grain defects, the density of which decreased with depth.[66] Buscher *et al.*[67] examined *in vivo* (retrieved implant cups) and *in vitro* worn surfaces, and reported a similar NC layer on both surfaces which was ~ 1 μm deep with ~ 50 nm crystallite size. Additionally, they reported the presence of strain-induced martensite (HCP) in the subsurface (below the NC layer) of both *in vitro* and *in vivo* worn surfaces.[67] Pourzal *et al.*[69] also observed an NC layer on retrieved implants which was 250 – 400 nm thick with a grain size of 25 – 40 nm. The development of the NC layer is dependent on both applied load and initial surface deformation[64] and hence the differences in reported thicknesses. Zeng *et al.*[64] reported that mechanically polished samples (with greater depth of deformation and surface strain) developed a thicker NC layer, upon wear testing, compared to electro-polished surfaces. The authors suggested that a threshold strain is required to induce the formation of the NC layer through the acting shear stresses. The reported deformation sequence as a function of strain was as follows: glide of dislocations and formation of stacking faults, followed by the formation of mechanical twins and strain induced martensite, and finally the formation of the NC layer.[64] Although it was suggested that surface fatigue in the NC layer may be an acting wear mechanism in CoCrMo implants and that the NC layer forms the origin of the smaller wear nanoparticles;[67] some authors suggested that the smaller grains of the NC layer lead to increased strength, based on the Hall-Petch relationship, and therefore the layer may lead to reduced wear.[63] Zeng *et al.*[64] reported a reduction in wear rate with increased applied load due to the development of the NC layer.

2.2.3 Effect of Protein on CoCrMo Wear

The cavities of synovial joints are filled with lubricating synovial fluid which is rich in proteins. Proteins may adsorb on to the alloy surface and may play a critical role in the tribological behaviour. In tribological contact, the presence of protein was found to result in the formation of a carbon-rich tribolayer (also known as tribofilm or biofilm) on the alloy surface. The tribofilm has been observed on many retrieved implants surfaces,[70–72] and during *in vitro* tribometer studies.[66,73–75] It has been suggested that the tribolayer was formed through the mechanical mixing of proteins with the NC layer (refer to section 2.2.2 on the presence of NC layer) of the metal surface.[71,76] Chemical analysis, using X-ray photoelectron spectroscopy (XPS) and Energy dispersive X-ray spectroscopy (EDX), showed that the tribolayer contained metal nanoparticles (presumably detached from the metal surface), a substantial amount of carbon, as well as possible calcium, phosphorus, magnesium, nitrogen, sodium and chlorine.[71,72,77] The

tribofilm has been commonly assumed to consist of denatured proteins (proteins that lost their higher-order structure, due to thermal effect and high strain during tribological contact). However, Liao *et al.*[70] found, using electron energy loss spectroscopy (EELS), that tribolayers were composed predominantly of graphitic carbon and a small fraction of possibly degraded proteins. The authors hypothesised that a graphitic film may have formed due to the action of transition metals as catalysts removing water and ammonia from organic materials: as a result, a hydrogenated carbon film would be left behind and could be converted from an amorphous structure to a graphitic material during tribological sliding.[70]

The tribofilm may play a critical role in the alloy's wear and degradation. It may act as an effective lubricant and has been found to reduce the coefficient of friction in tribology studies.[66,73] Sun *et al.*[78] simulated abrasive wear of the alloy, using abrasive particles (SiC and Al_2O_3 particles), in both NaCl and bovine serum solutions; the results indicated that bovine serum reduced wear only at a low volume fraction of abrasive particles. However, the presence of proteins led to enhanced wear, at higher abrasive volume fraction, which was attributed to enhanced particle entrainment facilitated by the protein film. Other authors also suggested that the retainment of abrasive particles by proteins was behind enhanced wear of stainless steel.[79]

Furthermore, the presence of protein may affect wear behaviour by causing changes in the microstructure of worn surfaces. Wang *et al.*[66] reported the microstructure difference of surfaces worn in phosphate buffer solution (PBS) compared to PBS with bovine serum albumin (BSA). Apart from the presence of a tribolayer above the surface, the NC surface layer was deeper (500 nm) in PBS-BSA compared to 200 nm in PBS only. Additionally, the deformed zone beneath the NC layer was thicker and contained a higher density of stacking faults. The authors concluded that this multilayer structure leads to severer subsurface deformation. The mechanism proposed was that the presence of a tribofilm could keep the passive film intact and suppress stacking fault annihilation by blocking their access to the surface. The diffusion of stacking fault towards deeper regions instead leads to strain accumulation in the subsurface. Therefore, overall it appears that the effect of protein on the alloy wear may be governed by a complex mechanism with opposing effects such as friction reduction (lubrication) and inducing larger subsurface strain.

2.3 CoCrMo Electrochemical and Corrosion Behaviour

Corrosion of metals in aqueous solutions (electrolyte) is an electrochemical process which can be described by the chemical reaction in equation 2.1; where a metal atom M is oxidised to form a dissolved metal ion M^{n+} plus *n* number of electrons. These electrons are consumed by reduction reactions of oxidising agents in the electrolyte such as hydrogen ions (in acidic solutions), dissolved oxygen, and water according to the chemical reactions in equations 2.2, 2.3 and 2.4 respectively. The corrosion rate of a metal M is determined by the net rate of reactions 2.1 against 2.2, 2.3 and 2.4 which depends on the electrochemical potential established across the

metal/electrolyte interface. Equation 2.1 is valid when the metal is in 'active' conditions. However, in passive electrochemical conditions, the oxidation reaction of the metal results in the formation of a thin oxide film (passive film) on the metal surface, according to equation 2.5. The passive film is usually a few nm thick and acts as a barrier to further oxidation. The corrosion resistance of a metal is therefore defined by its tendency to passivate, and the stability of its passive film, in the operating environment.

$$M \rightarrow M^{n+} + ne^- \quad \text{Equation 2.1}$$

$$2H^+ + 2e^- \rightarrow H_2 \quad \text{Equation 2.2}$$

$$O_2 + 2H_2O + 4e^- \rightarrow 4OH^- \quad \text{Equation 2.3}$$

$$H_2O + 2e^- \rightarrow 2OH^- + H_2 \quad \text{Equation 2.4}$$

$$M + nH_2O \rightarrow MO_n + 2nH^+ + 2ne^- \quad \text{Equation 2.5}$$

2.3.1 The Passive Film on CoCrMo Alloys

The tendency of a metal to form metal ions in a solution depends on its standard electrode potential for the metal/metal ion reaction (equation 2.1) which represents the thermodynamic driving force for the metal dissolution. A more negative standard potential represents a greater tendency for the metal to dissolve. The standard electrode potentials for the Co^{2+}/Co and Cr^{3+}/Cr reactions are -0.28 V and -0.74 V (vs standard hydrogen electrode SHE) respectively. Although these values alone indicate that Cr is more likely to corrode compared to Co, the dissolution of metals is also dependent on their tendency to passivate (the standard potentials for equation 2.5) and the stability of the formed passive film. Cr forms a very protective oxide film which makes it the most stable metal in the alloy.

Cobalt metal forms two different passive films in alkaline solution (pH 9.3): between 0 – 0.7 V (vs standard hydrogen electrode, SHE) the passive film is composed of Co(II) compounds, CoO and $Co(OH)_2$, while above 0.7 V (vs SHE) the Co(III)-containing compounds Co_2O_3 and Co_3O_4 are formed. [83] Chromium spontaneously forms a Cr(III) based film containing Cr_2O_3 and $Cr(OH)_3$, and at higher (transpassive) potentials, Cr(VI) species are incorporated in the film.[84] It is known that the Co oxide film is much more soluble than Cr as well as Mo oxides.[85]

CoCrMo alloys exhibit strong corrosion resistance due to the spontaneous formation of a surface passive film both in air and simulated biological fluids.[80,81] The alloy's passive film is more protective than the films formed on other commonly used biomedical alloys such as 316L stainless steel.[81,82] Several studies assessed the corrosion behaviour of CoCrMo and the composition of its passive film using electrochemical techniques, along with surface characterisation techniques such as X-ray photoelectron spectroscopy (XPS) and Raman spectroscopy. The nature of the passive film would vary according to solution chemistry and applied potential. The composition of the CoCrMo alloy passive film was studied in 0.15 M NaCl using *in situ* Raman spectroscopy and was found to be

hydrated chromium and cobalt oxides (Cr_2O_3, $Cr(OH)_3$, $Co(OH)_2$).[86] Consequently, Hanwa *et al.* [87] used XPS to characterise the alloy's passive film before and after immersion in different biological media. While the film was originally 2.5 nm thick and composed of Co, Cr, and Mo oxyhydroxides, Co species dissolved upon immersion in Hank's solution leaving mainly Cr (III) oxide with some Mo oxides. Milosev *et al.* [88] also reported, using XPS, the predominance of Cr_2O_3 in a 3 nm thick film both in air and after electrochemical polarisation up to 0.3 V (vs saturated calomel electrode, SCE) in simulated body fluid (SBF, pH 7.5). At potentials above 0.3 V (vs SCE) more Co oxide, and minor contribution of Mo oxide, (mainly as CoO and MoO_3) form in the passive film with a significant increase in its thickness. Cr(VI) species were detected in the film after transpassive polarisation (above 0.6 V vs SCE). Furthermore, Hodgson *et al.* [89] confirmed, using XPS, the Cr-rich nature of the alloy's passive film in 0.14 M NaCl (pH = 7.4) reporting a composition of ca. 90 % Cr(III) species and only 5 % Co at potentials below 0.5 V (vs SCE). A small concentration (*ca.* 1 %) of Mo was also detected in the form of Mo(IV) oxide. Above 0.5 V (vs SCE) the Co content increased to a maximum 20 %.

Lewis et al. [90] characterised the surface layer of CoCr pellets after five days of immersion in human serum, bovine serum and synovial fluid, using time-of-flight secondary ion mass spectrometry (ToF-SIMS). The surface layer was found to be 25, 10 and 1.5 nm thick respectively compared to 3 nm in water. The composition of the surfaces consisted of Cr oxides, hydroxides and phosphates, whereas Co existed mainly as hydroxides and phosphates only. The formation of a thinner layer in synovial fluid was attributed to its hydrophobic nature which prevents metal-water contact and hence no hydroxides were formed while only oxides could form due to oxygen diffusion. Furthermore, Milosev[91] compared the thickness and composition of the CoCrMo passive film after potentiostatic polarisation in different solutions including 0.9 % NaCl, Hanks solution, and Hanks solution with the addition of 1 ml synovial fluid (all at pH 7.4). The film thicknesses were comparable after passive polarisation (0.4 V vs SCE) likely due to the predominance of Cr_2O_3. However, after transpassive polarisation (0.7 vs SCE) the surface film thickness increased by fivefold in the Hanks solutions (with and without synovial fluid) and by only two-fold in the 0.9 % NaCl. Transpassive polarisation would lead to the formation of Co(II), Co(III) and Mo(VI) oxides in the films. The thicker films observed in Hanks solution are likely due to the additional formation of calcium phosphates which would not be present in NaCl solutions. Additionally, the Hanks solution plus synovial fluid included the formation of organic compounds.

In conclusion, a protective passive film is instantly formed on CoCrMo surfaces and is predominately composed of Cr(III) oxide. The thickness and composition of the film may vary according to the conditions and environment. Passive-domain polarisation leads to the slow thickening of the Cr(III) oxide layer. On the other hand, under transpassive polarisation, other metal oxides become incorporated in the surface film; additionally, calcium phosphates may form in phosphate containing environments, and organic compounds may form in organic media.

2.3.2 CoCrMo Polarisation

With a Cr-rich passive film, it comes as no surprise therefore that the CoCrMo electrochemical polarisation curves demonstrate a Cr-like behaviour (figure 2.1).[85,88,89] It is worth noting that a higher polarisation resistance of the alloy compared to Cr metal was observed using electrochemical impedance spectroscopy (EIS) signifying a role of Co and Mo oxides on the alloy passivity.[85] The alloy's polarisation curves (from cathodic to anodic), in the relevant solutions reported in the literature, are typically described by four potential domains: the cathodic domain where the current is dominated by oxygen and/or water reduction (as per equations 2.3 and 2.4 above), the cathodic-anodic transition (Tafel region), the passive domain characterised by a constant low current, and finally the transpassive domain characterised by an increase in current due to the dissolution of alloy elements (and water oxidation). A small hysteresis was observed after cyclic voltammetry (forward and reverse polarisation cycle) indicating that current increase in the transpassive domain is not due to pitting corrosion.[92,93] While an active-passive transition was observed by Hodgson *et al.*[89], a more Cr-like immediate passivation after the Tafel region was recorded by Milosev *et al.*[88] (both in pH 7.4). The ageing of the passive film, with increased exposure time to the electrolyte/SBF, leads to an enhanced passive behaviour (demonstrated with an increase in the potential required for cathodic-anodic transition and in lower passive current densities).[89] Nevertheless, at higher potentials, above 0.6 V vs SCE, transpassive dissolution of the alloy occurs with the surface film no longer protective as the Cr(III) species are oxidised to soluble Cr(VI) species (according to equations 2.6(a-c)).[88,89,94] It is, therefore, the Cr(III)-based film which protects the alloy and defines its passive behaviour; while it has been suggested that Mo(VI) oxide plays a role in inhibiting transpassive dissolution by attaching to the outermost surface of the film.[95] Additionally, it has been proposed that the high current densities observed in the transpassive region are not only due to the dissolution of the alloy elements, but are also contributed to by water oxidation according to the reaction in equation 2.7.[96] Co has been shown to be a catalyst for water oxidation; in addition, after the oxidation of Co(II) from the alloy's surface film to Co(III), the later can also catalyse water oxidation.[97–99] Therefore, it is hypothesised that water oxidation may occur at relatively lower potentials and may become a dominant contributor to the observed transpassive current densities.

$$Cr_2O_3 + 10OH^- \rightarrow 2CrO_4^{2-} + 5H_2O + 6e^- \quad \text{Equation 2.6a}$$

$$Cr_2O_3 + 5H_2O \rightarrow 2CrO_4^{2-} + 10H^+ + 6e^- \quad \text{Equation 2.6b}$$

$$Cr_2O_3 + 5H_2O \rightarrow 2HCrO_4^- + 8H^+ + 6e^- \quad \text{Equation 2.6c}$$

$$2H_2O \rightarrow O_2 + 4H^+ + 4e^- \quad \text{Equation 2.7}$$

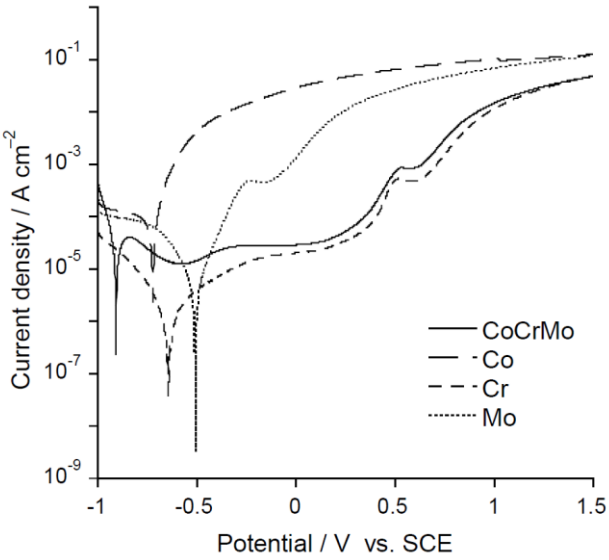


Fig. 2.1 Polarisation curves of CoCrMo alloy and its constituting metals in 0.14 M NaCl (pH 7.4). The passive and transpassive behaviour of the alloy is similar to Cr (reproduced with permission from[89]).

2.3.3 CoCrMo Dissolution

Many studies examined the extent and nature of ions released into the electrolyte/SBF, after immersion or polarisation of the CoCrMo alloy, using techniques such as inductively coupled plasma-mass spectrometry (ICP-MS) and atomic absorption spectroscopy (AAS). Several authors reported the concentration ratio of released Co ions to be higher than alloy composition stoichiometry after immersion (at open circuit potentials, OCP) or passive-domain polarisation.[85,89,93,100–103] For instance, analysis of Hank's solution after immersion of CoCrMo revealed high levels of Co ions in the solution which were higher than the stoichiometric ratio of the alloy when compared to Cr and Mo ions.[85] The overall ion levels in the solution increased when the pH of the solution was decreased from 6.8 to 2 (only Mo oxide is known to be more stable in acidic solutions compared to neutral or slightly alkaline ones[104]). Lewis *et al.*[100] reported that the Co:Cr ions ratio varied between 4 and 28 after up to 35 days of immersion in one of three solutions: synovial fluid, phosphate buffer solution or water. Furthermore, under both cathodic and passive-domain polarisation, Espallargas *et al.*[102] recorded high concentration percentages of Co ions (Co:Cr ratio varied between 4 and 8) in both NaCl and PBS solutions. The high concentration of Co ions after passive-anodic polarisation had also been reported by Hodgson *et al.*[89] in NaCl. However, after transpassive polarisation, both Hodgson *et al.*[89] and Espallargas *et al.*[102] reported stoichiometric dissolution. Stoichiometric dissolution was also observed by Zhang *et al.*[95] after transpassive polarisation (1.2 V and 1.5 V vs SCE) in highly acidic media (pH 0.69 and 1.25).

Transpassive polarisation leads to an increase in ion concentration in the electrolyte by several hundred and up to a thousand times.[102,103] Hedberg *et al.*[103] examined the speciation of chromium ions released in PBS, using AAS,

and reported Cr(VI) ions after 0.7 V vs Ag/AgCl polarisation. Ouerd *et al.*[94] had also reported the detection of Cr(VI) ions in PBS electrolyte after polarisation at 0.75 V vs SCE using ultraviolet-visible (UV/vis) absorption spectroscopy.

The enrichment of Co ion concentrations observed in media, after immersions at OCP or under passive polarisation, has been attributed to the solubility of the oxidised Co species in contrast to Cr which forms a solid oxide that remains on the surface.[102,105] This theory conforms with the stoichiometric ion concentrations usually reported after transpassive polarisation when all elements could form soluble species in the electrolyte. Furthermore, the high Co ion concentrations were also attributed to the preferential dissolution of the Cr/Mo–depleted matrix sites surrounding Cr/Mo-rich inclusions (further details are in section 2.3.6).[95]

2.3.4 CoCrMo Tribocorrosion

The degradation of CoCrMo implants or other metal articulating implants, *in vivo* would result from a combination of both mechanical wear and chemical corrosion. The synergistic effect of these two processes is termed tribocorrosion, which can be studied using similar rigs utilised for volumetric wear studies (as discussed in section 2.2) with an incorporated electrochemical set-up. A recent and comprehensive review of tribocorrosion behaviour of CoCrMo alloys was reported by Toh *et al.*[106]

Both mechanical friction and corrosion would modify the materials' surfaces and hence each process would affect the other resulting in complex degradation mechanisms. Therefore, knowledge of the tribological behaviour in the absence of a corrosive environment, and that of electrochemical behaviour in the absence of mechanical wear may not be sufficient for understanding the tribocorrosion behaviour of a material.[107] It is generally believed that the interplay between wear and corrosion results in accelerated degradation. Mathew *et al.*[108] found out the total weight loss of CoCrMo discs undergoing tribocorrosion (concurrent wear and corrosion) exceeded the sum of the weight losses from isolated wear and isolated corrosion. Mechanical load and friction at bearing surfaces causes damage to the passive oxide film (depassivation); the continuous cyclic depassivation and repassivation of the surface, under tribological contact, leads to higher rates of material dissolution.[109–111] This increase in material dissolution under tribological conditions is referred to as wear-accelerated corrosion. Conversely, changes to the passive film chemistry may modify third body behaviour and thus affects mechanical wear.[110–112] It was found that alloy mechanical wear was negligible under cathodic polarisation and during the cathodic-anodic transition but increased considerably as the potential increased in the passive domain (in pH 7.4), thus demonstrating the effect of corrosion on mechanical wear.[110] Furthermore, some authors have shown that the wear coefficient of CoCrMo increased considerably after a threshold applied potential of 0.2 V (vs SHE).[111]

One of the methods proposed to quantify material loss due to tribocorrosion, T was given by equation 2.8:[113,114]

$$T = W + C + S \qquad \text{Equation 2.8}$$

(Where, W is the material loss due to mechanical wear only, C is the material loss due to corrosion only (static conditions), and S is the material degradation due to the synergistic effects of wear and corrosion).

Several authors designed and performed an experimental protocol to measure these parameters for CoCrMo alloys; this involved measuring weight loss due to isolated corrosion (C) through a static polarisation measurement (at the free corrosion potential E_{corr}), weight loss due to isolated mechanical wear (W) through dynamic (*i.e.* under tribological contact) cathodic polarisation (cathodic protection), and total weight loss (T) through dynamic polarisation test (at E_{corr}). Mathew *et al.*[108] found that the synergistic component, S accounted for approximately 34 % of total weight loss. Furthermore, the overall corrosion related degradation (C + S) has been reported to contribute between 27 – 48 % of the total alloy volumetric wear, using conventional pin-on-disc tribometers,[115] and 22 – 32 % using a hip simulator.[116]

A second tribocorrosion quantification method is the mechanistic approach originally proposed by Uhlig *et al.*[117] where an expression for the total volume loss, V_{total} is given in equation 2.9:

$$V_{total} = V_{mech} + V_{chem} \qquad \text{Equation 2.9}$$

(Where, V_{mech} is the volume loss due to pure mechanical wear, and V_{chem} represents the volume loss due to wear-accelerated corrosion).

These values could be quantified experimentally, where V_{chem} can be obtained by monitoring the current during the mechanical rubbing and applying Faraday's law (equation 2.10). Consequently, V_{mech} can be calculated by subtracting the chemical volume loss V_{chem} from the total volume loss V_{total}; the later would be estimated through obtaining wear track profiles (cross-sectional surface area of wear tracks) and wear track length *via* techniques such as 3 D optical microscopy. A number of studies used this approach to quantify volumetric losses in CoCrMo discs where wear-accelerated corrosion V_{chem} was found to pose a significant contribution to the overall degradation of the alloy. Espallargas *et al.*[102] used optical profilometry to calculate the total volume loss from CoCrMo discs after tribocorrosion experiments in different media (mechanical rubbing with reciprocating tribometer and an applied anodic-passive polarisation) and estimated that V_{chem} accounted for 30 - 40% of the total volume loss. Furthermore, experiments by Munoz *et al.*[110] suggested that wear-accelerated corrosion may have a greater contribution to degradation in some scenarios with a range of 26 - 63%, where variations occurred according to applied potential (all anodic-passive potentials) and electrolyte (with or without protein).

$$V_{chem} = \frac{ItM}{nF\rho} \qquad \text{Equation 2.10}$$

(Where, I is the current, taken as the difference between the current observed during tribological sliding and the baseline current recorded before or after the mechanical sliding (thus it represents wear-accelerated corrosion only, eliminating contribution from corrosion occurring elsewhere away from the wear track), t is duration of the

experiment, M is the molecular mass of the alloy, n is the charge number of the oxidation reaction, F is the Faraday constant (96,500 C/mol), and ρ is the density of the alloy).

The accelerated corrosion by the mechanically-induced surface depassivation would still remain an underestimate of dissolution *in vivo;* this is due to the great number of wear particles generated which provide a large working surface area for further corrosion.[54,118]

2.3.5 Effect of Electrolyte Chemistry on CoCrMo Corrosion

Solution chemistry may modify the electrode-electrolyte interface and the passive film and therefore affect the corrosion mechanisms. The solution pH would affect the dissolution of metals in accordance with Pourbaix diagrams. Therefore the choice of environment for corrosion studies is important to mimic the corresponding *in vivo* conditions and provide accurate insight on the corrosion behaviour of biomedical alloys. The presence of proteins, phosphates, and oxidising species such as hydrogen peroxide (H_2O_2) have been shown to influence CoCrMo corrosion behaviour.

2.3.5.1 Effect of Phosphate

A comparison of CoCrMo polarisation curves in NaCl versus phosphate buffer solution (PBS) has shown that phosphates may act as anodic inhibitors (reducing the rate of the anodic reactions)[81,119] as well as cathodic inhibitors.[102] It has been suggested that phosphates adsorb strongly on the alloy and are responsible for blocking effect on the passive film.[81,94] This could be attributed to the formation of cobalt phosphates.[120] The precipitation of cobalt phosphate over time on the surface leads to an increase in film resistance. Furthermore, the presence of phosphates appears to induce transpassive dissolution at lower potentials compared to the behaviour in saline solution; with an early rise in current density (marked by a shoulder or a pronounced peak) observed in the polarisation curves (figure 2.2).[81,91,94,112,119] Similar effect was observed when Na-citrate complexing agent was added to an SBF solution.[88] This suggested that phosphate may also form complexes such as phosphate-chromium complexes which in turn activates transpassive dissolution. Ouerd *et al.*[94] who detected chromate (CrO_4^{2-}) ions in the electrolyte using ultraviolet-visible (UV/Vis) spectroscopy after transpassive polarisation, found out that the chromate ions concentration increased as the concentration phosphate in electrolytes increased. This was explained by a second mechanism for the production of chromate ions in phosphate solutions. While the first mechanism is the transpassive oxidation of Cr oxide from the passive layer (refer to equation 2.6), the proposed mechanism was the dissolution of a chromium phosphate layer which had formed upon immersion of the alloy (according to equation 2.11).

$$CrPO_4 + 8OH^- \rightarrow {CrO_4}^{2-} + {PO_4}^{3-} + 4H_2O + 3e^- \qquad \text{Equation 2.11}$$

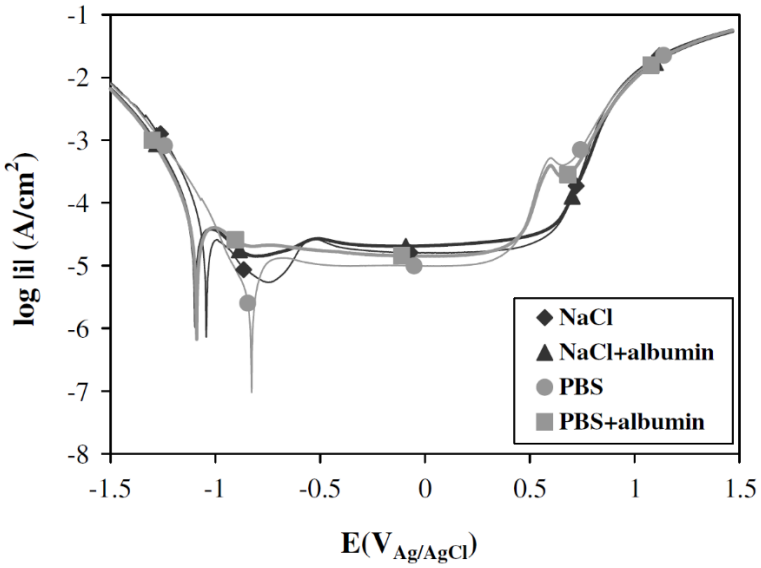


Fig. 2.2 Potentiodynamic polarisation curves of CoCrMo in NaCl and PBS with and without protein (reproduced with permission from [81]).

2.3.5.2 Effect of Proteins

Proteins may adsorb rapidly on metal surfaces and influence their corrosion behaviour. The extent of protein adsorption and its kinetics are influenced by a number of factors including surface conditions such as surface charge, surface energy, hydrophobicity, roughness, and thickness of the oxide layer.[121–125] Additionally, similar protein properties such as charge, size, hydrophobicity, and concentration may influence the adsorption process.[126] Solution properties may also play a role, for instance, the solution pH affects the charge of proteins and consequently, it may affect their adsorption on the metal surface. The isoelectric point of bovine serum albumin (BSA) is pH 4.9,[127] above which they are negatively charged and vice versa. Thus less acidic environments and higher anodic polarisation potentials (which favours the adsorption of negatively charged species) would encourage the adsorption of protein film resulting in greater surface coverage.[128,129] Nonetheless, protein adsorption may also occur when both the protein and the metal surface possess the same charge.[122]

The presence of proteins have reportedly had different effects on the corrosion behaviour explained by various mechanisms. For instance, proteins could bind to metal ions (forming metal-protein complexes) and transport them away from the interface thus encouraging further dissolution.[130] Furthermore, an adsorbed proteins film my restrict oxygen diffusion to the surface thus making it harder for the surface to repassivate (after mechanical depassivation). Enhanced alloy dissolution in the presence of proteins has been reported by some authors and attributed to the formation of organometallic complexes between metal ions and proteins.[65,129] Some studies reported an increase in Co ion concentrations in protein-containing electrolytes attributed to the formation of Co-protein complexes.[118,131] Moreover, the increased dissolution of Mo, in particular, has been well documented recently, which was also attributed to the formation of Mo-protein complexes.[102,132] Surprisingly, Mo ions

represented the highest concentration percentage in BSA-containing electrolytes after static immersion experiments at OCP[132] as well as cathodic and passive-anodic polarisations[102](however, under transpassive polarisation the ion concentrations were close to the alloy stoichiometry as discussed in section 2.3.3). While the data by Espallargas *et al.*[102] suggested that Co returned to be the highest concentration ratio in electrolytes (including BSA) after dynamic (tribocorrosion) conditions; Simoes *et al.*[132] still observed highest concentration ratios of Mo after tribocorrosion owing to filtering the electrolyte with a nanoporous filter (to remove contributions from metallic nanoparticles) prior to ICP-MS analysis.[132]

On the other hand, several authors have reported a corrosion inhibition behaviour of proteins. It was hypothesised that a metal/protein/hydroxide complex forms and becomes adsorbed to the surface restricting metal dissolution.[127] In addition, it was also suggested that the protein film acts as a diffusion barrier restricting metal dissolution[133] or, as a negatively charged barrier, preventing corrosive anions (such as chlorides) from reaching metal surface.[100] In fact, Sun *et al.*[65] reported enhanced dissolution in the presence of proteins only in static conditions, whereas in tribological conditions reduced dissolution was observed, likely due to the formation of the tribolayer. Nonetheless, in static conditions BSA has been reported to act as a cathodic inhibitor in neutral environments,[81,102,112,119] as well as in acidic conditions.[133] Increasing the BSA concentration was also found to increase the stability of the passive film.[134] Furthermore, in the presence of BSA, the repassivation rate (after induced mechanical depassivation) was increased in neutral/alkaline pH compared to acidic pH. The opposite effect was observed in inorganic electrolytes. This was explained by a further mechanism whereby the suppression of Co oxide formation in the presence of BSA[90] leads to the undisturbed formation of the protective Cr oxide. Furthermore, Hedberg *et al.* [93] observed a drop in released metal ion concentrations when BSA was contained in the electrolyte. Additionally, Mathew *et al.,*[108] who measured weight loss of CoCrMo discs in tribocorrosion experiments, concluded that BSA reduced the tribocorrosion rate (however in this study this observation could be attributed to either the proteins inhibition of corrosion or mechanical wear or both). The fraction of volumetric wear loss due to wear-accelerated corrosion, V_{chem} out of total volumetric loss, V_{total} (refer to section 2.3.4 and equation 2.9) was found to be lower in BSA solutions compared to NaCl, under applied anodic-passive polarisation, for both HC and LC alloys[110,112](although this effect was not as conclusive when BSA was compared to PBS[112]). Furthermore, the presence of a tribolayer (which forms on the alloy surface during tribological contact in the presence of proteins, as discussed in section 2.2.3) on tested HC and LC CoCrMo discs reportedly resulted in lower corrosion rate.[75]

The contradictory conclusions made on the effect of protein on CoCrMo corrosion are possibly a result of discrepancies in the various factors affecting protein adsorption on the metal surface. Additionally, it was recently argued that the kinetics of protein-metal interactions play a role in changing the effect of protein on the metal degradation process.[126] While the adsorbed protein film may act as a coating inhibiting cathodic reactions and initial corrosion, it was argued that this is a short-term (few hours) effect. The formation of protein-metal bonds on

the surface oxide layer of stainless steel was relatively sluggish and the subsequent detachment of metal-protein complexes from the surface was an even slower process.[123,124] Thus, enhanced metal release in the presence of protein may be observed in longer-term studies. An oxidative environment (mimicking the *in vivo* inflammatory conditions) may also affect protein-metal interactions. For instance, direct interaction of proteins with the metal surface (as opposed to the oxide layer) is more rapid and hence protein may lead to faster dissolution in non-passive conditions. Nonetheless, the process may remain relatively slow: enhanced metal release in the presence of both proteins and hydrogen peroxide was recently observed only after 24 hours in Ti6Al4V alloys.[135,136]

The presence of both phosphates and BSA in the solution may lead to interactive mechanisms due to adsorption competition between the two species. Munoz *et al.*[119] suggested that BSA may limit adsorption of phosphates on the CoCrMo surface but without increasing corrosion rate, due to acting as a cathodic inhibitor. Some authors observed a similar cathodic inhibition behaviour by BSA both in the presence and absence of phosphates.[81] However, other authors reported a little effect of BSA in the presence of phosphates.[94,112]

2.3.5.3 Effect of Simulated Inflammatory Conditions

The *in vivo* inflammatory response associated with metal implants presents a harsh oxidising environment which may lead to enhanced metal corrosion. The electrochemical behaviour of the CoCrMo was examined in simulated inflammatory environments to mimic the conditions of an activated macrophage cell. This included the presence of hydrogen peroxide (an oxidising agent) in PBS solution, lowering the pH (using HCl), as well as the addition of Fe(III) ions with H_2O_2 (Fenton reaction which converts the hydrogen peroxide to a hydroxyl free radical).[137,138] Significant increases in open circuit potential (OCP) and corrosion currents were observed in the simulated inflammatory solutions compared to PBS only.[138] Furthermore, simulated inflammatory conditions altered the surface oxide film properties such as a decrease in resistance and an increase in capacitance (as measured by EIS),[138] as well as a decrease in surface roughness, which was observed by AFM.[137]

2.3.6 Effect of Microstructure on CoCrMo Corrosion

The microstructure and composition of the alloy naturally affect their corrosion behaviour due to changes in surface chemistry. While some authors showed that HC alloys demonstrated better corrosion resistance compared to LC;[139] the general consensus indicates that increasing volume fraction of the metal carbide precipitates leads to enhanced dissolution. A lower carbon content in the CoCrMo could contribute to greater chemical and microstructural homogeneity and thus a better corrosion resistance.[140,141] The positive effect of microstructure homogeneity on corrosion resistance was also reported more recently by Hedberg *et al.,*[93] who observed higher metal ion release from as-cast CoCrMo compared to CoCrMo alloys fabricated by selective laser melting (SLM). The SLM process involves rapid cooling rates which suppresses both the formation of carbide precipitates as well as the martensitic (γ-fcc to ε-hcp) transformation (due to the slow kinetics of the phase transformation) resulting in

a more homogenous structure. Several authors have established that carbide boundaries and grain boundaries are preferential dissolution sites susceptible to localised attack.[52,58,92,137,142–144] Since the metal carbide precipitates tend to be Cr and Mo-rich, the adjacent matrix regions are deprived of Cr, the element responsible for the alloy's protective passive film. These Cr depleted regions have been suggested as the reason behind increased corrosion in HC alloys.[142] Nanoscale Cr depleted regions at grain and inclusion boundaries were found to be the corrosion initiation sites leading to grain boundary crevice corrosion.[145] The presence of fewer carbide inclusions results in increased resistance against the intergranular attacks.[146] Higher levels of dissolution have been observed in as-cast alloys compared to heat treated alloys at transpassive potentials.[144] One order of magnitude higher impedance was observed (*via* EIS) in double heat treated (solution annealing and HIP) versus single heat treated (solution annealing only) indicated the presence of a thicker passive film on the former.[143] These observations are attributed to the dissolution of the carbide precipitates by heat treatments (refer to section 2.1.4). Atomic force microscopy (AFM) has shown etching-like dissolution surrounding the Cr-rich metal carbide precipitates at transpassive potentials.[92] Furthermore, several authors revealed that the increase in grain boundaries can accelerate the anodic reactions.[147,148] This observation was restated in both protein and non-protein solutions.[58] Bettini *et al.*[144] revealed Cr depletion at grain boundaries, using EDX, which was due to the presence of submicron carbide precipitates. Although the previously mentioned studies observed this selective dissolution of carbide boundaries under anodic polarisation, Wang *et al.*[52] observed the same phenomenon at open OCP but under tribological conditions. They detected a drop in the Volta potential in the alloy matrix surrounding carbide precipitates thus a galvanic couple may form between the carbide (as the cathode) and its surrounding boundary (as the anode). Galvanic corrosion is then facilitated by the removal/damage of the passive film by the mechanical wear. In addition, they suggested that the selective dissolution of these carbide boundaries facilitates the release of carbide particles where they contribute to abrasive wear when trapped between the two articulating surfaces (as discussed in section 2.2.2). The selective dissolution of these Cr and Mo depleted regions surrounding these inclusions have been suggested as one of the mechanisms behind the observation of high Co ions content in electrolytes (refer to section 2.3.3).[95] Further studies on microstructure effects on the alloy dissolution included the effects of sigma σ-phase area fraction on the corrosion behaviour.[149] The authors varied the area fraction of σ-phase by changing thermal ageing time and concluded that it had no effect on the passive and transpassive behaviour of the alloy through electrochemical polarisation tests. However, while the amount of Co ions released did not vary, they concluded that release of Cr and Mo ions increased with the increasing area fraction of σ-phase.

While microstructure aspects influence alloy dissolution, an applied electrochemical potential may lead to microstructural changes. It has been shown that an increase in applied electrochemical potential leads to a severer subsurface plastic deformation layer. The dominant mechanisms governing this plastic deformation included the formation of stacking faults, grain subdivision and martensitic transformation (γ-FCC to ε-HCP). In addition,

transmission electron microscopy revealed the formation of an ultra-fine grain nanocrystalline layer on surfaces polarised at 0.2 V (vs Ag/AgCl).[150] These effects are similar to the effects of mechanically-induced strain on the surface microstructure (as discussed in section 2.2.2).

2.4 CoCrMo Biological Impact

Although CoCrMo alloys have been used as a biomaterial, including in the first generation MOM implants, since the 1940s,[151] their use declined after the introduction of low friction MOP utilising a polyethylene acetabular component. However, osteolysis (briefly defined as periprosthetic bone resorption – which occurs due to an immune response provoked by implant-derived wear) led to the aseptic loosening of implants and caused considerable concern as the most common failure mechanism of hip implants.[152] This triggered a revived interest in what would be called the second generation of CoCrMo-based MOM implants (featuring higher levels of carbon for enhanced wear resistance). Characteristics such as high wear and corrosion resistance provided optimism on the potential of CoCrMo as a suitable implant material for younger and more active patients. However, evidence indicated that failure rates of CoCrMo implants are much higher than expected with some patients requiring revision surgery after only five years.[18,20] The consequences were the withdrawal of many CoCrMo devices from markets, large product liability lawsuits,[22,23] and a growing economic burden due to implant revisions.[19]

In general, osteolysis is associated with inflamed periprosthetic membrane rich in activated macrophages, cytokines and implant-derived wear particles. Further details on the mechanisms underlying osteolysis were reported by many authors.[13,153–157] Many studies indicated that the inflammatory response associated with osteolysis is provoked by polyethylene (PE) and Ti particles from MOP implants[12,153,156,158,159] (although evidence of osteolysis in the case of CoCrMo MOM implants has also been reported[160,161]). Although Goodman[162] suggested that metal particles are more likely to induce osteolysis than polymer particles, it was reported that Ti particles (associated with MOP implants) induced the release of bone resorption mediators (which cause osteolysis) significantly more than CoCrMo particles.[163] In fact, second-generation CoCrMo MOM were introduced in the early 1990s with the aim of eliminating MOP- induced osteolysis. However, MOM exhibited high failure rates; a significant number of patients suffered early pain which was found to be associated with abnormal soft tissue reactions.[164] It appears that the reason for early MOM implant revisions is a different inflammatory mechanism which may be associated with the formation of pseudo-tumours.[26,165] For instance, while Ti particles induced the release of bone resorption mediators more than CoCrMo particles, the latter was found to cause significantly higher levels of stress factors (hypoxia associated responses and inflammatory cytokines) in human macrophages and periprosthetic tissue.[166] It has been reported that although periprosthetic tissue reactions surrounding MOM implants have some histologic characteristics similar to the ones surrounding MOP implants, they appear to be less intense and are characterized by fewer histiocytes.[76,167]

The inflammatory tissue response in failed MOM implants was also attributed to implant-derived wear particles after histological evidence revealed small black particles were associated with macrophages in superficial and deep tissue.[4,26,165,168] Additionally, several studies suggested that the probability for the inflammatory conditions occurring is directly proportional to the wear debris levels: through comparing the observed volumetric wear [2] as well as the metal ion levels in serum.[3]

2.4.1 Particle-Induced Inflammation

MOM junctions demonstrated low volumetric wear both in hip simulators[169–171] and in early clinical studies.[9,172–174] However, despite exhibiting lower volumetric wear compared to MOP implants, it was suggested that MOM implants produced more, but only smaller, wear particles.[175] MOM wear particles were reported to be an order of magnitude smaller than PE particles and that 100-fold more particles were produced per unit volume of wear compared to PE.[55] Moreover, other studies predicted the number of MOM wear particles to be 13,500 times more than MOP wear,[176] and *one trillion* MOM particles were estimated to be generated in one patient annually.[24]

The lower rates of osteolysis and different inflammatory mechanism observed in MOM compared to MOP may suggest that wear particle size plays a role in the mechanism of failure. It is generally hypothesized that these differences are likely to be related not just to total particle volume but also to specific particle features.[1] For instance, some studies have already shown how nanoparticles from air pollution are more biologically active and lead to greater inflammation than larger particles.[177,178] Many studies have revealed the difference in cellular response to implant wear particles of different size, shape and composition.[179–183] Papageorgiou *et al.*[182] used TEM to study the interaction mechanisms between human fibroblasts and both nano and micro-sized CoCr particles. They observed a rapid dissolution and corrosion of nanoparticles which were distributed within cell vacuoles across the cytoplasm. On the other hand, micro-particles were accumulating around the nucleus and persisted for at least five days.

In addition to particle type affecting particle-cellular interactions, cell type may also result in different conclusions. Shah *et al.*[184] have demonstrated that the cellular uptake and processing mechanisms of CoCr particles differed between human osteoblasts and primary human osteoclasts.

Wear particles have a greater interaction surface area per mass and thus their corrosion inside the body could lead to significant release of metal ions. These metal ions could potentially induce the release of pro-inflammatory cytokines more than particulate wear debris.[185] The increase in inflammation would lead to the generation of more reactive oxygen species (ROS) and rise in local electrochemical potential, hence leading to more dissolution. The dissolution of wear particles also poses major health concerns due to the toxic nature of released metal ions (more details in section 2.4.3).

2.4.2 CoCrMo *in vivo* Distribution

Studies on the periprosthetic tissue (surrounding failed implants) have shown that CoCrMo wear-particles are typically found inside macrophage cells (figure 2.3).[4,168,176] Widespread dissemination of metal wear debris has also been established in post-mortem studies with particles found within macrophage cells in the splenic, hepatic, and cardiac tissue.[186,187] Furthermore, particles were also found in extracellular locations in the synovial membrane, lymph nodes and bone marrow.[188] Additionally, high levels of Co and Cr ions have been observed in the blood of patients with failed implants and it is understood that the increased ion levels are a result of implant wear and corrosion products.[189,190] Jacobs *et al.* [191] compared Co and Cr blood levels before and one year after implant surgery and found they were increased by 6 and 21 times respectively. A retrospective analysis found that elevated Co and Cr ion levels in patients' blood and synovial fluid did not vary across different implant manufacturers or femoral head size.[192]

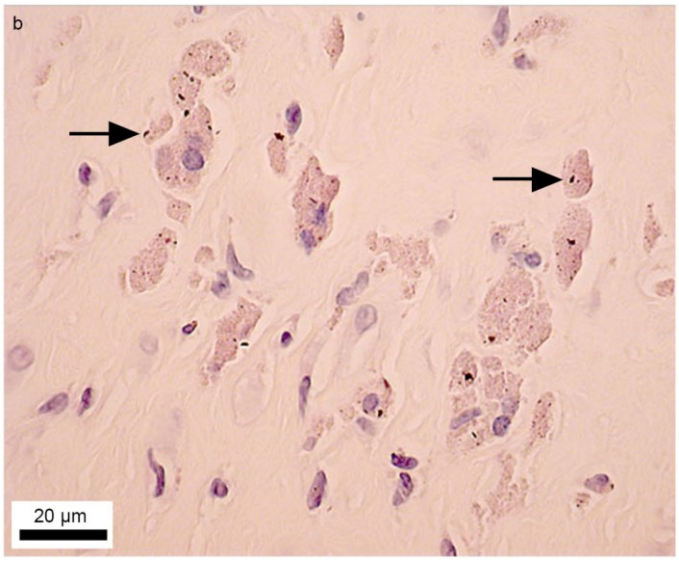


Fig. 2.3 Light microscopy image showing wear particles (black spots) in macrophage cell from periprosthetic tissue (adapted and reproduced with permission from [4])

2.4.3 CoCrMo Toxicity

The immune system's inflammatory response is known to cause a local oxidising environment with a rise in local electrochemical potential *via* the production of reactive oxygen/nitrogen species.[193,194] Surface damage on retrieved CoCrMo metal implants has been reported as inflammatory cell-induced (ICI) corrosion being the result of the cells sealing on the metal surfaces and releasing reactive oxygen species (ROS).[195,196] In addition, these oxidising conditions drive the dissolution of the metal wear particles.

The large number of CoCrMo wear particles produced *in vivo* provides a much greater active surface area compared to their geometrical surface area. The potential dissolution of these wear particles would lead to the release of metal ions with cytotoxic, genotoxic and immunological risks. Great attention has been given in the

literature to the potential biological effects of Co and Cr ions and the reader is referred to literature reviews such as Hosman *et al*.,[193] Gill *et al.,*[27] and Konttinen *et al*.[25]

Yue *et al*.[183] have shown evidence that the cellular uptake rate maybe size dependent (although using chitosan rather than metallic particles) as smaller particles (~ 400 nm) accumulated in macrophages quicker than micro-particles (~ 2 μm and 5 μm). In addition, they demonstrated that smaller particles (~ 400 nm) are transported in macrophages *via* the lysosomal pathway while larger particles may remain in the cytoplasm. The lysosomes are acidic compartments (pH ~ 5)[197,198] which are naturally used for degradation of unwanted cytoplasmic material and organelles;[199] therefore, they form a corrosive environment for metallic particles with the risk of toxic ions release. Figures 2.4 and 2.5 illustrate proposed mechanisms for wear generation, cellular uptake of CoCr species and their intracellular effects.

Cytotoxicity effects have been one of the major health concerns. *In vitro* cell viability studies suggested that Co is the element posing a more cytotoxic risk. Catelas *et al.*[200] demonstrated a significant reduction in macrophage viability at concentrations of 8 – 10 ppm Co(II) and 350 – 500 ppm for Cr(III). Furthermore, Kwon *et al.*[201] studied macrophage viability against concentrations of Co and Cr nanoparticles as well as Co(II) and Cr(III) ions. In both cases (nanoparticles and ions), concentrations of Co reduced the cell viability significantly more than Cr. Cytotoxicity of the Cr(VI) ion has been demonstrated on human lymphocyte cells although it remained lower than the Co(II) ion.[202]

Genotoxicity is another major health concern associated with metal particles and has been observed in MOM patients.[203]Several transition metals are known to be mutagenic and genotoxic.[204] The genotoxic effects of CoCr particles have been demonstrated in a number of *in vitro* studies.[205–207] Both Co and Cr could induce genotoxic effects but Cr was considered the metal of more concern, particularly Cr(VI) species. Cr(VI) species are classified as carcinogenic to humans and are associated with elevated incidence of respiratory cancers.[208] Furthermore, when Cr(VI) is reduced inside cells to Cr(III)[184] it leads to the production of reactive oxygen species which may, in turn, cause DNA damage.[27] Cr(III) may also cause DNA damage *via* a number of mechanisms.[209,210] Ladon *et al.*[211] studied chromosome aberrations in peripheral blood lymphocytes of MOM patients. There was a significant increase in chromosome translocations and aneuploidy (the presence of an abnormal number of chromosomes in a cell) over time, accompanying a significant increase in Co and Cr ion levels in the blood. Chromosomal aberrations and translocations were higher in MOM patients compared to MOP patients and a control group [203].

While cellular uptake through phagocytosis may be recognised as the critical path for wear particle-cell interactions, direct interactions between particle and cell membranes may be sufficient to activate an adverse response. Bhabra *et al.*[212] revealed that small CoCr nanoparticles (~ 30 nm) can damage human fibroblasts across an intact cellular barrier (without having to cross the barrier).

Further effects on health have been examined through studies on the influence of CoCr wear on the immune system. Hosman *et al.*[193] suggested that the large dissemination of metal wear particles across many body organs is maybe an indication that the immune system has been hampered. They note that the presence of a foreign body reduces the number of bacteria required to cause an infection. However, on the other hand, the toxic nature of CoCr wear may inhibit bacterial growth. Therefore, the authors concluded that whether CoCr particles lead to an increase or decrease in infection risk remains questionable.

In conclusion, the biological toxicity effects are the most significant concern with MOM implants and in particular the strong genotoxic effects of Cr(VI). Although currently there is no strong epidemiologic evidence of carcinogenic consequences, and the mortality rates of MOM patients are similar to those of the general public [213,214] it is well known that these effects are expected to have long-latency times.[215] Long-term monitoring of patients is required to discover the effects of CoCr wear debris.

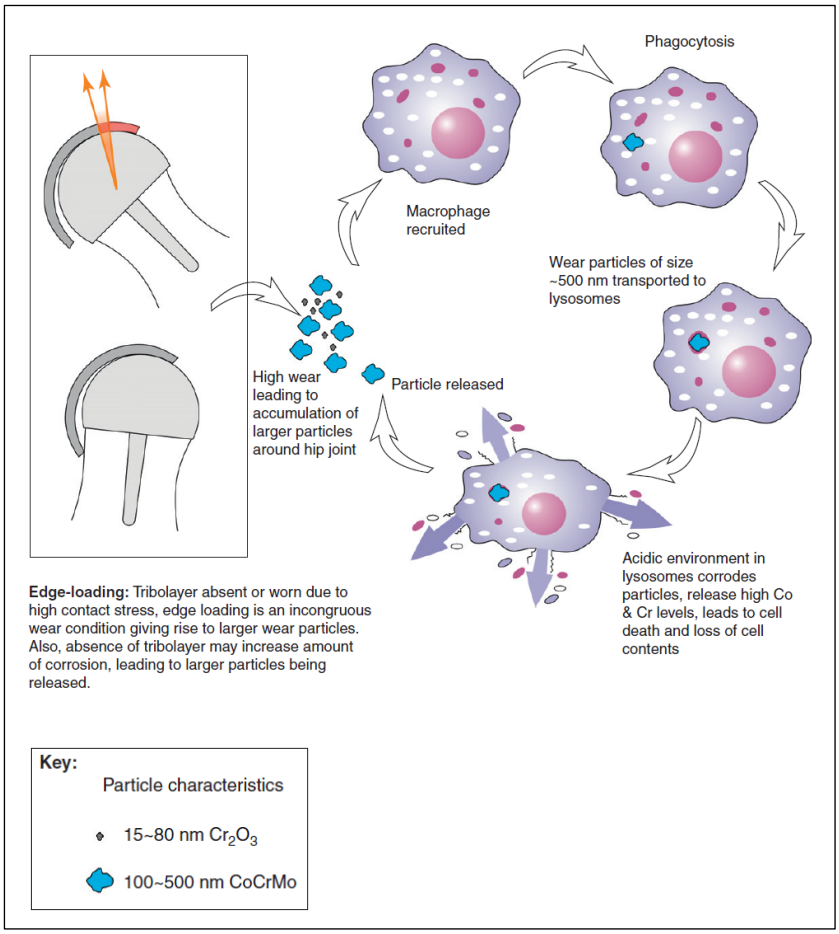


Fig. 2.4 Model for the process leading to inflammatory tissue reaction. The relatively bigger wear particles, which are metallic and of the bulk alloy composition, are phagocytised by macrophages and transported to the acidic environment in the lysosomes where they corrode releasing metal ions. (adapted and reproduced with permission from [27])

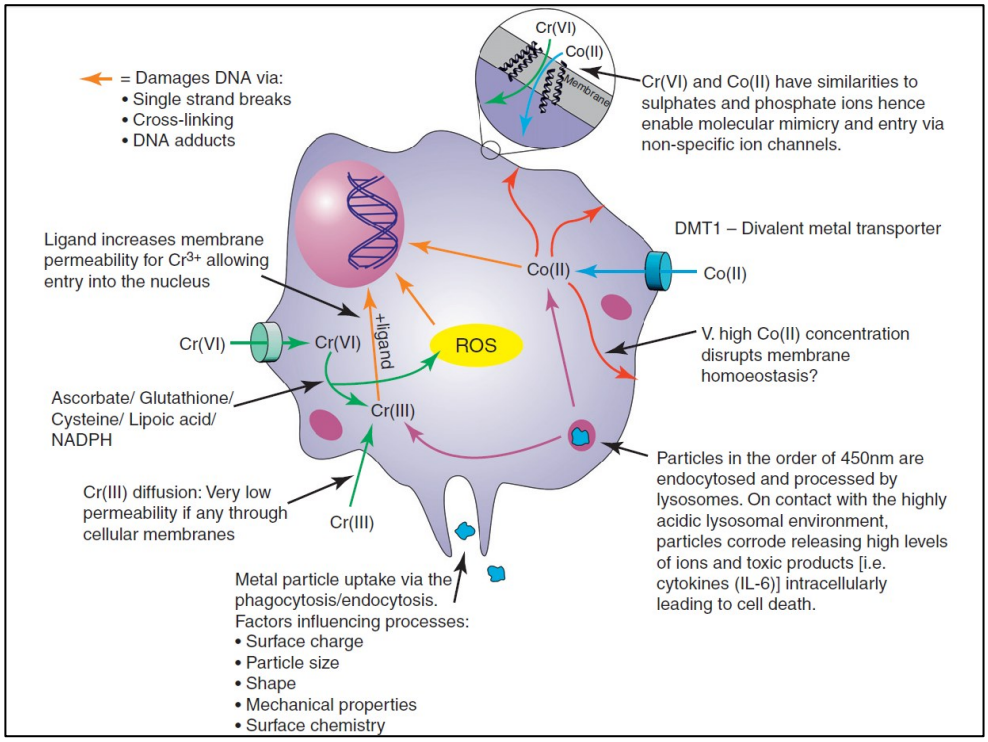


Fig. 2.5 Schematic illustrating the mechanisms of cellular uptake of wear products, their intracellular metabolism, and effects (reproduced with permission from [27]).

2.5 CoCrMo Wear Particles

2.5.1 Characterisation of *in vitro* Wear Particles

Various studies characterised *in vitro* produced wear particles, such as those produced by reciprocating pin-on-disc wear machines or hip simulators. The wear debris was found to be formed in many different shapes: globular, oval, needle, as well as irregular shaped particles. These particles have been found to be in a good approximation of size and shape with *in vivo* generated particles. Catelas *et al.*[1] reported particles with an average size of 50 nm using a hip simulator. Other authors have reported globular particles up to 100 nm in diameter and needle-shaped particles up to 1 µm in length.[67] It has been shown that pin-on-disc particles may fall within two size distributions: a majority group with a size range of 10 – 100 nm and second minority group with ranges of ≥ 1 µm.[118] Two distinctive chemical compositions have also been reported: small Cr-rich particles hypothesized to be Cr-oxide from the passive film, as well as metallic CoCrMo.[1,67,118] The CoCrMo particles may exhibit varying Co and Cr ratio which may possibly be due to the difference in the origin of particles whether it is the matrix material or inclusions.[1]

Simoes *et al.*[216] have also produced wear particles by ball milling of CoCrMo powder. The milling process involved bombarding CoCrMo powder using a zirconium ball in a zirconium vial. This technique was employed due to the limitation of pin-on-disc and hip simulator devices in generating a large volume of wear particles in a reasonable amount of time. The resulting particles shared similar size and shape characteristics to particles produced by traditional wear devices, with a majority size distribution within the range of 10 - 200 nm. While the original powder

exhibited a predominantly FCC structure, the produced wear particles showed a significant increase of HCP phase. In particular, smaller particles (< 200 nm) consisted of a predominantly HCP structure. This change in microstructure is due to the strain-induced transformation of the FCC to HCP phase.

2.5.2 Chemical Characterisation of *in vivo* Produced Wear Particles

In order to obtain insights on the *in vivo* reactivity of the CoCrMo wear particles, a number of studies have characterised the chemical composition of particles from the periprosthetic tissue. In general, it was found that wear debris existed in two main states; a metallic state, as a result of the mechanical wear of the implant, and metal corrosion products, resulting from reactivity with the surrounding biological environment. The size of the wear particles ranges from 10 nm to few microns, with the metallic particles usually responsible for the latter end of the scale.

Huber *et al.*[217] examined tissue from 11 cases where the inflammatory reactions characteristic of an immune response were evident in all. Using scanning electron microscopy-energy dispersive X-ray (SEM-EDX) and Fourier transform infrared (FTIR) spectroscopies they reported Cr phosphate-like corrosion products as well as un-corroded metallic particles. However, Doorn *et al.*[176] and Catelas *et al.*[218], using EDX in the transmission electron microscope (TEM), reported Cr oxide corrosion products, and a lack of Co, in tissue surrounding different types of failed MOM implants. Addressing this difference in the reported Cr species, Hart *et al.*[24] used microfocus X-ray absorption spectroscopy (μ-XAS), at synchrotron facilities, which would provide additional speciation information, higher sensitivity to lower concentrations, and avoids electron beam effects (compared to EDX). They reported the most abundant species to be Cr-phosphate residues which did not vary across four different MOM manufacturers and patients' blood metal ion levels. Consequently, Goode *et al.*[4] used scanning transmission X-ray microscopy-X-ray absorption spectroscopy (STXM-XAS) and scanning transmission electron microscopy- electron energy-loss spectroscopy (STEM-EELS) combining chemical analysis at both high energy and spatial resolution. Their results confirmed the presence of debris in two phases, a minority metallic phase (often found as the 'core' of the reacted particle) and a more abundant Cr(III) phase with only trace amounts of oxidised Co. The reported deficiency of Co in wear particles, across all the above studies, would indicate rapid dissolution of Co, likely into aqueous Co(II), which could then reach the bloodstream and be transported away. The particles examined in these studies include relatively large particles, which therefore are not particles to have originated from the Cr-rich passive film, but are likely to have originated from alloy bulk with a near stoichiometric composition.

Given that CoCrMo alloys are a nominally stable material, the large extent of Co dissolution reported from CoCrMo particles was unexpected, unless the *in vivo* environment imposes highly oxidising (transpassive) conditions. Therefore, these results raise questions from material science regarding the dissolution mechanism of CoCrMo. Additionally, the speciation of Cr in the process is a major clinical concern given the carcinogenic nature of Cr(VI)

species. None of the above *ex vivo* studies reported the detection of Cr(VI) species but would not be conclusive evidence on its absence *in vivo*. Cr(VI) is an unstable (transient) species in the generally reducing biological environments and would be reduced to Cr(III) once oxidising conditions are removed.[184,219] Only recently, Swiatkowska *et al.*[187] detected concentrations of Cr(VI), using μ-XAS, in post-mortem splenic, hepatic, and cardiac tissue from hip implant patients who had been diabetic. They hypothesised that the elevated levels of oxidants (reactive oxygen species) in the blood of diabetics[220,221] could have encouraged the oxidation of implant-derived Cr(III) species.

The studies on the composition of wear particles in explanted tissue provide no information on the history of the wear debris, such as length of exposure to the various conditions in the body. They provide information on the final state of the wear debris (after implant failure) but little insight on intermediate species, reaction rates, and mechanisms triggering an inflammatory response could not be concluded. In addition, tissue preparation treatments for sample characterisation may affect the results reported by these studies. The development of an *in situ* approach is therefore essential to gain more understanding on wear-particle dissolution.

2.6 *In situ* Spectromicroscopy

Developing an understanding of the *in vivo* dissolution mechanism of wear particles requires the monitoring of chemical and physical changes to the particles in a controlled environment. A more holistic understanding can be achieved with a correlative - spectroscopy and microscopy - approach where complementary information on chemical and morphological changes can be connected. Many characterisation techniques, as discussed throughout this chapter, had been used *ex situ* (after immersion or polarisation of alloy discs in SBF, or on explanted tissue samples from patients) including: XPS for identifying chemical composition of passive films, EDX for elemental composition of *bulk* samples and explanted wear particles, synchrotron XAS for high resolution chemical speciation analysis, as well as optical, electron and X-ray microscopes. However, not all techniques provide the capability for *in situ* measurements, in particular for corrosion studies where the intrinsic requirement for wet environments could be challenging. The development of an *in situ* approach would be a vital step towards elucidating the dissolution mechanisms of wear debris, in particular identifying the onset of morphological or chemical changes and the existence of transient species such as Cr(VI). A high spatial resolution would be essential for monitoring nanoscale morphological changes, and a high energy resolution would be necessary for sensitive chemical speciation analysis, especially with low concentrations/nanoscale materials. TEM and synchrotron TXM both provide *in situ* microscopy capabilities; and combined with EELS and XAS respectively, they offer spectromicroscopy approaches providing spatially resolved chemical information. In principle, TEM-EELS offers an atomic-scale spatial resolution, and a monochromated instrument can allow for 0.1 eV energy resolution.[222] However, TEM-EELS is limited to a sample thickness of a 100 nm or less and strict vacuum

conditions. In addition, water radiolysis by the electron beam produces radicals and therefore causes changes in the local chemistry.[223] It may be argued that this would mimic the production of reactive oxygen species associated with the *in vivo* inflammatory response, however, the exact conditions of the study may not be accurately known. In other words, the electron beam poses a problem for accurate control of electrochemical environments. These reasons make the use of liquid cells in TEM challenging. On the other hand, synchrotron-based TXM-XAS provides a high energy resolution up to 0.05 eV,[224] and current state-of-the-art X-ray microscopes have spatial resolution on the order of 10 nm and are continuing to improve.[225] Additionally, X-rays have a longer path length compared to electrons (of the same energy) and the water X-ray absorption edge is at energies far below absorption edges of CoCrMo metals. Although synchrotron hard X-ray imaging on realistic *in situ* samples often provides the relatively inferior (compared to TEM) sub 30 nm spatial resolution, it remains of increasing interest for *in situ* studies due to its natural characteristics: relatively non-destructive, chemically sensitive, and highly penetrative.

Synchrotron XAS has been used for *in situ* investigation for the corrosion and passivation behaviour of different alloys for a few decades. In 1990 Kerkar *et al.*[226] used *in situ* XAS to study the structure of the passive film which forms on both Fe and FeCr alloy in an aqueous environment. Additionally, *in situ* XAS has been used to study changes to passive film composition of FeCr and NiCr alloys during passive and transpassive polarisation.[227,228]Furthermore, *in situ* XAS was used to study speciation changes of sputter-deposited Cr_2O_3 and Fe_2O_3 thin films (as artificial passive films).[229] *In situ* X-ray spectromicroscopy is of increasing interest recently with applications such as chemical mapping studies on battery materials,[230,231] and observation of nanoparticle growth.[232]

2.7 Summary and Aims

The choice of CoCrMo alloys for MOM implants, and as a biomaterial in general, relied on favourable properties such as their high fatigue strength, wear resistance, and corrosion resistance. MOM implants exhibited less volumetric wear than the most commonly used MOP bearings; moreover, their mechanical properties allow for the use of thin-walled acetabular components and hence larger femoral heads can be used (which minimises dislocations). Additionally, they allow for hip resurfacing designs which preserve femoral bone stock (and hence could be used in younger, more active, patients). All these factors made MOMs an attractive choice for hip replacements, becoming increasingly popular in the first decade of the century, making up to 35 % of total hip replacements procedures in the USA. However, an unexpectedly high failure rate of MOM implants was observed owing to a degradation-induced adverse bodily response. The alloy's degradation results in both micro and nano wear particles and corrosion products which trigger macrophage cells and result in an inflammatory reaction. Regulatory agencies in the UK and USA have issued alerts for MOM hip implants in 2010 and 2011 respectively. The unexpected high failure rate of hip implants has fuelled extensive research on multiple fronts including the

alloy's wear and corrosion behaviour, clinical risks of alloy wear, as well as methods for improving the alloy performance such as surface coatings,[233] plasma nitriding,[234,235] and other fabrication techniques (such as selective laser melting[93] and electron beam melting[236]).

CoCrMo alloys are available in several different conditions defined primarily by their starting composition (*e.g.* low or high carbon content), the conditions of manufacture (*e.g.* cast, wrought, or forged alloys) and subsequent thermal treatments (solution heat treatment, hot isostatic pressing or sintering) that are also time and temperature dependent. Variation of any of these factors can significantly alter the materials microstructure and therefore the mechanical and electrochemical properties. Optimisation of these parameters is challenging due to the different opposing effects they may have on the alloy degradation (for instance hard carbide precipitates may improve the alloy's strength, but carbide boundaries are selective dissolution sites leading to increased corrosion. Furthermore, dissolution of carbide boundaries causes carbide particles to be released and act as abrasive particles, thus increasing the wear rate).

CoCrMo wear particles can be generated in large numbers *in vivo* with estimates of *one trillion* particles or more could be generated in one patient annually.[24] CoCrMo wear particles are generated at femoral head-acetabular bearing surfaces and also at other implant junctions such as the taper junction (femoral head-neck with implant stem).[237] The wear particles induce an immune inflammatory response which leads to the eventual failure of the implant and the need for revisions surgeries. Wear particles disseminate systematically to different organs with potential cytotoxic and genotoxic consequences. Due to their small size, wear particles generate a relatively large surface area to react with the biological environment, and elevated Co and Cr ion levels have been routinely observed in patients' blood.[189,190] Chemical speciation of *in vivo* produced wear particles consistently revealed a composition predominately rich in Cr with only trace amount of Co, despite the original alloy stoichiometry Co:Cr being 2:1. CoCrMo is predicted to be an extremely stable material with a robust passive film, therefore such a large extent of Co dissolution is not expected, and the mechanism of CoCrMo-particles' dissolution is not well-understood. The speciation of Cr in the process is clinically critical, as the transpassive dissolution of the alloy film would result in the release of the highly carcinogenic Cr(VI) ions.

The lessons learnt from MOM hip implants are expected to aid in the development of safer future medical innovations.[238] CoCrMo alloys are not limited to hip implants and have been used in other devices featuring articulating junctions and potential for wear debris releases such as total knee replacements and total disc replacements.[239] Even though generally recognized as a key issue in the success of metallic implants, many questions still remain for a complete elucidation of the complex corrosion mechanisms at play. The dissolution of wear particles may not be the only source of metal ions *in vivo*; tribocorrosion of the bulk material at implant junctions (such as the taper junction[240]), as well as at the alloy-cement interface[105] are other potential routes for ion release. However, corrosion of the bulk material under tribological contact could be explained by mechanical

depassivation of the surface, while the dissolution of metallic particles is not so readily understood. Additionally, the sub-micron sized wear particles present a large active surface area and they can be transported to different organs through the bloodstream, presenting a major source of clinical risks.

The drawback of studying *in vivo* produced particles is that insufficient exposure history (and the relevant time points) is known which in turn presents challenges such as unfeasibility of studying the effect of single-parameter variations, evolution kinetics and transient states. Moreover, studying *in vivo* debris requires the analysis of tissue from failed implants. On the other hand, *in vitro* experiments inherently lack the direct correlation to the real case, as a reasonable simulation of the *in vivo* case is difficult. To bridge the gap between *in vitro* and *in vivo* extensive collaboration between disciplines is required.[130,238]

The aim of this work was to elucidate the mechanism behind the *in vivo* dissolution of CoCrMo particles. Advanced material characterisation techniques are employed to enable a correlative spectroscopy and microscopy approach. Chemical and morphological changes to CoCrMo samples are monitored through a combination of *ex situ* and *in situ* studies. The extent of CoCrMo dissolution has been studied in the literature through monitoring electrochemical current and metal ions concentrations in electrolytes which offer limited insight on the underlying mechanisms and the appropriate length-scale; however here, the correlated analysis of the chemical and morphological evolution of CoCrMo should provide the basis for an understanding of the particles' dissolution mechanism.

3 Experimental Techniques

In this chapter, the theoretical aspects of experimental and characterisation techniques used in this research are discussed. Additionally, the instrumentation of some of these techniques is illustrated. Furthermore, the general methodology and parameters used in this work are reported here; however, specific materials and methods for each results chapter are described in the respective chapters.

3.1 Electrochemical Measurements of Corrosion

Electrochemistry is the study of chemical changes caused by the passage of an electric current and the production of electrical energy by chemical reactions (electrochemical reactions). Metal corrosion occurs mainly through electrochemical reactions at the interface between the metal and an electrolyte solution. Electrochemical techniques are therefore used for the study of corrosion process in electrochemical cells. As a complete electrical circuit, electrochemical cells consist of at least two electrodes separated by a conductive electrolyte, as well as an external connection between them. Electrochemical studies are concerned with the factors that affect charge transport across the interface between an electronic conductor (electrode/metal) and an ionic conductor (electrolyte).

3.1.1 Electrochemical Kinetics

Metal corrosion rate is determined by the net rate of two opposite (redox) reactions. The oxidation (anodic) reaction is where metal atoms are oxidised releasing metal ions into the electrolyte and electrons into the metal. The accumulation of electrons in the metal increases the potential difference between the metal and the solution (electrode potential). This build-up of electrons encourages the reverse reaction where metal ions from the solution are reduced and deposited back onto the metal surface. The rate of each of these two reactions is proportional to the concentration of the reactant R=kC (where R=rate, k=rate constant, and C=concentration). Therefore, the net metal dissolution rate is $R_{net}=k_xC_r - k_yC_o$. Theoretically, an equilibrium is eventually attained where the rate of dissolution is equal to the rate of deposition. Hence, there is no further net dissolution of the metal ($R_{net}=0$) and this occurs at an equilibrium constant = C_o/C_r. The electrode potential attained at this equilibrium point is called the equilibrium potential and is dependent on the equilibrium constant and the standard electrode potential E^0 according to the Nernst equation:

$$E_{eq} = E^0 + \frac{RT}{nF}\ln\frac{C_o}{C_r} \qquad \text{Equation 3.1}$$

(Where R = gas constant, T = absolute temperature, F = Faraday constant, and n = the number of electrons transferred per ion).

In practice, the potential of the metal in a solution does not attain equilibrium potential but instead remains relatively positive. This is because the released electrons, from the oxidation of metal atoms, facilitate other cathodic reactions in which electrolyte species, adsorbed on the metal surface, (often O_2 or H^+) are reduced. Therefore, the corrosion of a metal in a solution continues by the redox couple: oxidation of metal ions, reduction of oxygen molecules and hydrogen ions. The difference between the actual resultant potential E and its equilibrium potential is termed the overpotential $\eta = E - E_{eq}$. The overpotential is related to the net rate of the reactions (equivalent to the electric current) according to the Tafel equation:

$$\eta = E - E_{eq} = i_0 + b \log i \qquad \text{Equation 3.2}$$

(Where i_0 = the current of the reversible redox reactions (exchange current) at theE_{eq}, and the constant b is the slope dE/d $\log i$ termed the Tafel slope).

3.1.2 Electrochemical Polarisation

As described by the Tafel equation (3.2) the potential of the metal affects the rate of the corrosion reactions. When the rate of the anodic reaction (metal dissolution) is equal to the rate of the cathodic reactions (reduction of oxygen and/or hydrogen ions) the potential assumed by the metal is termed the corrosion potential E_{corr}. Shifting the potential of the metal to more positive values increases the rates of the anodic reaction while decreasing the rate of the cathodic reaction. The opposite effect on the reactions occurs when shifting the potential to a more negative value. In potential controlled electrochemical measurements the potential of the metal is forced away from the corrosion potential and the metal is said to be polarised. Polarisation curves describe the relationship between the applied potentials and current (equivalent to the rates of the reactions). Initially, the current varies linearly with the potential for the first few millivolts. Afterwards, the current rises exponentially as the potential moves away from the corrosion potential (in either anodic or cathodic directions), in accordance with the Tafel equation (3.2). This behaviour is characteristic of the occurrence of a single electrochemical reaction on a metal surface under activation control (*i.e.* when electrode potential is the only factor affecting the reaction rate irrespective of concentration/diffusion effects); thus indicating that the shift in potential is large enough that the rate of one of the reactions (anodic or cathodic depending on the direction of the potential change) has reduced to a negligible value compared to the rate of the reaction being accelerated.

As cathodic polarisation is increased, the rate of the reduction of oxygen molecules and hydrogen ions may increase to an extent where it exceeds the rate at which these species are transported from the solution to the metal surface. This transport occurs *via* the processes of diffusion and convection (and in the case of hydrogen ions by electromigration). At such high cathodic potentials, the rate of transport of these species controls the rate of the reduction reactions. The current reaches a limited (constant) value, independent of potential, which is equal to the rate of transport. Further increase of cathodic polarisation eventually leads to an increase in the rate of an

additional reduction reaction: the reduction of water to hydrogen gas and hydroxide ions. As the rate of the water reduction increases beyond the rate of transport of oxygen molecules and hydrogen ions, the cathodic current rises again after the transport limited plateau.

On the other hand, anodic polarisation increases the rate of metal dissolution up to a maximum value before the current drops abruptly due to the formation of a surface oxide film. The oxide film is formed by the reaction of the metal atoms with water to form a metal oxide and hydrogen ions. When the oxide film covers the full metal surface its thickness continues to increase up to an equilibrium point where a constant current value is reached (independent of potential). This effect is observed as the transport of metal ions through the oxide film is slow and hence the anodic current of metal dissolution attains a low value. At this stage the metal is said to be in the passive state and the corresponding potential at which this state is initiated is called the critical passive potential. The formation of the passive oxide film is a key aspect of corrosion protection. Different metals exhibit different critical passive potentials as it depends on the standard potential E^0 of the reaction between the particular metal and water as per the Nernst equation (3.1). In the absence of localised corrosion,[a] the system remains in the passive state, as the potential is increased, until the potential required to kick-start an oxidation reaction of the metal to form a soluble ion (*e.g.* reaction of Cr with water to produce dichromate ions) is met. This process is known as transpassive dissolution causing a rise in observed current away from the passive plateau. Increasing anodic potentials further leads to further increase in current courtesy of the oxidation of water to form oxygen gas and hydrogen ions.

In conclusion, electrochemical polarisation measurements are utilised for studying the corrosion behaviour of metals. The corrosion environment (the electrolyte) can be composed to mimic the intended application conditions. Figure 3.1 illustrates a typical electrochemical measurement circuit made up of an electrochemical cell, and a potentiostat incorporating: an adjustable voltage source, an ammeter, and a voltmeter. The three electrodes of the electrochemical cell are the working electrode WE (the metal being studied), the reference electrode RE, and the counter electrode CE. The voltage source for the potential scan is applied between the WE and CE. The potential E between the RE and WE is measured with the voltmeter, and the overall voltage is adjusted to maintain the desired potential at the WE with respect to the RE. The resulting current flowing to or from the WE is measured with the ammeter. An ideal CE is an ideally polarisable electrode where no current flows in response to an applied potential, and hence is made of electrochemically inert materials. Furthermore, the surface area of the CE is often much larger than that of the WE to ensure that the half-reaction at the CE occurs at a relatively high rate and thus does not limit the process occurring at the WE. On the other hand, an ideal RE is an ideally non-polarisable electrode where its potential remains constant (the electrode potential does not deviate from its equilibrium potential) and hence precise control of the WE potential (which is measured against the RE) can be maintained.

[a] Localised (pitting) corrosion is not expected in biomedical CoCrMo alloys due to the high Cr content.

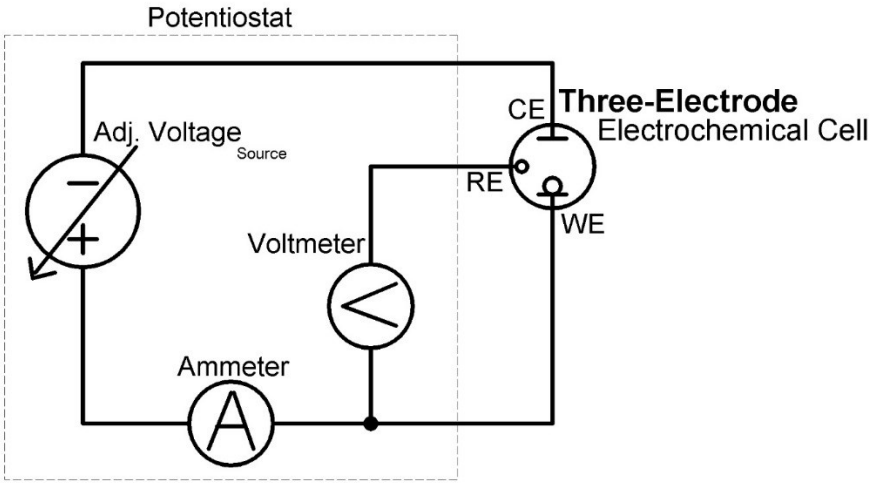


Fig. 3.1 Simplified illustration of the circuit required for performing electrochemical polarisation measurements

3.2 Introduction to Particle-Matter Interactions

When energetic particles (*e.g.* photons, electrons, ions) are accelerated towards a target specimen they have a probability to pass through unaffected, if the target is thin enough, or interact with the target giving rise either to elastic or inelastic scattering of the incident particle. These interactions can be between the incident particles and bound electrons, or nuclei, or whole atoms of the target specimen. Elastic scattering conserves the kinetic energy of the incident particle, while an inelastic scattering of incident particles is due to an energy transfer interaction with the target. The transferred energy could result in effects such as excitation/ionisation of target atoms, secondary emissions, and even the ejection of atoms from the target. Energy transfer interactions happen through a number of mechanisms; for a given irradiation some processes dominate while others do not occur depending on the incident particle type, incident particle energy and the target material. For instance, charged particles (*e.g.* electrons, ions) interact with matter differently from neutral particles (*e.g.* photons). This section will describe the interactions relevant to the material characterisation techniques used in this work.

Characterisation techniques provide information such as microstructure and/or chemical information on materials through analysing the interactions between an incident 'probe' and the specimen. This covers a wide range of techniques utilising different types of probes such as energetic electromagnetic beams (*e.g.* light or X-ray photons), energetic electron beams, and even sharp solid needles (as is the case in Scanning Probe Microscopy techniques). The characterisation techniques used in this work employed electron and X-ray probes, and their operating principles and instrumentation are discussed in more details in sections 3.3 and 3.4 respectively. Electromagnetic radiation and electron techniques have similar operation principles. These techniques are based on the particle-wave duality of photons and electrons. Firstly, a source is used to generate the probe which is then focused to form a coherent beam. The beam interacts with the sample to produce different signals, some of which could be focused

and magnified using lenses to produce an image (microscopy techniques), others could be recorded and analysed to produce spectral patterns providing chemical information (spectroscopy techniques). Generally, the transmitted waves (unaffected through the specimen) and elastically scattered waves are the ones used in microscopy to form an image of the spatial distribution of features in the specimen. On the other hand, spectroscopic information arises from the energy loss interactions between the probe and the sample. Probe attenuation or lost energy in the form of secondary signals are detected. The magnitude of these energy losses is a characteristic of the atoms of specific elements in the sample.

It is worth noting that particle-target interactions do not only form the basis of signal generation in many characterisation techniques but moreover, the detection of these signals by specialised detectors is also based on the principles of such interactions between signal particles and the detector material.

3.2.1 Interactions of Incident Electrons

If an incident electron *e* interacts with a target atom *A*, the resulting interactions can be grouped into three main channels: elastic scattering of the electron, inelastic scattering of the electron *via* atomic excitation/ionisation, or inelastic scattering of the electron *via* other channels such as Bremsstrahlung radiation (Cherenkov radiation *etc.*).

$e + A = e + A$	Elastic scattering: electron's kinetic energy conserved
$e + A = e' + A^*$ **or** $e + A = e' + A^* + e_s$	Inelastic scattering: electron excites or ionises atom
$e + A = e' + A + \gamma$	Inelastic scattering: Bremsstrahlung - energy lost *via* a photon

The probability of a particular type of interaction occurring is determined by the interaction cross section σ. Assuming that elastic and inelastic scattering processes are independent of each other, a total interaction cross section is given by the sum of both cross sections.

$$\sigma_{Total} = \sigma_{elastic} + \sigma_{inelastic} \qquad \text{Equation 3.3}$$

For an interaction with a single atom, the cross-section is defined in terms of the effective radius of the atom as:

$$\sigma = \pi r^2 \qquad \text{Equation 3.4}$$

An incident particle may undergo multiple scattering events in a specimen and a total scattering cross section *Q* is regarded as the number of scattering events per unit path that a particle travels through the specimen, and is given by:

$$Q = N\,\sigma_{Total} \qquad \text{Equation 3.5}$$

(Where N is the number of atoms per unit volume).

3.2.1.1 Elastic Scattering

Elastically scattered electrons experience a change in the trajectory without losing kinetic energy upon interaction with the target atom. Elastic scatterings arise from the Coulomb interactions between the incident electron and either the electron cloud or the nucleus of the target atom. Due to the much larger charge of the nucleus, the interaction potential of an electron-nucleus interaction is larger, compared to an electron-electron interaction, leading to larger scattering angles. The elastic scattering angles θ for an electron-electron and electron-nucleus interactions are defined as:

$$\theta = \frac{e}{Vr_{electron}} \quad \text{Equation 3.6}$$

$$\theta = \frac{Ze}{Vr_{nucleus}} \quad \text{Equation 3.7}$$

(Where *e* is the electron charge, V is the accelerating potential of the incident electron, *r* is the effective radius of the target electron/nucleus, and Z is the atomic number of the target atom, thus Ze is the charge of the nucleus).

From equations 3.6 and 3.7 it can be deduced that heavier atoms scatter electrons at wider angles compared to lighter atoms, and electrons are scattered at lower angles with higher accelerating voltages. Furthermore, the scattering angle increases as the effective radius decreases (*i.e.* the closer the incident electron is to the target electron/nucleus).

Electron-nucleus coulomb interactions are known as Rutherford scattering and lead to high angle scattering that even backscattered electrons (BSE) are realised. Rutherford defined the probability of this scattering by the Rutherford differential cross section (equation 3.8), which is usually given with respect to a solid angle dΩ. The solid angle Ω is related to the scattering angle by equation 3.9.

$$\frac{d\sigma}{d\Omega} = \frac{e^4 Z^2}{16(E_0)^2 sin^4\frac{\theta}{2}} \quad \text{Equation 3.8}$$

(Where E_0 is the incident energy).

$$\Omega = 2\pi(1 - \cos\theta) \quad \text{Equation 3.9}$$

Therefore,

$$d\Omega = 2\pi \sin\theta \, d\theta \quad \text{Equation 3.10}$$

3.2.1.2 Inelastic Scattering: Atomic Excitation/Ionisation

The principles of atomic excitation/ionisation by an incident beam are exploited by many material characterisation techniques. Atoms may be excited not only by an incident beam of electrons but also photons or ion beams. The

subsequent relaxation of the atoms also leads to the emission of electrons, or photons (and ions only in the case of a nuclear excitation). Information is gained by analysing either the attenuated incident beams or the subsequent emissions of atomic relaxation. The techniques used in this work utilised atomic excitation by incident electron beams or photon beams (incident photon beams are discussed in section 3.2.2).

Atomic excitation begins with the stimulation of the electronic shell of the atom by the electric field of the incident particle. The electric field causes a transient distortion of the electron cloud relative to the atom's nucleus (electric dipole excitation). This results in energy transfer depending on the amplitude and duration of the electric field. The transferred energy may alter the electronic configuration where an inner shell electron moves to an outer shell (higher energy state) leaving the atom in the excited state. Higher transferred energy, larger than the binding energy of an inner shell electron, leads to the ejection of this electron (termed secondary electron) and leaves the atom in an ionised state. Excited or ionised atoms have an unstable energy configuration and must lose the excess energy to return to a stable state (relaxation process). The relaxation process occurs when an outer shell electron drops to occupy the inner shell vacancy caused by the departing secondary electron. The energy lost by this electron transition is emitted either by fluorescence (photon emission) or the auger process (electron emission). The emitted photon, or Auger electron, has a characteristic energy value that depends primarily on the atomic number of the target atom.

3.2.1.3 Inelastic Scattering: Bremsstrahlung

An incident electron may interact with target atoms losing energy without transferring that energy to the atom (*i.e.* unlike the case in atomic excitation/ionisation). The relatively strong electric field of the atom's nucleus deflects the incident electron causing it to decelerate. The lost kinetic energy is emitted in the form of a photon and this process is known as Bremsstrahlung radiation. While Bremsstrahlung radiation does not provide information on the target atom, the principle is utilised as means for producing incident photon beams from X-ray tubes to synchrotron radiation (see X-ray Sources section 3.4.1.1).

3.2.2 Interactions of Incident Photons

3.2.2.1 Photoabsorption

The principle of photoabsorption (figure 3.2) is similar to the atomic excitation described in section 3.2.1.2. However, an incident photon, with an energy equal to or exceeding the binding energy of an inner shell electron, is absorbed. Additionally, the ejected electron, when an atom is ionised by a photon, is called the photoelectron (as opposed to the secondary electron). The ionisation cross section of a photon is orders of magnitude smaller than that of an electron. It is possible for photons to also be inelastically scattered when its incident energy is much large than the binding energy of the target atom's inner shell electron (Compton Scattering); at even higher incident

energies the process of pair production (ejection of an electron and positron pair) dominates, however, these processes are outside the scope of this work.

Different signals arise from the photoabsorption process; the element specific binding energies that give rise to the absorption processes allow for chemical information to be obtained from the attenuated photon beam, as well as the fluorescence signal (see XAS section 3.4.2). In addition, absorption contrast spatial images can be obtained by recording the spatial variations of X-ray transmission through a sample (see TXM section 3.4.3).

It is worth noting here that the detection of fluorescence signals generated by an incident photon beam involves relatively low noise background due to only photoelectron Bremsstrahlung; while in the case an incident electron beam a higher background is present due to Bremsstrahlung radiation from primary and secondary electrons.

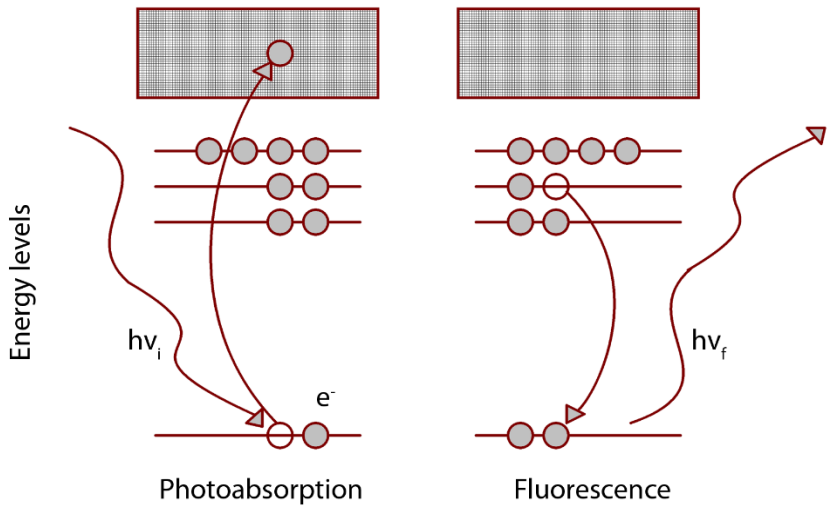


Fig. 3.2 Schematic of X-ray photoabsorption followed by fluorescence. An incident photon of energy hv_i is absorbed by the atom, ejecting an electron from an inner shell of the atom. The atom relaxes by filling the vacancy by emitting an X-ray photon with a characteristic energy hv_f. (adapted and reproduced with permission from [241]).

3.3 Electron Characterisation Techniques

Electrons provide a highly versatile probe which can be easily accelerated and readily focused by electromagnetic fields. Electron characterisation techniques comprise a set of microscopy techniques, providing spatial images of the specimen (transmission electron microscopes TEM and scanning electron microscopes SEM) as well as incorporated spectroscopy techniques. Both TEM and SEM can be fitted with X-ray detectors to provide quantitative elemental analysis through Energy Dispersive X-ray Spectroscopy (EDX). In addition, in a TEM the inelastically scattered electron which passed through the specimen can be detected and separated according to their different energy losses in Electron Energy Loss Spectroscopy (EELS). These electron energy loss spectra provide information not only on elemental composition but also on electronic states and atomic bonding.

High spatial resolution images can be obtained by electron microscopy (up to atomic resolution in a TEM). The resolution of a microscope is dependant theoretically, on the wavelength of the incident beam. The electron wave-

particle duality provides the bases that allow the electrons to be used as a probe. The de Broglie equation defines the wavelength of a particle as:

$$\lambda = \frac{h}{mv} \quad \text{Equation 3.11}$$

(Where *h* is Planck's constant, *m* is the particle mass and *v* is the particle velocity).

Therefore, by accelerating electrons, lower wavelengths can be achieved. The kinetic energy of accelerated electrons can be given by the equation:

$$eV = \frac{1}{2}mv^2 \quad \text{Equation 3.12}$$

(Where *e* is the charge of an electron, and *V* is the accelerating voltage).

Substituting for *v* in equation 3.11, the wavelength of an accelerated electron can, therefore, be deduced as:

$$\lambda = \frac{h}{\sqrt{m2eV}} \quad \text{Equation 3.13}$$

At the high velocities employed in electron microscopy, relativistic effects (when a particle's velocity is comparable to the velocity of light) mean that the rest mass m_0 of the electron is significantly less than its relativistic mass *m*. Taking these effects into account, the wavelength equation becomes:

$$\lambda = \frac{h}{\sqrt{m_0 2eV\left(\frac{1+eV}{m_0 2c^2}\right)}} \quad \text{Equation 3.14}$$

(Where *c* is the velocity of light).

At an accelerating voltage of 200 kV (typically used in TEM) the electron wavelength is 0.0025 nm which is approximately two orders of magnitude less than the interatomic spacing in solids. In practice, however, the resolution of an electron microscope is limited by imperfections of the focusing and imaging lenses. As a charged particle, electrons can be deflected in magnetic fields by Lorentz forces. Therefore electromagnetic lenses, replace the optical lenses in electron microscopy.

3.3.1 Electron Techniques Instrumentation

3.3.1.1 Electron Sources (Guns)

There are two main types of electron guns employed in TEMs: Thermionic Emission Gun (TEG) and Field Emission Gun (FEG). TEGs consist of a filament which is heated to give electrons enough energy to overcome the attractive forces of the nucleus (overcome their binding energies) and break free of the atoms. The released electrons are subsequently accelerated and collimated by a gun electrostatic force. FEGs consist of a very thin tip (radius of ~ 1

μm) acting as a cathode across which a high electric field is applied. The strength of an applied electric *E* is considerably increased at a sharp point according to the relationship *E= V/r* (where *V* is the applied voltage and *r* is the radius of the tip). The strong electric field facilitates the escape of electrons by quantum tunnelling.

Generated electron beams are defined by the beam source size, the divergence angle of the beam, the brightness (current density per unit area per unit solid angle), the electrons' energy E, and the energy spread within the beam ΔE (*i.e.* how well defined the beam's wavelength is). The ΔE is directly proportional to the temperature of the source. The high temperature required in TEG leads to the release of beams with higher energy spread (~ 3 eV) compared to FEG beams (~ 0.25 eV). Additionally, FEGs produce a higher current density than TEGs. Some FEGs utilise heating, as well as the applied electric field and, are called Schottky guns. Schottky guns produce beams with an intermediate energy spread (~ 0.5 eV) but have a longer working life and less stringent vacuum requirements.

3.3.1.2 Electromagnetic Lenses

Electromagnetic lenses consist of copper coils around a soft iron core. The current flowing through the coils generates the magnetic field. The Lorentz deflection force is perpendicular to the magnetic field and velocity of the electron, causing the electron to move in a circular motion. If the electron is already travelling with a velocity approximately in the direction of the magnetic field, the net movement follows a helical path down the axis of the magnetic field. A comparison of the ray movement across an optical lens and the electromagnetic lens is illustrated in figure 3.3. The image from an optical lens is inverted, while an electromagnetic lens produces an inverted and rotated image. The focal length of electromagnetic lenses can be altered as required by changing the strength of the magnetic field through adjusting the current in the coils.

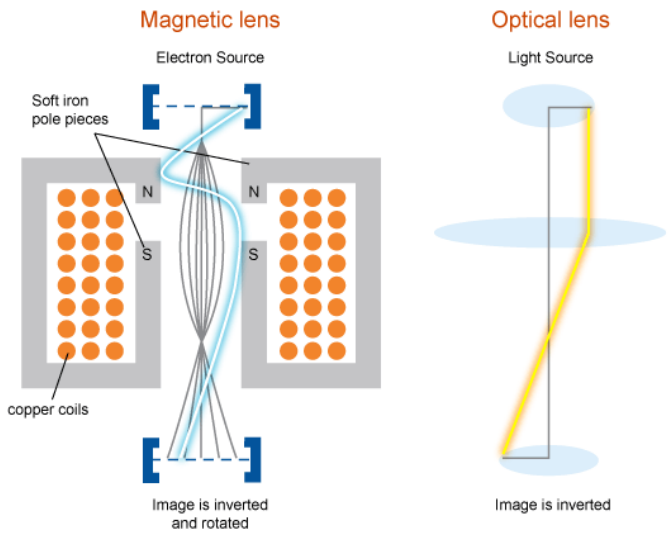


Fig. 3.3 Schematic of the structure of an electromagnetic lens (left), and an illustration of the difference in ray path between electromagnetic lenses and optical lenses (from [242] *licensed under CC BY-SA 2.5).*

Imperfections of electromagnetic lenses limit the spatial resolution of the electron microscope. The main imperfections are spherical aberrations, chromatic aberrations and astigmatism. Spherical aberrations arise due to the inhomogeneity of the magnetic field effect on electrons travelling off the optical axis. The further the electrons are from the optical axis, the more strongly they are deflected towards the axis. This effect causes a point object to be imaged as a disc, as illustrated in figure 3.4. Spherical aberrations are the main limitation to resolution in TEM but they are reduced in some instruments (such as FEI Titan) with the use of an aberration corrector. Chromatic aberrations arise due to the energy spread of the beam (non-monochromatic beam). As discussed in section 3.3.1.1, the electron source produces a beam with an inherent energy spread, but the greater source of energy spread is the beam's interaction with the specimen. Electrons lose energies at varying degrees as they pass through a sample leading to a greater energy spread typically 15 – 25 eV.[243] Lower energy electrons are deflected more strongly, by the objective lens, leading to a point object being imaged as a disc. Astigmatism arises due to asymmetries in the magnetic field. These asymmetries cause local variations in the magnetic field strength and they may arise due to defects in the iron core in the lenses or apertures which are not properly centred on the optical axis. Astigmatism can be corrected by introducing a compensating field, to balance the asymmetries causing the aberration, using stigmators.

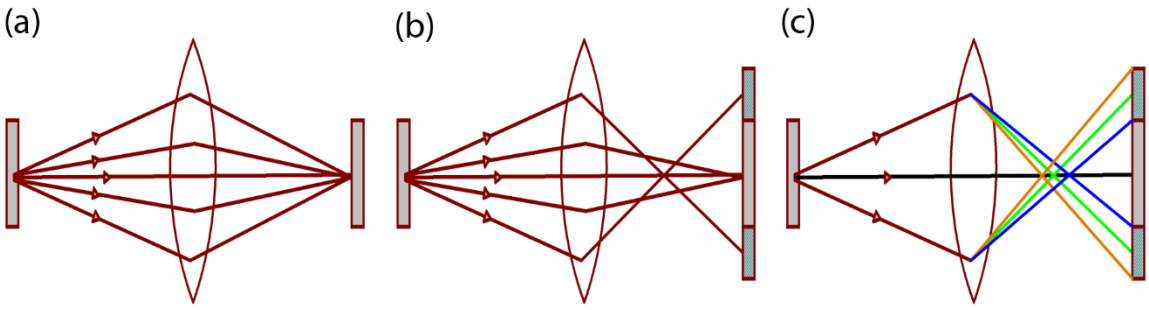


Fig. 3.4 Schematic illustrating (a) a perfect lens imaging a point object as a point, (b) spherical aberration where a point object is focused as a disc called the disc of uncertainty, due to over-focusing of the rays which are further away from the optical axis, and (c) chromatic aberration where beams of different energies (indicated by the different colours) are focused at a different strength by the lens.

3.3.2 Transmission Electron Microscopy

The TEM is analogous to an optical microscope but with an inverted set up where the beam source is at the top of the microscope column; the beam interacts with a specimen down the column and the image is formed on a screen at the bottom of the column. The microscope column is maintained at a high vacuum to minimise electron scattering from gas molecules. The probe source in a TEM is an electron gun which generates the beam. The electrons are accelerated by an electric field typically between 80 kV and 300 kV. The electron beam interacts with a specimen (for TEM specimens are ~ 100 nm thick). The transmitted and elastically scattered electrons contribute to the image.

Figure 3.5(b) shows a schematic diagram of a typical TEM set up. The first condenser lens de-magnifies the gun crossover and the second condenser controls the convergence of the beam at the sample and the diameter of the exposed region. A condenser aperture helps control the intensity as well as the angle of divergence of the beam hitting the sample. The objective lens magnifies the image by a factor of X50. Further magnification, by hundred to hundred thousand times, is achieved by intermediate and projector lenses.

3.3.2.1 TEM Image Contrast (Mass-thickness contrast)

Elements with high atomic numbers scatter electrons at larger angles than lighter elements. Thicker areas of the sample will also scatter electrons with larger angles. An objective aperture is used in the back focal plane of the objective lens to select the scattered electrons that contribute to the image. Therefore if the objective aperture is positioned centrally, in relation to the optic axis of the microscope, it allows electrons which are unscattered, or scattered at low-angles, to pass through and contribute to the image. This makes heavier elements, and thicker regions, appear darker (lower intensity) in what is called the bright field image. Dark-field images can also be obtained by positioning the aperture to select a portion of the electrons scattered at large angles. This contrast mechanism is called the mass-thickness contrast. In a TEM it's possible to produce images with other contrast mechanisms (*e.g.* phase contrast) which can be reviewed in.[244]

3.3.3 Scanning Electron Microscopy

In an SEM, instead of a full field beam, the electron beam is focused into a fine probe which is then raster scanned over a region in the sample. The SEM beam is accelerated up to moderate energies (accelerating voltages in SEMs range from 1 – 30 kV). The information content of SEM and TEM images are different; while a TEM image shows the internal structure of very thin specimens, SEM provides microstructure information from the surface of a bulk specimen. The spatial resolution of SEMs is typically around 10 nm but can reach subnanometer when operated at a low beam energy (1 kV) and using a FEG source.[245] Although TEMs provide the highest spatial resolution, the SEM strengths lies in its inherent versatility utilising multiple signals. SEMs can provide information on topographical features, surface morphology, phase distribution, crystal structure and orientation, as well as elemental composition (spectroscopic) information. Moreover, SEMs instruments can be equipped with focused ion beam sources (FIB-SEM) for cross-sectional imaging. FIB-SEMs employ a gallium ion beam which can be used to *mill* specimens *via* sputtering, exposing cross sections.

SEM images can be produced using elastically scattered backscattered electron BSE (high angle Rutherford scattering), which make the majority of emitted electrons from the specimen at high beam voltages. Additionally, SEM images can also be produced by the secondary electrons SE emitted as a result of the inelastic scattering of the incident probe (section 3.2.1.2). All SEM images in this work were obtained using the secondary electrons signals. The secondary electrons' escape depth is approximately 5 - 50 nm,[245] and their emission are greatly

affected by the incident angle of the beam. When the electron beam is perpendicular to the sample, the interaction volume inside the sample is uniform. If the incident angle increases, the electrons' escape distance decreases and hence a greater number of electrons are emitted and detected. Therefore, secondary electron images provide surface topography contrast with edged features appearing brighter than uniform surfaces.

The electromagnetic lenses in the SEM are only used to focus the beam into the fine incident probe but play no part in image formation. This gives rise to a large depth of field (depth of field is a measure of the nearest and furthest surfaces from the lens that appear in focus), which facilitates imaging of surface topography. The SEM has more than 300 times the depth of field of an optical microscope.[245] Image construction in SEM is accomplished by detecting and mapping the intensity of the signal (either BSE or SE) onto a viewing screen or film. This intensity information is transferred point-to-point as the SEM scan generator simultaneously drives both the incident beam across the surface of the specimen and the signal beam on the viewing screen or film. Magnification of the SEM image is defined as the length of the scan line on the recording device divided by the length of the scan line on the specimen. Magnification is therefore independent of lenses but rather adjusted by changing the size of the area scanned on the specimen (while the recording film size is held constant).

3.3.4 Scanning Transmission Electron Microscopy

Scanning transmission electron microscopy STEM is based on a combination of elements from TEM and SEM. Thin specimens are viewed in transmission mode (in a TEM instrument) but the images are formed serially by scanning a focused electron probe. The spatial resolution of STEM is defined by the probe size, which in turn depends on the quality of the electron source and electromagnetic lenses. In particular, while the objective lens aberrations limit resolution in TEM, the condenser lens governs the resolution of STEM as it is the lens that focuses the beam into the fine probe. In aberration corrected instruments it is possible to form probes well below atomic dimensions, and thus atomic resolution images can be achieved.[246] Multiple detectors acquiring multiple signals can be used in STEM imaging: in addition to a bright field detector (detecting unscattered and low-angle scattered electrons $\theta < 10$ mrad), annular dark field detector (θ = 10-15 mrad) and high angle annular dark field detector HAADF ($\theta > 50$mrad) are also available. The high-angle scattered electrons detected by HAADF detectors result from electron-nucleus interactions (Rutherford scattering, section 3.2.1.1). Rutherford scattering angles are sensitive to the atomic number Z of the target atoms, as discussed earlier by equation 3.7, and thus HAADF imaging is highly sensitive to the atomic numbers in the sample. The intensities of a HAADF image is dependent on Z^n (n~2) and thus this contrast is called Z-contrast.

3.3.5 Energy Dispersive X-ray Spectroscopy

Energy Dispersive X-ray Spectroscopy EDX is an elemental analysis technique utilising the inelastic scattering interaction of electron beam probes with the sample and hence is often incorporated in TEM and SEM instruments.

The atomic excitation by the incident electron beam (described in section 3.2.1.2) leads to the emission of characteristic X-rays. EDX analysis produces a spectrum of detected X-ray intensity versus the X-ray energy.

All elements except H and He produce these characteristic X-ray (since H and He only have one electron shell (the K or 1s)). In addition, Li is also undetectable because the energy of its characteristic X-ray photons is below the practical detection limit (and self-absorption of the X-ray occurs by the sample). The detected X-ray intensity is translated to the concentration of elements in a sample (weight or atomic percentages) by performing corrections to account for the inter-element modifications to the generated X-rays. [247]

EDX detectors employ semiconductor crystals typically Si or Ge. The incident X-rays are absorbed by the semiconductor atoms leading to the generation of a photoelectron and an X-ray photon. The new X-ray photon may be reabsorbed in a lower energy shell leading to the production of a new photoelectron and X-ray photon. The photoelectrons released from a cascade of these events travel in the crystal and are scattered inelastically giving up their energy to other electrons in the crystal and in the form of phonon excitations. Electrons in the valence band of the semiconductor gain energy from these interactions with photoelectrons to rise to the conduction band. Under an applied voltage the electron in the conduction band moves freely leaving a hole behind. The energy required to generate one electron-hole pair in the semiconductor is pre-known (*e.g.* for silicon it is 3.6 eV). The number of electron-hole pairs generated are proportional to energy of the incident X-ray photon. Therefore by measuring the resultant charge, the energy of the original X-ray photon can be identified.

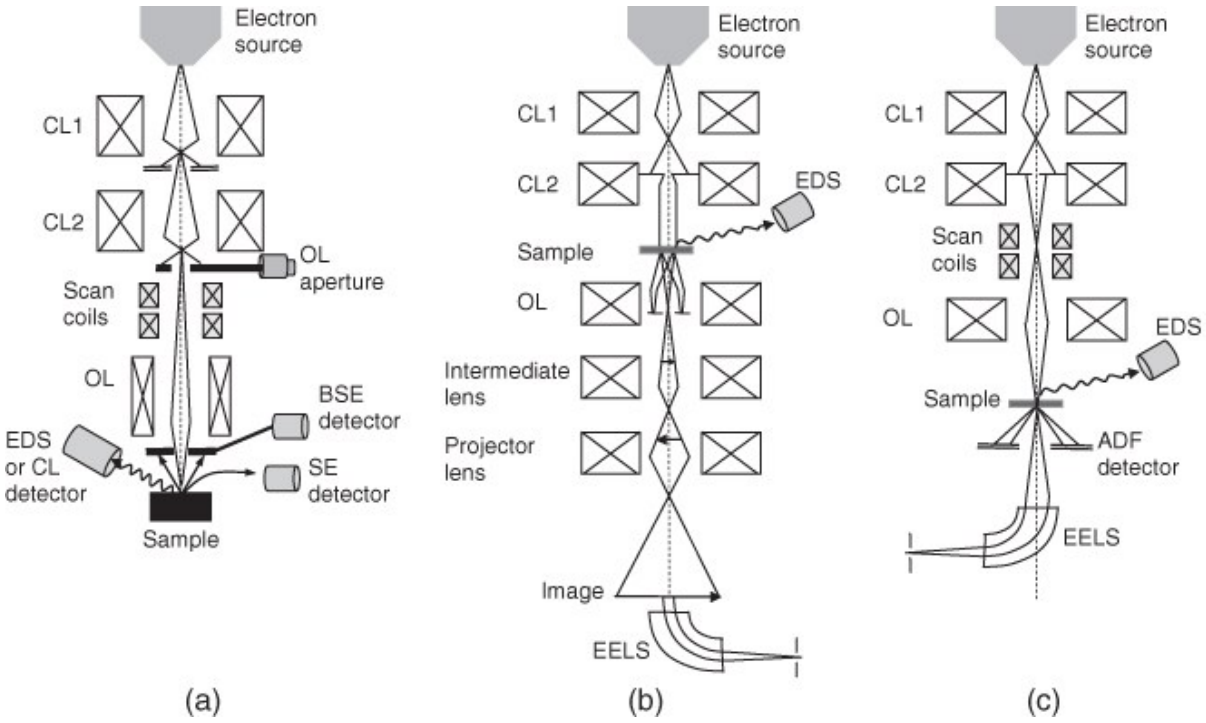


Fig. 3.5 Simplified schematics of the instrumentation for (a) SEM, (b) TEM, and (c) STEM. CL stands for condenser lens, while OL stands for objective lens (reproduced with permission from [248])

3.4 X-ray Characterisation Techniques

X-ray techniques presented in this work are based on the photoabsorption interaction between incident photons and target atoms (section 3.2.2.1). Similar to the utilised electron characterisation techniques, this work involved both microscopy and spectroscopy with X-ray techniques. While X-ray microscopy does not provide the high spatial resolution of electron microscopes, XAS provides a high spectral resolution necessary for accurate chemical speciation analysis of small amounts of material. Although EELS can reach a reasonable spectral resolution, TEM-EELS is limited with a sample thickness of a few nanometres and strict vacuum conditions which makes the use of realistic liquid cells (electrochemical cells) challenging. Therefore, X-ray techniques have a major advantage when it comes to *in situ* measurements. X-ray based characterisation presented in this work was carried out at several synchrotron facilities: National Synchrotron Light Source II (NSLS-II), Upton, NY, USA; Stanford Synchrotron Radiation Lightsource (SSRL), Menlo Park, CA, USA; and Diamond Lightsource, Didcot, UK.

3.4.1 X-ray Techniques Instrumentation

3.4.1.1 X-ray Sources: Synchrotron Radiation

Generating an X-ray beam requires first the generation of an electron beam. X-rays beams can be generated in laboratories using X-ray tubes. In X-ray tubes, a target material is bombarded with an electron beam giving rise to a spectrum of continuous X-ray radiation (Bremsstrahlung radiation) as well as characteristic fluorescence X-rays from the target material used. Photons are emitted in all directions and only a small fraction interacts with the specimen and contributes to the signal. Although X-ray microscopy and spectroscopy could be performed using laboratory sources, the intrinsically divergent radiation from X-ray tubes limits what can be measured. To achieve high spatial and spectral resolution the high intensity collimated radiation of synchrotron X-ray sources is required. In addition, photon energies from synchrotron radiation can reach 100 keV or higher.[249]

Synchrotron radiation facilities involve a large storage ring where electrons are circulated at relativistic velocities. The electrons are initially produced by an electron gun and accelerated in a linear accelerator (linac) before entering the storage ring where they are accelerated further. The electrons are steered around the ring by magnetic fields applied by either a single bending magnet or arrays of magnets called insertion devices. The energy lost from the deceleration of electrons as their trajectory is bent by magnets is emitted in the form of electromagnetic radiation. Insertion devices are periodic arrays of dipole magnets which produce sinusoidal oscillations in the electron trajectory. There are two types of insertion devices: wigglers which cause large deflection angles in the trajectory and generating a continuous spectrum of X-rays; and undulators which cause smaller deflection angles and emit photons with a small spectral bandwidth (figure 3.6). This spectral bandwidth can be tuned by adjusting the magnetic field through changing the gap between the top and bottom magnets.[250] The radiation is emitted into

beamlines (BL) which convey the photons to the experimental chambers. Synchrotron facilities (figure 3.7) comprise many beamlines providing a wealth of characterisation techniques.

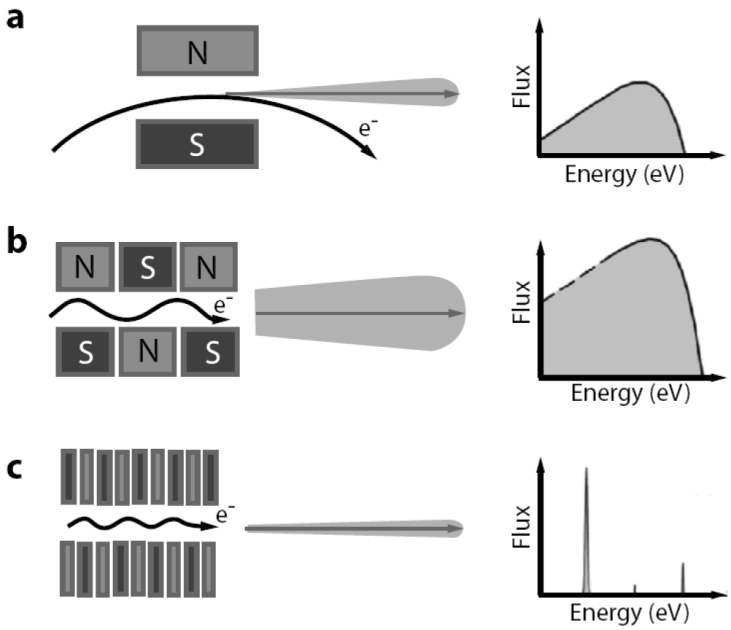


Fig. 3.6 Schematic illustrating the X-ray spectra emitted from (a) a bending magnet, (b) wiggler, and (c) undulator. (adapted from [250]).

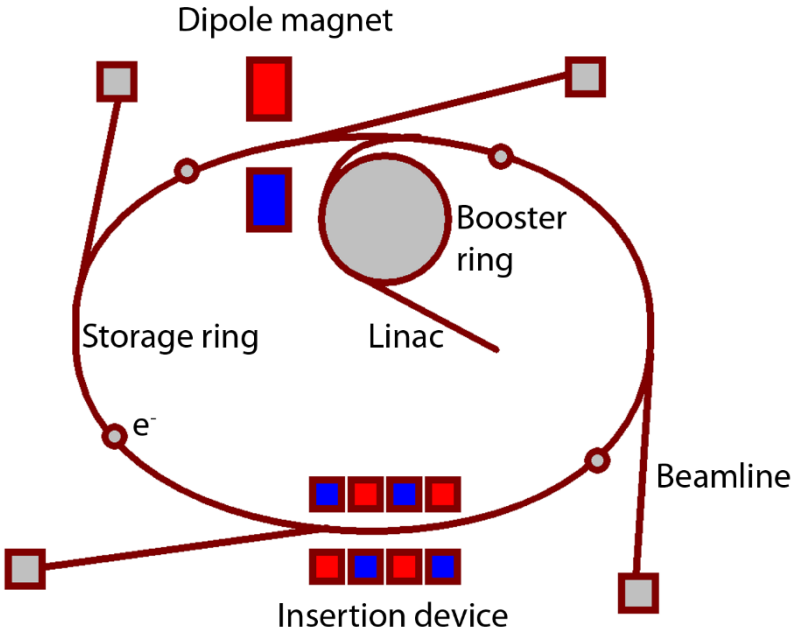


Fig. 3.7 Schematic of the main structure of a synchrotron facility.

3.4.1.2 X-ray Beamlines

This section covers the structure of a typical synchrotron beamline designed for X-ray absorption spectroscopy (XAS). In brief, XAS beamlines contain: slits to define the X-ray profile, a monochromator to select the energy of

the X-ray beam, a harmonic rejection mirror to reduce the harmonic content of the X-ray beam, ionisation or other detectors to measure the intensity of the X-ray beam, and a sample stage.

3.4.1.2.1 Slits

Slits are employed on beamlines to define the X-ray beam profile and block unwanted X-rays. Slits may exist as fixed slits, with a pre-cut opening of fixed size, or adjustable slits with metal plates that could be moved to define the beam edges. Slits may be placed upstream and downstream of the monochromator, as well as before the incident X-ray, I_0 detector. Slits placed downstream or upstream of the monochromator can be used to increase the energy resolution of the X-ray incident on the sample at the expense of some loss in X-ray intensity.[251]

3.4.1.2.2 Monochromator

Monochromators are used to select the X-ray energy incident on the sample. X-ray monochromators typically consist of two parallel crystals (double-crystal monochromator) or a single crystal with a slot cut nearly through it (channel-cut monochromator). Monochromator crystals are made of silicon or germanium and are designed such that a particular atomic plane is parallel to the surface of the crystal. Common monochromator crystals are Si(111), Si(311), and Ge(111).[251] The energy of X-rays diffracted by the crystal is controlled by rotating the crystals in the X-ray beam. Only the X-rays with energies that satisfy Bragg's Law (Equation 3.15) are diffracted by the crystal.

$$n\lambda = 2d\ \sin\theta \qquad \text{Equation 3.15}$$

(where λ is the wavelength of the diffracted X-ray (proportional to energy), d is the spacing of the atomic planes of the crystal parallel to its surface, θ is the angle of the crystal with respect to the impinging beam, and n is an integer. The fundamental X-ray energy corresponds to n = 1, and X-rays of higher harmonic energies correspond to n > 1).

Therefore, the energy of the sample-bound X-ray beam can be controlled by varying the angle of the monochromator crystal relative to the incident X-ray beam. Typically the monochromator angle is stepped through the XAS scan range or it can be run continuously. The latter scanning mode is called quick-scanning of the monochromator.[251]

Other types of monochromators may also be employed in beamlines (generally for lower energy photons, < 2 keV) such as diffraction gratings (periodic array of lines which can be rotated to reflect different photon energies) as well as other crystals such as quartz and InSb.[252]

The high energy tunability is a major advantage of synchrotron radiation. The energy resolution is defined by ΔE/E which equals 1.3×10^{-4} for Si (111).[252] The highest resolution is achieved with ideally collimated beams; the resolution is affected by the beam divergence which is determined by the source and/or any focusing objects that precede the monochromator in the beamline.

3.4.1.2.3 Harmonic Rejection

X-rays of higher harmonic energies would adversely affect the XAS measurement. Therefore, the harmonic X-ray intensity needs to be reduced, while maintaining the intensity of the fundamental X-ray energy. Harmonic X-rays that are diffracted from the crystal depend on the crystal lattice and the cut of the crystal.[251] The intensity of the second harmonic is generally considerably greater than the intensity of the higher harmonics; therefore, crystals that do not diffract the second harmonic are usually used.

There are two commonly used approaches for reducing the harmonic X-ray intensity which are: detuning the second crystal of the monochromator or the use of a harmonic rejection mirror. In the first method, instead of two parallel monochromator crystals, the angle of the second monochromator crystal is slightly offset with respect to the angle of the first crystal. This slightly decreases the fundamental X-ray intensity while dramatically decreasing the higher harmonic intensity. The degree of detuning is defined by the change in the incident X-ray intensity (I_0) relative to its maximum value obtained by parallel crystals. Monochromator detuning is usually done at approximately 200 eV above the absorption edge.[251]

The second method involves the use of a harmonic rejection mirror placed at a grazing angle to the beam. The mirror angle is such that only fundamental X-ray energy beam is reflected onto the sample while harmonic energies are not. This occurs because the critical angle for reflectance depends on the incident energy. The mirror angle is optimised by measuring the reflected beam intensity as a function of mirror angle. The optimum angle of the mirror is one which allows maximum reflection in the energy region of interest while reflecting insignificant X-rays of higher harmonics. Additionally, slits are placed downstream of the mirror to block the non-reflected direct beam containing the harmonic X-ray energies. Harmonic rejection mirrors are usually made of Si for low energies, Rh for X-ray energies below the Rh absorption edge (23 keV), or Pt for higher X-ray energies.[251]

3.4.1.2.4 Detectors

The X-ray intensities for XAS are typically measured using ionisation chambers or solid state detectors. Ionisation detectors consist of two parallel plate electrodes separated by a gas-filled chamber. The incident radiation ionises the gas resulting into a gas ion and electron pair. An electric field imposed by an applied voltage between the electrodes separates the charges to the corresponding oppositely charged electrode. The resulting current is measured and is proportional to the intensity of the incident radiation.

The incident X-ray energy (I_0) is measured by an ionisation chamber upstream of the sample, while a downstream ionisation chamber measures the intensity of the transmitted beam (I), as shown in figure 3.8(a). In general, the suitable attenuation of the X-ray intensity by the detectors is 10 to 20 % for the incident intensity (I_0) detector and 70 to 90 % for the transmitted intensity (I) detector.[251] The absorption of the X-ray beam by a detector increases with the increasing atomic number of the gas and increasing detector length. The ionisation detectors may be filled

with one or two inert gases, where the gas mixture inside the chamber could be adjusted to achieve the required absorption for a given edge energy.

Besides measuring the transmitted X-ray intensity through the sample, XAS measurements could alternatively be achieved by measuring the intensity of fluorescence X-rays (I_f) from the sample (more details on the principles of XAS both in transmission and fluorescence modes are discussed in section 3.4.2). Fluorescence X-ray detectors are usually positioned at a 90° angle relative to the incident beam direction, with the sample being positioned at a 45° angle, as illustrated in figure 3.8(b). The 90° angle between the detector and the incident beam direction is used because the intensity of scattered X-rays is a minimum at 90° while the fluorescence X-rays are emitted from a sample in an isotropic manner. Therefore, the greatest signal to background noise ratio is obtained at a 90° angle between the incident beam and the detector. The intensity of fluorescence photons may be detected using ionisation chamber detectors, however, this may only be practical in samples with low background signals. This is because ionisation chamber detectors do not distinguish X-rays photons based on their different energies. Therefore, samples containing secondary elements with an absorption edge closely prior to the absorption edge of the element of interest will have a large background signal. In these cases, solid-state detectors present better detection option. Solid-state detectors utilise a semiconducting material (usually a germanium or silicon crystal) as a sensor for fluorescence. Incident radiation generates a number of electron-hole pairs in the semiconductor (proportional to the energy of the incident radiation), which are then separated under the influence of an electric field. The resulting current pulse is amplified and analysed to determine the number and energy of the incident fluorescence photons. The solid-state sensor on a germanium detector is usually protected from the external environment by a thin beryllium window and is operated at liquid nitrogen temperature. Nowadays, multi-element detectors (MEDs) have multiple detector channels within the same detection unit, and the fluorescence signal from each detector channel are collected and summed.

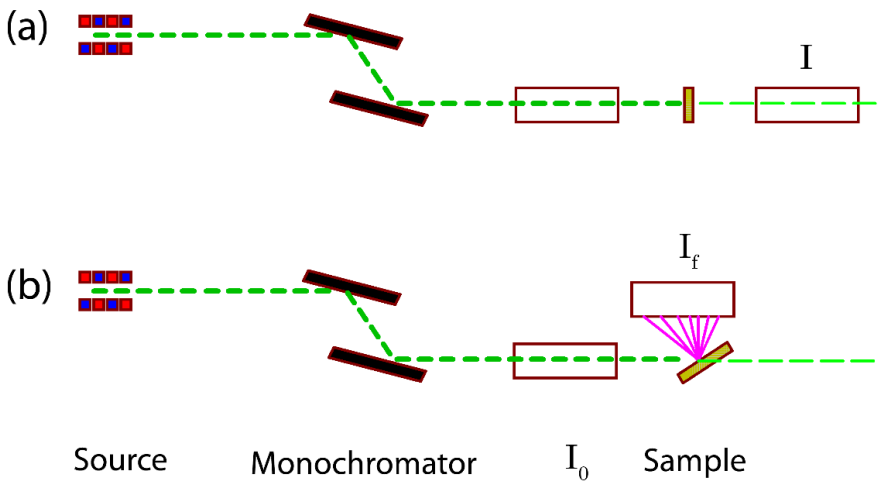


Fig. 3.8 Beamline configuration and typical apparatus for XAS measurements in (a) transmission geometry and (b) fluorescence geometry.

3.4.1.3 X-ray Lenses

Diffractive and reflective X-ray optics are used for focusing of the incident beam and image forming objective lenses. Fresnel zone plates (FZP) diffractive optics are the most often used on X-ray beamlines. FZPs consist of a series of alternating opaque and transparent concentric rings (zones) which act as a diffraction grating. The zone widths are decreasing as the plate radius increases (figure 3.9) in order to focus the X-rays by increasing the diffraction angle. The spatial resolution in a zone plate microscope is largely dependent on the width of the outer most zone. The radius for the nth zone is given by:

$$r_n = \sqrt{n\lambda f + \frac{n^2\lambda^2}{4}} \qquad \text{Equation 3.16}$$

(Where λ is the X-rays wavelength and f is the desired focal length). The focal length is defined by:

$$f = \frac{2r_N\Delta r_N}{\lambda} \qquad \text{Equation 3.17}$$

(Where r_N is the full radius (radius at the outer most zone) and Δr_N is the width of the outer most zone). The depth of field, before and after the focal point, is defined as:

$$DOF = 2.44\ \frac{\Delta r_N^2}{\lambda} \qquad \text{Equation 3.18}$$

At low X-ray energies, the absorbing element of the FZP is dominant (acts as an opaque plate), and the loss of X-ray due to absorption and different diffraction orders limit the maximum FZP efficiency to approximately 10% in the first order.[253] At higher X-ray energies the FZP primarily phase shifts the X-rays and maximum theoretical efficiency becomes 40%. Ideally, unwanted diffraction orders are suppressed to achieve a higher efficiency. To absorb or phase shift high energy X-rays, FZPs must be manufactured from heavy metals and at thicknesses above 1 μm. Zone plates are fabricated *via* nanofabrication techniques using electron beam lithography and electroplating/etching of a metal. The zone widths Δr_N are usually in the range of tens of nanometres. This means that the zones have a high height-width aspect ratio. State of the art zone plates have an aspect ratio around 15-20 or more,[254] and these structures usually degrade over time.

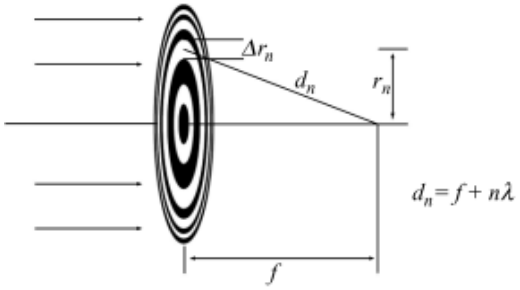


Fig. 3.9 Structure and parameters of the Fresnel Zone Plate (adapted and reproduced with permission from[255]).

Another type of diffractive optics introduced for better resolution and efficiency in focusing hard X-rays is the multilayer Laue lenses which can focus X-rays beams to nanoprobes.[256] These are one dimensional zone plates which can be fabricated of several thousand zones with an outermost zone width of 4 nm and thickness greater than 10 μm.[253] Laue lenses are used side by side at a tilt angle (figure 3.10(d)) and currently provide a state-of-the-art resolution of 11 nm, at the nanoprobe beamline in the National Synchrotron Light Source II, USA.[257]

Reflective optics (mirrors) are also used in focusing especially in the field of hard X-rays. However, reflective optics are challenging to fabricate with the required optical shape and subnanometer surface roughness. Errors in the shape of reflective optics affect images in a similar manner to aberrations, while surface roughness affects the contrast and throughput.[253] Figure 3.10 illustrates common types of lenses used for X-ray focusing and imaging.

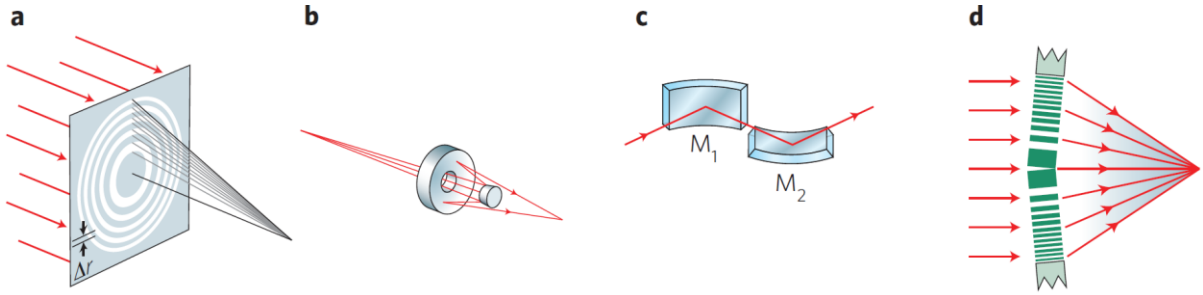


Fig. 3.10 Schematics of four common X-ray microscopy optics. (a) A Fresnel zone plate lens is a circular diffractive grating that can be used for focusing or imaging X-ray. (b) A multilayer-coated two-bounce Schwarzschild reflective objective for focusing or imaging. (c) A KB glancing incidence mirror pair for focusing hard X-rays. (d) A multilayer Laue lens for focusing X-rays (adapted and reproduced with permission from [253]).

3.4.2 X-ray Absorption Spectroscopy

3.4.2.1 X-ray Absorption Coefficient

The relationship between the intensity of an incident X-ray beam (I_0) and the intensity of the transmitted beam (I) through a sample of thickness (x) is given by Beer Lambert's law (Equation 3.19)

$$I = I_0 e^{-\mu x} \qquad \text{Equation 3.19}$$

(Where μ is the linear attenuation coefficient which describes the fraction of the beam that gets absorbed or scattered per unit thickness of a sample of a specific element, and μx is known as the absorbance).

When a number of elements (i) are present in a sample, the mass absorption coefficient μ_ρ is the weighted sum of absorptions by the constituent elements:

$$\mu_\rho = \sum_i \omega_i \mu_{\rho i} \qquad \text{Equation 3.20}$$

(Where ω_i is the mass fraction of element i with a mass attenuation coefficient $\mu_{\rho i}$).

The X-ray absorption coefficient μ is the probability for an incident X-ray to be absorbed by a sample and is a function of the incident X-ray energy. X-ray absorption spectroscopy involves measuring μ as a function of X-ray energy. The incident X-ray intensity is measured by an upstream detector before the beam then travels through the sample, and the transmitted intensity is measured by the downstream detector. The X-ray absorption coefficient can subsequently be determined by rearranging equation 3.19:

$$\mu x = -\ln \frac{I}{I_0} \qquad \text{Equation 3.21}$$

Since the atomic relaxation (fluorescence) processes are proportional to the preceding photoabsorption, the absorption coefficient may also be derived from the number of fluorescence X-rays (I_f):

$$\mu x \propto \ln \frac{I_f}{I_0} \qquad \text{Equation 3.22}$$

From equation 3.19 it can be deduced that increasing the intensity of the incident X-ray beam, increases the intensity of the transmitted beam linearly, while a thicker sample reduces the intensity of the transmitted beam exponentially. Increasing the thickness of the sample by one absorption length decreases the transmitted X-ray intensity by approximately 63 %. This exponential relationship between media thickness and beam transmittance was utilised in this work to exclude signals from the sample while detecting only dissolving species: by employing a thick enough *in situ* electrochemical cell with the CoCrMo sample fitted downstream, the X-ray could be fully attenuated by the electrolyte before reaching the sample. Thus, fluorescence signals could be detected from the electrolyte only.

The probability for absorption of an X-ray, by the target atom, increases sharply when the incident X-ray energy equals the energy required to excite a target electron (photoabsorption). These steps in the absorption coefficient are termed absorption edges.

3.4.2.2 X-ray Absorption Edges

Each element has a characteristic set of absorption edges corresponding to the binding energies of its electrons. The energy of a given absorption edge increases as the atomic number of the element increases. This is because

elements with greater atomic numbers have more positively charged nuclei (due to a greater number of protons), and therefore, they have a higher binding energy of an electron in a given atomic orbital. The K-shell electrons are closest to the atom's nucleus, and therefore they have higher binding energy than the L-shell electrons. The most commonly used edges in XAS are the K (1s) edge and the L_3 ($2p_{3/2}$) edge. In principle, XAS measurements could be carried out for any absorption edge, however, experiments are simpler when performed at atmospheric pressure and therefore, in order to avoid excessive beam attenuation, higher energy measurements (K-edges) are preferred. On the other hand, XAS measurements could be difficult above a certain energy (approximately 30 keV),[258] thus, for heavy elements with high K-edge energies, the more accessible L-edge may be used.

Scanning the X-ray energy across a particular edge in a specific sample gives rise to a distinctive X-ray absorption spectrum (figure 3.11). XAS spectra are not only defined by the steps at the binding energies of the elements but other features exist that allow further information about the sample to be extracted. The region of the spectrum which is near the absorption edge step is termed X-ray absorption near edge spectroscopy (XANES), while the region at 50-100 eV beyond is called the extended X-ray absorption fine structure (EXAFS). XANES provides information on the oxidation state of the atom as well as the binding geometry. EXAFS can provide information on local environments including the type, the number of neighbouring atoms and interatomic distances (this work does not involve EXAFS analysis, but the principles behind both XANES and EXAFS information are discussed briefly).

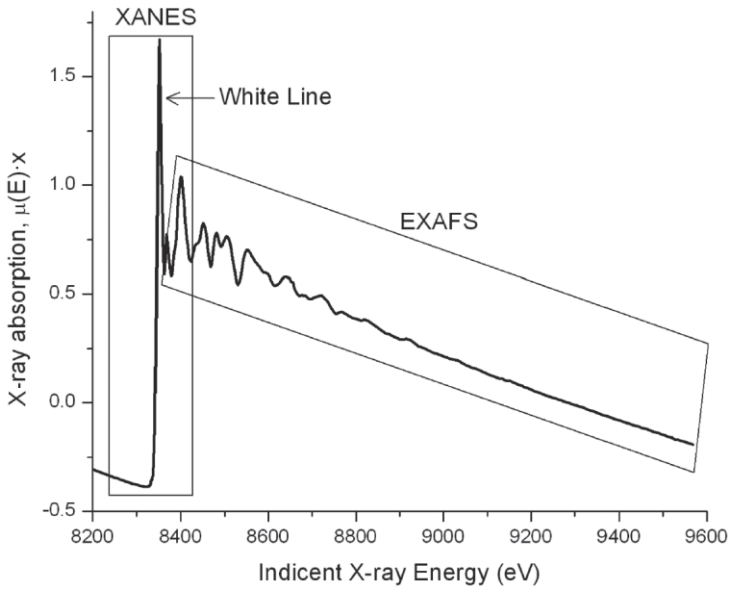


Fig. 3.11 An example of an X-ray absorption spectrum, with the main spectrum regions (XANES and EXAFS) indicated (from[251]*).*

The shape of the absorption edge is related to the density of states available for the excitation of the photoelectron. For some elements, the edge step region may include features such as a pre-edge peak, shoulder, or a strong peak at the top of the edge step referred to as the *white* line. These different features are caused by differences in the density of unoccupied electron orbitals that can be occupied by the excited photoelectron.

The oxidation of an element (higher oxidation states of an element) shifts its absorption edge to a higher X-ray energy. In a neutral atom, the positive charge of the nucleus is screened by the negative charge of the electrons. The presence of a lower number of electrons, compared to protons, in an oxidised atom lowers the energy states of the remaining electrons, which causes the absorption edge energy to increase. Additionally, the change in an element's oxidation state is usually accompanied by a change in centrosymmetry, which will change the features at the absorption edge region.[251] An example of a species exhibiting an isolated peak in the absorption spectrum before the edge-step is hexavalent chromium (Cr(VI)), which exhibits a sharp pre-edge peak.

Absorption edges occur when the energy of the incident X-ray (E_i) equals the binding energy of a core electron (E_b). In the post-edge region, when the incident photon has higher energy, the electron is knocked out with a specific energy of $E=E_i-E_b$ (and thus a specific wavelength). The electron wave is backscattered from neighbouring atoms. Considering the wave properties of electrons, the backscattered photoelectron wave interacts with its core state. As the energy of the incident X-ray changes, the energy of the photoelectron E changes and hence its wavelength. This causes the interaction between the photoelectron and the initial core state to go in and out of phase. This phase oscillation results in oscillation in the absorption probability giving rise to the oscillatory behaviour seen in the absorption spectra (figure 3.11). This is defined in this expression for a single backscattering event:

$$\chi(k) = \frac{\mu(k)-\mu_0(k)}{\mu_0(k)} = \sum_j \frac{N_j}{kR_j^2} A_j(k) \,.\, p_j(\hat{e}) \,.\, \sin[2kR_j + \psi_j(k)] \qquad \text{Equation 3.23}$$

(Where $\chi(k)$ is the normalised oscillatory absorption defined as the difference between the total absorption, μ, and the smooth absorption, μ_0, normalised by the smooth absorption).

The frequency of the oscillation depends on the distance to the neighbouring scattering atoms. Therefore, for multiple scattering from different atoms, Fourier transform is applied to identify individual contributions. Neighbouring atoms can then be identified because each element has characteristic variations in the amplitude and phase of the backscattered wave with energy.

3.4.2.3 XAS Scan Parameters and Data Collection

The main parameters to be selected prior to an XAS scan are the energy range, energy step size, the detection (exposure) time, and the monochromator settling time. The energy range is selected to cover values before, across, and after the absorption edge of interest. The energy range prior to the absorption edge is used to determine background contributions, while the energy range after the edge may be extended according to the study requirements. The energy step size determines the energy resolution of a scan, with the lower limit given by the energy resolution of the monochromator. The exposure time is the duration that the detector signal is measured at each energy point. The monochromator settling time is a pause interval after each monochromator movement,

usually for 0.2–0.5 s,[251] to allow settling of mechanical vibrations before collecting the detector signal. It is also possible to conduct time scans at a single energy point to monitor the absorbance of the sample at a specific energy over time, which may change due to sample dissolution or change in chemical speciation.

The time period required for an XAS scan increases with increasing energy range, decreasing the energy-step size, and increasing detection or settling time. To increase the efficiency of data collection, the spectrum could be divided into regions that have different energy resolution requirements. An XAS scan could be divided into the following regions: (i) the pre-edge region, (ii) the edge region, and (iii) the post-edge region. The region before the edge defines the background baseline, so large steps of 5 - 10 eV are usually taken. Smaller step sizes of 0.05 to 0.5 eV are required to resolve the features in the edge region. In the EXAFS part of the spectrum, the oscillations broaden with increasing energy and step sizes may be adjusted accordingly. Furthermore, for time-sensitive measurements such as in a dynamically changing chemical system, it may be possible to reduce the number of energy points to a few distinguishing energy points. The detection time at each step typically varies from 2 to 4 s, with longer times used to measure the weaker signals. It is recommended to collect and average data from multiple scans on a sample to obtain better signal to noise ratios.[251]

Conventional XAS typically uses millimetre-size probes obtaining information from a millimetre-size portion of the sample. Higher spatial resolution measurements are possible with micro and nanoprobe XAS measurements, utilising a focused X-ray beam that probes the sample on the micrometre and nanometre scales respectively.

XAS can be collected both in transmission and fluorescence modes. Samples studied in fluorescence mode are placed at a 45° angle with respect to the incident X-ray beam. Samples for transmission measurements can be placed perpendicular to the beam, or at a 45° angle which increases the X-ray path length through the sample. In transmission, the absorbance is determined by measuring the attenuation of the incident beam as it passes through the sample (as per Beer-Lambert's law given in equation 3.19 and discussed in section 3.4.2.1). Transmission mode samples should absorb a large number of X-ray photons to produce a high-quality absorption signal, while simultaneously transmitting enough X-ray photons to be detected by the downstream intensity transmitted intensity detector. In the fluorescence measurement mode, the emitted fluorescence photons resulting from atomic relaxation are detected. Since each element has a characteristic fluorescence energy, the fluorescence photons from the element of interest can be measured separately from the total absorption (distinguishing photon energy is only possible with solid state detectors). The fluorescence mode is the preferred measurement mode for more dilute samples (the element of interest is more dilute in the sample). This is because in transmission mode the signal to noise ratio (SNR) applies to the total absorption data and for dilute elements, the SNR will be degraded by a factor related to the dilutions which may make it difficult to extract in practice. On the other hand, highly concentrated samples may pose a problem in fluorescence mode measurements. In highly concentrated samples

the fluorescence X-rays may be reabsorbed by the element of interest in the sample, causing an attenuation of the fluorescence signal. This effect is termed self-absorption.

XAS spectra could be recorded using the typical relatively large beams, defined only by slits, with sizes in the order of millimetres. When studying wear particles, large beam sizes provide population-averaged measurements of hundreds or thousands of particles. Additionally, advances in X-ray focusing optics facilitated spatially resolved XAS measurements. Nowadays, X-ray micro and nanoprobes are available in many synchrotron facilities worldwide. These focused beams could be used to collect XAS measurements on single particles. Furthermore, focused beams could be raster scanned across bigger samples and obtain spatially resolved information.

3.4.2.4 XAS Data Analysis

XAS data analysis can be complex but, in the context of XANES data only, it may be summarised in a few main steps. Firstly, background subtraction removes the contribution from background represented in the pre-edge region. The spectra are then normalised to allow comparison between different spectra. If the sample comprises two or more oxidation states of the element of interest, it can be fitted to a linear combination of standard absorption spectra to determine the composition ratio of each species.

3.4.2.4.1 Normalisation

Normalisation standardises XANES spectra to remove variations between samples due to effects of analyte concentration, sample thickness and detector effects. Therefore, variations in the features of normalised spectra are attributed to the chemical speciation of the analyte element and local binding environment. Normalised XANES spectra of various samples could then be overlaid for qualitative comparisons. Sample spectra are normally overlaid with spectra of chemical standards to obtain an idea of the possible chemical species represented in the sample spectra.

The normalisation process involves fitting a linear function to the pre-edge region of the XAS spectrum and a linear or a quadratic function to the post-edge region. First, background removal is completed by subtracting the pre-edge line from the entire data spectrum. The post-edge line is extrapolated to the edge energy and the difference between post edge line and the pre-edge line at the absorption edge is called the edge step. The entire data spectrum is divided by the edge step to produce the normalised spectrum. Thus, in a normalised spectrum, the pre-edge region is at zero absorption, while the edge step is equal to 1, as shown in figure 3.12.

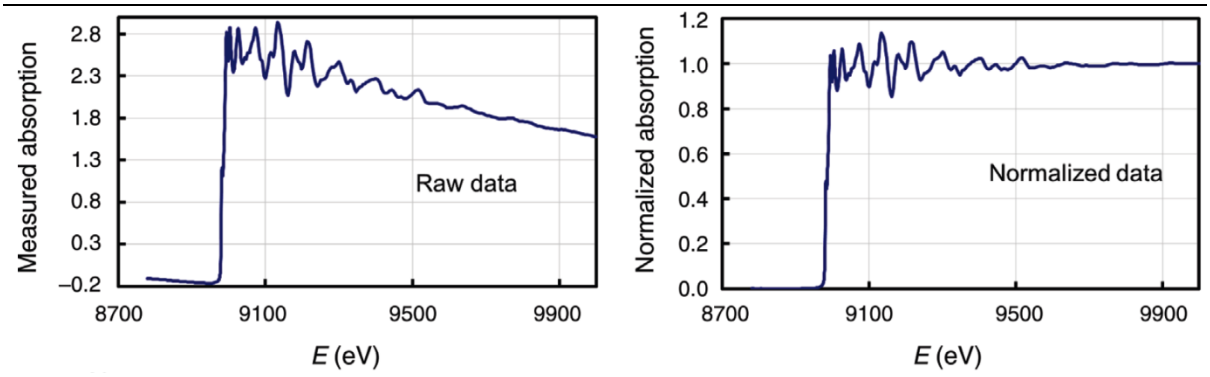


Fig. 3.12 Example of an XAS data illustrating the raw data acquired and after normalisation to the edge step (adapted and reproduced with permission from [252]).

3.4.2.4.2 Linear Combination Fitting

As shown in equation 3.20, the total absorption coefficient is the sum of individual coefficients of the different elements in the sample. This also includes the sum of different chemical speciation of particular elements in the sample. Based on this additive nature of absorption from different species in the sample, linear combination fitting is a quantitative analysis which can be used to determine the composition fraction of species in the sample. Linear combination fitting models the spectrum from a sample of unknown speciation with a linear combination of spectra from standards (of known structure and composition) that are candidate species within the sample.

3.4.3 Transmission X-ray Microscopy

In addition to spectroscopy, X-ray absorption can also be utilised to produce absorption contrast images. These images display the spatial variation of X-ray transmission through a sample. X-ray images display the spatial variation of the transmittance I/I_0 (or absorbance, *i.e.* opposite contrast) and can be thought of as maps of the thickness variation Δx in a material. The smallest detectable Δx depends on the smallest $\Delta I/I_0$ that can be distinguished from noise.

X-ray imaging has been utilised since X-rays were discovered by Röngten, who obtained the first radiograph. The majority of X-ray imaging since then (*e.g.* medical radiographs, security scans) was performed using a similar direct projection imaging where a sample is placed close to the X-ray source and detectors are placed behind the sample to record the transmitted X-rays. The resolution of this set up is limited and depends on the size of the X-ray beam, detector pixel size, and magnification (distance relationship between X-ray source and sample, and between sample and detector). High-resolution X-ray microscopy was not developed until advancements in nanofabrication techniques led to the production of the Fresnel Zone Plates diffraction lenses (discussed in section 3.4.1.3). Today, transmission X-ray microscopy (TXM) can achieve a resolution of 10 nm using soft X-rays,[259] and better than 20 nm with hard X-rays.[260] The TXM (figure 3.13) is analogous to the optical microscope and TEM. It consists of a probe source (in this case an X-ray source) and a condenser lens to project the beam onto a sample and an

objective lens which projects a magnified image onto the detector. The detector system employs a scintillator screen which converts the X-rays to visible light. The light is subsequently projected with an optical objective lens (providing an extra magnification factor) onto a CCD camera.

X-ray microscopy provides many advantages when compared to transmission electron microscopes, such as lower sample damage and greater tolerance of wet samples. A summarised comparison between TXM and TEM is given in table 3.1.

Table 3.1 Comparison between the TXM and TEM techniques (adapted from[255])

	TXM	**TEM**
Imaging beam energy	250 eV – 100 keV	10 keV – 1 MeV
Spatial resolution	≈ 20 nm	Atomic resolution
Spectral resolution	0.05 eV	0.1 eV[b]
Sample thickness	Hundreds of micrometres to many millimetres	~ 200 nm
Imaging environment	Compatible with *in situ*, high temperatures & aggressive chemical environments	Vacuum required[c]
Material analysis	XAS, X-ray fluorescence, X-ray diffraction	EDX, EELS

3.4.3.1 Data Collection and Interpretation

Morphological information can be obtained through absorbance contrast X-ray images. Furthermore, simultaneous chemical information (spectromicroscopy) can be performed by obtaining a series of images with fine energy increments, thus XANES and EXAFS features can be acquired. These absorption spectra can be obtained for every pixel in the image. The typical TXM data collection rate at synchrotron facilities is 1 s per image.[261] By analysing the individual pixel spectra a chemical composition map, with the spatial resolution of the pixel size, can be produced. *In situ* samples, where some movements may occur, can present a challenge to how accurately this can be achieved. However, this can be corrected by computationally aligning the images before extracting the spectra. Repeating the overall procedure at different time points offer the possibility of tracking the chemical changes *in situ*. There is a trade-off between collecting large spectra using more images, at closely separated energy points, to achieve a more accurate chemical composition quantification, versus obtaining more, less resolved, spectra in a given time period to track chemical changes at an improved temporal resolution and reduced

[b] This can be achieved only in monochromated instruments
[c] Vacuum is required for the highest spatial resolution; *in situ* TEM is available but beam effects such as water radiolysis limits accurately controlled measurements in wet electrochemical cells

X-ray dosage. Either way, noise in the data could limit the accuracy of the chemical quantification process and therefore a middle ground may be achieved at a lesser cost.

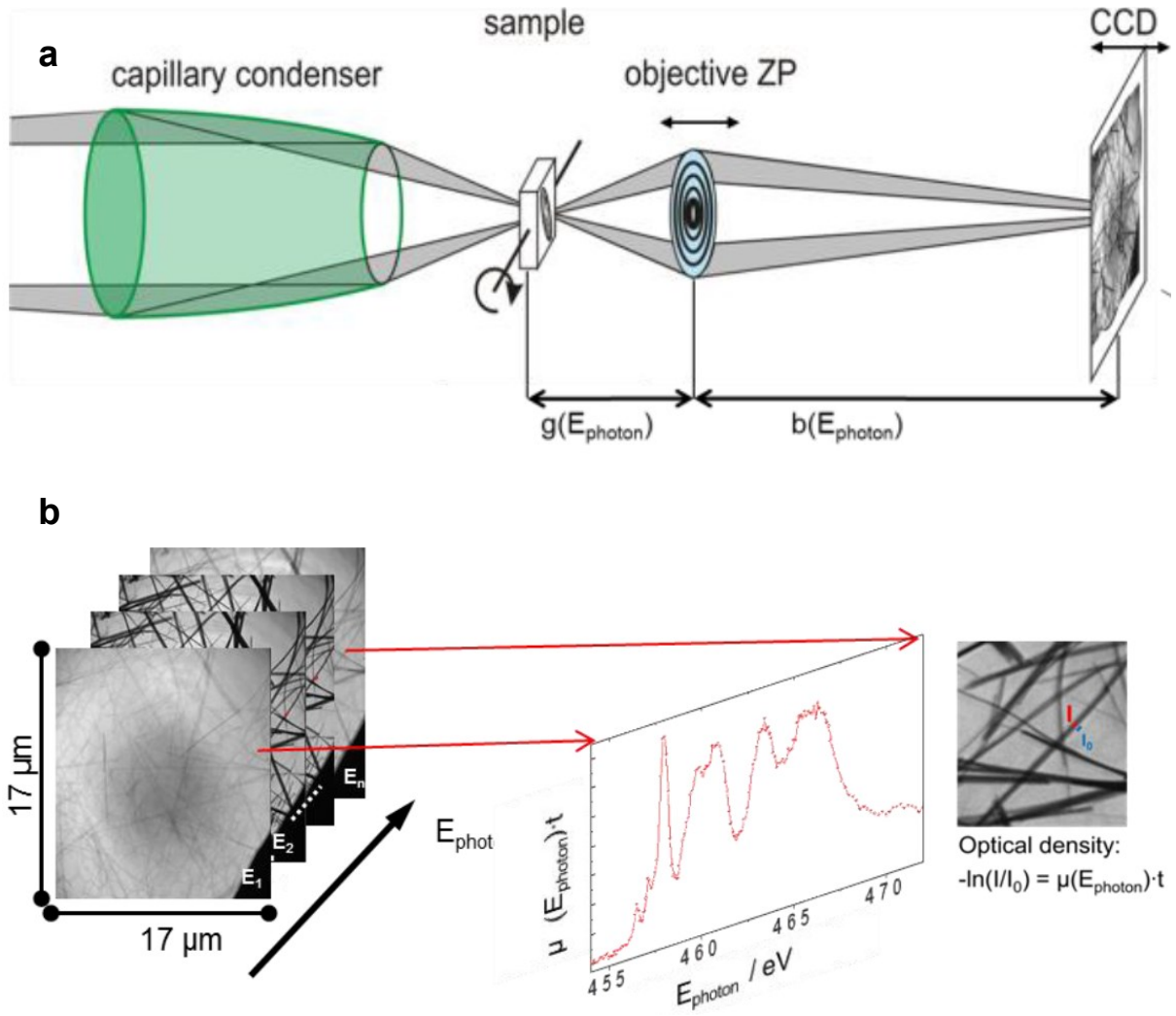


Fig. 3.13 (a) Schematic illustrating the set-up of a TXM. (b) Illustration of spectromicroscopy performed through obtaining a stack of multiple images at different photon energies and thus image intensities can be translated to absorption spectra. (Adapted and reproduced with permission from [262]).

3.5 Magnetron Sputtering

Sputtering is the erosion of a material upon bombardment by energetic particles. In this process, collisions occur between incident ions, with energies much higher than the binding energies of atoms in the target, and atoms in the near-surface layers of the target material. Through binary energy transfer, the created recoil (displaced and moving) atoms undergo further collisions with other atoms in the target initiating a cascade of collisions. When reaching the surface with sufficient energy, these collisions lead to the ejection of surface atoms. The primary collision can directly eject an atom but only if the incident ion is not normal to the surface. The key parameter describing the sputtering process is the sputtering yield which is defined as the number of ejected atoms per

incident ion. The sputtering yield is dependent on the target atoms and their binding energies, the relative mass of the incident ions and target atoms, the energy of the incident ion, and the angle of incidence. While sputtering is damaging to the target solid, it is utilised as a physical vapour deposition (PVD) technique for thin film deposition.

As a physical vapour deposition method sputtering can be used to produce homogenous coatings of a material on a substrate. The deposition is achieved by ejecting the material of interest from a source (the target solid) using accelerated argon ions. Subsequently, the ejected target atoms condense on the substrate *via* diffusion. Deposition is performed in chambers initially maintained at high vacuum (typically 10^{-5} to 10^{-8} Torr) before argon gas is fed into the chamber at a specific set pressure. Accelerated electrons are used to ionise argon atoms to produce a plasma of positively charged argon ions. The Ar ions are accelerated by an electric field to bombard the negatively charged target (cathode). As a result, target atoms are ejected into random directions, forming a 'vapour', before condensing on surrounding surfaces including the substrate. Target bombardment collisions may also lead to the release of secondary electrons due to ionisation of the target atoms. In magnetron sputtering the secondary electrons are used to increase the argon ionisation rate *via* the use of a ring magnet placed under the target. The magnetic field 'traps' the secondary electrons into helical paths movement around magnetic field lines where more ionising collisions with argon atoms occur. The principle of magnetron sputtering is illustrated in figure 3.14. Eventually, a thin film coating of the target material is formed on the substrate. The uniformity of the produced film can be improved by steadily rotating the substrate. Films of desired thicknesses can be produced using favourable deposition parameters. The sputtering power and deposition rate are proportional to the sputtering yield. The deposition rate is maximum at an optimum argon pressure. Choosing the argon pressure is a trade-off between more Ar ions for sputtering collisions (achieved at higher pressures) versus maintaining low scattering rate of Ar ions due to collisions with neutral Ar atoms (achieved at lower pressures). The scattering of Ar ions by neutral Ar atoms could hinder sputtering collisions. Therefore increasing the number of Ar ions without increasing the number of Ar atoms, as is the case in magnetron sputtering, is desirable and allows operation at lower pressures.

Magnetron sputtering was utilised in this research (using LAB 18 thin film deposition system, Kurt J. Lesker) to produce CoCrMo thin films on different substrates: microscope glass slides (VWR, UK), polyimide (Kapton) films (Advent Research Materials, UK), and gold-coated TEM grids (TAAB Laboratories, UK), depending on the experiment to be performed.

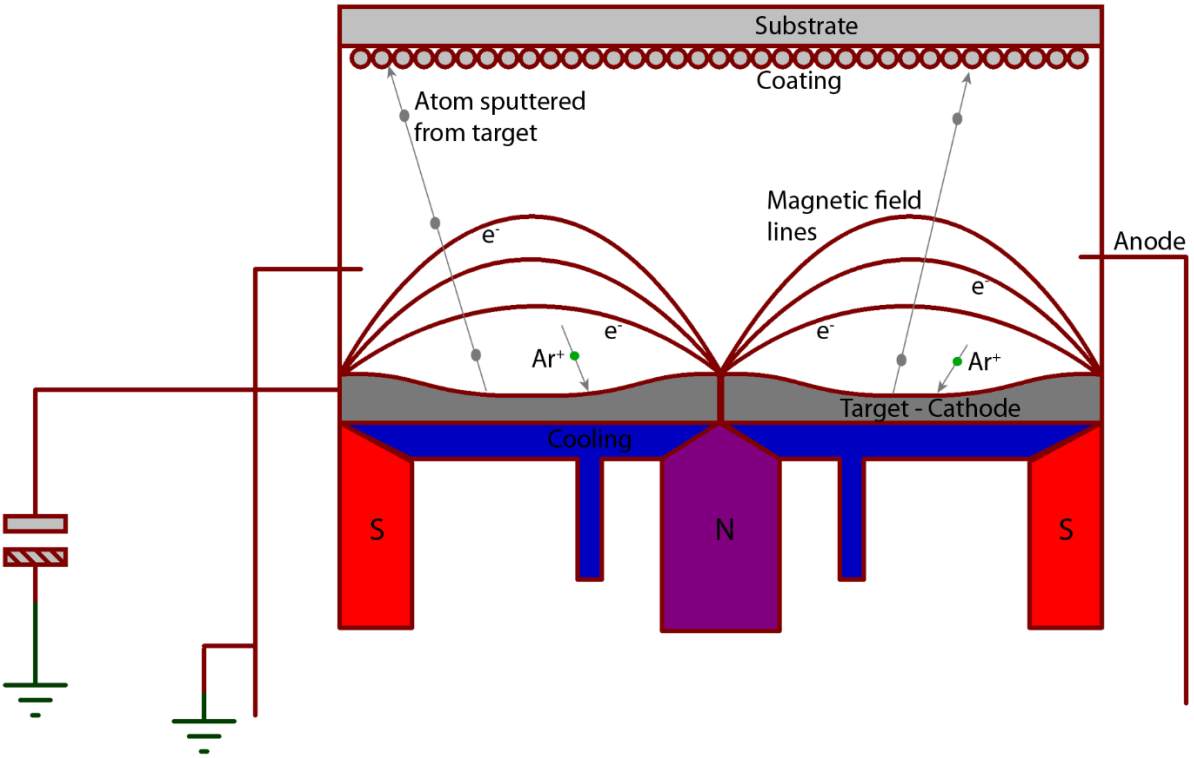


Fig. 3.14 Schematic showing the principle of operation of a magnetron sputtering system. Ar ions are accelerated by an electric field towards the target, leading to the ejection of target atoms which condense on the substrate. The magnetic field is used to trap secondary electrons emitted from the sputtering collision which are then used to increase the ionisation rate of Ar atoms.

3.6 General Experimental Procedures

This section includes details on general methodology that was employed in this work and remained constant throughout the study unless otherwise stated.

3.6.1 Simulated Biological Environment

The simulated biological environment applied in this study consisted of two main aspects: simulated body fluids, and an applied electrochemical potential to mimic the increasingly oxidising environment of *in vivo* inflammation. The simulated body fluid (SBF) consisted of 25 mM MES buffer, 0.5 mM $CaCl_2.2H_2O$, 1 mM $MgCl_2$, and 200 mM KCl. The pH of the SBF was adjusted with NaOH to 5.2 which represents the acidic lysosome environment of a macrophage cell.[197,198] The effect of protein was studied by adding 1 µg/ml of bovine serum albumin to the SBF (serum-SBF). The electrolytes were always maintained at body temperature of 37 °C using a heating element (*in situ* electrochemical cells) or a hotplate (*ex situ* measurements).

3.6.2 Electrochemistry Methods

In this work, electrochemical methods were not only used to study the electrochemical behaviour of CoCrMo; additionally, anodic polarisation was utilised to mimic the oxidising *in vivo* environments during *ex situ* and *in situ* studies of morphological and chemical changes in CoCrMo.

All electrochemical experiments were performed with a three-electrode set up and using the Ivium Compactstat potentiostat (Ivium Technologies, Netherlands). A platinum wire (Sigma-Aldrich, UK) was used as the counter electrode, while Ag/AgCl microelectrode, +199 mV vs SHE, (Microelectrodes Inc., USA) was utilised as the reference electrode. Electrochemical potential values in this thesis are quoted against Ag/AgCl unless otherwise stated.

3.6.3 Electron Microscopy

In this work, two TEM instruments were used: JEOL 2000 Plus and FEI Titan with accelerating voltages of 200 kV and 300 kV respectively. The electron source in the JEOL 2000 Plus microscope was a TEG, while FEI Titan was equipped with a FEG.

SEM images were obtained using two instruments: LEO Gemini 1525 and the Zeiss Auriga FIB-SEM. Both instruments use a FEG electron source. Images were generally collected using SE signals and an accelerating voltage of 5 kV. SEM-EDX was performed with an accelerating voltage of 15 kV.

3.6.4 CoCrMo Particles

CoCrMo particles used in this work were sourced from the University of Leeds where they were produced by ball milling.[216] In general, ball milling is a grinding process performed in a cylindrical shell containing a ball (as the grinding media) and rotating about its axis. In this case, the milling process involved bombarding CoCrMo powder using a zirconium ball for 150 minutes in a zirconium vial. The size of the resultant particles ranges from 10 nm to a few microns. Full details on the production process and a microstructural characterisation of the particles were reported by Simoes *et al.*[216] (and discussed in more detail in section 2.5.1).

3.6.5 3-D Printed Electrochemical Cells

The electrochemical cells deployed for *in situ* measurements at synchrotron beamlines were produced by 3-D printing. Computer-aided designs CAD of the cells were first made on the CAD software Solidworks. The designs were subsequently printed out of polylactic acid PLA using the 3-D printer Ultimaker 2+ with a 100 μm layer resolution.

4 Dissolution of Multiscale CoCrMo

4.1 Introduction

One hypothesis that the *in vivo* reactivity of CoCrMo was not predicted prior to clinical approval is that material assessment tests were conducted only on the *bulk* form of the alloy. It was later discovered that the superior wear resistance of the alloy was only a volumetric measure as large numbers of small wear particles, which can be only a few nanometres in size, are released *in vivo*. At the nanoscale, many properties of materials are different, including chemical reactivity and electrical conductivity. Additionally, a much larger surface area of the material is now exposed to the surrounding environment. Furthermore, it was also revealed that these wear particles are phagocytised by macrophage cells where they are exposed to harsher environments (compared to what is required for regulatory approval). Studies on the electrochemical behaviour of CoCrMo alloys, in the literature, are mainly on *bulk* samples and in neutral pH solutions. The focus in this chapter will be to compare the behaviour of *bulk* and nanoscale CoCrMo in SBF simulating the lysosome environment inside macrophages. CoCrMo nanoscale behaviour was studied *via* thin films which could be electrochemically studied in similar set-up and conditions as the *bulk* samples (unlike nanoparticles). In additions, given their higher surface area to volume ratio, the thin film form would highlight the observable dissolution measurements such as emphasising the morphology development.

4.2 Methods

CoCrMo TFs were grown by sputtering using the LAB 18 thin film deposition system (Kurt J. Lesker), and a CoCrMo sputtering target (Testbourne Ltd, UK) with a composition (63Co-30Cr-7Mo wt. %) similar to the ASTM F75 standard. These films consist of columnar grains with an HCP crystal structure and grain sizes of approximately 15 – 25 nm.[263,264] The growth time, argon pressure and sputtering power were exclusively altered to observe their effect on the resulting films' thicknesses. TFs thicknesses were measured using a profilometer. Two different TFs thicknesses were selected for electrochemical experiments (above and below 100 nm).

CoCrMo *bulk* samples were cylindrical discs machined from the stem of a resurfacing hip system. The discs were 8 mm in diameter discs, with a 5 mm thickness. All *bulk* discs used in this study were polished to 1200 grit followed by a fine polish, using a 1 µm diamond polishing compound. Similar polished CoCrMo surfaces consist mainly of FCC phase and a small amount of HCP martensite phase (the presence of martensite is due to a strain-induced martensitic transformation at the surface resulting from the mechanical polishing process).[64]

Electrochemical experiments were conducted in SBF and Serum-SBF electrolytes at 37^{o} C. Potentiodynamic polarisation measurements were performed by scanning the applied potential in the anodic direction from -500 mV to 900 mV at a rate of 0.5 mV s^{-1}. Potentiostatic tests were conducted at applied potentials in the passive (400

mV) and transpassive domains (800 mV). All electrochemical characterisation was carried out in aerated conditions.

Surface morphology and relative concentrations of Co and Cr were characterised before and after potentiostatic polarisation experiments using electron microscopy and EDX respectively, for both TFs and *bulk* discs. Additionally, X-ray fluorescence microscopy (XFM) was used to map the spatial distribution of Co and Cr in TFs before and after potentiostatic polarisation. The XFM mapping was conducted at beamline 3-ID at the National Synchrotron Light Source (II) in Brookhaven National Laboratory (NY, USA). The TFs samples were raster scanned by the nanoprobe X-ray beam (beam size 65 nm), across 8 μm x 8 μm regions, with an X-ray incident energy of 7727 eV (just above Co absorption edge). Fluorescence maps for both Co and Cr were produced from with approximately 40 nm spatial resolution with signal detection time of 50 ms per pixel. For this experiment, the TFs were grown on silicon membranes with a size of 0.5 mm x 1.4 mm x 0.01 mm (Norcada, USA).

4.3 Results and Discussion

4.3.1 Thin Film Growth

For the experiments reported in this chapter, TFs were grown on glass (microscope slides) substrates (unless otherwise stated). The effect of the three sputtering parameters (time, power and argon pressure) on TF thickness is illustrated in figure 4.1. Each data point represents the average of three independent thickness measurements. While one parameter was varied, the remaining two parameters were maintained at a constant 'base' value. The three base values were: growth time 500 s, argon pressure 3 mTorr, and sputtering power 300 W. Film thicknesses were recorded for argon pressures between 2 mTorr and 6 mTorr. Sputtering was also attempted at 1 mTorr but no deposition was observed. This suggests that argon pressure must reach a threshold higher than 1 mTorr to initiate deposition; otherwise, no obvious trend between film thickness and argon pressure was observed. However, film thickness increased linearly when either time or power was increased. Generally, the thickness of sputtered films would increase at low rates as the values of either time or power increase away from zero, until certain threshold values are met where a constant linear relationship occurs as observed here. These threshold values depend on the extent of surface oxidation on the target material. The rate of film growth was approximately 1.6 Å per second. The TF samples used for the remainder of this study where grown at 500 s and 1000 s (*i.e.* thicknesses of ~ 80 nm and 160 nm), while power and argon pressure were kept at 300 W and 3 mTorr respectively.

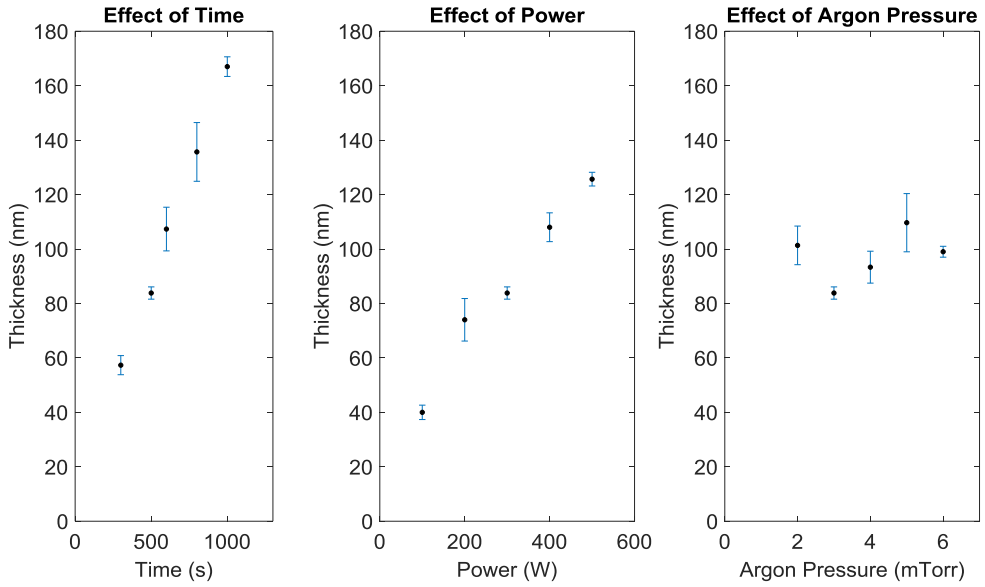


Fig. 4.1 The effect of three sputtering parameters on the deposited film thickness. While no obvious trend could be concluded between film thickness and argon pressure, a linear relationship between thickness and both growth time and power was observed.

4.3.2 Potentiodynamic Polarisation

Three independent potentiodynamic measurements were performed on each sample group (TFs – 80 nm, TFs – 160 nm, and *bulk* discs), in each of the two electrolytes (SBF, Serum-SBF). The polarisation curves, shown in figure 4.2, can all be divided into five main regions in agreement with the literature (refer to chapter 2, section 2.3.2). Firstly, the cathodic domain incorporated potentials below a value between -300 mV and -400 mV (depending on each measurement). The current in the cathodic domain is dominated by the reduction of hydrogen ions and, partially, of dissolved oxygen (equations 2.2 and 2.3, stated in section 2.3). The second domain is described by the transition from cathodic to anodic currents at the corrosion potential which had a value between -300 mV and -400 mV across all measurements. Thirdly, the passive domain characterised by the constant low current which extends until 600 mV. Instant passivation, without an active-passive transition, was observed in all cases. Fourthly, the transpassive domain after 600 mV marked with an increase in current due to the dissolution of the alloy facilitated by the onset of transpassive oxidation of Cr(III), from the passive film to soluble Cr(VI). The onset of the transpassive domain remained very consistent across all measurements of all sample types in this study. As the potential increases, the transpassive current plateaus due to the metal oxidation reactions becoming diffusion controlled. Finally, this is followed by a further rise in current at *ca.* 800 mV due to the onset of water oxidation. The main chemical reactions associated with each region are defined in figure 4.2(c). The drop in current noted at the end of the potential scan in the case of the 80 nm TFs is attributed to the complete dissolution of some areas of the films due to a geometrically inhomogeneous dissolution process. Overall, the alloy exhibited a Cr-like behaviour as previously reported[89] and shown in figure 4.3 comparing the polarisation curve of the alloy to those of pure Co and Cr metals.

Bovine serum albumin reportedly acted as a cathodic inhibitor during CoCrMo polarisation in both neutral and acidic environments.[81,102,119,133] However, it was also reported to accelerate the cathodic reaction in neutral solutions.[110] The results here show variations in cathodic current and corrosion potentials across the six measurements of each sample group, including measurements in the same electrolyte. These variations could not be attributed to presence or absence of serum and therefore the effect of serum on cathodic regime was inconclusive from polarisation curves. Variations in the cathodic domain in these results is likely attributed to differences in sample history (such as sample age before the electrochemical experiments, which may affect factors like oxidation and organic contamination levels in the sample). The *bulk* samples exhibited the most consistency in cathodic current and corrosion potentials.

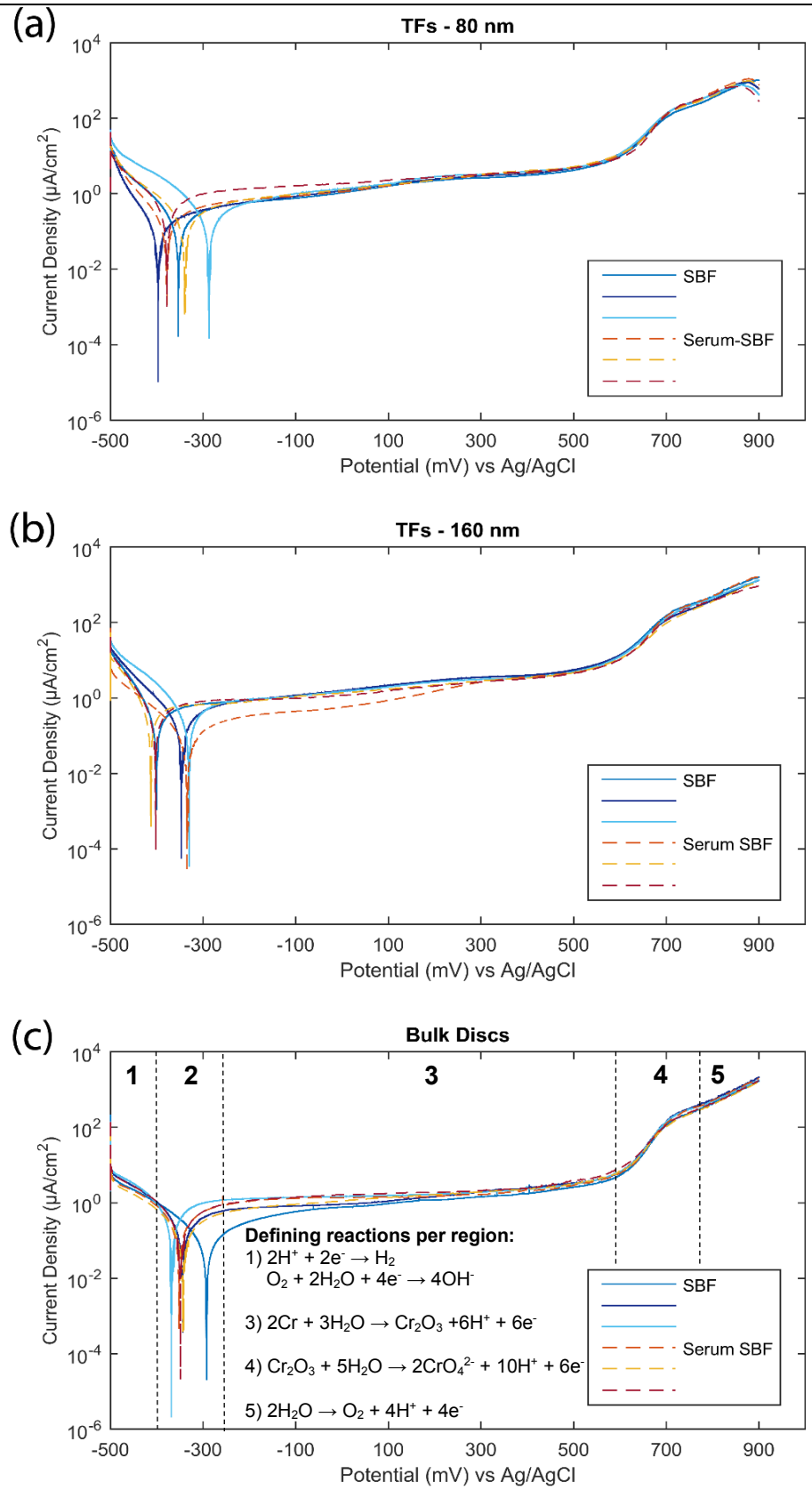


Fig. 4.2 Potentiodynamic polarisation curves of CoCrMo as (a) 80 nm thin films, (b) 160 nm thin films, and (c) bulk discs; in simulated body fluids. Three repetitions were measured for each sample in SBF (solid lines) and in Serum SBF (dashed lines).The main chemical reactions associated with the different domains are annotated in (c). While the passive and transpassive domains (regions 3 and 4) will be dominated by the stated Cr reactions, the measured current densities will also include contributions from Co and Mo. (37° C and pH 5.2).

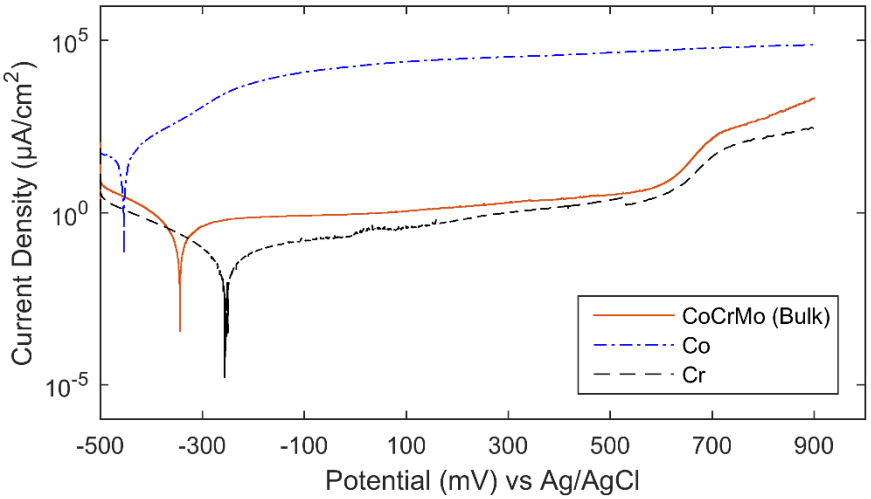


Fig. 4.3 Polarisation curves of CoCrMo alloy, as well as pure metals Co and Cr (polarised in SBF).

4.3.3 Potentiostatic Polarisation

Potentiostatic measurements were conducted by switching the potential from the cathodic domain at -500 mV to both passive and transpassive potentials at 400 mV and 800 mV respectively. Figure 4.4 (a-c) shows the data per each sample group, while figure 4.4 (d-f) displays the same data per potential and/or electrolyte. At cathodic potentials the passive oxide film undergoes reduction and thus the switch from the cathodic to anodic-passive polarisation would simulate the depassivation-repassivation process. The data shows that after the switch to the passive potential, 400 mV, the current exhibits a peak immediately after the potential is applied followed by a rapid decrease in current which is characteristic of the fast kinetics of the passivation phenomenon. In the transpassive domain, at 800 mV, the initial current peak is present but followed by an immediate gradual rise in current, particularly noticeable in the TFs samples, indicative of the alloy dissolution. The late drop in current in the 80 nm TFs, similar to the observations in the potentiodynamic polarisation curves, is owing to the entire dissolution of film sites due to the inhomogeneity of the process as shown in figure 4.5. In addition, a lower current was observed in the TFs, compared to the *bulk* at 800 mV in both SBF and Serum-SBF. However, this is most likely because the recorded current density in *bulk* samples is overvalued as a result of the higher surface roughness of the *bulk* samples (leading to an active surface area greater than their geometric surface area). The effect of serum was examined at 800 mV polarisation and it led to a reduction in current in all of the sample groups.

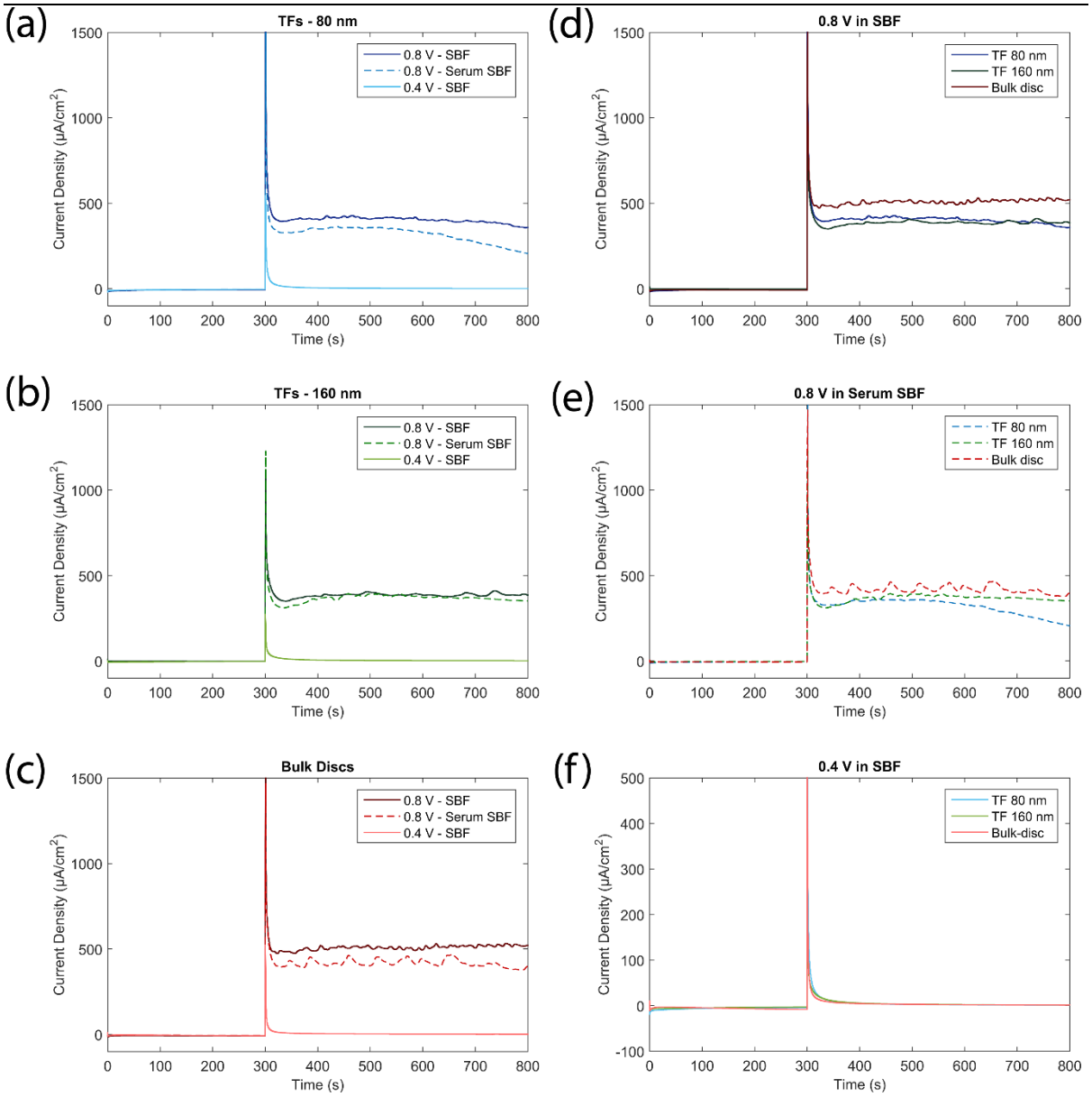


Fig. 4.4 Potentiostatic polarisation measurements of CoCrMo as (a) 80 nm thin films, (b) 160 nm thin films, and (c) bulk discs; recorded when switching the applied potential from -500 mV in the cathodic domain, to either 400 mV (passive domain) or 800 mV (transpassive domain). (d-f) show the same data rearranged per potential/electrolyte.



Fig. 4.5 Optical images recorded at different times during the polarisation of CoCrMo 80 nm TF at 800 mV in SBF. The images reveal the geometrically inhomogeneous dissolution of the film. The red colour in the 1800 s and 2400 s images is the background colour behind the glass substrate (upon which the TF was grown); hence the appearance of the red background colour is indicative of regions where the TF dissolved. Scale bars = 1 mm.

4.3.4 Surface Morphology

Surface morphology was examined, using SEM, in four different conditions: (a) As-received (AR) which compromises samples prior to any polarisation or exposure to SBF; (b) after potentiostatic polarisation at 400 mV for 30 minutes in SBF; and after potentiostatic polarisation at 800 mV for 30 minutes in both SBF (c), and in serum-SBF (d). High magnification, secondary electrons, SEM images of the four conditions for 80 nm TFs, 160 nm TFs, and *bulk* samples are shown in figures 4.6, 4.7 and 4.8 respectively. The AR TFs' images (figure 4.6(a) and 4.7(a)) reveal the growth of the TFs into nanocrystals. The formation of thin films in such cluster morphologies is thermodynamically favoured over the formation of uniform films.[265] The scratches on the AR *bulk* surface (figure 4.8(a)) are due to the polishing process.

4.3.4.1 Effect of Applied Potential

No obvious morphological changes could be perceived between the AR samples and those polarised at 400 mV. However, after 800 mV polarisation, the development of nanoporosity on the samples' surfaces (both TFs and *bulk*) was apparent. The nanopores covered the entire surfaces and had a size range of 10 nm – 25 nm (as measured by the image analysis software ImageJ). The nanopores evidently develop into local networks which are particularly noticeable in the 160 nm TF, and *bulk* samples polarised at 800 mV in SBF (figures 4.7(c) and 4.8(c)). Additionally, a similar behaviour was observed, using STEM, on an 80 nm TF polarised (in SBF at 800 mV) for 5 minutes only, as shown in figure 4.9 (in this case the TF had been grown and polarised on a gold TEM grid).

The evolution of the nanoporous morphology in alloys is characteristic of the process of dealloying. Dealloying (discussed in more detail in section 4.3.7) is the dissolution of the less stable metal (in this case Co, due to its soluble oxide and despite its more positive standard dissolution potential as discussed in section 2.3.1), leading to the aggregation of the more stable component (Cr) into clusters by a process similar to phase separation.[266,267] Hence, instead of a uniform protection of the surface, aggregation of Cr atoms only passivates the surface locally. The dealloying morphology is consistent over time where the number of positive/negative curves (which form the pores) remains constant while the pore size increases, eventually leading to the coarsening of the pores and hence the development of networks.

The results here suggest that this behaviour (development of nanoporosity) is consistent across the size scale (TFs vs *bulk* form) of the alloy. However, this behaviour is dependent on the polarisation potential as the results indicated that the development of this nanoporosity required the onset of transpassivity.

4.3.4.2 Effect of Protein

The presence of protein also affected the morphology development. The presence of serum albumin (serum-SBF) inhibited the development of the nanopores evident through smaller pores and lack of local network development

(figures 4.6(d), 4.7(d), and 4.8(d)). The reduced porosity in the presence of protein is possibly a result of its adsorption to the surface. At pH 5.2, bovine serum albumin is negatively charged which leads to the formation of an adsorbed film on the surface of the samples during anodic polarisation.[81] It was hypothesised that a metal/protein/hydroxide complex forms and becomes adsorbed to the surface restricting metal dissolution.[127] In addition, it was also suggested that the protein film acts as a diffusion barrier restricting metal dissolution.[133] This reduced porosity also comes in agreement with the lower current density observed, in the presence of serum, during potentiostatic measurements. It is possible that the observed protectiveness of protein is a short-term effect. New studies found that the effect of protein on the corrosion of Ti6Al4V was time dependent.[135,136] This is related to the kinetics of metal-protein interactions (as discussed in section 2.3.5.2). Recently, Hedberg[126] suggested that increasing both time and oxidative conditions may cause a negative transition on the effect of protein on metal alloy degradation. Here, the positive effect of protein on CoCrMo degradation is observed even in transpassive conditions, albeit after a relatively short period of time (30 minutes).

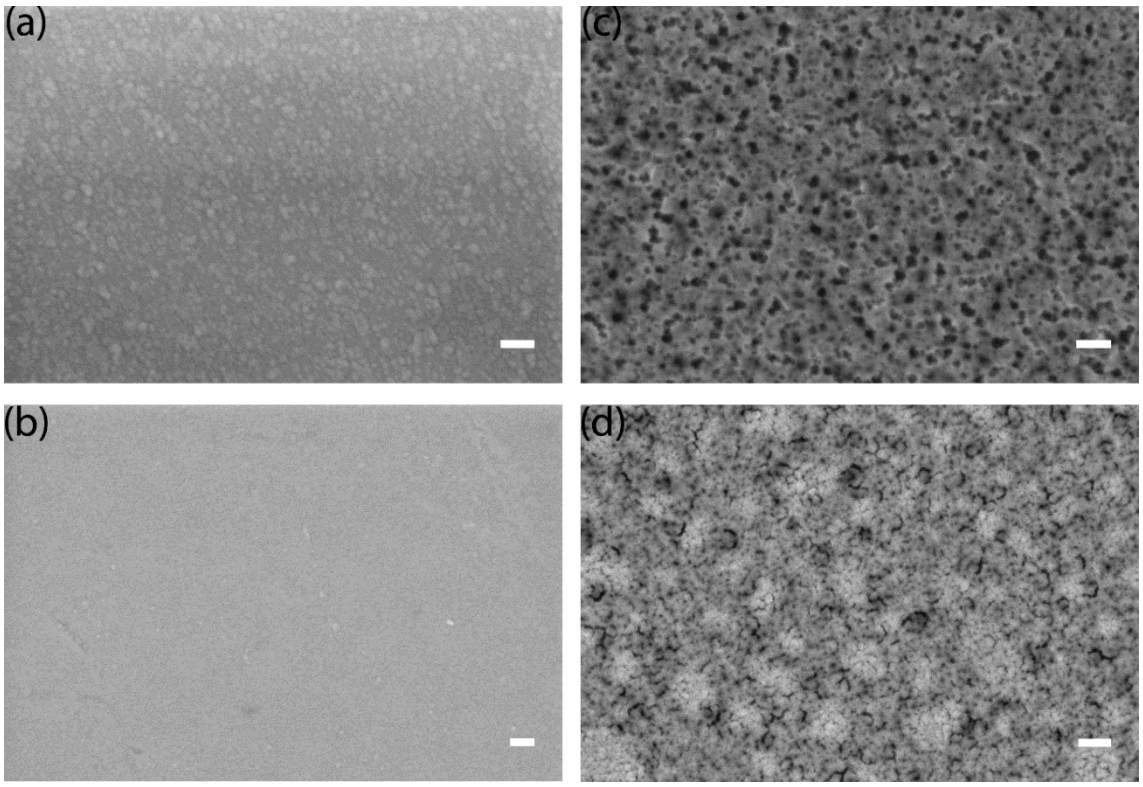


Fig. 4.6 Secondary electron SEM images of CoCrMo 80 nm TFs (a) as received, (b) after 30 min polarisation at 400 mV in SBF, (c) after 30 min polarisation at 800 mV in SBF, and (d) after 30 min polarisation at 800 mV in Serum-SBF. Scale bars = 100 nm.

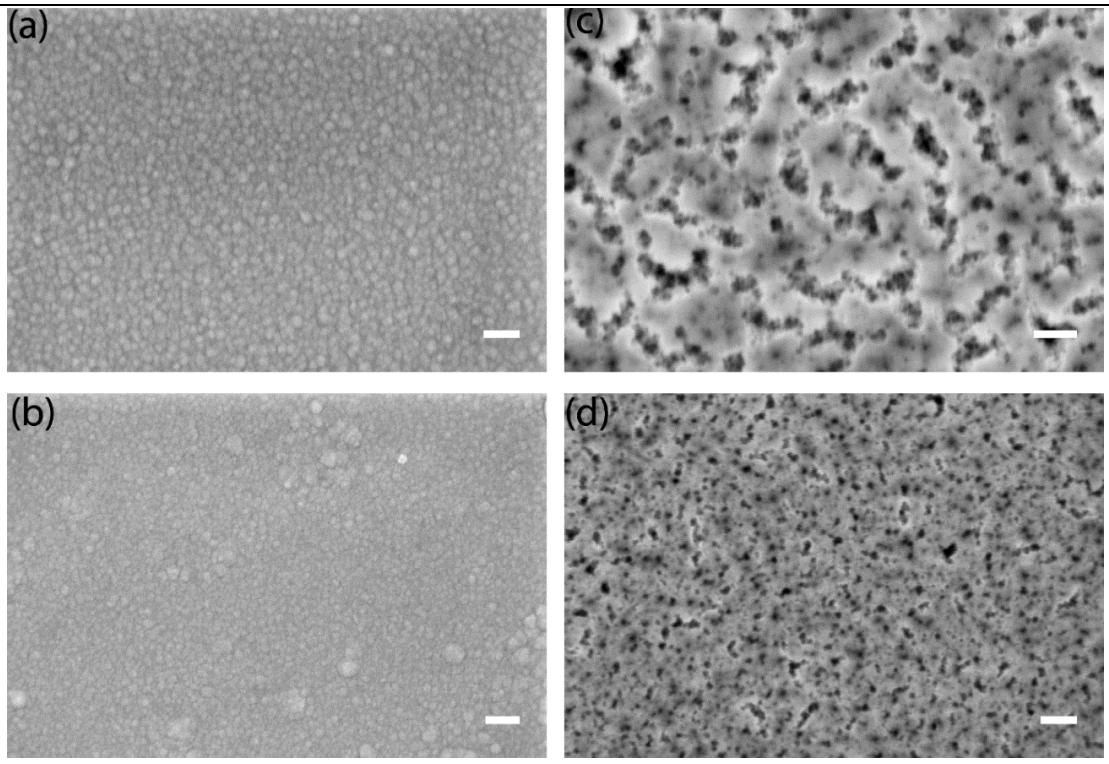


Fig. 4.7 Secondary electron SEM images of CoCrMo 160 nm TFs (a) as received, (b) after 30 min polarisation at 400 mV in SBF, (c) after 30 min polarisation at 800 mV in SBF, and (d) after 30 min polarisation at 800 mV in Serum-SBF. Scale bars = 100 nm.

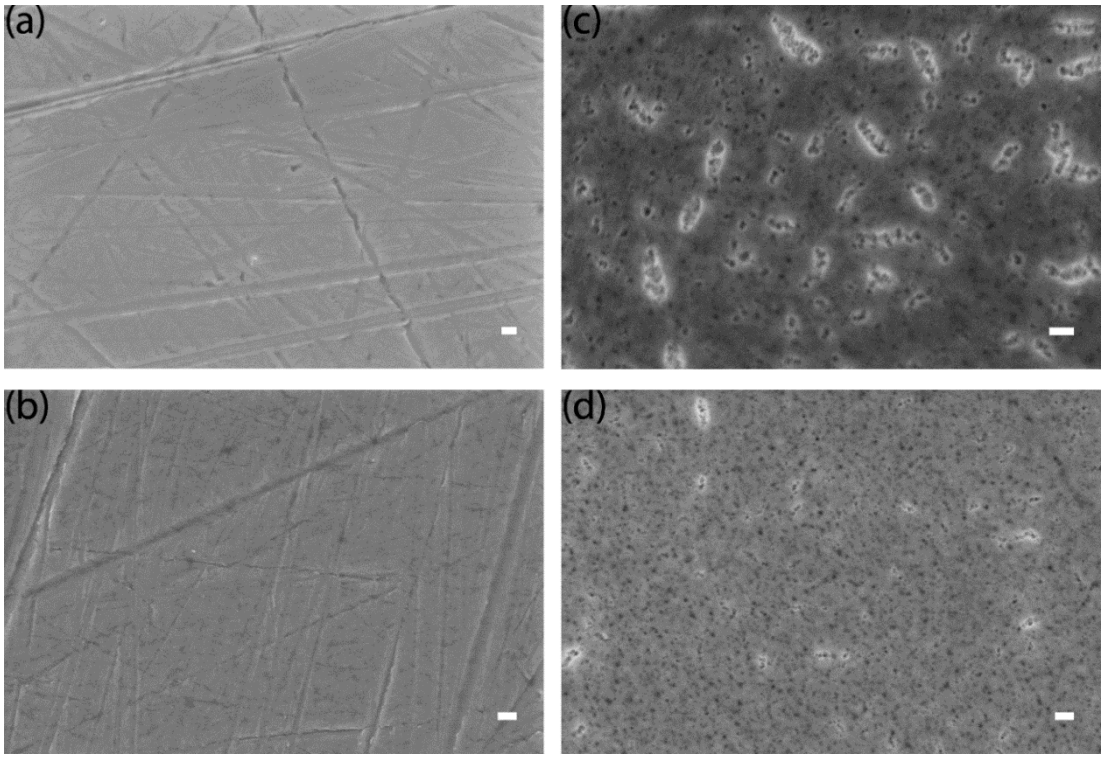


Fig. 4.8 Secondary electron SEM images of CoCrMo bulk discs (a) as received, (b) after 30 min polarisation at 400 mV in SBF, (c) after 30 min polarisation at 800 mV in SBF, and (d) after 30 min polarisation at 800 mV in Serum-SBF. Scale bars = 100 nm.

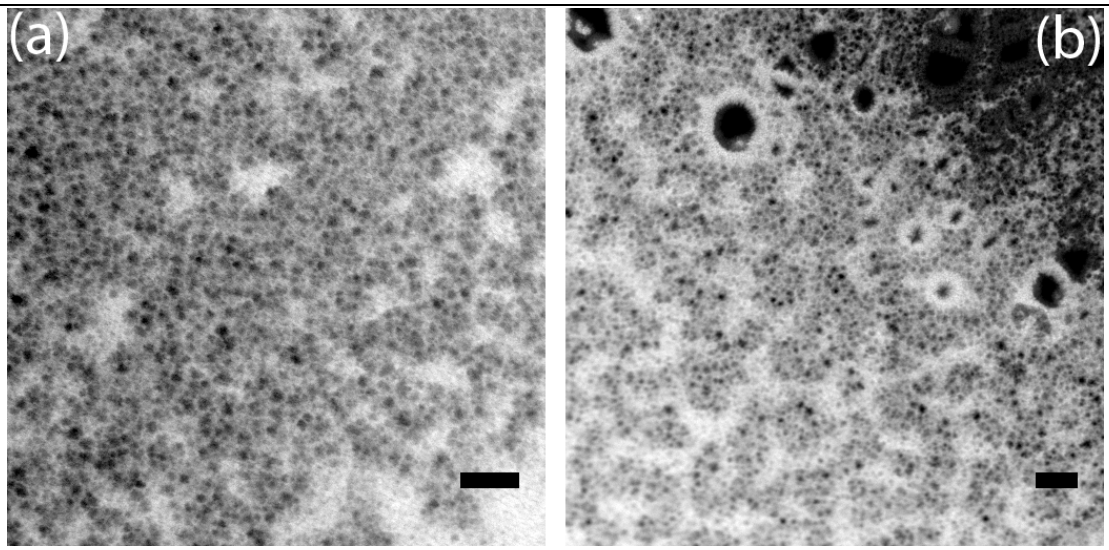


Fig. 4.9 Dark-field STEM images from two regions of CoCrMo TF polarised at 800 mV for 5 minutes in SBF. Scale bars = 100 nm.

4.3.4.3 Effect of Microstructure (Inclusions)

The presence of inclusions in the *bulk* alloy matrix is well known and discussed in the Literature Review (chapter 2, section 2.1.4). These inclusions are mixed phase precipitates mainly including metal carbides with a formula of $M_{23}C_6$. SEM images of the *bulk* samples (figure 4.10) illustrate the presence of these inclusions on the sample surface. In a similar manner to the *bulk* matrix (and the TFs), the morphology of the inclusions is unaffected after polarisation at 400 mV. However, inclusion sites develop a different morphology, after transpassive polarisation, compared to the matrix surface: larger, random shaped pores develop as opposed to the fine circular pores observed in the matrix. Comparison of the different morphology across the interface of the two regions is shown at higher magnification in figure 4.11. It is likely that both the matrix and inclusions undergo the same dealloying behaviour, however, the difference in the visible morphology is hypothesised to be due to differences in the process kinetics as well as the heterogeneous (multi-phase) nature of the inclusions. This multi-phase structure (as discussed in section 2.1.4) could be revealed through the varying SEM image contrast within the inclusion region in figure 4.11(a). The solid/void bi-structure of an inclusion after polarisation (figure 4.11(c)) is comparable to the original multi-phase distribution. This suggests that a selective phase dissolution process could be behind the rise of the observed morphology in inclusions. This hypothesis could explain why dealloying also occurs in these Cr-rich inclusions: while the Cr-rich carbide phases would be expected to be stable, the dissolution of other phases within the inclusion, such as the alloy FCC phase, could give rise to this morphology. Furthermore, it is suggested that the continued development of local porous networks (seen in early stages in the matrix and TFs) eventually leads to the morphology observed in inclusion sites (further discussion on dealloying morphologies is presented in section 4.3.7).

Focused ion beam/scanning electron microscopy (FIB-SEM) was used for cross-sectional imaging of the inclusions. Figure 4.12 shows the cross-section of a number of inclusions in a *bulk* disc sample after 30 minutes polarisation at 800 mV in SBF. The images reveal that the developed porosity extended to approximately 500 nm below the surface. Figure 4.12(e & f) show the same cross-sectional area, at different magnifications, where a platinum layer was deposited by the gallium ion beam onto the top surface prior to the FIB cross-section milling. This Pt layer was deposited in an attempt to reduce the curtaining artefact (the white vertical lines across the cross-section). These striations may occur due to an uneven topography of the surfaces being milled, or due to the inhomogeneous composition of the surface. For further details, the reader is referred to the work of Friedrich *et al.,*[268] who presented a theory explaining the formation of striations during FIB milling.

Grooves could be observed across the inclusion boundaries (figures 4.10(d), 4.11(c) and 4.12). These grooves are likely the result of the selective dissolution of these boundaries as reported in the literature and discussed in section 2.3.6. Since the metals in the metal carbides formed in these inclusions are likely to be Cr and Mo, as previously reported,[48,50–52] and as shown in this work by EDX elemental maps in figure 4.13, the adjacent matrix become chromium-depleted zones.[49,145] Chromium is the main constituent of the alloy's passive film, and therefore the chromium-depleted zones surrounding the carbide inclusions are more susceptible to localised attacks[49] leading to the development of these grooves.

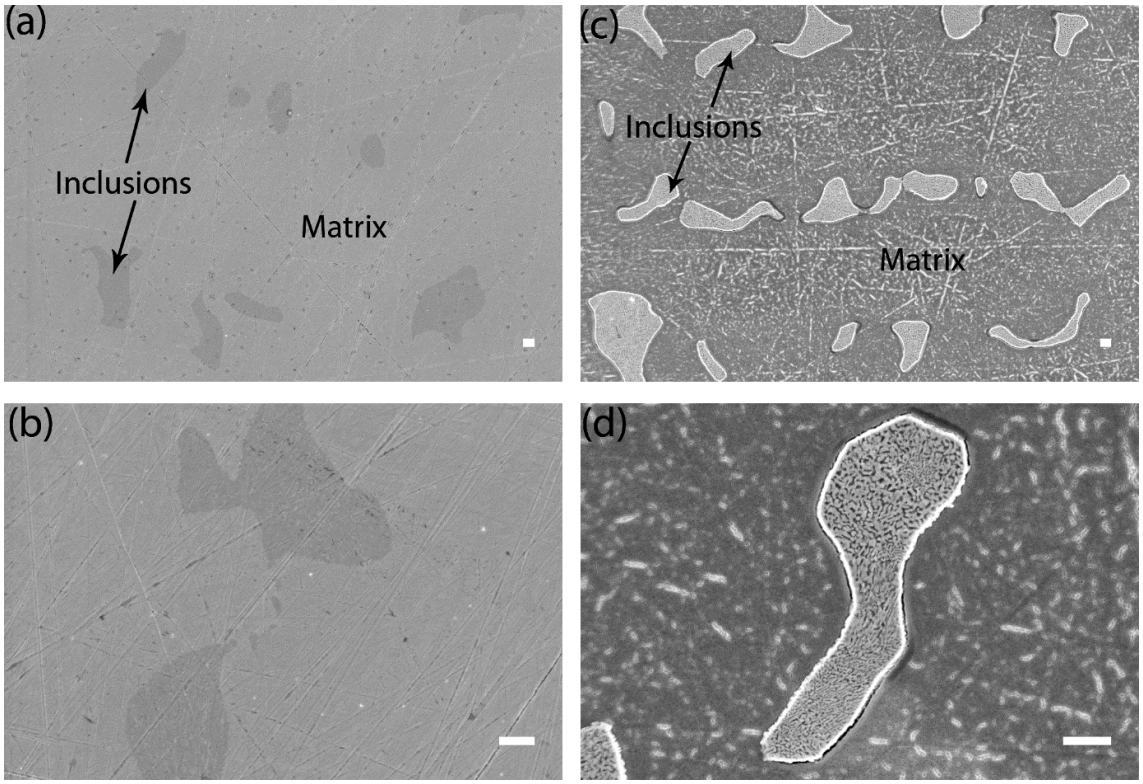


Fig. 4.10 Secondary electron SEM images of CoCrMo bulk discs surfaces showing the randomly shaped inclusions across the alloy matrix. (a-b) as received, (c-d) after 30 min polarisation at 800 mV in SBF. Scale bars = 1 µm.

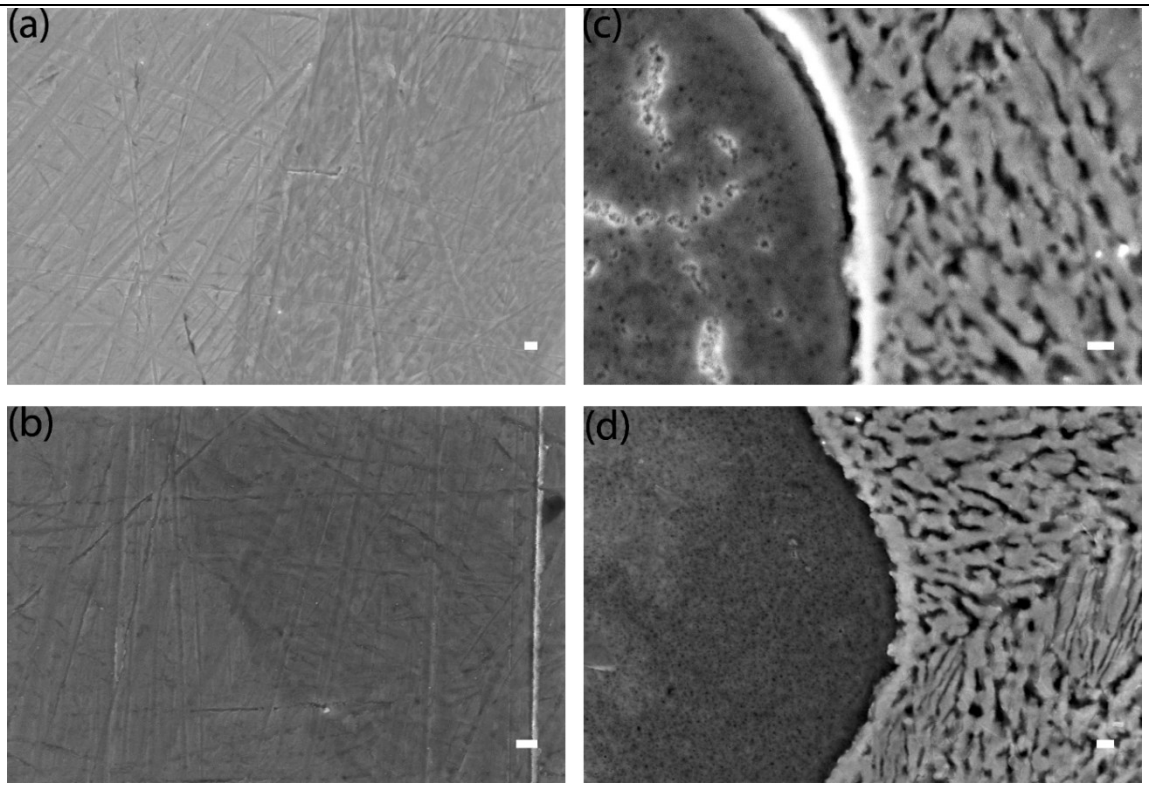


Fig. 4.11 Secondary electron SEM images at the matrix/inclusions interface of CoCrMo bulk discs (a) as received, (b) after 30 min polarisation at 400 mV in SBF, (c) after 30 min polarisation at 800 mV in SBF, and (d) after 30 min polarisation at 800 mV in Serum-SBF. Scale bars = 100 nm.

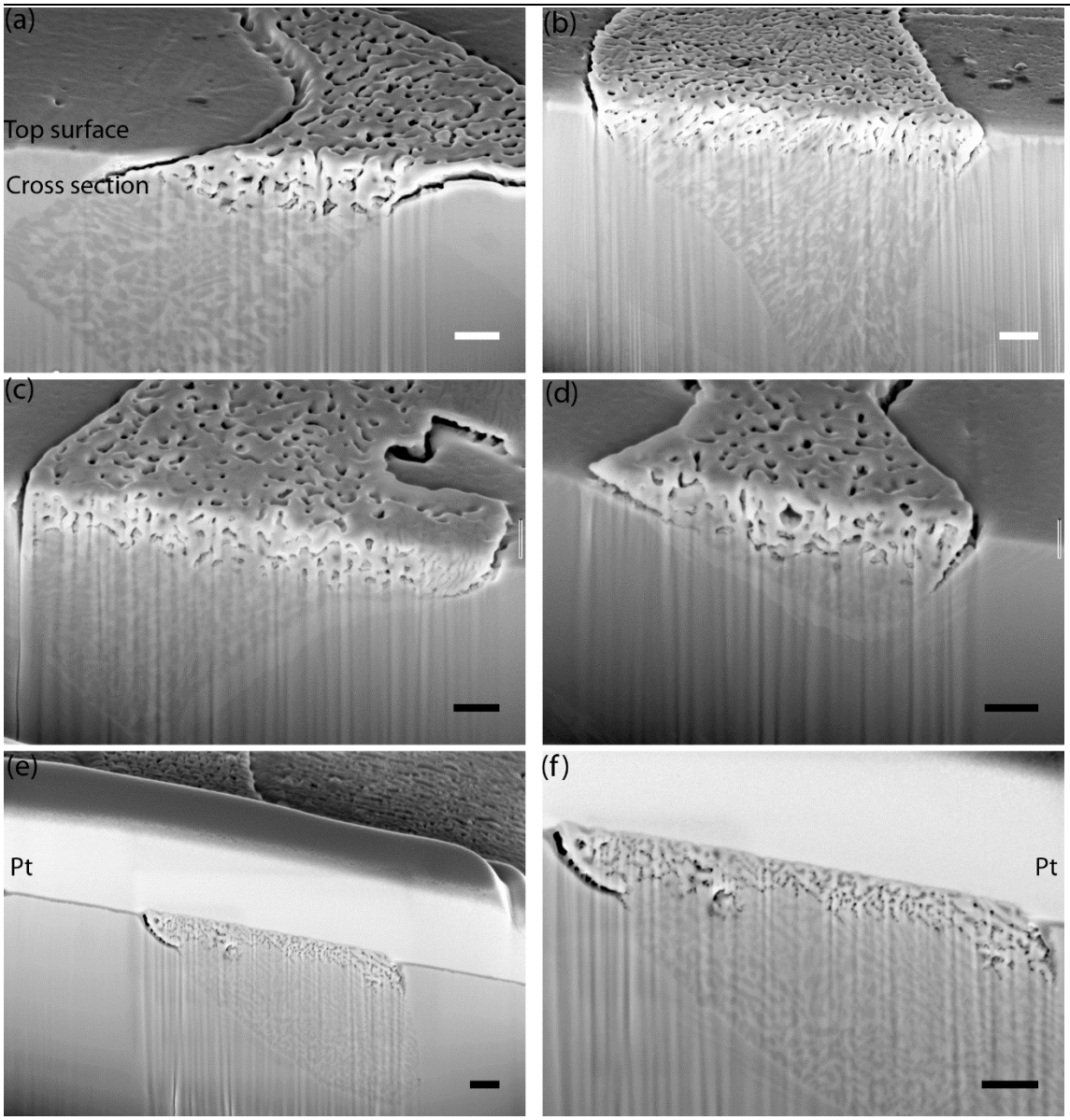


Fig. 4.12 Secondary electron SEM images of CoCrMo bulk samples after using FIB to expose the cross-section at inclusion sites revealing that the developed morphology extends to approximately 500 nm below the surface. Scale bar = 500 nm

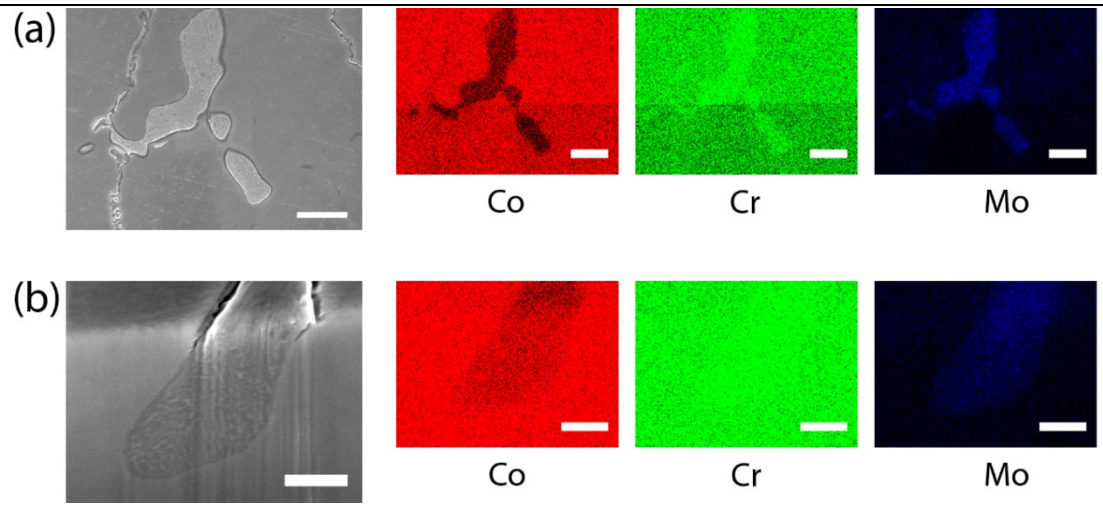


Fig. 4.13 Secondary electron SEM images and EDX elemental maps at inclusion sites showing a lack of Co and enrichment of Cr and Mo in inclusions. (a) Top view SEM and EDX with scale bars = 5 µm. (b) Cross-sectional view (at a different site) with scale bars = 1 µm.

4.3.5 Relative Elemental Concentrations

The relative concentrations of Co:Cr (at. %) were analysed, using SEM-EDX, in TFs and *bulk* samples under four conditions (the same conditions presented in the surface morphology results): (a) As-received (AR) which compromises samples prior to any polarisation or exposure to SBF; (b) after potentiostatic polarisation at 400 mV for 30 minutes in SBF; and after potentiostatic polarisation at 800 mV for 30 minutes in both SBF (c), and in Serum-SBF (d). Ten different measurements were collected from each TF group (80 nm and 160 nm) under each of the four conditions. In the case of the *bulk* discs, ten different EDX spectra were recorded from: inclusions sites only, matrix sites only, and larger overall (mixed) sites, under each of the four conditions. Figure 4.14 outlines the results into bar charts representing the means of the Co:Cr ratio (at.%) for each sample group in each of the four conditions. Additionally, a t-test was used to evaluate the statistical significance of the difference between the means of each condition. The results could be summarised in the following statements: The Co:Cr ratio in the unpolarised condition (as-received) is approximately 2 for all groups except the carbide inclusions where the ratio drops to 1 (confirming that these inclusions are chromium rich regions); There was no significant difference observed in the Co:Cr ratio of all groups after polarisation at an applied passive potential (400 mV in SBF); However, a statistically significant drop in the Co:Cr ratio occurs, in all groups, after polarisation at an applied transpassive potential (800 mV in SBF); Finally, the Co:Cr ratio after transpassive polarisation in serum-SBF was significantly higher than transpassive polarisation in SBF in all groups except the case of the 160 nm TFs were no significant difference was observed.

A drop in the Co:Cr (at. %) ratio is indicative of the faster rate of Co dissolution compared to Cr. Therefore, the Co:Cr ratio results, presented here, reveal a preferential Co dissolution but only after transpassive polarisation. This was evident in both TFs and *bulk* samples and hence the higher rate of Co dissolution could not simply be

attributed to Cr-depleted zones at inclusion boundaries of the *bulk* alloy. It is worth noting that the drop in the Co:Cr (at. %) ratio, after transpassive polarisation, was larger in TFs compared to the *bulk* (matrix and overall sites measurements). This could be explained by considering the EDX interaction volume and the material depth affected by dealloying. In TFs the percentage of dealloyed layers, in the depth covered by the EDX interaction volume, is larger compared to the *bulk* (where EDX signals are detected from subsurface regions of a stoichiometric composition). This illustrates the nature of TFs in amplifying/emphasising such dissolution measurements.

The faster rate of Co loss (compared to Cr) occurs despite its onset coinciding with Cr transpassivity; however, it could be explained because the Co oxidation reaction to Co(II) is under a large overpotential compared to the Cr dissolution reaction. Subsequently, large-scale Co dissolution is facilitated by the breakdown of the Cr rich passive film. Many studies in the literature suggested the non-stoichiometric dissolution of Co, from *bulk* alloy discs, at OCP and passive potentials through analysing ion concentrations in the electrolyte. Such dissolution may be limited to surface Co, which would also be concurrent with the oxidation of Cr. However, at passive potentials, Cr would form solid Cr oxide leading to the thickening of the passive film, and thus is not detected as ions in electrolyte measurements. The data here suggest that Cr would eventually passivate the surface of the alloy to prevent large-scale Co dissolution at passive potentials whereas the non-stoichiometric dissolution process is only provoked after the breakdown of the Cr oxide film at transpassive potentials. In fact, it was previously reported that analysis of alloy surface chemistry was in disagreement with metal ion release analysis. Hodgson *et al.*[105] reported a stoichiometric composition on implant surfaces using Auger Electron Spectroscopy, whereas metal ion concentrations in tissue revealed an enrichment in Co. This was attributed to the dissolution of Co into mobile soluble ions as opposed to the solid Cr oxide. This work presents the first observation of non-stoichiometric dissolution through chemical analysis of alloy surface. The preferential dissolution of Co is consistent with the hypothesis of dealloying.

In most cases, the presence of serum albumin led to a smaller drop in the Co:Cr (at. %) ratio when compared to the drop in SBF only environment. This suggests that protein inhibited the Co dissolution relative to Cr. Overall, the change in the relative Co:Cr concentration, observed here, is in agreement with the surface morphology results (presented in section 4.3.4): the development of nanoporous surfaces was only observed after transpassive polarisation and was also inhibited in the presence of protein. To complement these results, TEM-EDX spectra were collected from regions with different degrees of porosity on a TF polarised (on a TEM grid) in SBF for 5 minutes. STEM images of six regions and the corresponding Co:Cr at. % ratio from each region is shown in figure 4.15. The regions with more prevalent porosity (figure 4.15(a-c)) exhibited a lower corresponding Co:Cr (at. %) ratio compared to regions with lacking porosity (figure 4.15(d-f)), and thus emphasised the relationship between the development of nanoporosity and the preferential dissolution of Co.

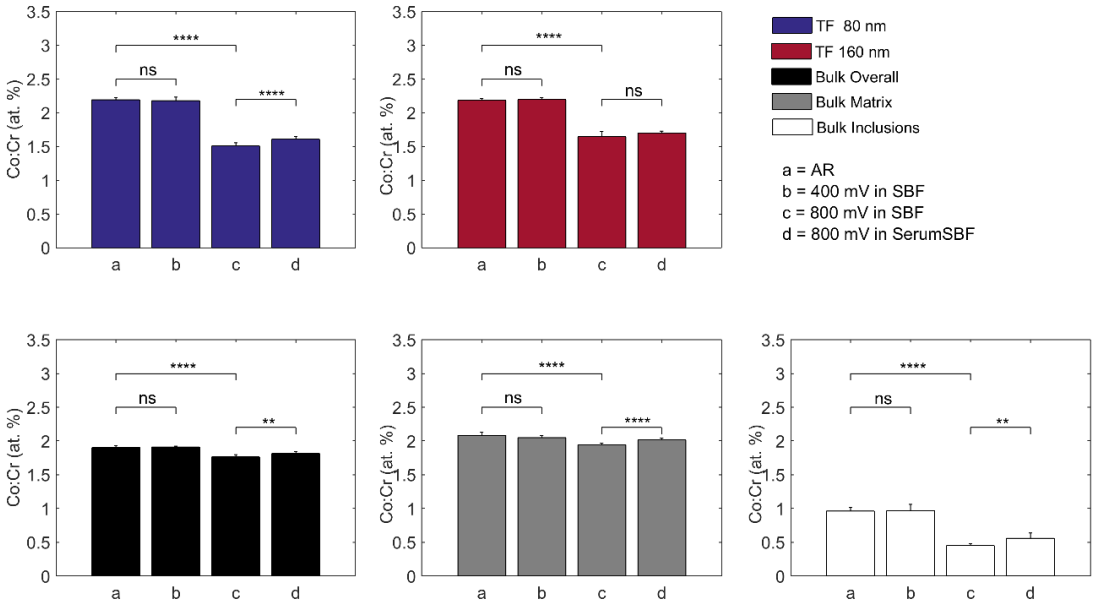


Fig. 4.14 Bar charts of the mean Co:Cr at.% ratio, obtained by EDX, from TFs and bulk samples under four different polarisation conditions. Each bar represents the average of ten different measurements. Error bars represent standard deviation. ('ns' indicates 'non-significant', and asterisks indicate 'significant' as follows: 2 asterisks = p<0.01, 3 asterisks = p<0.001, 4 asterisks = p<0.0001).

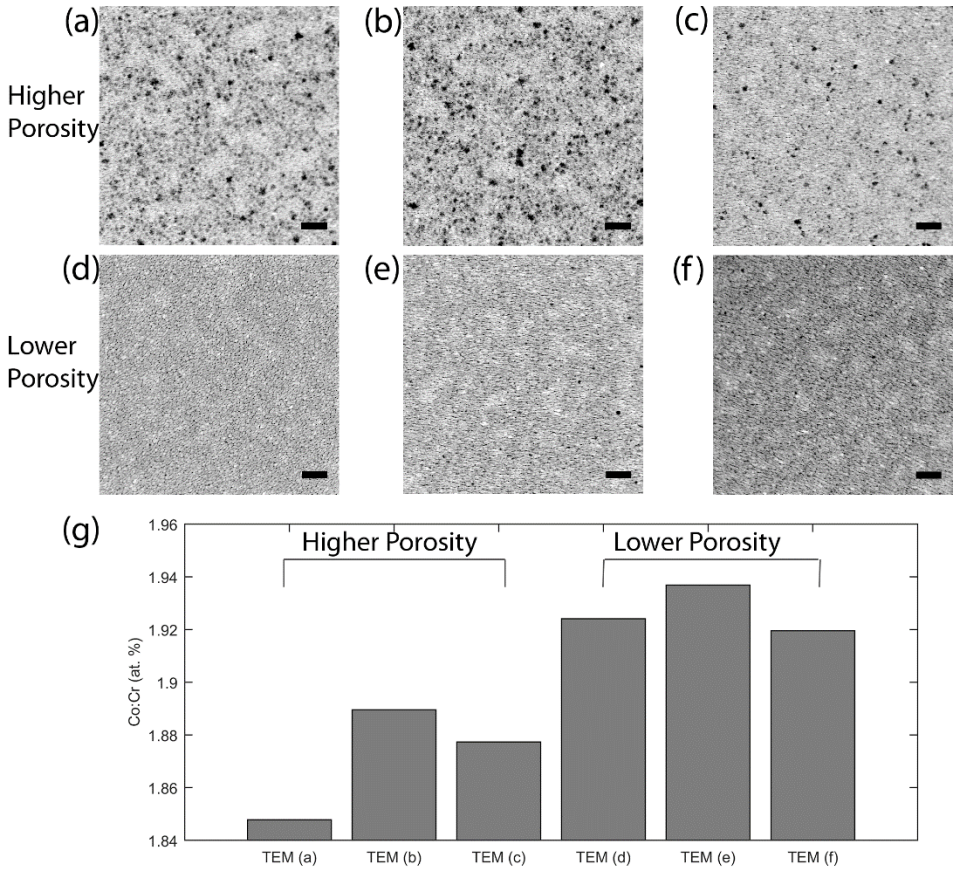


Fig. 4.15 (a-f) Dark field STEM images from six different regions of a CoCrMo TF polarised at 800 mV for 5 minutes in SBF. Nanoporosity is more prevalent in some regions compared to others. Scale bars = 100 nm. (g) Bar chart showing the Co:Cr (at. %) ratio across the six regions.

4.3.6 Spatial Elemental Distribution

Co and Cr XFM maps of as-grown and polarised (0.8 V in SBF) 160 nm TFs are shown in figure 4.16. A reasonably uniform distribution of both elements could be observed in as-grown films. However, polarised films reveal a sparse Co distribution while Cr exhibits greater surface coverage with small pores. XFM maps of more regions in the polarised TF are shown in figure 4.17. The structures portrayed by Cr XFM maps are analogous to the morphologies observed by SEM images (figure 4.17). These results suggest that Cr is the element behind the rise of the observed surface morphologies.

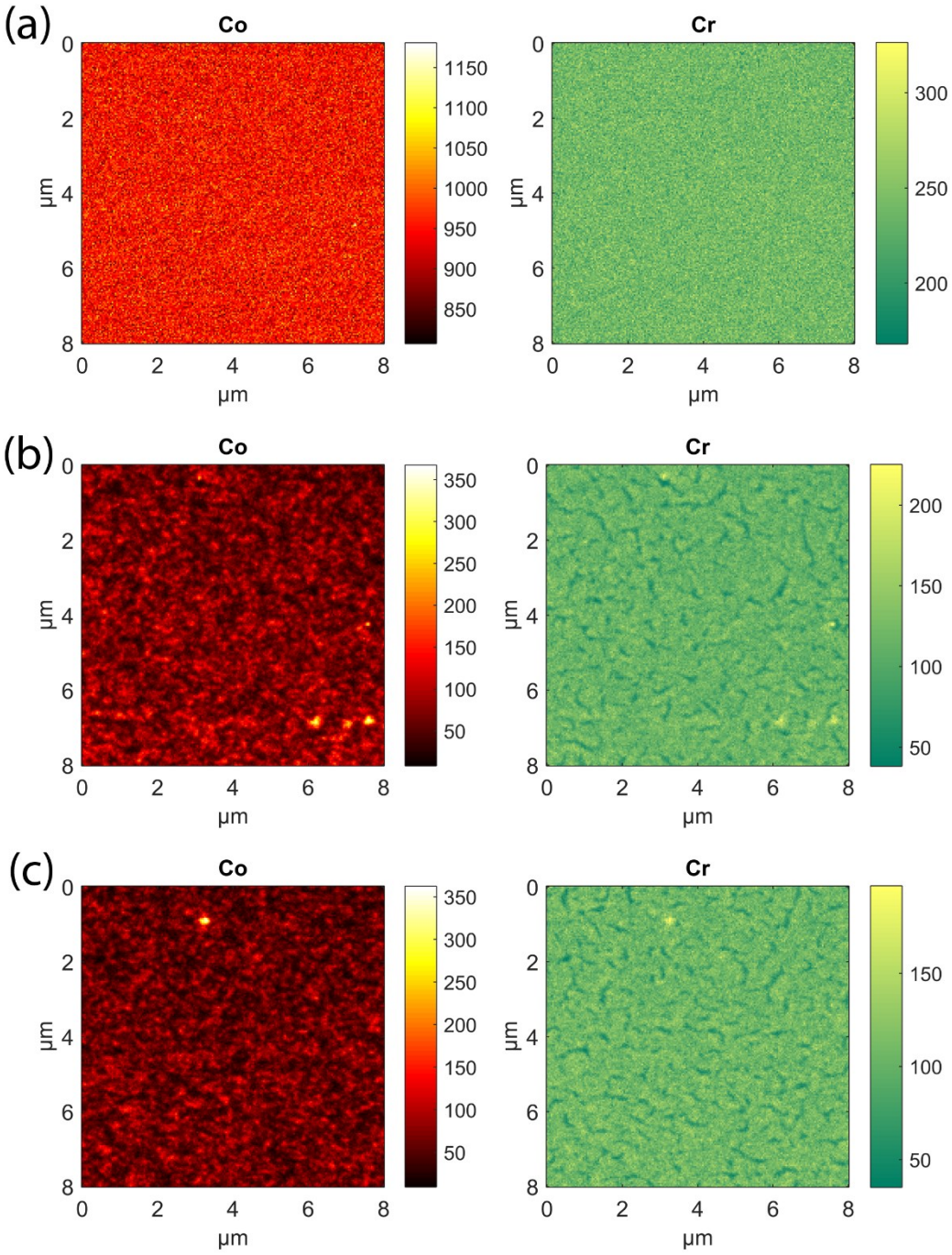


Fig. 4.16 XRF maps revealing the distribution of Co and Cr in (a) as grown TF, and (b-c) two different sites of the TF polarised at 0.8 V in SBF. Colour bars indicate absorbance intensity (a.u.).

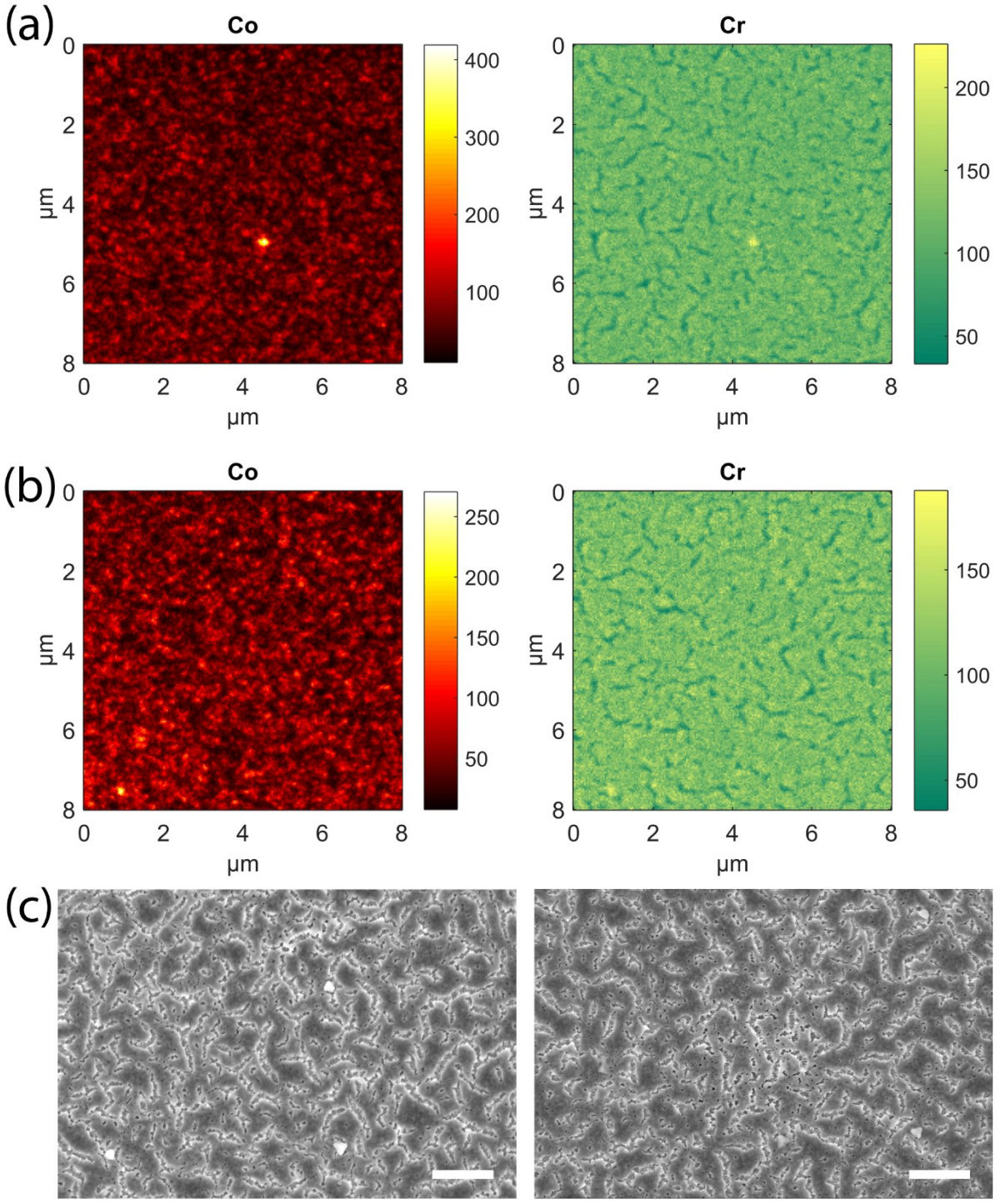


Fig. 4.17 (a-b) XRF maps of Co and Cr distribution at two different sites of a TF polarised at 0.8 V in SBF (Colour bars indicate the absorbance intensity (a.u.)). (c) SEM images of the same polarised TF revealing that surface morphology is consistent with the Cr distribution (Scale bars = 1µm).

4.3.7 Dealloying Mechanisms

Dealloying is the preferential electrochemical dissolution of the less stable of the two elements of an alloy.[266] For dealloying to occur, the concentration of the less stable element must exceed a dealloying threshold termed the parting limit. Above the parting limit, dealloying will occur at a critical composition-dependant-potential. Below the critical potential only surface dealloying can occur, followed by the formation of a conformal layer of the more stable metal which separates the electrolyte from the alloy. Hence, this eventually results in a passive system. Above the critical potential dealloying may occur *via* one of three major proposed mechanisms (depending on the system), where each mechanism results in the evolution of a different morphology. The mechanisms of dealloying and the subsequent resultant morphologies were discussed by Chen and Sieradzki[269] and are summarised here. These mechanisms are namely: (a) simultaneous dissolution of both components followed by re-deposition of the more stable component, (b) percolation dealloying and (c) vacancy-mediated lattice diffusion of the less stable element.

The dissolution/re-deposition mechanism is explained by an initial preferential dissolution of the less stable metal from the alloy surface resulting in the formation of unstable regions rich in the more stable component. Consequently, these regions would stabilise by reducing their energy or surface area by coarsening *via* different transport mechanisms including dissolution/re-deposition. This mechanism is theoretically feasible if the dissolution of the less stable metal is occurring at a potential not far below the standard potential of the more stable metal. The predicted resultant morphology would be the evolution of nodules similar to observed growth by electrodeposition.

Percolation dealloying is based on the principle that, above a certain concentration of the less stable element (percolation threshold), continuous channels of the less stable element are present, therefore as the element dissolves the channels become void allowing the electrolyte to penetrate and continuously attack the alloy. At this composition, the less stable element is always present at the electrolyte/alloy interface thus eliminating the need for any solid state diffusion. This mechanism results in a solid/void bi-continuous morphology.

When the percolation threshold is not attained dealloying will require solid state diffusion of the less stable metal into vacancies arising from its dissolution. The dissolving metal must occupy lattice rather than interstitial sites in the crystal structure. Since surface vacancies can only arise through a change in the occupied lattice sites, dissolution of interstitial atoms does not lead to any perturbation at the electrolyte/alloy interface. The expected morphology from this lattice-diffusion controlled mechanism is negative (void) dendrites. This is analogous to the dendritic morphologies evolving from deposition under mass transport control.

The observed morphologies in this work suggest that the diffusion/re-deposition and vacancy-mediated diffusion are not the mechanisms operating in this system. The morphology observed particularly in the inclusion regions resembles bicontinuous structure characteristic of percolation dealloying. In the matrix regions, as well in TFs, the

morphologies may be described as early stage percolation, especially in the absence of serum, where coalescence of pores is evident and reveals the development porous networks locally. A faster dealloying process occurring in the inclusions is maybe counterintuitive given that they are Cr-rich sites, and hence the composition ratio of the less stable to more stable metals is lower compared to the surrounding matrix. Although these observed morphologies do not resemble classic percolation morphologies (usually observed in Au alloys), this can be attributed to the lower diffusivity of Cr compared to Au. Similar morphologies, to those observed here, have been previously found in Pt-Cu alloys due to the low surface diffusivity of Pt.[270]

4.4 Summary

Taken together, this work revealed the appearance of nanoporous morphology across the surface of CoCrMo alloys which was consistent with a drop in Co concentrations relative to Cr. These observations are consistent with the process of dealloying. Here, the process was evidently dependent on the applied potential and, to a lesser extent, the presence of protein in the electrolyte. The higher rate of Co dissolution compared to Cr occurred despite its onset coinciding with Cr transpassivity. However, the dealloying characteristics were not observed when the applied potential was in the passive domain (400 mV): no nanoporosity was observed in the surface morphology images and no significant difference in the Co:Cr (at. %) ratios were found. The presence of proteins, in transpassive conditions, reduced the dissolution of Co relative to Cr and led to a subsequent lesser degree of porosity.

The dissolution behaviour of CoCrMo in TF and *bulk* forms was constantly similar as evident through polarisation curves, surface morphology, and relative Co:Cr composition. The dealloying behaviour was evident in both TF and *bulk* forms of the alloy. These results imply that no specific nanoscale effect influenced the chemical reactivity of the alloy. However, the use of TFs highlighted the nanoporous morphology of dealloying as well as the inhomogeneity of the dissolution process (in an exaggerated manner compared to *bulk* form). Additionally, the results suggest that the TFs are a representative form for studying the alloy dissolution. Therefore, X-ray absorption spectroscopy was used (as discussed in chapters 6) to study the chemical speciation changes during the CoCrMo dissolution process.

In conclusion, the results suggest that CoCr alloys undergo stoichiometric dissolution in passive conditions. However, in transpassive conditions, the alloy dissolution is *via* a non-stoichiometric mechanism similar to dealloying. This dissolution mechanism was previously unreported for this material.

5 Dissolution Mechanism of CoCrMo Particles

5.1 Introduction

In this chapter, further understanding of CoCrMo dissolution mechanism is pursued with a focus on CoCrMo particles. While a similar approach to that used for studying morphological and chemical changes of CoCrMo *bulk* discs and thin films (in chapter 4) was employed; the work here also aimed at the *in situ* monitoring of these changes using synchrotron-based X-ray techniques. The use of *in situ* studies, enabled by synchrotron radiation, provided valuable insights into the CoCrMo dissolution process. In particular, XAS allowed the dynamic monitoring of Co and Cr content independently. Furthermore, real-time morphology development during local dissolution behaviour was followed by TXM, for the first time.

5.2 Methods

A complementary spectroscopy and microscopy approach was used to develop an understanding of the dissolution of CoCrMo particles based on chemical and morphological changes. Synchrotron-based X-ray techniques provided the ability to monitor these changes *in situ* in wet electrochemical cells. Electron techniques were used for *ex situ* analysis particularly for high spatial resolution imaging of particle morphologies.

The CoCrMo particles were obtained from Dr Thiago Simoes and Prof Rik Brydson of the University of Leeds where particles were produced by mechanical ball milling as described in further detail by Simoes *et al.*[216] and in section 3.6.4. The particles were stored suspended in isopropyl alcohol at 4 ^{o}C. The suspensions were sonicated in a water bath prior to use and subsequently, particles were drop-cast on different substrates depending on the experiment and characterisation technique to be employed. The substrates acted as the working electrodes during electrochemical polarisation.

5.2.1 *Ex situ* Studies

Ex situ analysis involved studying how both particle morphology and Co:Cr ratio (at. %) varied as a function of simulated environment. Particle morphology was observed using SEM, STEM and STEM tomography, while Co:Cr ratios (at. %) were examined using TEM-EDX. For SEM analysis, CoCrMo particles were polarised and imaged on gold-coated glass slides (15 nm gold film was deposited on microscope glass slides by sputtering). For STEM imaging, cross sections from the particles polarised on these slides were lifted out, deposited onto copper TEM grids (TAAB, UK), and thinned using a gallium ion beam in a FIB-SEM (Helios NanoLab 600). In the case of TEM-EDX and STEM tomography, CoCrMo particles were polarised and characterised on carbon-coated gold TEM grids (TAAB, UK).

5.2.2 *In situ* Spectroscopy at Diamond Beamline I20

Conventional (large beam) XAS was used to directly monitor the Co and Cr elemental content of a population of wear particles as a function of time and potential. Based on a design by Kerkar *et al.*,[226] particles drop-cast on gold-coated Kapton films (15 nm gold film was deposited on 8 μm Kapton (Advent Research Materials, UK) by sputtering) were attached to a custom-made electrochemical cell such that the substrate working electrode became the X-ray window in the cell (figure 5.1). The beam size was 400 μm x 300 μm covering a population of *ca.*2000 particles. The cell was mounted 45° to the incident beam and data collected in fluorescence geometry. In this arrangement the intensity of the fluorescence signal is directly proportional to the amount of material remaining in substrate-bound particles; this presents a very sensitive method to measure *in situ* the dissolution process, as species which rapidly diffuse away from the X-ray window do not contribute to the signal. Fluorescence intensity scans were recorded as a function of time and applied potential at photon energies of 6009 eV and 7757 eV, which are just above the Cr and Co K-edges respectively. Three of such scans were obtained for each of the two elements at each of the two electrolytes (SBF and serum-SBF). The system was maintained at OCP for the first five minutes before the potential was stepped from 400 mV to 800 mV, in 100 mV increments. The three scans of each scenario were averaged and all scans were normalised against the average absorbance intensity of the first five minutes (the intensity at OCP). Full XANES spectra were collected at the beginning and end of the *in situ* experiments.

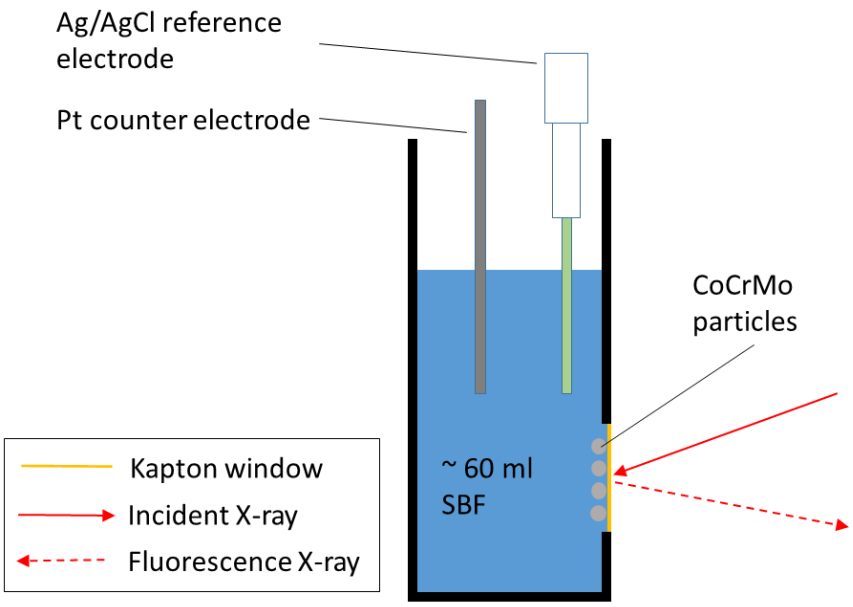


Fig. 5.1 Schematic of the electrochemical cell set up used during in situ spectroscopy by XAS

5.2.3 *In situ* Microscopy at SSRL Beamline 6-2

CoCrMo particles were imaged *in situ* using a 3D printed electrochemical cell, shown in figure 5.2, which was adapted from the cell previously reported by Tay *et al.*[271] The cell comprised a large reservoir which narrowed

down to a 1 mm wide channel which has two, front and back, Kapton-sealed windows facilitating X-ray transmission. The downstream Kapton window was first coated with a 15 nm gold film, which acted as the working electrode before CoCrMo particles were drop-cast onto the gold film. The cell included a second channel of both front and back windows (the *reference* image channel) which was designed to be isolated from samples and electrolyte, in order to facilitate measurement of the incident beam intensity (I_0 signal). A heating element and a thermometer were placed inside the cell to maintain a temperature of 37 ^{o}C.

To capture the onset of morphological changes, TXM images were collected as the potential was scanned from 0 to 0.7 V at a rate of 0.5 mV s^{-1}. An X-ray energy of 7810 eV was used to provide contrast at the Co edge. The TXM images had a spatial resolution of 30 nm and a time resolution of 3 s. Agarose (Sigma, UK) was added to the SBF (Agar-SBF) to increase the electrolyte viscosity and hence slow down the diffusion of dissolved species, increasing the chance of capturing diffusing material (away from the particle surface).

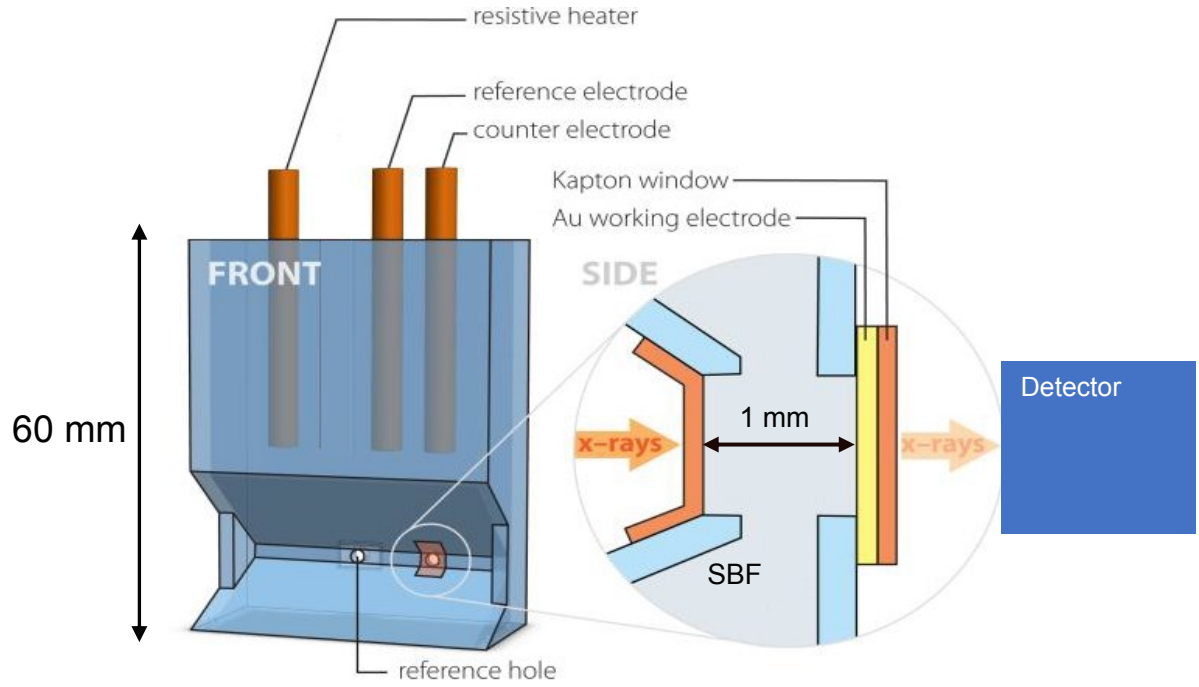


Fig. 5.2 Schematic of the 3D-printed electrochemical cell used for in situ imaging by TXM (adapted and reproduced with permission from[271])

5.3 Results and Discussion

The CoCrMo particles used in this study had a range of sizes and shapes. Figure 5.3 shows TEM images of as-received particles where their sizes ranged from approximately 100 nm to few microns (in the longest dimension).

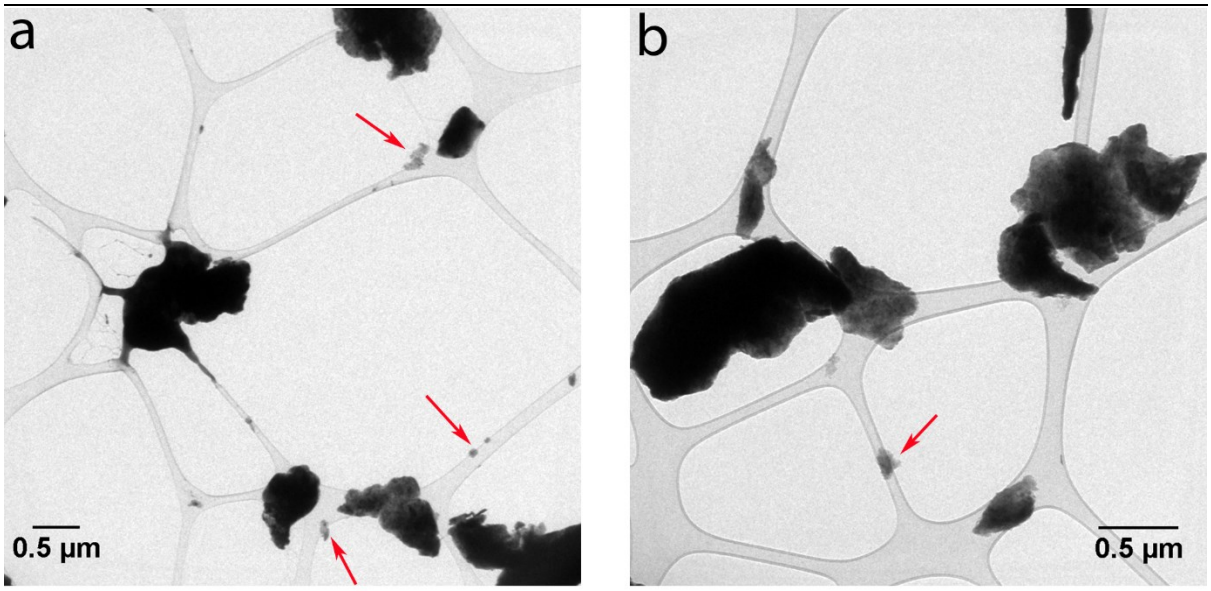


Fig. 5.3 TEM images of AR CoCrMo particles. The particles had a range of sizes and shapes (red arrows point to examples of smaller particles).

5.3.1 *Ex situ* Spectroscopy

The atomic Co:Cr elemental ratio was examined, by TEM-EDX, across four different particle conditions: i) as-received (AR); or 10 minutes immersion in either ii) simulated body fluid (SBF) at open circuit potential (OCP); iii) SBF while being polarised at 1 V; and iv) serum-SBF while being polarised at 1 V. The high electrochemical potential of 1 V was used in this case as an accelerated test to provide insight on later-stage dissolution. The bubble plot in figure 5.4 illustrates the variation in Co:Cr atomic ratios, across 54 particles, with each exposure condition. The Co:Cr ratios were divided into bins and the size of each bubble is proportional to the frequency (count) of particles that fall in the corresponding bin. The 54 AR particles had a mean Co:Cr ratio 1.97 (σ =0.04) and were all entirely included in the highest two bins (1.9-2.2 and 1.6-1.9). The particles which were exposed to SBF, at OCP, were also entirely included in the highest two bins. However, a higher percentage of these particles had a ratio that belonged in the lower 1.6-1.9 bin, and the overall mean was 1.91 (σ =0.05). The difference between the means of those two conditions (AR and exposure to SBF at OCP) were significantly different ($p<0.0001$) suggesting the onset of limited cobalt dissolution. In clear contrast, the Co:Cr ratios of both polarised samples were spread over a larger number of lower bins (down to the 0.4-0.7) bin. The mean Co:Cr ratio of particles polarised in SBF was 1.70 (σ =0.35), while those polarised in serum-SBF had a mean of 1.58 (σ =0.53). However, the difference in the mean between particles polarised in SBF and serum-SBF was not significant ($p=0.16$).

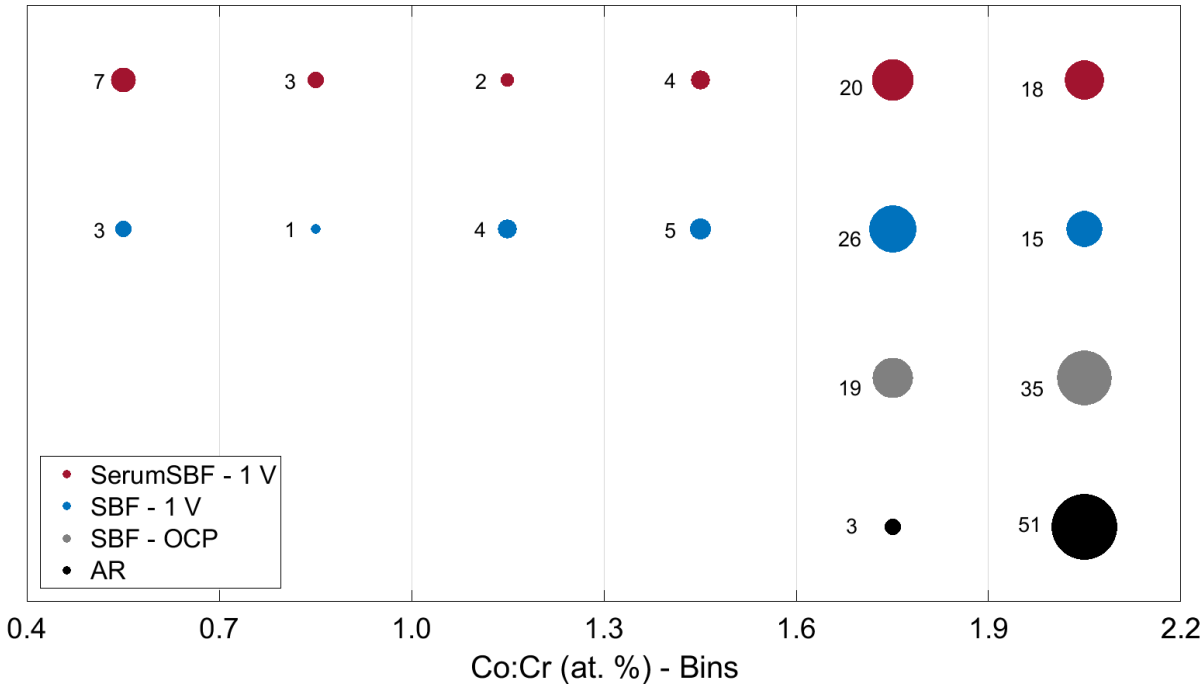


Fig. 5.4 Histograms of Co:Cr atomic ratios calculated from EDX analysis of CoCrMo particles in four conditions: As Received (AR), after exposure to SBF at OCP, after exposure to SBF at 1 V polarisation, and after exposure to serum-containing SBF at 1V polarisation (54 particles in each condition).

The drop of Co:Cr (at. %) ratio after transpassive polarisation reveals the preferential dissolution of Co from the particles. This is similar to what was observed on TFs and *bulk* forms (as reported in chapter 4, section 4.3.5). Here the value of the Co:Cr ratio in some particles reached as low as < 0.7 which was not observed previously on TFs and *bulk* forms of the alloy. This is likely because the conditions used here on particles involved a higher applied potential of 1 V which accelerated the dissolution process.

5.3.2 *In situ* Spectroscopy

To study the dynamics of Co and Cr dissolution from particles, *in situ* XAS experiments were conducted at Beamline I20, Diamond Lightsource, UK. Time scans (using a selected single X-ray energy for each of Co and Cr edges) were used to directly monitor the Co and Cr elemental content of a population of wear particles on a gold working electrode window. The experiments were carried out in fluorescence geometry with the particles' window upstream to the X-ray beam (as shown in figure 5.1). In this arrangement, the measurements were sensitive to the wear particles and not the SBF solution. Figure 5.5(a) shows the XAS data for both Co and Cr as a function of time and potential, in SBF and serum-SBF. Each plot represents the average of three independent repeats. Changes in fluorescence intensity can be noticed at the 0.6 V step but a clear drop in the intensity (and hence the amount of each element *remaining* in the particles) was observed for both Co and Cr after the 0.7 V and 0.8 V steps. The drop in intensity (amount of element loss) was larger for Co compared to Cr, indicating a non-stoichiometric dissolution. In SBF, the amount of Co remaining was noticeably lower than Cr after both 0.7 V the 0.8 V steps (see

figure 5.5(b)) suggesting an accelerated Co dissolution kinetics. In serum-SBF, the amount of Co remaining was also noticeably lower than Cr but only after the 0.8 V step. This suggests that the presence of protein slows Co dissolution kinetics.

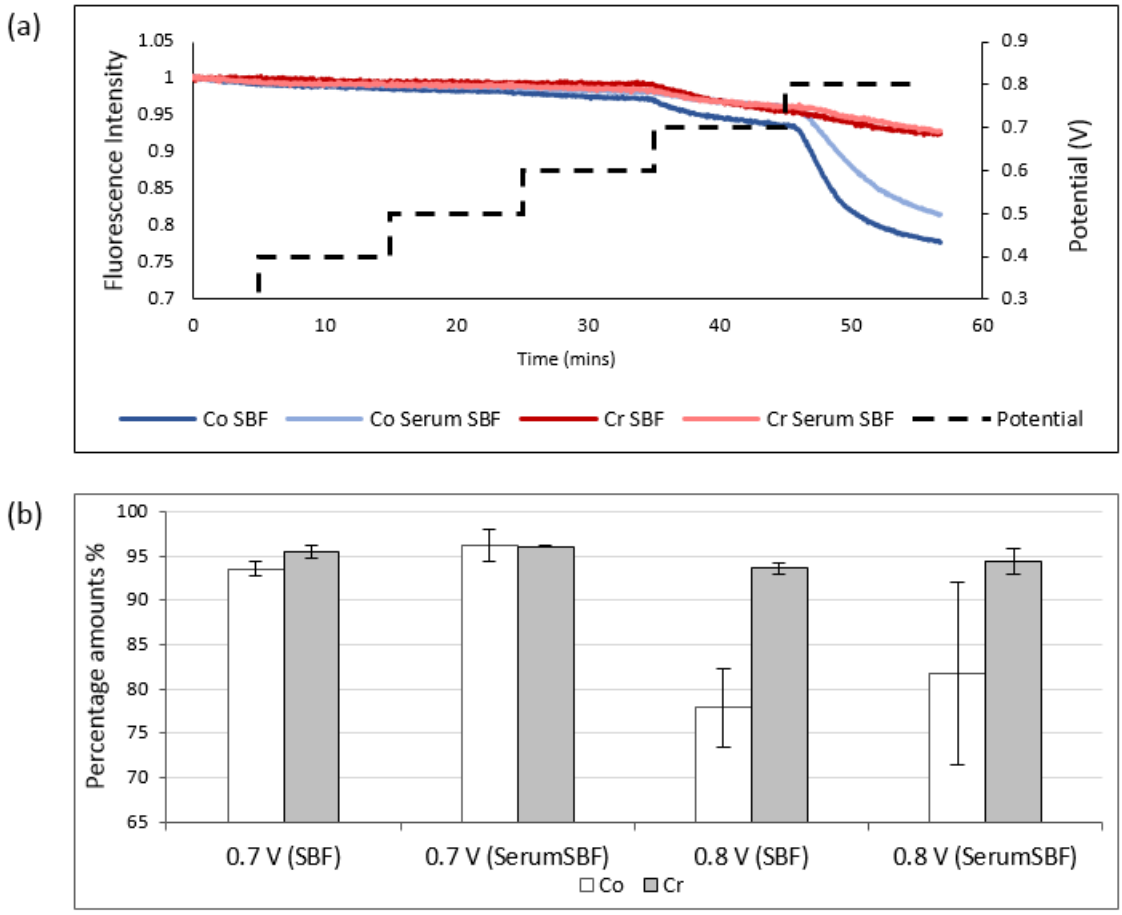


Fig. 5.5 (a) Fluorescence intensity of Co (at 7757 eV) and Cr (at 6009 eV) over time. The particles were at OCP for the first five minutes before the potential (dashed line) was stepped from 0.4 to 0.8 V. Drops in the Co and Cr amounts are observed after the 0.7 V and 0.8 V steps. The drop in the amount of Co is noticeably larger compared to Cr, particularly after 0.8 V polarisation. (b) A bar chart illustrating the levels of Co and Cr at the end of the 0.7 V and 0.8 V potential steps in (a), where 100% Co and Cr amounts were taken to be the average fluorescence intensity before the first potential step was applied. Error bars represent the standard deviation over three scans recorded for each case. (reproduced from[272] licensed under CC BY 4.0).

XANES spectra were acquired before and after polarisations (*i.e.* before and after the time-scans reported above in figure 5.5). Figure 5.6 shows a set of both normalised and unnormalised XANES spectra at each of the Co and Cr edges in both SBF and serum-SBF. The figure also illustrates the energy points selected for the time scans by the vertical dashed lines displayed in figure 5.6(a, c). Although elemental dissolution may not be monitored dynamically (as was the case through the single-energy time scans) the final overall extent of elemental dissolution could be deduced by comparing the edge step of the pre- and post-polarisation XANES spectra (unnormalised spectra). For instance, the edge step of Co XANES spectra in SBF (figure 5.6(a)) was 1.3 times lower after polarisation, while that of Cr XANES spectra in SBF (figure 5.6(c)) was 1.09 times lower after polarisation. These reductions in the edge steps correspond to approximately 23 % and 8 % loss of Co and Cr respectively. These

values are consistent with the results indicated by the time scans in figure 5.5(a) at the end of the final polarisation step (0.8 V).

In all cases, the features of the pre- and post-polarisation XANES spectra were similar revealing no significant changes in speciation. This validates the use of a single-energy scan to monitor the dissolution of Co and Cr from particles. The lack of change in the observed speciation indicates that no or little solid corrosion deposits formed (which would have contributed to the measured signal in the single energy time scans). Therefore the observed drops in fluorescence intensity during time scans are representative of the alloy dissolution. While these results show no significant change in the oxidation state of Cr, it should be noted that the speciation of wear particles in periprosthetic tissue, (discussed in section 2.5.2), showed solid Cr(III) deposits. It is hypothesised that this is a kinetic effect and the residual Cr observed in this work would have transformed to Cr(III) species in a sustained oxidising environment.

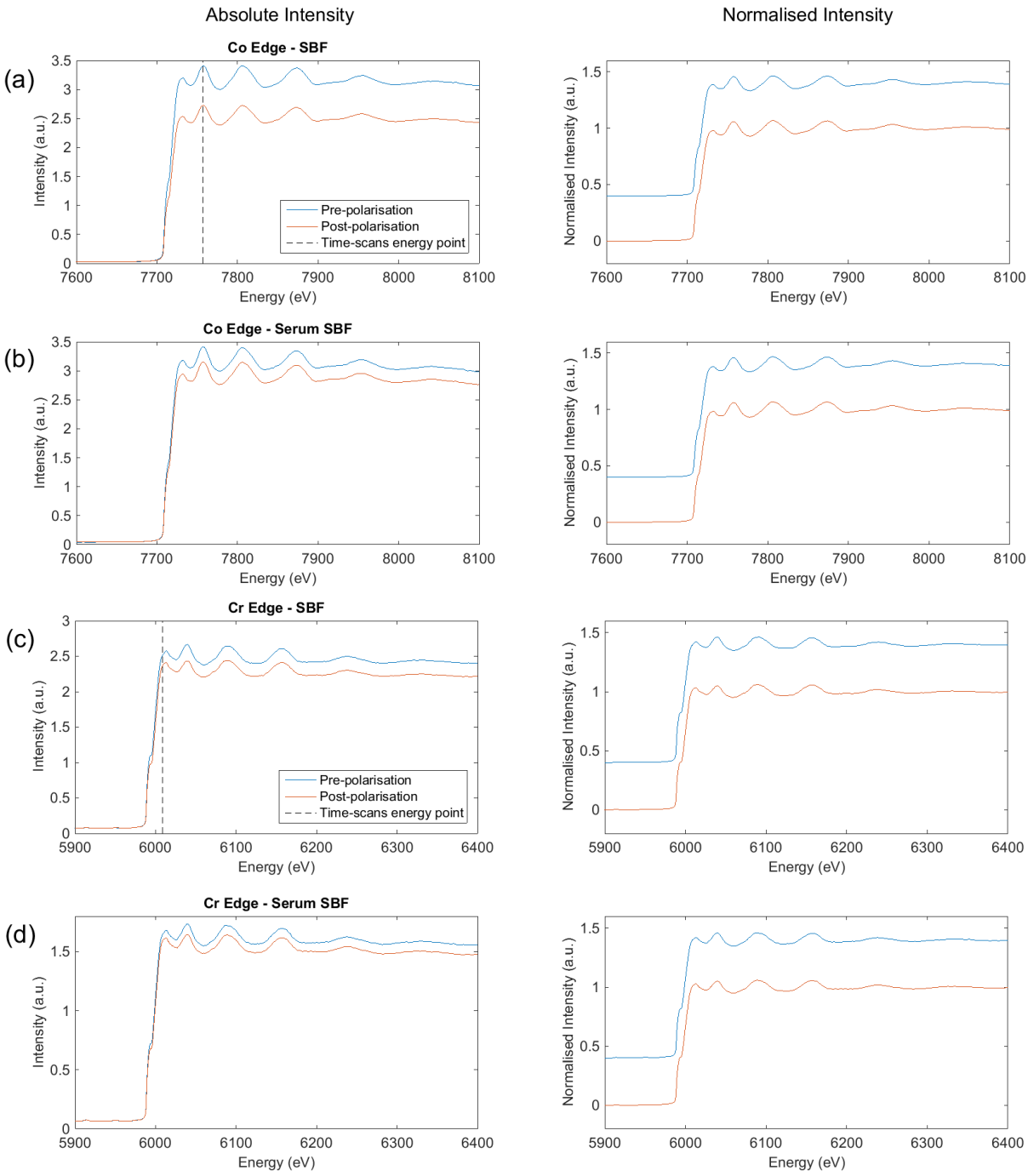


Fig. 5.6 Co (a-b) and Cr (c-d) K-edge XANES spectra collected before and after polarisation in SBF and serum-SBF. The difference in the edge steps between unnormalised pre- and post-polarisation spectra is proportional to the amount of elemental dissolution. The vertical dashed lines in (a) & (c) illustrate the energies at which time-scans reported in figure 5.5(a) were collected.

The use of *in situ* XAS to monitor Co and Cr amounts has provided more insight into the particle's dissolution process. *Ex situ* studies of Co:Cr (at. %) ratio only indicated the relative dissolution of the elements, while in this *in situ* work the absolute loss of Co and Cr was directly measured independently. The non-stoichiometric dissolution behaviour was particularly prominent above 0.7 V polarisation. Additionally, the XAS results present the Co:Cr drop averaged over a much larger population of particles (thousands compared to only 54 particles measured by TEM-

EDX). They showed an approximately 22 % drop in Co compared to a 6 % drop in Cr at the end of the 0.8 V step in SBF (figure 5.5(a)). This corresponds to Co:Cr ratio drop from 2 to 1.66. Although 0.7 V is in the transpassive domain for this alloy, the kinetics of Cr dissolution is slower than that of Co at this potential; since there is a large effective overpotential for Co^{2+} dissolution. Hence the alloy dissolves non-stoichiometrically. The presence of serum *decreased* the Co dissolution kinetics, as non-stoichiometric behaviour was only evident after 0.8 V polarisation. This is likely due to protein adsorption forming a protective film on the particles' surface.[81,127,133] Several studies reported a lack of Co in wear particles obtained from periprosthetic tissue (as discussed in section 2.5.2). The results of this work suggest that this large extent of Co dissolution is likely due to transpassive conditions being imposed *in vivo,* thus initiating the non-stoichiometric dissolution.

5.3.3 *In situ* Microscopy

To further elucidate dissolution mechanisms, the spectroscopy results were complemented with *in situ* observation of morphological changes in CoCrMo particles. Additionally, while the spectroscopy results presented above describe population-averaged measurements, the morphological changes were observed in single particles. An *in situ* transmission X-ray microscopy (TXM)-based approach was used to follow local dissolution behaviour. The TXM imaging was performed well above the Co K-edge (7810 eV), at Beamline 6-2, SSRL, USA. TXM images in figure 5.7 (see supplementary video 1) show CoCrMo particles in Agar-SBF at different times while electrochemical potential was scanned. No morphological changes were observed at low potentials, however, at 0.56 V (vs Ag/AgCl), changes in the particle shape can be noted, along with the rapid egress of dissolving the material. This sudden onset of morphological change is consistent with the onset of dissolution detected during *in situ* spectroscopy (~ 0.6 V) but provides further insights into the nature of the process.

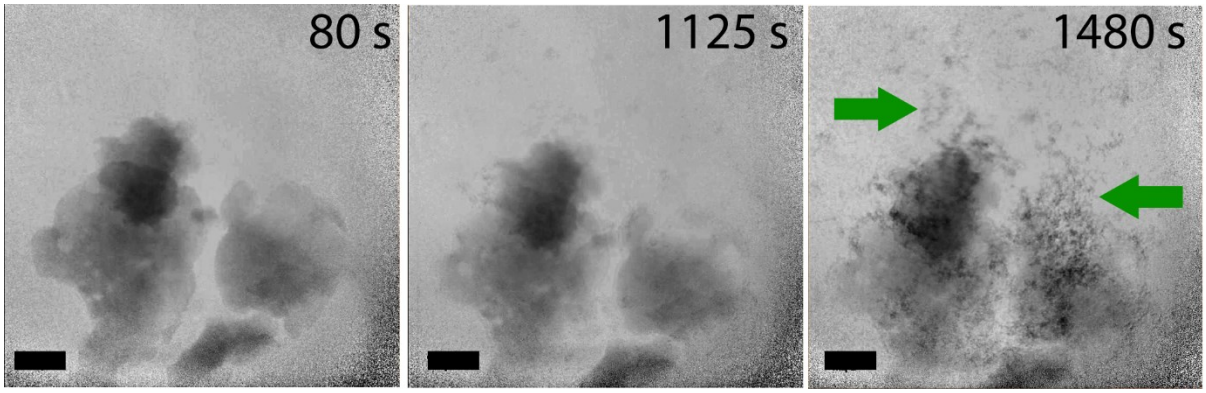


Fig. 5.7 A series of in situ TXM images of CoCrMo particle in Agar-SBF recorded during the potential scan, revealing the onset of release of diffuse material which corresponded to 0.56 V. Scale bars = 3 µm.

Since the images were collected above the Co edge, the observed discharge is likely Co dissolution. Additionally, the realised materials appears to be emitted from the entire surface of the particles simultaneously, which is

consistent with the appearance of nanopores, characteristic of dealloying, over whole surfaces of CoCrMo alloys (as seen on TFs and *bulk* forms in chapter 4, section 4.3.4; and on particles in section 5.3.4 of this chapter).

The observed “diffuse material” in these TXM images is analogous to the morphology of *in vivo* wear debris as observed by TEM in macrophage cells from periprosthetic tissue shown in figure 5.8 (TEM images of particles in periprosthetic tissue were provided by Dr Angela Goode). In particular, figure 5.8(b-d) shows CoCrMo particles surrounded by released diffuse material, similar to what is observed *in situ* by TXM (figure 5.8(g)).

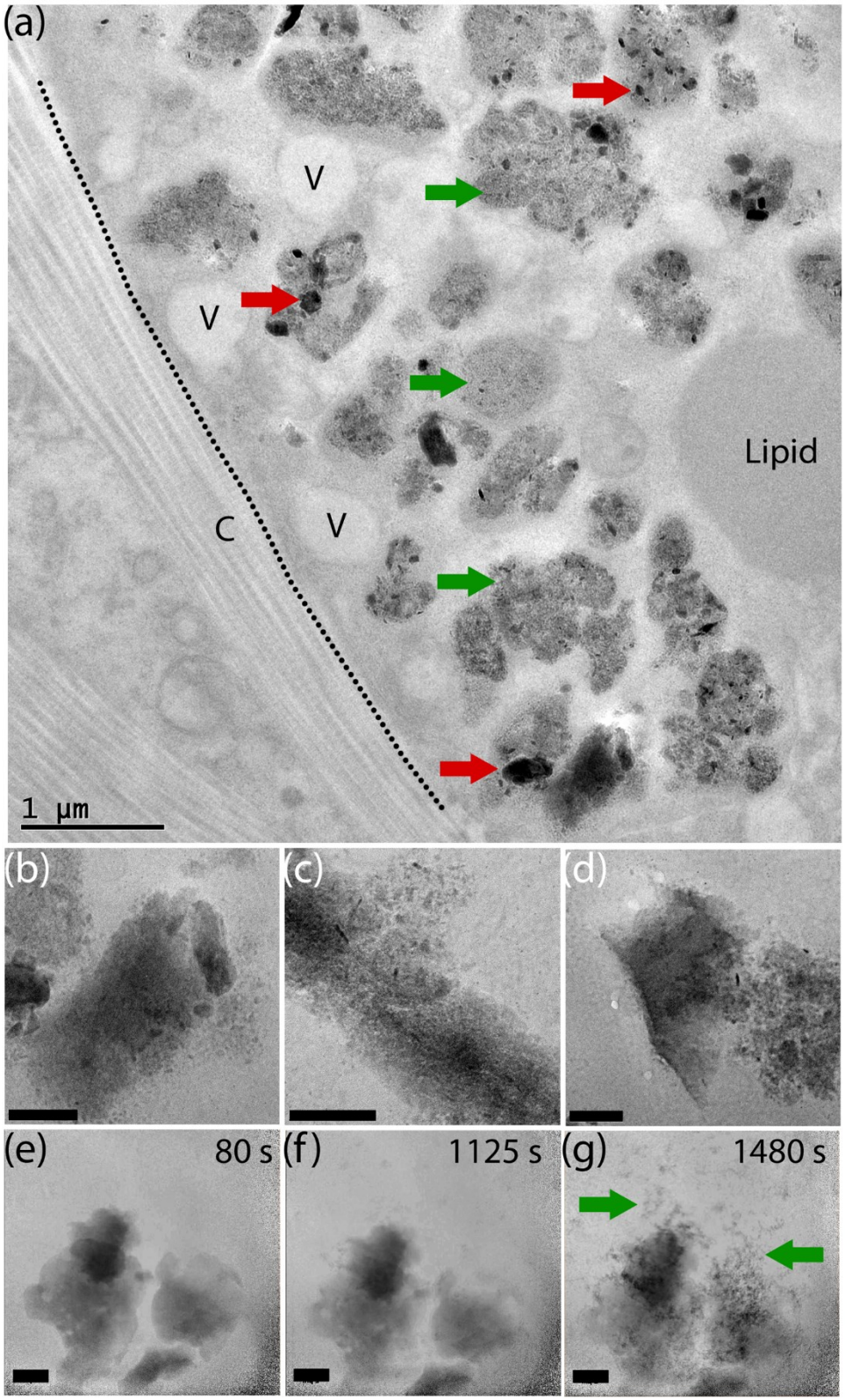


Fig. 5.8 (a) TEM image of a macrophage cell from periprosthetic tissue recovered from a patient showing CoCrMo wear debris marked by the red (solid particles) and green (diffuse, less electron dense material) arrows. (Legend: C= collagen, V= vesicles, dotted line = plasma membrane). (b-d) Higher magnification TEM images of CoCrMo wear debris from within the cell in (a), Scale bars = 200 nm. (e-g) A series of in situ TXM images of CoCrMo particle in Agar-SBF recorded during the potential scan, revealing the onset of release of diffuse material, Scale bars = 3 µm. Images (a-d) were provided by Dr Angela Goode. (reproduced from[272] licensed under CC BY 4.0).

5.3.4 *Ex situ* High-Resolution Microscopy

To complement the *in situ* microscopy data and obtain further insights into the morphological changes of particles under oxidising conditions, spatially-resolved studies of the morphological changes in single CoCrMo particles were carried out *ex situ* using scanning and transmission electron microscopes (SEM and TEM). SEM images were obtained of CoCrMo particles, drop-cast on to gold-coated glass slides, in four different conditions: i) as-received (AR); ii) immersed in SBF at OCP for 30 minutes; and polarised at 0.8 V for 30 minutes in both iii) SBF and iv) serum-SBF. SEM micrographs, figure 5.9, show the development of a nanoporosity on the surface on a particle polarised in SBF (figure 5.9(c)). This porous surface is not as obviously visible in particles polarised in serum-SBF (figure 5.9(d)) possibly due to masking of surface topography by the presence of strongly surface-adsorbed proteins. A similar effect of proteins on surface morphology was observed on CoCrMo TFs and *bulk* discs as discussed in chapter 4. Further evidence of surface nanoporosity in different particles - polarised in SBF - are illustrated in figure 5.10. Additionally, sections from individual particles (lamella) were lifted out using FIB-SEM and deposited on a TEM grid to obtain cross-sectional images using STEM (figure 5.11). The images revealed extensive porosity particularly at the bottom surface (adjacent to the gold film) of the particle.

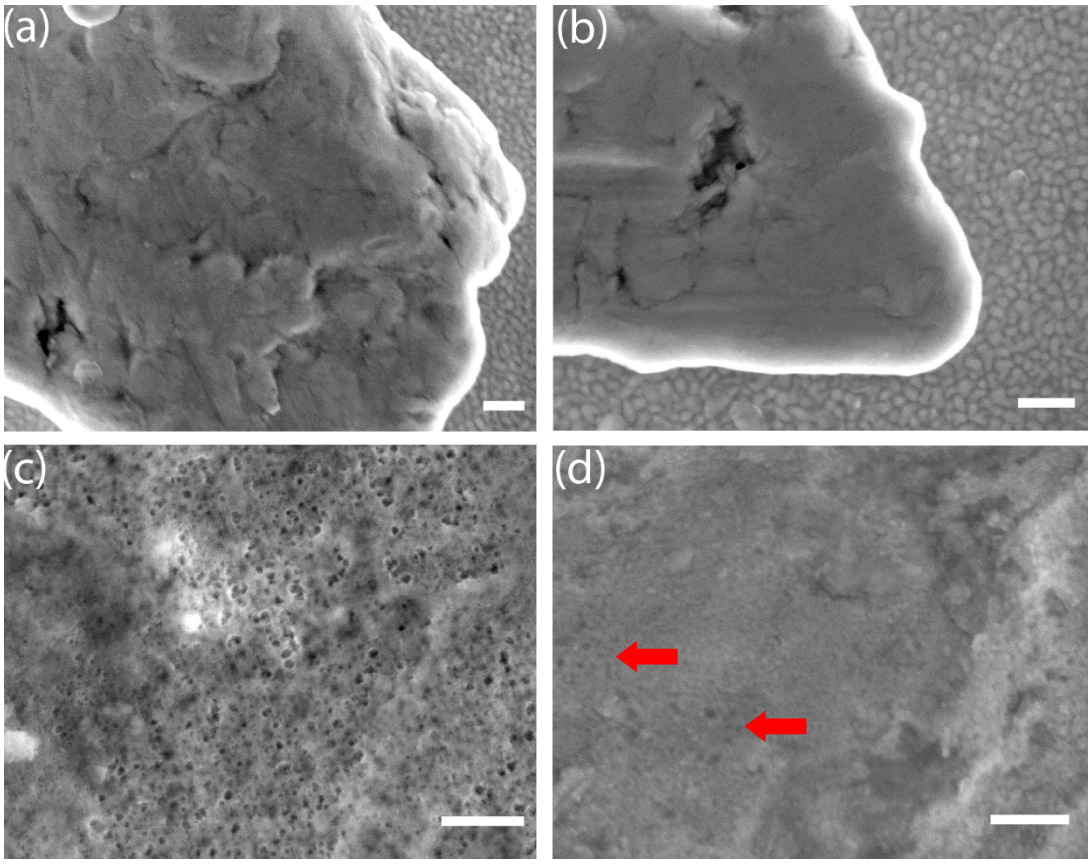


Fig. 5.9 Secondary electron SEM images of (a) AR particle, (b) a particle after immersion in SBF at OCP, (c) a particle after polarisation in SBF at 0.8 V showing the development of a nanoporous surface, (d) a particle after polarisation in serum-SBF at 0.8 V, with little porosity observed (red arrows). Scale bars = 200 nm. (reproduced from[272] licensed under CC BY 4.0).

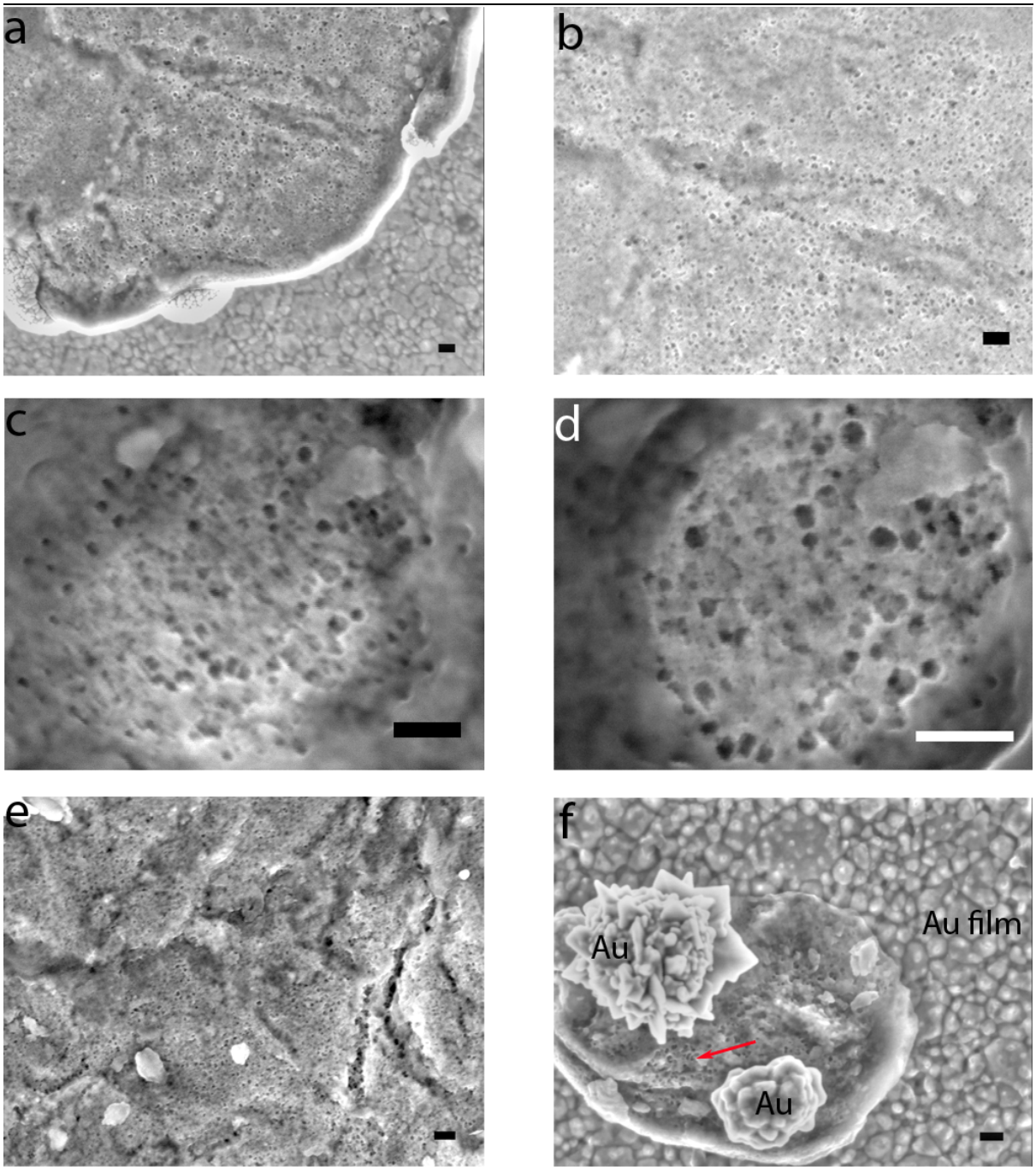


Fig. 5.10 (a-f) Secondary electron SEM images showing the development of nanopores on the surface of CoCrMo particles after polarisation at 0.8 V in SBF. The image pairs (a-b) and (c-d) show different magnification images of the same particles. Gold particles (labelled Au in (f)) were formed from the Au film during polarisation. Scale bars = 100 nm.

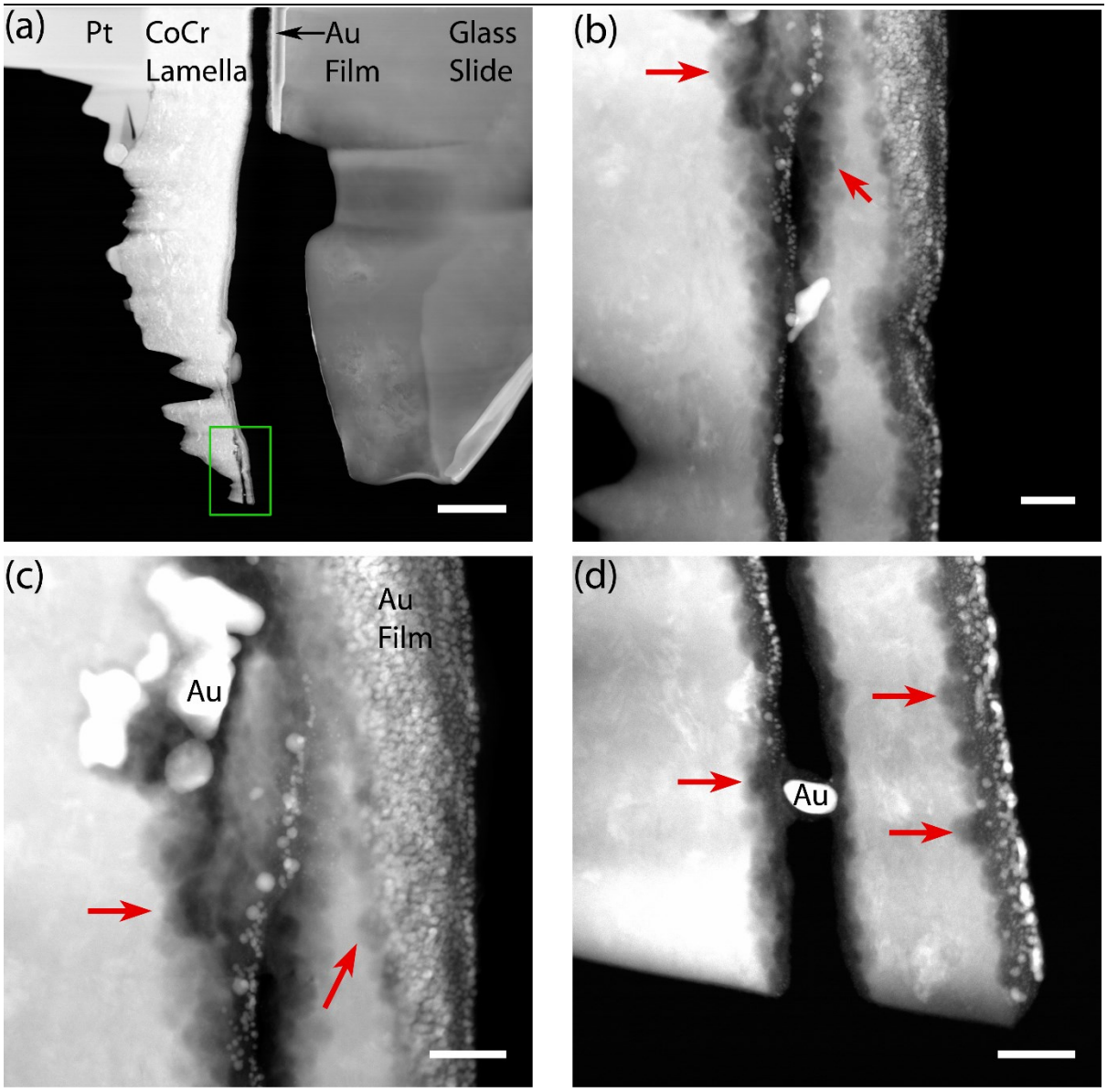


Fig. 5.11 (a) High angle annular dark field (HAADF) STEM image of the complete layered structure of the FIB-section including the Pt layer deposited to protect the particle's top surface during the lift-out procedure, the CoCrMo cross-section, the sputtered gold film, and the glass substrate, scale bar = 1µm. (b-d) higher magnification HAADF STEM images of the area marked by the green box in (a) revealing the nanoporosity network across particle surface, examples of porosity are indicated with the red arrows, scale bar = 50 nm.

Furthermore, in order to accelerate the dissolution process and gain better insight on the additional development of nanoporosity, STEM tomography was used to reveal the sub-surface morphology of particles polarised at a higher applied potential (1 V). Particles were drop-cast on the gold TEM grid which was in turn polarised in SBF. Figure 5.12(a) shows a dark field STEM image of the particle after polarisation at 1 V. Tomographic reconstructions revealed extensive porosity and a 'sponge-like' structure of the particle (see supplementary video 2). Figures 5.12(b-e) display cross-sections through the 3 D reconstruction illustrating the sub-surface porosity and thus the development of a porous network through the particle. The cross-sections were 8 nm apart through the depth of the particle (STEM tomography images were provided by Dr Angela Goode).

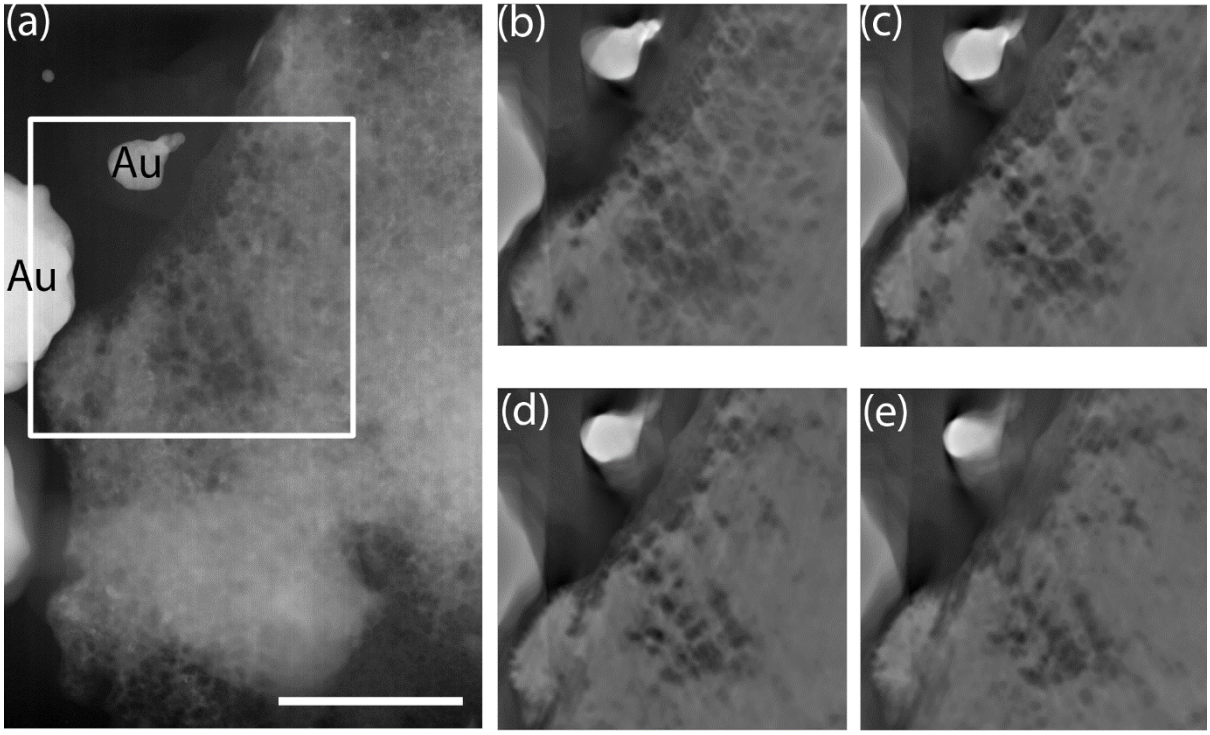


Fig. 5.12 (a) Dark field STEM image of CoCrMo particle (biased in SBF at 1 V), (b-e) Cross-sections through tomographic reconstructions, 8 nm apart, taken from a 370 x 360 x 40 nm section outlined by the white box in (a). Gold particles (labelled Au) were formed from the TEM grid during polarisation. Scale bar = 200 nm. Images were provided by Dr Angela Goode. (reproduced from[272] *licensed under CC BY 4.0).*

The evolution of the nanoporous structure is characteristic of a dealloying-like process. The process of dealloying is consistent with the higher rate of Co loss compared to Cr observed in this work and *in vivo*. Similar conclusions were drawn on the behaviour of alloy in TF and *bulk* forms as discussed in chapter 4. The mechanisms behind the process of dealloying have been discussed in more detail in section 4.3.7. While surface nanoporosity is evident on the particles after transpassive polarisation, the use of even higher potentials (1 V) accelerated the process and resulted in lower Co:Cr (at. %) ratios as well as the development of 'sponge-like' structure (however, this structure was observed in a thin particle which facilitated transmission electron microscopy).

5.4 Summary

The present work employed a correlative approach between microscopy and spectroscopy together with a combination of *ex situ* and *in situ* studies to elucidate the dissolution mechanism of CoCrMo particles. This multimodal approach has provided consistent insights into the particles dissolution behaviour. The data consistently showed a significantly higher rate of dissolution of Co compared to Cr under transpassive polarisation conditions. Furthermore, *in situ* TXM shows clear evidence of a rapid and inhomogeneous dissolution process, leading to the porous sponge-like structure observed *via* electron tomography. Taken together these data suggest that the particles undergo a dealloying-like process which was not evident in studies required for the clinical approval of

materials. The chemical composition and morphology of *in vivo* released wear particles is analogous to those observed in this work under transpassive polarisation conditions. Whilst these findings alone are not directly indicative of the formation of the carcinogenic Cr(VI), it is noted that the onset of this non-stoichiometric dissolution may require some local Cr dissolution, and is facilitated by the onset of transpassivity. In chapter 6, synchrotron radiation was employed for conducting chemical speciation studies at both Co and Cr edges; in particular, direct evidence for the Cr speciation during the dissolution process was pursued.

In conclusion, the correlative multimodal approach employed here provided valuable evidence on the likely behaviour of particles *in vivo* and suggests that current methods for material assessment and approval are insufficiently discriminating.

6 Chemical Speciation Studies

6.1 Introduction

The chemical speciation of Co and Cr from wear particles in explanted periprosthetic tissue has been extensively studied (as discussed in section 2.5.2). However, such studies, which are feasible only after implants' failure and revision surgeries, provide little insight into the dissolution process of these particles. Information on the history of the wear debris, such as local conditions in the body and length of exposure, remains unknown and any intermediate products that form during the process are not identified. From a clinical point of view, in addition to the cytotoxic[201] and genotoxic[207,212] nature of Co(II) ions, the speciation of Cr in the dissolution process is a major concern as Cr(VI) species are known to be carcinogenic. It is known that Cr(VI) forms at transpassive potentials due to the oxidation of Cr(III) from the alloy's passive film. The inflammatory response associated with implant wear particles leads to a rise in local electrochemical potentials, through the production of reactive oxygen species, but whether such an environment imposes transpassive conditions is unknown. Although the existence of Cr(VI) in tissue was not reported (except recently in diabetic patients,[187] as discussed in section 2.5.2), this could not conclusively exclude its formation *in vivo* since Cr(VI) species are reduced to Cr(III) once oxidising conditions are removed. Furthermore, the time scale (kinetics) of the reduction of Cr(VI), in biological environments, is unknown. Studying the development of Co and Cr speciation in selected and controlled environments could, therefore, provide a further understanding of the dissolution behaviour of wear particles *in vivo*. In particular, utilising an *in situ* approach is essential to acquire insights such as the kinetics of transient process (such as the evolution of Cr(VI) and its subsequent reduction to Cr(III)).

Synchrotron-based techniques provide *in situ* capability in wet electrochemical cells. Additionally, they offer the high energy resolution necessary for an accurate speciation analysis especially given the nanoscale/small concentrations of materials involved. The use of both spatially resolved and volume averaged X-ray spectroscopy techniques to study CoCrMo particle and TF dissolution, at both Co and Cr X-ray absorption edges, was explored and is discussed in this chapter.

6.2 Methods

Spatially resolved chemical information was obtained by TXM-XAS spectromicroscopy at Beamline 6-2, SSRL. This technique was mainly utilised to study the changes in Co speciation in CoCrMo particles (in SBF and under an applied electric potential). Cr speciation was examined under similar conditions using conventional population-averaged XAS at Beamline 4-3, SSRL. Cr speciation studies were developed with a focus on identifying the conditions and kinetics of Cr(VI) existence. Furthermore, the aforementioned work was complemented with *ex situ* speciation data of Co and Cr in TFs using XFM-XAS at NSLS-II Beamline 3-ID.

6.2.1 Co Speciation: Spectromicroscopy of CoCrMo Particles

TXM measurements were facilitated by the 3D printed electrochemical cell previously described in section 5.2.3, and shown in figure 5.2. *In situ* images were recorded in SBF and under an applied electrochemical potential. The TXM optical design (involving a Fresnel zone plate lens) provided a spatial resolution of 30 nm when used with a field of view of ~30 μm. Spectral information could be obtained by recording a stack of images, of the region of interest (ROI), using different incident X-ray images. The incident X-ray intensities I_0 (at each selected incident energy) are recorded as a separate image through a *reference* window in the cell which facilitates direct X-ray transmission to the detector, without encountering SBF or CoCrMo samples. The *reference corrected* absorbance images of the ROI, per selected incident energy j are then computed according to Beer-Lambert's law:

$$absorbance\ of ROI_j = (-\ln \frac{I}{I_0})_j \qquad \text{Equation 6.1}$$

Consequently, X-ray absorption spectra, of each pixel in the ROI, were analysed and compared to the relevant standard X-ray absorption edges. Thus, the combination of TXM-XAS would provide spatially resolved chemical information.

The relevant oxidation states of Co are the metallic Co and Co(II). Standard X-ray absorption edges of both Co metal and Co(II) were obtained using a Co foil and CoO powder respectively. Subsequently, the normalised spectrum of each pixel, in the imaged ROI, was fit to the linear combination of the standard spectra as represented by equation 6.2.

$$ROI_n = x_n\ Co + \ y_n Co(II) \qquad \text{Equation 6.2}$$

(Where n is the pixel number in a given ROI, x and y are the least squares fitting weights with values between 0 and 1; and their sum equals 1).

Therefore a spatial speciation map of the ROI, representing the ratio of Co(II):Co, could be formed by plotting the map of y_n. The percentage of absolute Co(II) amount in the ROI could be quantified by first considering the absorbance intensity of the ROI at an isosbestic energy point. The isosbestic point is the incident X-ray energy where the absorption of both Co and Co(II) is equal. Hence absorbance intensity variations across the imaged ROI is proportional to the total amount of Co present irrespective of speciation (*i.e.* variations in the sample thickness) according to equation 6.3 of Beer Lambert's law.

$$absorbance = a(\lambda)\ \times t\ \times c \qquad \text{Equation 6.3}$$

(Where a(λ) is a wavelength-dependent absorptivity coefficient, t is the X-ray path length, and c is the analyte concentration).

The quantification of the percentage of Co(II) content in the ROI could, therefore, be calculated

$$\%\ Co(II) = \frac{\sum_n (y_n \times I_n)}{\sum_n (I_n)} \qquad \text{Equation 6.4}$$

(Where y_n is the percentage of Co(II) in an individual pixel n (as obtained by the least square fitting discussed in equation 6.2), and I_n is the absorbance intensity, of pixel n, at the isosbestic energy point).

The work developed here aimed at dynamically quantifying the changes of Co(II) content in CoCrMo particles during applied electrochemical potentials in SBF.

6.2.2 Cr Speciation: Conventional XAS at SSRL Beamline 4-3

Studies of Cr speciation were designed with the aim of identifying the onset of Cr(VI) release from CoCrMo samples; additionally, since Cr(VI) is a transient species (subsequently reduced to Cr(III)) the studies aimed at measuring the kinetics of its subsequent reduction and hence quantifying its transient presence. Cr(VI) absorption is characterised by a sharp pre-edge peak (1 eV wide) which makes it relatively straightforward to distinguish from other Cr oxidation states (Cr metal and Cr(III)). Initially, the studies were conducted in TXM-XAS mode, at SSRL beamline 6-2 (used in Co speciation studies), by measuring changes in absorbance intensity at the Cr(VI) pre-edge peak energy as a function of time and potential. In these experiments Cr(VI) was not conclusively detected even at electrochemical potentials where it is known to form. This was due to the low signal to noise ratio acquired due to the low analyte concentration available when studying a single CoCrMo particle. Therefore population-averaged XAS measurements were carried out to enhance chemical sensitivity. Population-averaged XAS measurements were carried out at Beamline 4-3, SSRL. The electrochemical cell, previously used in TXM-XAS measurements, was adapted to include a larger front (X-ray entrance) and downstream (sample) windows which made use of the larger beam size (1 x 9 mm) available and increased our exposed sample size. Additionally, the gap between the two windows (X-ray path length) was increased to 3 mm and measurements were carried out in fluorescence geometry. In this setup, when the cell was filled with SBF, the measurements were only sensitive to signal from the solution (SBF electrolyte) rather than the sample (since the X-ray path length is long enough to cause complete attenuation of the X-ray beam in SBF), as illustrated in figure 6.1. The transmitted X-ray intensity through one absorption length of a medium is equal to 1/e of the incident intensity as per Beer Lambert's law (equation 3.19, section 3.4.2.1). The absorption length of X-ray through water at the Cr-edge energies is approximately 410 µm. The 3 mm electrolyte path length in the designed electrochemical cell is approximately more than six times the attenuation length of X-ray in water at the Cr-edge energies, and thus the portion of the beam reaching the CoCrMo sample would be negligible. Therefore, this geometry would provide measurements of the dissolved species only. In addition to CoCrMo particles, CoCrMo 80 nm TFs samples were also used. This meant that the sample encompassed the full field of view which enhanced the signal to noise ratio, thus, increasing

the sensitivity to capture Cr(VI) release. The exact Cr(VI) absorption pre-edge peak energy was determined using a Cr(VI) standard (10 wt.% $Na_2Cr_2O_7$ in boron nitride pellet). Absorbance intensity was measured at the determined pre-edge peak energy as a function of time and potential. Following the end of the final applied potential step (800 mV), the system was left at OCP while absorbance intensity was continually measured for 20 minutes. At OCP, no further Cr(VI) would be expected to be dissolving from the sample and hence the already dissolved concentration of Cr(VI) can be monitored as a function of time to measure the kinetics of its reduction to Cr(III).

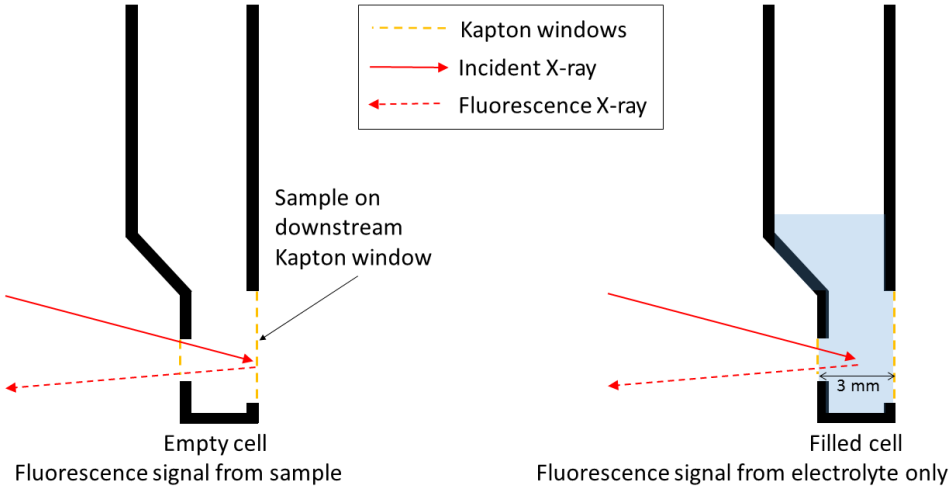


Fig. 6.1 Schematic illustrating the XAS measurement setup and the source of the detected signal. This set up was employed for XAS measurements at Beamline 4-3, SSRL for Cr speciation studies.

6.3 Results and Discussion

6.3.1 Spatial Co Speciation Mapping

Firstly, an illustration of the speciation mapping process is discussed in section 6.3.1.1. The steps undertaken in the process of obtaining a single speciation map are discussed utilising an initial dataset. Subsequently, in section 6.3.1.2, dynamic changes in Co speciation, as a function of applied electrochemical potential, are revealed through serial speciation maps obtained of a CoCrMo particle.

6.3.1.1 Illustration of Mapping Procedure

6.3.1.1.1 Data Collection

The first step of the spatial speciation mapping process was selecting the data collection parameters such as the X-ray energy range, the energy step size and the detection time. The dataset chosen for this illustration case study was collected on CoCrMo particles maintained in an SBF-filled cell at open circuit conditions. A series of TXM images, providing the spatial information, were collected at different X-ray energies, to obtain the chemical information. The images were recorded across the Co K-edge at an overall energy range of 7644 eV to 7808 eV.

The energy range could be divided into three main regions: i) the pre-edge (background), ii) the near-edge region, and iii) the post-edge region. Different energy step sizes were used across the different regions, as described in table 6.1. A total of 101 X-ray energy points were used; ten TXM images were recorded at each energy, with a 1 s detection time each, which were ultimately averaged to produce a single image at each energy point. The images were initially aligned, using a Matlab based software TXM Wizard, to ensure that feature positions remained constant across the image stack. The software could also be utilised to obtain absorbance intensity images by performing the calculation described by equation 6.1 (an image of incident photon flux I_0 had to be obtained at each of the selected X-ray energies, using the *reference* window in the cell). Consequently, XAS spectra could be obtained for each 30 nm pixel in the imaged region which consisted of approximately 670,000 pixels. Standard Co and Co(II) absorption edges were also recorded as shown in figure 6.2. Examples of the TXM images obtained on the CoCrMo sample are shown in figure 6.3, at selected X-ray energies marked by the vertical *dotted* lines in figure 6.2. Furthermore, examples of XAS spectra extracted from three different regions (pixels) in the sample are shown in figure 6.5(a).

Table 6.1 The energy steps at which the TXM images were recorded

Region	**Energy range eV**	**Steps between images**
Pre-edge (background)	7644-7694	5 eV
Near-edge (background & XANES)	7695-7730	0.5 eV
Post-edge (EXAFS)	7732-7750	2 eV
	7758-7808	10 eV

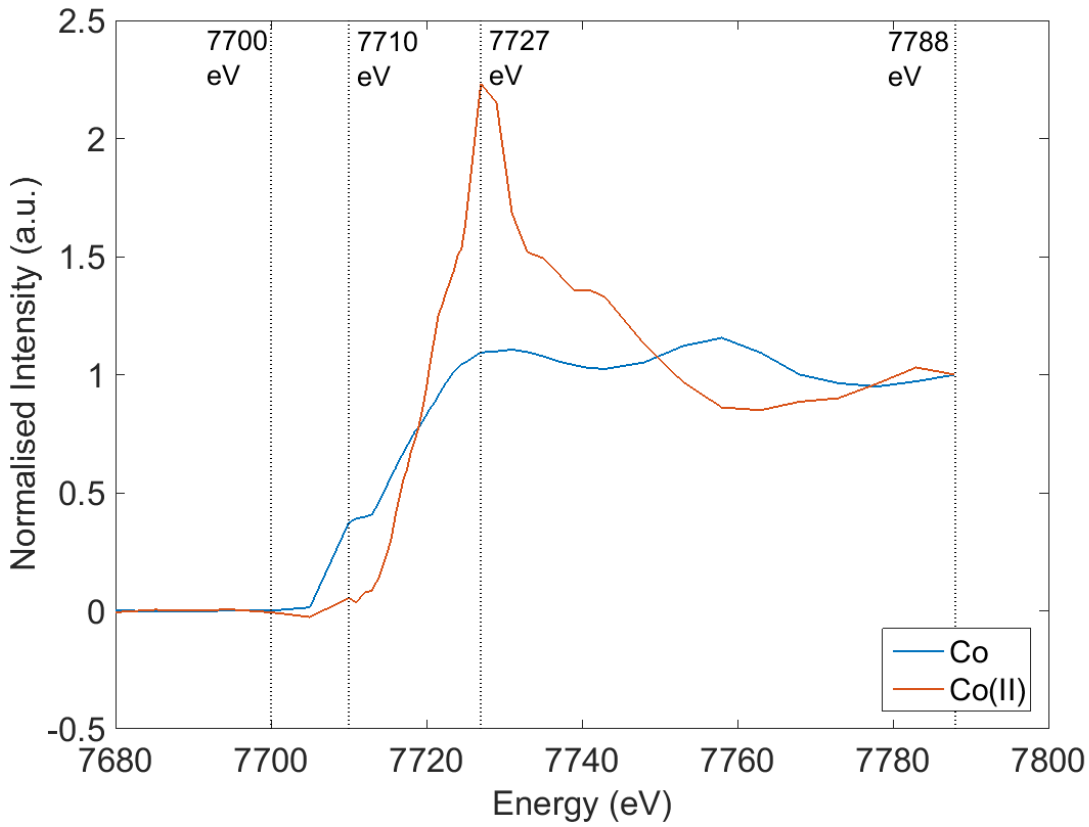


Fig. 6.2 Standard XAS spectra for Co metal and Co(II) as obtained from Co foil and CoO powder respectively

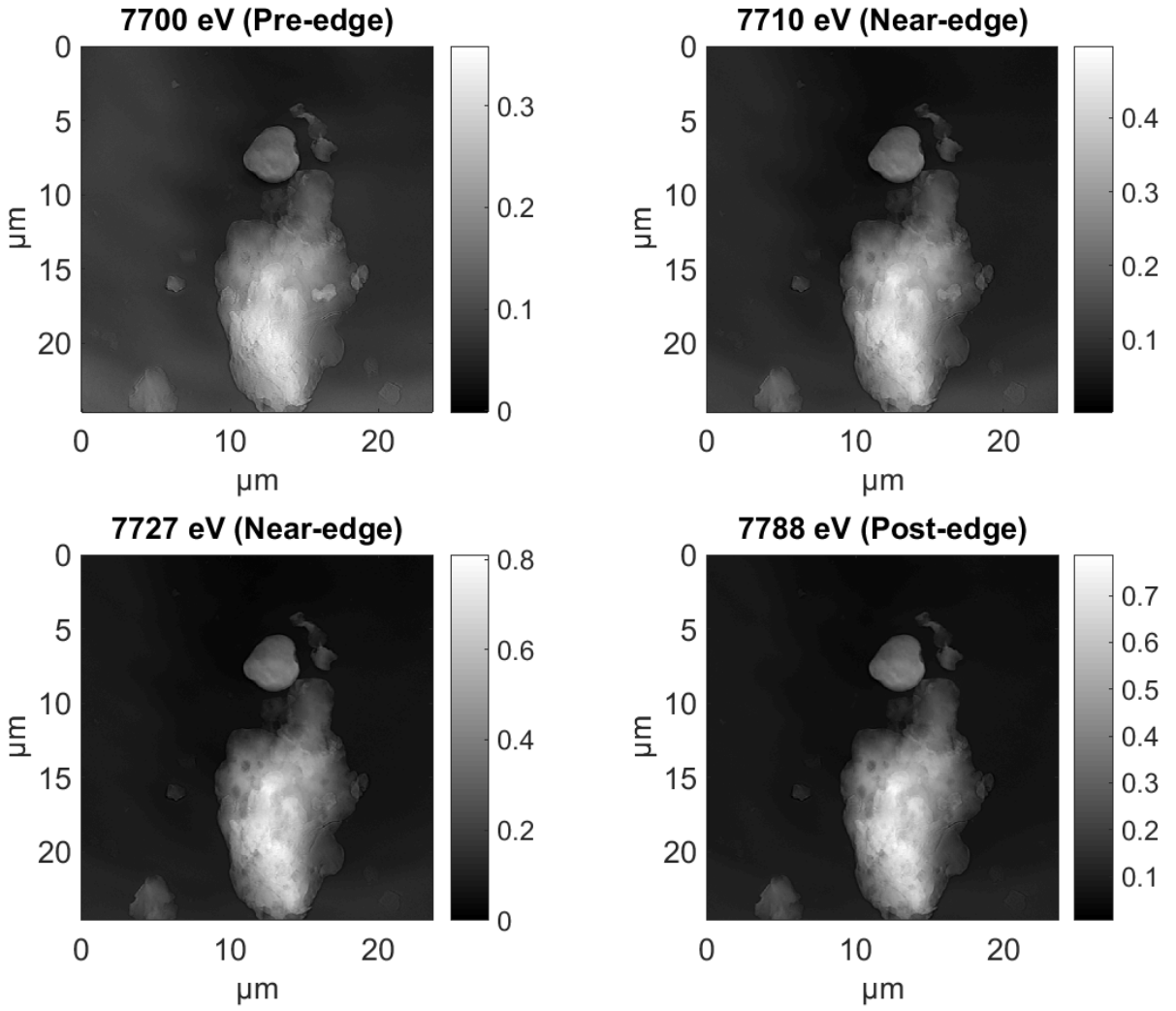


Fig. 6.3 TXM images of CoCrMo particles at four selected energies. The selected energy points here are indicated on the XAS spectra in figure 6.2. Colour bars indicate absorbance (a.u.).

6.3.1.1.2 Noise Reduction

Improving the signal to noise ratio could be achieved during data collection by increasing the exposure (detection) time at which images are recorded or similarly by recording multiple images (using the same incident X-ray energy) and obtaining an average. Once the data are collected, principal component analysis (PCA) can be used to further improve the signal to noise ratio.

PCA is a mathematical technique which determines the significant variations in a dataset, defined as the dataset's principal components. The data dimensionality can be reduced by selecting and keeping only the most significant components of a dataset (the components which contribute the biggest variance). Therefore, one of the applications of PCA has been noise reduction; and it has been previously applied for this purpose on X-ray microscopy data.[273] The components with the lowest eigenvalues would be regarded as the experimental noise and the data could be reconstructed excluding those components.

The data from TXM consists of a series of 2D images, with each image collected at a different X-ray energy. Once this image stack is aligned, this data were collated into a single 2D matrix D_{PxN} of absorbance intensity, where P is the individual pixel number (number of observations) and N is the number of X-ray energy points used (number of variables observed). The covariance matrix Z is then calculated by multiplying the data matrix D by its transpose. The eigenvectors of Z represent the principal components of the data and their associated eigenvalues indicate the statistical variation each component represents. A scree plot ranks the principal components by the amount of variance they capture in the data. The inflexion point of the scree plot determines the number of components to keep where the components with the lowest eigenvalues are discarded.

PCA was applied to the collected data set of 101 TXM images. Figure 6.4 shows the scree plot ranking the number of components by their eigenvalues in descending order. The data were reconstructed using the top six components which represented 99.5 % of the variance in the original data. A comparison of individual XAS spectra from the dataset before and after noise reduction by PCA is shown in figure 6.5(a) and 6.5(b) respectively.

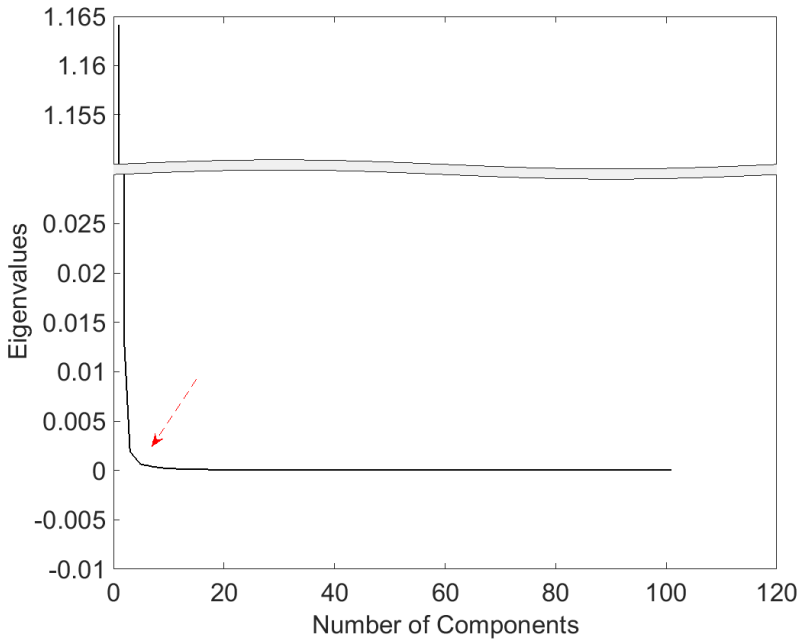


Fig. 6.4 A scree plot ranking the TXM dataset principal components by their eigenvalues in descending order. The data was reconstructed using the first six components (as marked by the red arrow at the inflexion point) which represented 99.5 % variance of the original dataset.

6.3.1.1.3 Spectral Background Removal and Normalisation

Background removal involves subtracting the residual absorbance intensity, in the pre-edge region, from the dataset. Background removal was performed for each XAS spectrum in the data by computing the line of best fit for the intensity values in the pre-edge energy range of 7644 eV – 7699.5 eV and subtracting this background line value from each corresponding intensity value across all energy points.

Background removal is followed by the normalisation step which standardises XAS spectra through removing variations due to analyte concentration or sample thickness. Any differences in XANES features between normalised spectra are attributed to the difference in chemical speciation. All data spectra were normalised by dividing corresponding intensity values by the value of the line of best fit for the post-edge energy range 7740 eV – 7808 eV. Figure 6.5 demonstrates sample XAS spectra as raw data, after background-removal, and after normalisation. Figure 6.6 compares original raw TXM images (at a pre-edge and a post-edge energy points) to corresponding images reconstructed after background removal.

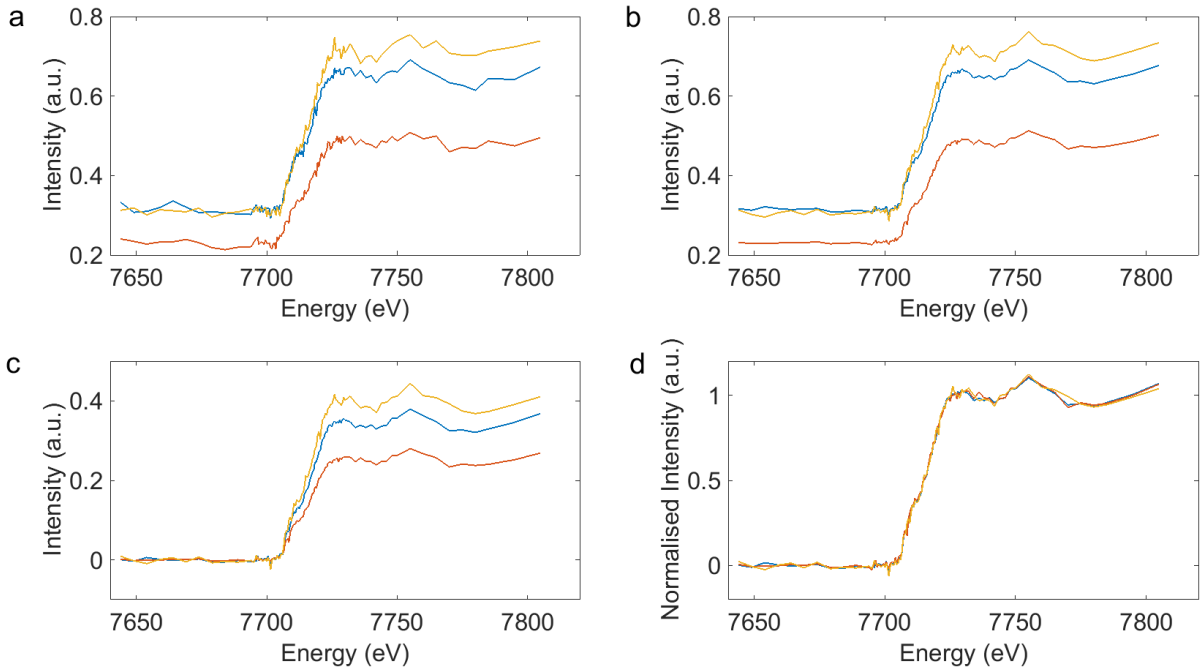


Fig. 6.5 Examples of three XAS spectra from three different locations in a CoCrMo particle extracted from the TXM-XAS images dataset. (a) raw spectra, (b) Reconstructed spectra after PCA, (c) Spectra after background removal, (d) Normalised spectra.

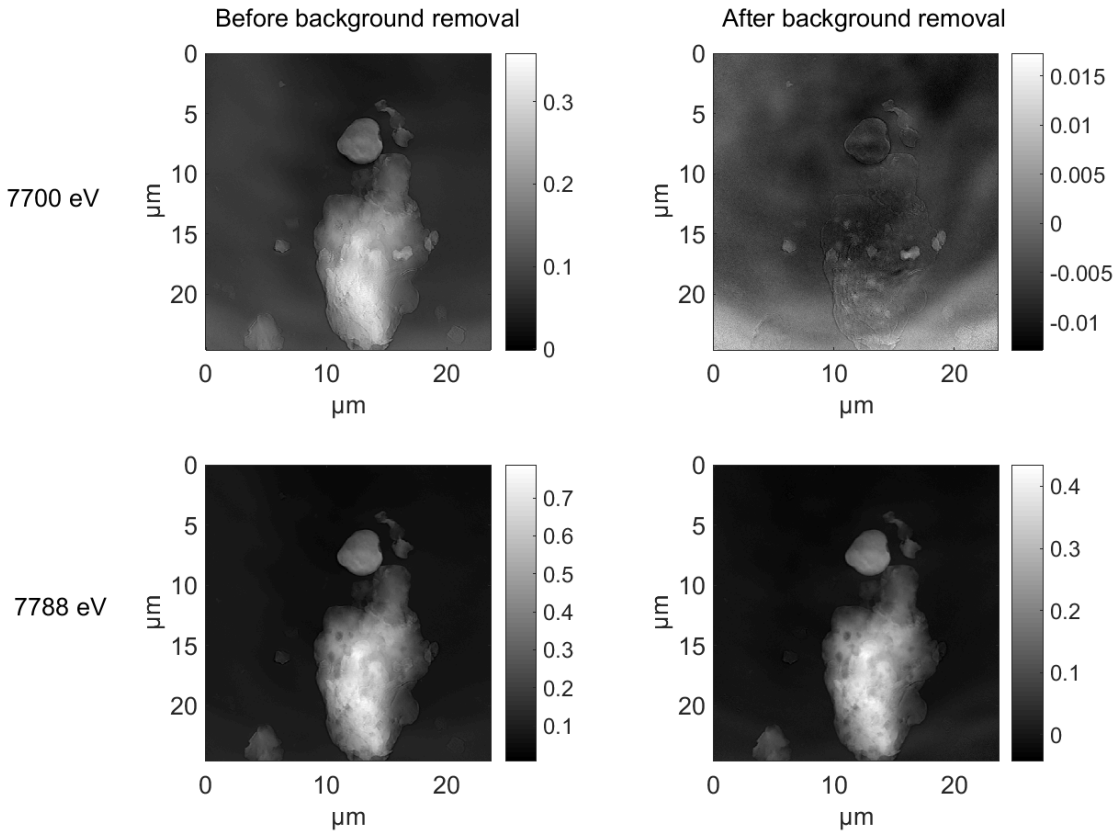


Fig. 6.6 Illustration of TXM images before and after background removal at both a pre-edge energy point 7700 eV, and a post-edge energy point 7788 eV. Colour bars indicate absorbance (a.u.).

6.3.1.1.4 Identifying Spatial Background

The final preliminary step before the speciation mapping was identifying the spatial background regions. These were the pixels in the imaged field of view which did not contain the analyte (in this case Co from CoCrMo particles) and would, therefore, be excluded from the speciation analysis process. This may be achieved by identifying a threshold absorbance intensity value (at an isosbestic energy point). Pixels with intensities below this threshold would be considered as part of the spatial background. This process involved examining intensity profiles across the image at the isosbestic energy 7788 eV as illustrated in figure 6.7. A threshold absorbance of 0.025 was identified as the separation value between *background* and *sample* regions. This threshold absorbance was more than three times larger than the standard deviation (3.1σ) of the intensity values of spatial background pixels outlined in figure 6.7, indicating that intensities above this value would not represent spatial background regions with a confidence level 99.7%.

The process of identifying spatial background could also be achieved through a second method based on the ratio of pre-edge (E_{pre}) and post-edge (E_{post}) absorbance intensity. The spatial background is defined as those regions which do not contain Co and hence no absorbance intensity signal would be expected above Co absorption edge.

Therefore, variations in E_{post}: E_{pre} intensity ratio at spatial background regions would be defined by noise. Hence, a threshold intensity ratio could be used as a filtering criterion.

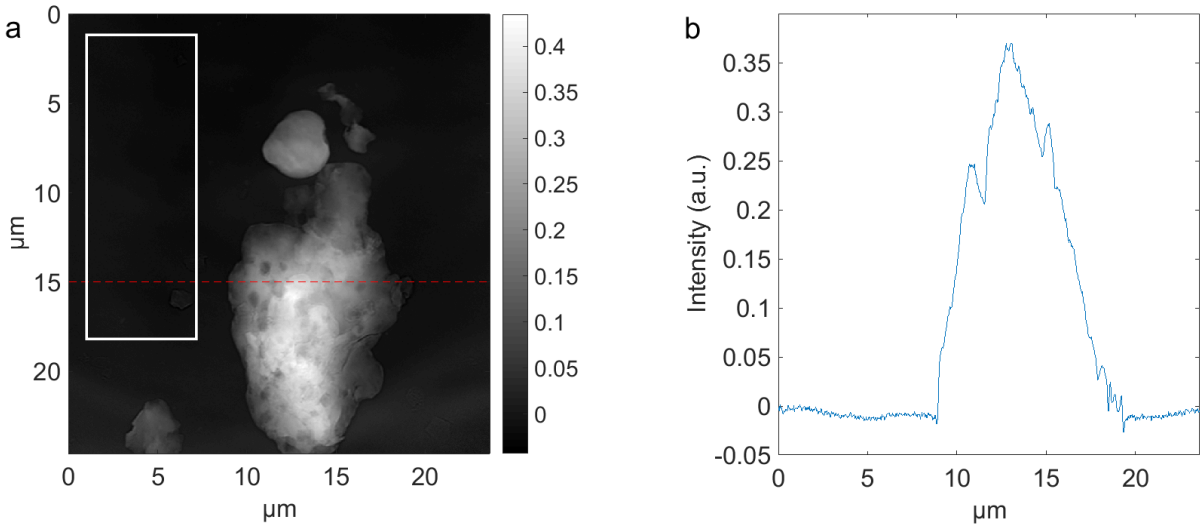


Fig. 6.7 Demonstration of spatial background filtering procedure. (a) TXM image at the isosbestic energy point 7788 eV, a line profile across the image is selected (indicated by the red dashed line). (b) a plot of absorbance across the line selected in (a). A threshold/cut-off absorbance value is selected to separate the spatial background regions from particles' (sample) regions. A cut-off value of 0.025 was selected, which equals 3.1σ of the absorbance values outlined by the white rectangle in (a).

6.3.1.1.5 Linear Combination Fitting and Mapping

The additive nature of absorption from each species in a heterogeneous sample is the underlying principle of linear combination fitting (LCF). The speciation composition ratio could be determined through fitting a linear combination of the standard spectra (in this case, standard Co metal and Co(II) spectra) to the measured sample spectra. This was computed for each pixel of CoCrMo particles in the data, according to equation 6.2. LCF is computing the scaling factors applied to each standard spectra which provide the best representation of the measured data (sample). The weighting parameter *x* was defined, for the standard Co metal spectrum, and constrained to be between 0 and 1. The weight parameter *y* for the standard Co(II) spectrum was *1-x*, thus constraining the standards to be 100 per cent of the sample. The weight parameters would then be varied to find the least-squares fit to a sample spectrum. Thus, each sample region (pixel) is assigned with a weight parameter *y (or x),* which describes the composition ratio of that region. Figure 6.8 shows a map of y representing the spatial distribution of Co(II):Co ratio. The map suggests that the CoCrMo particles were predominately composed of Co metal which would be expected given the system was at open circuit potential. However, the map of speciation ratio does not take into account variation in particle thickness. Thickness variation was accounted for when quantifying the overall Co(II) content, according to equation 6.4 which was found to be 0.2 %.

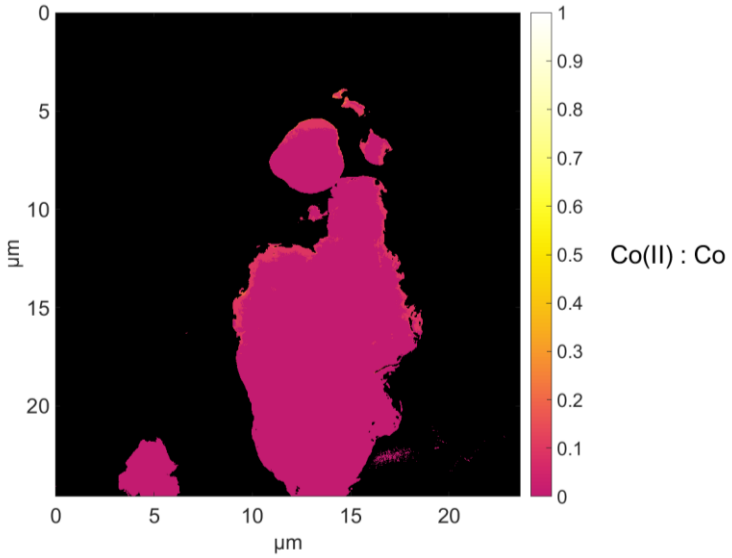


Fig. 6.8 Speciation map[d] representing the distribution of the Co(II) composition fraction as constructed by LCF of individual region/pixel spectra.

The goodness of fit, for each fitted pixel-spectrum, could be evaluated through statistical parameters. Reduced chi-squared χ^2_v is the commonly used parameter to evaluate the goodness-of-fit, as defined by equations 6.5 and 6.6.

$$\chi^2 = \frac{N_{idp}}{N_{pts}} \sum_i \left(\frac{data_i - fit_i}{\varepsilon_i}\right)^2 \qquad \text{Equation 6.5}$$

$$\chi^2{}_v = \frac{\chi^2}{v} \qquad \text{Equation 6.6}$$

(Where χ^2 is chi-squared, N_{idp} is the number of independent points in the model fit, N_{pts} is the number of data points, ε is the measurement uncertainty, and v is degrees of freedom (number of points *minus* number of variables)).

However, the interpretation of reduced chi-squared in linear combination fitting is challenging. There is no way of evaluating a measurement uncertainty ε for the XANES measurement. The commonly used XAS data analysis software *Athena* assumes a value of 1 for ε in the calculation for chi-squared.[274] Typically a reduced chi-squared value close to 1 indicates a good fit result and implies that the difference between observed data and the fit is consistent with the measurement uncertainty. However, in this case, reduced chi-squared tend to be very small numbers, much smaller than 1, indicating that the uncertainty is over-estimated. Therefore, it is not possible to use reduced-chi-squared to evaluate the quality of a single fit, although, relative changes between fits could be meaningful. Therefore, another statistical parameter, the R-factor, could be used to evaluate the goodness of fit in this case. The R-factor is the sum of the squares of the differences between the data and the fit at each data point

[d] The colour scheme (colour map) used in displaying Co speciation maps throughout this work was designed by Geissbuehler and Lasser.[275]

(in this case X-ray energy point), divided by the sum of the squares of the data at each corresponding point. This is defined by equation 6.7:

$$R\,factor = \frac{\sum_i (data_i - fit_i)^2}{\sum_i {data_i}^2} \qquad \text{Equation 6.7}$$

In general, R-factor values of up to 0.05 are considered to reflect a reasonable fit.[251] The R-factor for each fitted pixel spectrum was calculated and a histogram showing the frequency of R-factor values is shown in figure 6.9. The results reveal that 95.5 % of the fits had an R-factor ≤ 0.05, while the maximum R-factor was 0.29. Figure 6.10 displays the spatial distribution map of R-factor values. Generally, higher R-factor values correlated with spectrums of higher Co(II) composition fraction (found at the edges of the particles) or with diffuse material surrounding the particles. This correlation could be explained by the dynamic nature of the process: imaging dynamic processes are likely to present more challenges in speciation fitting compared to static structures as the speciation composition of a particular region would be changing during the spectrum collection process. Co(II) regions are likely to be continually evolving under polarisation and hence the least accurate fits are likely to correlate with these regions.

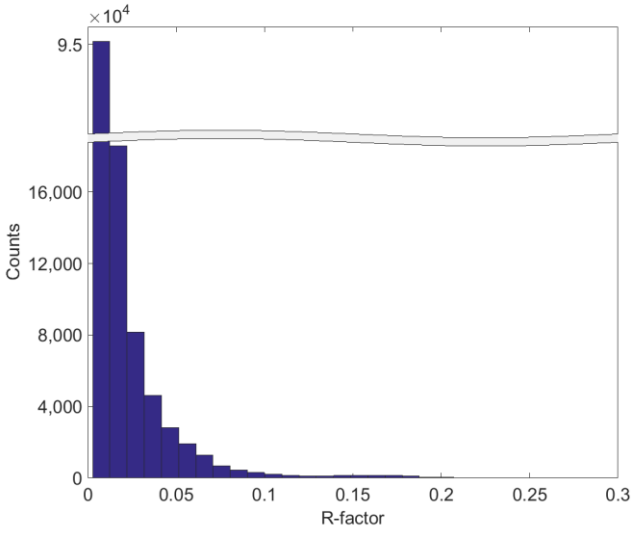


Fig. 6.9 A histogram of the frequency of R-factor values from all sample spectra fits. Bin size is 0.01. More than 95 % of the fits had an R-factor value of less than 0.05.

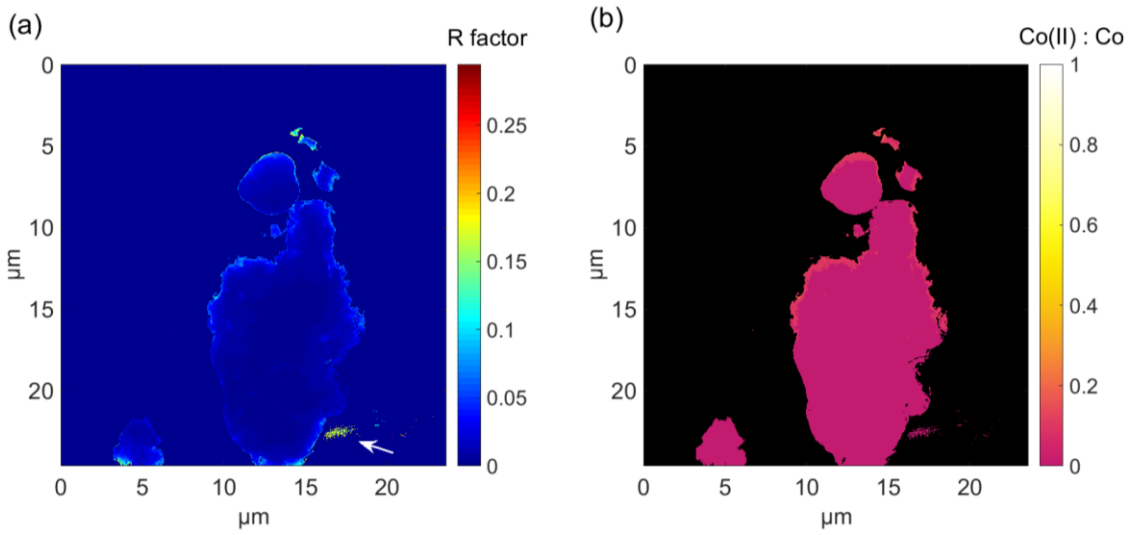


Fig. 6.10 The spatial distribution map of the R-factor values (a), compared to the speciation composition map (b). The regions with higher R-factors correlated with dynamically evolving regions such as those of higher Co(II):Co ratio, at the edges of particles, and diffuse material around the particles (marked by the white arrow in (a)).

6.3.1.1.6 Reducing Energy Data Points

Reducing the number of images/energies used in the speciation mapping process is important for two main reasons. Firstly, reducing the time required to collect a data set required for one quantification calculation and hence more quantifications can be completed in a given period to monitor changes over time (*i.e.* improving temporal resolution). Secondly, reducing the X-ray dosage to which the sample is subjected, and hence reduce any potential alterations to the sample resulting from exposure to X-rays. Therefore, the number of photon energies selected for imaging could be regarded as a trade-off between a more accurate chemical analysis on one side, versus temporal resolution and low X-ray dosage on the other. However, to be able to accurately comment on the required number of energy points required for accurate quantification of Co(II) percentages, a particle with a pre-known composition is required. Therefore, a simulation analysis was undertaken (Appendix A). This involved reconstructing images of a square-shaped particle of varying Co metal and Co(II) ratios at different energy points, using the standard absorption edges of the two Co species. After adding random noise to the *particle's* absorbance values, the Co(II) content was quantified and compared to that of the original composition. The results suggested that, for this specific Co speciation case, using three post-edge energy points is almost as accurate as using double that number.

6.3.1.2 Co Speciation as a Function of Applied Potential

The overall aim of this spectromicroscopy study was to dynamically monitor changes in Co speciation in CoCrMo particles as a function of potential. This was achieved through obtaining multiple TXM-XAS image stacks and producing multiple corresponding speciation maps, at different applied electrochemical potentials. The speciation mapping process was generally executed as described in section 6.3.1.1. However, the number of X-ray energy

points selected was dramatically reduced in order to enhance temporal resolution and increase chances of capturing speciation changes.

Six incident energy points were selected for this speciation analysis: three pre-edge points for the purpose of background removal, and three post-edge energy points for the speciation and quantification analysis. The first three (pre-edge) energies were: 7659 eV, 7679 eV, and 7699 eV. The fourth and fifth energies 7710 eV and 7727 eV were used as the key spectral differentiation points for the chemical speciation analysis, due to the large difference in X-ray absorbance between Co metal and Co(II) at these energies (as shown in figure 6.11(b)). The last energy was 7788 eV, an isosbestic point, at which the data were normalised. Each image was collected with an exposure (detection) time of 2 s and a total of ten images were obtained at each energy point to obtain an averaged image. Figure 6.11(a) shows a TXM absorbance image of the CoCrMo particle imaged for this analysis. Figure 6.12 shows the raw and normalised absorbance spectra obtained from two selected pixels. The normalisation process included the background removal by subtracting the line fitted across the pre-edge energies from the raw spectrum, and subsequently, the data is normalised against the isosbestic point (7788 eV).

Multiple six-energy image stacks were recorded on the CoCrMo particle: at open circuit potential (OCP) and at applied electrochemical potential steps from 400 mV to 800 mV (in steps of 100 mV for 400 s each). Speciation maps, at each applied potential, were computed by linear combination fitting of the standards (figure 6.11(b)) as described by equation 6.2 and the Co(II) content in each map was quantified according to equation 6.4.

Figure 6.13 shows the speciation maps of the Co(II):Co ratio (y_n, according to equation 6.2) and the calculated Co(II) amounts at each potential step. The results show a noticeable rise in Co(II) content (11 %) at the 800 mV step, however, small amounts of Co(II) species (4 to 5 %) were observed at earlier potential steps. Figure 6.14 displays the information in the form of a histogram of the frequency of y_n values (*i.e.* Co(II):Co ratios) at each potential.

Thus, the results suggest a limited Co dissolution at OCP and applied passive potentials followed by a noticeable rise at the 800 mV transpassive polarisation. This result is consistent with the *in situ* study of Co loss as a function of time and potential discussed in chapter 5, section 5.3.2. In the latter study, a significant increase in Co dissolution was observed during 800 mV polarisation of a population of particles; here, a rise in the oxidised Co content was observed in a single particle at the same polarisation potential of 800 mV. Therefore, both population-averaged and localised studies consistently confirm the rise in Co dissolution kinetics after transpassive polarisation, particularly after the 800 mV applied potential step.

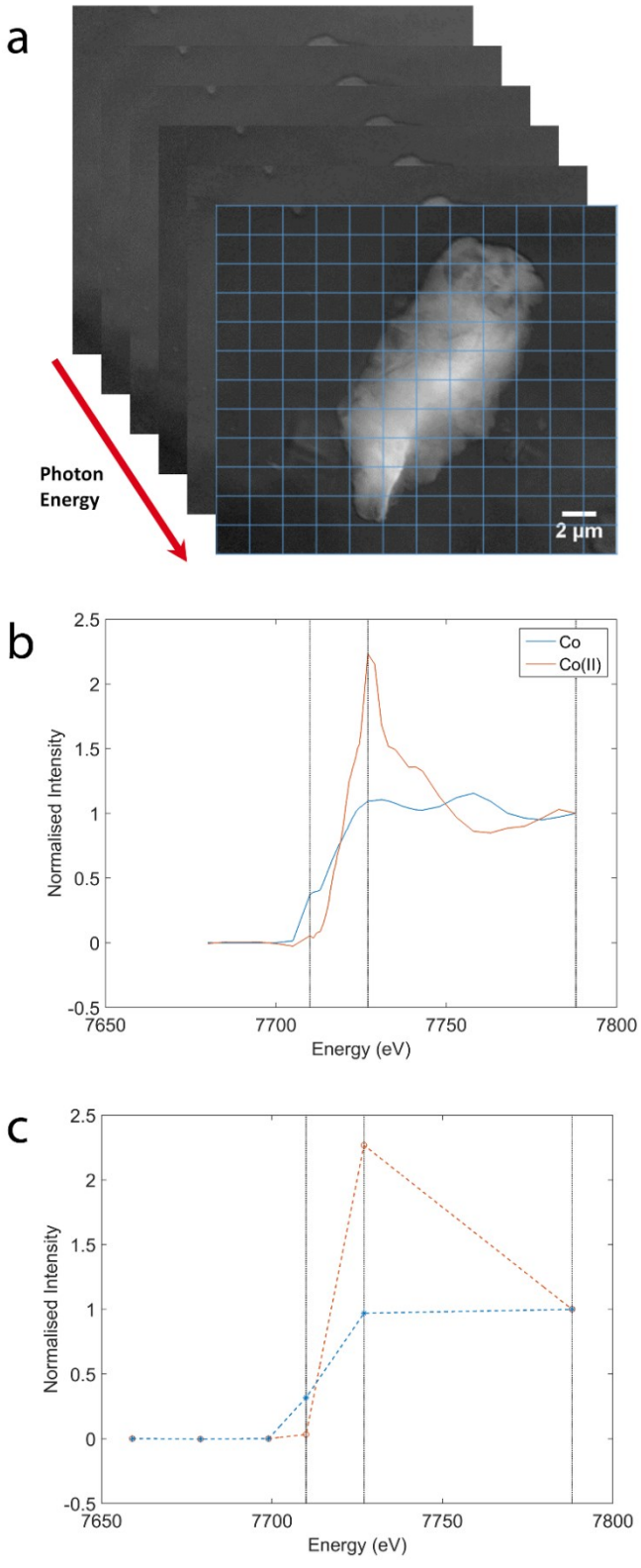


Fig. 6.11 (a) A stack of TXM absorbance images of a CoCrMo particle recorded at six different energies illustrating the TXM data collection procedure. (b) The recorded standard X-ray absorption spectra for Co metal and Co(II). The black vertical lines illustrate the three post-edge incident X-ray energy points selected for TXM imaging (in addition to three pre-edge energies). (c) Examples of the six-energy spectra of two different sample regions, resembling Co metal absorption (blue) and Co(II) absorption (red).

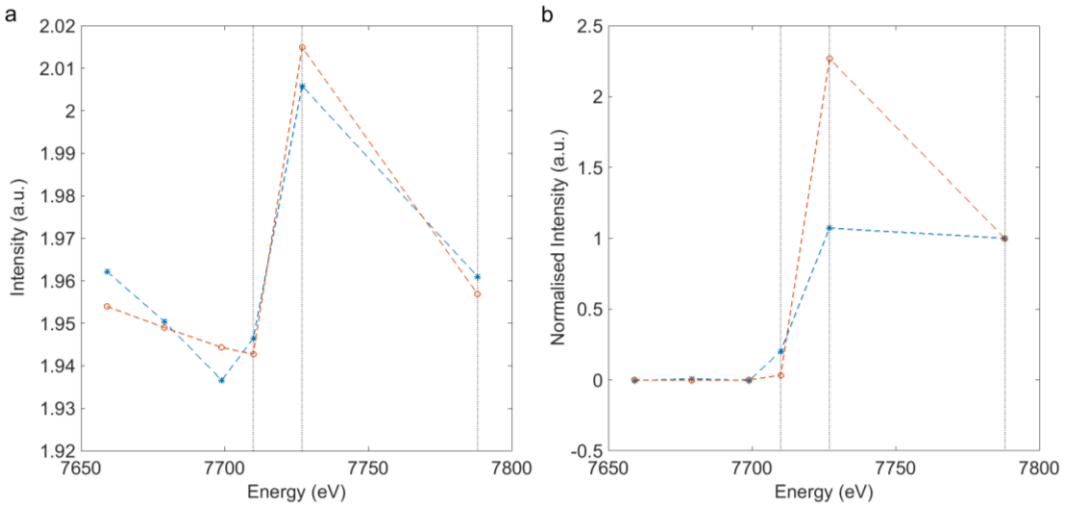


Fig. 6.12 (a) Raw six-energy spectra of two example sample regions. (b) The same spectra after normalisation.

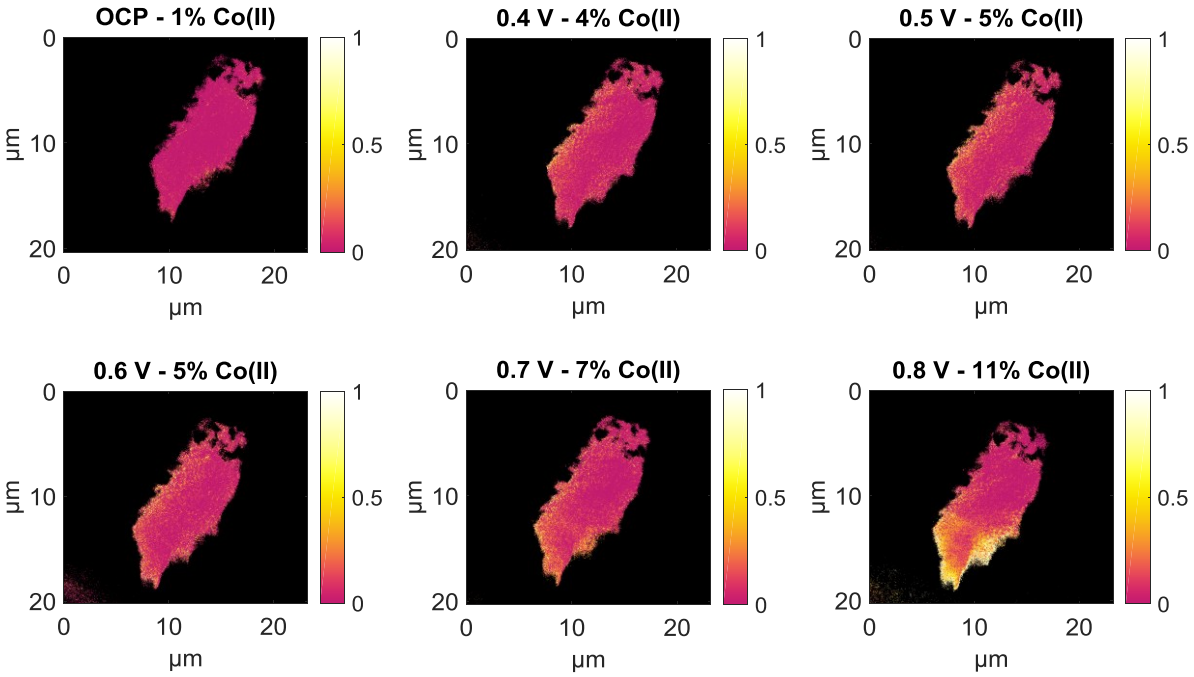


Fig. 6.13 Speciation maps representing the Co(II) composition fraction of every 30 nm pixel/region in the CoCrMo particle at different applied electrochemical potential. The total Co(II)% (displayed above each corresponding map) were calculated per equation (6.4) and was found to increase as the applied potential increased, with a noticeable rise at the 0.8 V step.

Figure 6.15 shows a histogram of the R-factor values for all fitted spectra in this analysis. The maximum R-factor values in the different maps were as follows: 0.55, 0.85, 1.46, 1.38, 0.70, and 0.79 for the OCP, 400 mV to 800 mV maps respectively. Although these were higher compared to the maximum R-factor observed in the high energy resolution fitting (using 101 energy points, discussed in section 6.3.1.1), 95 % of values still remained less than or equal to 0.05 for all maps.

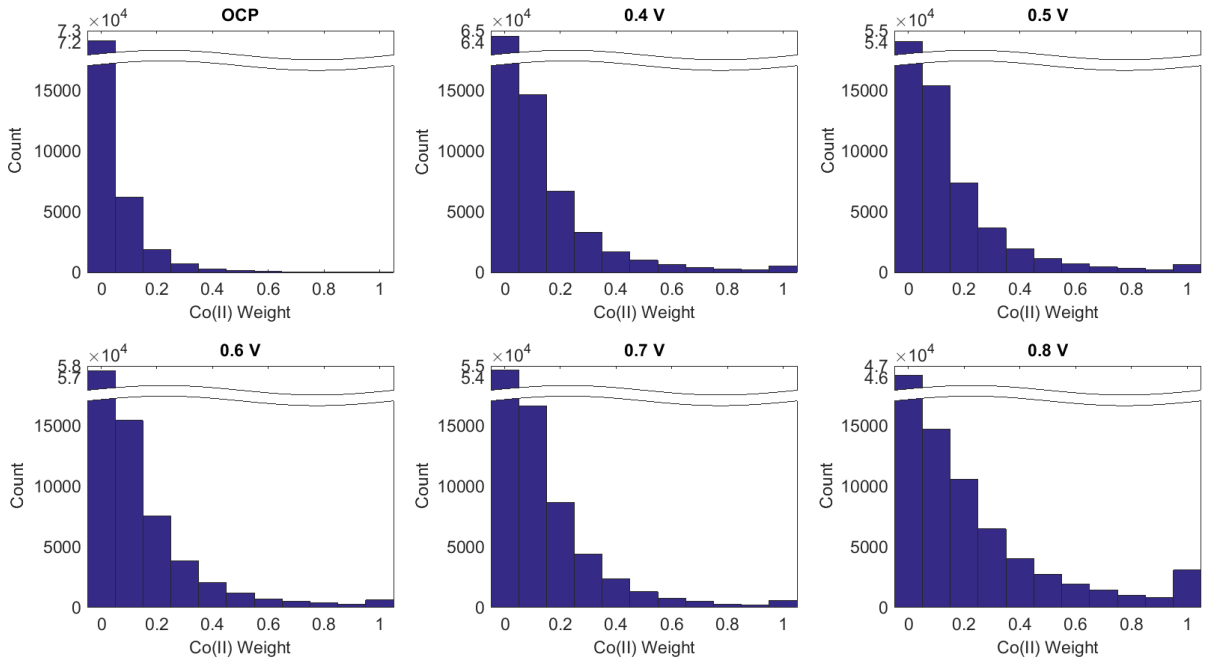


Fig. 6.14 Histograms of the frequency of Co(II) composition fraction (fitting weight) after the LCF of all sample spectra at the different applied potential. Bin size = 0.1. The increase in the frequency of high Co(II) fraction values is noted as potential increases, particularly at 0.8 V.

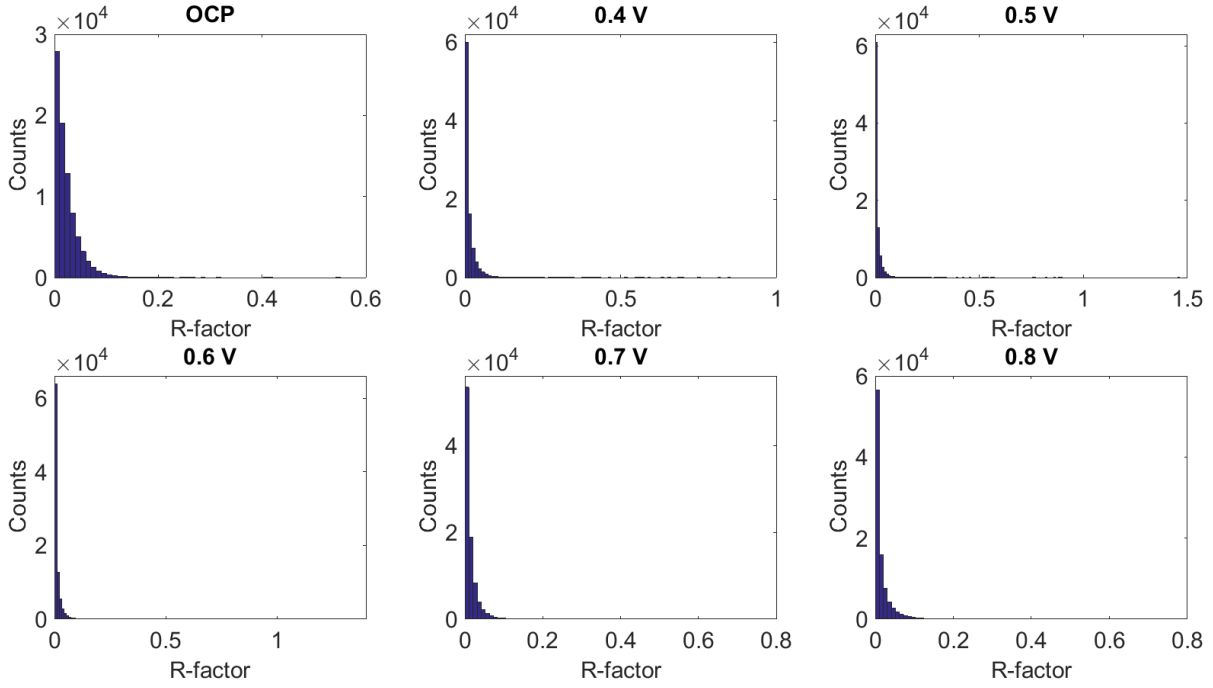


Fig. 6.15 Histograms of the frequency of R-factor values of all sample spectra fits at each applied potential. Bin size = 0.01. In each case, 95 % of values remained less than 0.05.

The egress of diffuse material from the particle was observed in TXM images during the 800 mV step as shown in figure 6.16. A similar release of material was previously observed during the *in situ* microscopy measurements discussed in chapter 5, section 5.3.3. This release of material from particles (observed here and in chapter 5) has always been observed across the whole particles' surfaces. On the other hand, the speciation maps (figure 6.13)

indicated the highest concentrations of Co(II) along the edges of the particle. This could be explained by the thickness effect of the particle whereby a certain amount of Co(II) would represent higher composition fractions in thinner regions. It is noted, from the TXM images of the particle (figure 6.16), that the edge regions of the particle have lower absorbance intensity compared to the particle's core. The speciation maps are a representation of the distribution of Co(II):Co ratio across three-dimensional pixels (*i.e.* voxels). Hence, even if Co(II) was to form uniformly across the particle's surface, its fraction will be larger in thinner voxels.

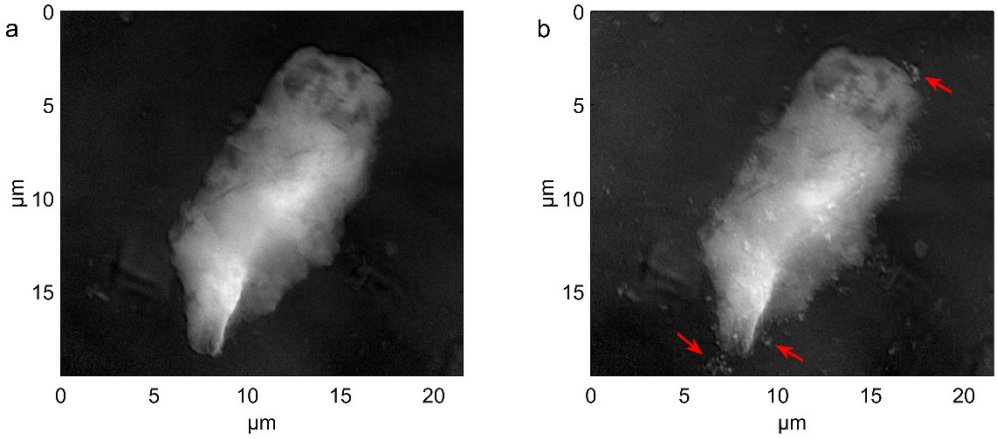


Fig. 6.16 TXM images (at isosbestic X-ray energy 7788 eV) (a) before and (b) during the 0.8 V applied potential step, showing the egress of diffuse material from the particle.

6.3.2 Tracing the Transient Cr(VI)

The standard XAS spectra for Cr metal, Cr(III), and Cr(VI), as obtained from Cr foil, 10 wt.% $CrCl_3$ in boron nitride, and 10 wt.% $Na_2Cr_2O_7$ in boron nitride respectively, are shown in figure 6.17. The Cr(VI) absorption pre-edge peak energy was determined to be 5993.25 eV as indicated in figure 6.17 (referred to as E1 from here onwards).

6.3.2.1 Detecting Cr Dissolution by TXM-XAS

Initially, studies were conducted using TXM-XAS at Beamline 6-2, SSRL. Successive TXM images of CoCrMo samples were recorded (at E1 with an exposure time (detection time) of 2 s) while, simultaneously, the electrochemical potential was applied from 400 mV to 800 mV in steps of 100 mV for 600 s per step. After every three successive images were recorded, a *reference* image of the incident photon flux I_0 was recorded. Generally, each three-image group was reference corrected (*i.e.* normalised by incident intensity I_0, as per the absorbance calculation in equation 6.1), using the corresponding subsequently recorded reference image. Figure 6.18(a) shows the variation of absorbance intensity recorded from CoCrMo 160 nm TFs as a function of time and potential. The time gap between each three data points corresponds to the time taken to obtain the I_0 image; this includes changing the cell alignment with reference to the X-ray beam so that the beam travels through the *reference* window (for the I_0 image), and aligning back to the *sample* window. Minor increase in the absorbance intensity could be

observed during both the 0.7 V and 0.8 V. The mean intensity recorded at each potential step was calculated and shown in figure 6.18(b). The significance of the difference between the mean intensities at each potential step was calculated by means of a t-test. The mean intensities at 0.7 V and 0.8 V were found to be significantly different from the mean intensity at 0.6 V and 0.7 V respectively. However, to improve the signal to noise to ratio the study would be conducted using conventional XAS with a large beam size to enhance sensitivity to capturing the release of Cr(VI) species.

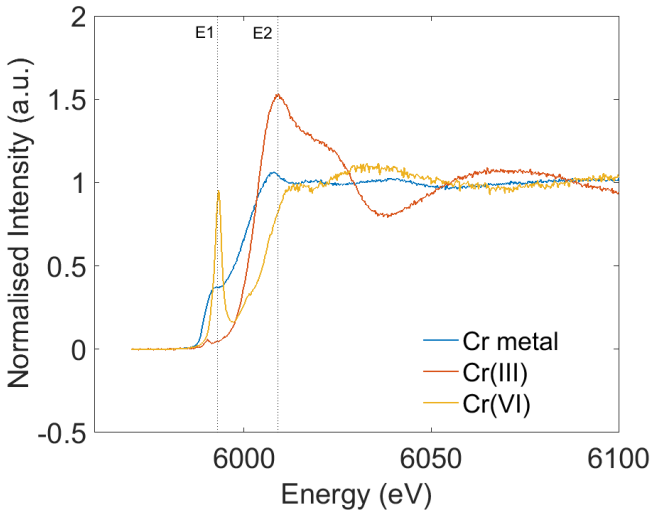


Fig. 6.17 Standard XAS spectra of Cr metal, obtained from a Cr foil, Cr(III), and Cr(VI), as obtained from boron nitride pellets containing 10 wt.% of $CrCl_3$ and $Na_2Cr_2O_7$ respectively.

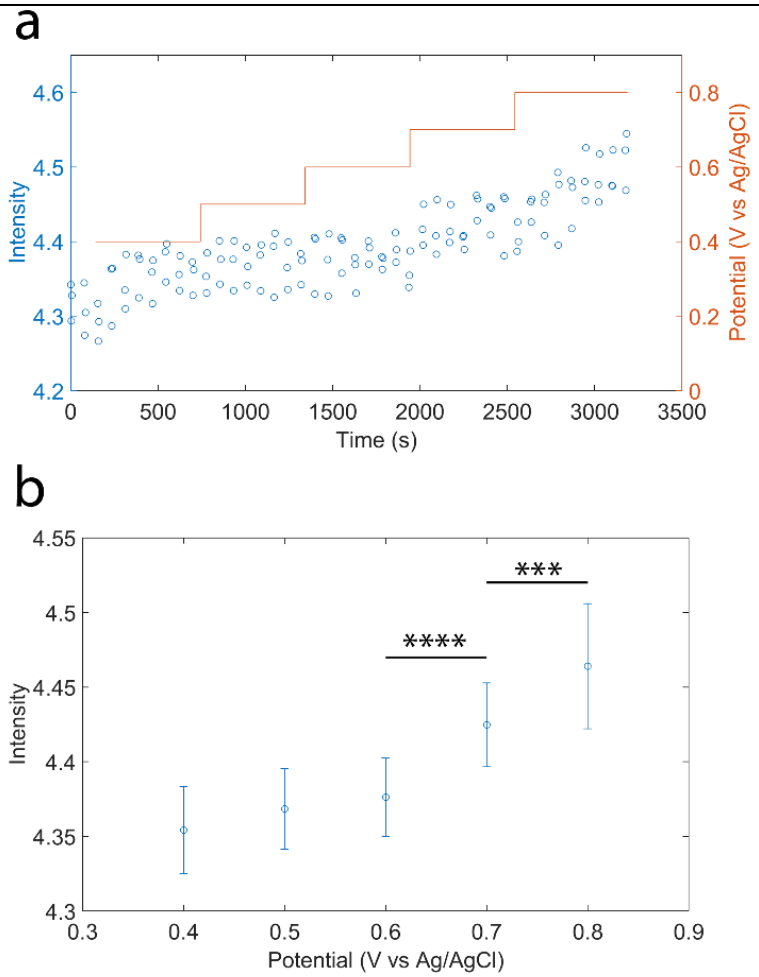


Fig. 6.18 In situ absorbance intensity from CoCrMo TF as a function of time and potential recorded at Cr(VI) pre-edge energy (E1) at the SSRL TXM beamline 6-2. (a) Scatter plot of absorbance intensity of CoCrMo thin-film at the Cr(VI) pre-edge peak energy (E1) while electrical potential (red plot) was applied in steps from 0.4 V to 0.8 V. A small increase in the absorbance intensity is observed at the 0.7 V and 0.8 V steps. (b) The average absorbance intensity from (a) at each potential step. Error bars represent standard deviation. The differences in intensity between 0.6 V and 0.7 V, as well as 0.7 V and 0.8 V, are statistically significant with p<0.0001 (indicated by 4 asterisks) and p<0.001 (indicated by 3 asterisks) respectively.

6.3.2.2 Detecting Cr Dissolution by Population-Averaged XAS

At Beamline 4-3, SSRL, measurements were conducted in fluorescence geometry with a large X-ray beam with a size of 1 mm x 9 mm. Fluorescence intensity was recorded, as a function of time, with a 0.33 s temporal resolution, at both the Cr(VI) pre-edge peak energy 5993.25 eV (E1) as well as just above the absorption edge of Cr species at an energy of 6009 eV (E2, as indicated in figure 6.17). An electrochemical potential regime was simultaneously applied as follows: five minutes in OCP condition, followed by 100 mV potential steps from 400 mV to 800 mV for 900 s each, and finally a further 20 minutes at OCP condition.

Figure 6.19 shows the fluorescence intensity as a function of time and potential at E1 (Cr(VI) pre-edge peak) recorded from an 80 nm TF sample. An increase in the intensity signal, corresponding to the detection of Cr dissolution into the electrolyte, is observed during the 0.8 V step (the onset of intensity increase observed at 0.7 V). However, the increase in the fluorescence intensity signal was found to be approximately ten times higher at

E2 compared to E1 as shown in figure 6.20. This observation suggests that the detected dissolved species is Cr(III) rather than Cr(VI). The absorption intensity of Cr(VI) at E1 and E2 is approximately equal as could be deduced from the standard spectrum in figure 6.21. Consequently, the minor intensity rise detected at E1 from the TFs reported here is likely due to the small pre-edge shoulder of Cr(III) absorption rather than the pre-edge peak of Cr(VI) (see figure 6.21). The signal intensity observed in the time-scans (figures 6.19 and 6.20) after the end of the polarisation (at OCP in the final 20 minutes) remained largely constant. This could be a further indication that the detected Cr species was Cr(III); because a signal from Cr(VI) species would be expected to decrease after the end of the polarisation (due to the transient nature of Cr(VI) which gets reduced to Cr(III)).

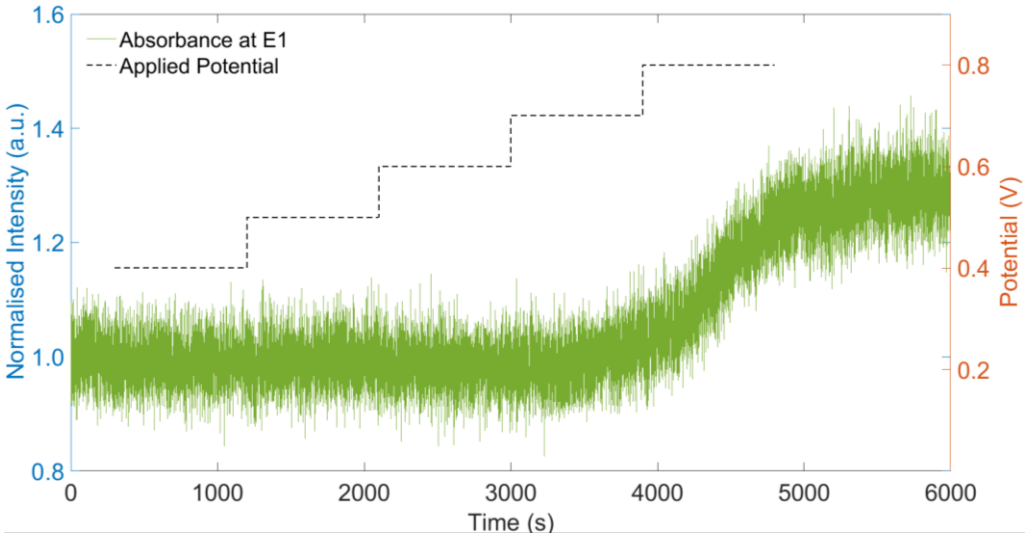


Fig. 6.19 In situ absorbance intensity as a function of time and potential recorded at the Cr(VI) pre-edge energy point (E1) at the SSRL conventional XAS beamline 4-3. An onset of absorbance intensity increase is observed at 0.7 V and continuous increase during 0.8 V. After the end of 0.8 V, when the system is at OCP, the absorbance intensity remains constant for the 20 minutes of recording.

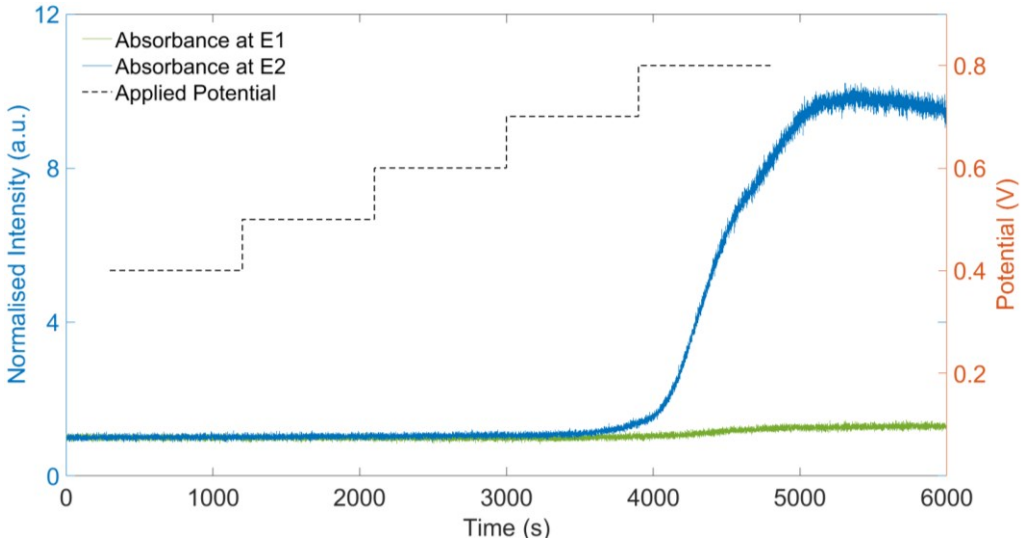


Fig. 6.20 In situ absorbance intensity as a function of time and potential at both the Cr(VI) pre-edge energy point 5993.25 eV (E1) and 6009 eV (E2) showing greater increase in the absorbance intensity signal at E2 suggesting that the detected signal is likely Cr(III) species rather than Cr(VI). The system was at OCP at the end of the 0.8 V step.

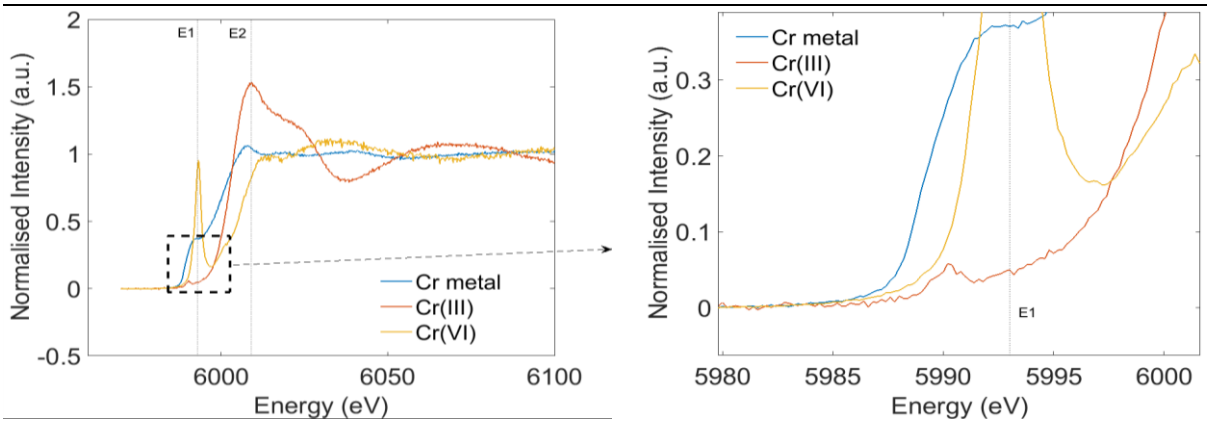


Fig. 6.21 Standard Cr metal, Cr(III), and Cr(VI) X-ray absorption spectra with a magnified view of the pre-edge region showing the pre-edge shoulder characteristic of Cr(III).

Thus, the data suggest that the detected dissolved species is Cr(III). However, the potentials at which dissolution was detected were in the transpassive region where Cr(VI) is known to be produced. This result reveals the extremely transient nature of Cr(VI) in this environment and its 'instant' reduction to Cr(III). This instant reduction of Cr(VI) is likely related to its rapid diffusion away from the electrode surface (the oxidising environment). However, this extremely transient nature of Cr(VI) evolution may not be the case under *in vivo* conditions as the reduction would be related to diffusion away from the inflammatory environment. In fact, Cr(VI) species were recently detected in diabetic patients' tissue samples.[187] It was hypothesised that Cr(VI) remained stable in those samples due to the increased oxidative stress associated with diabetes (as discussed in section 2.5.2).

Figure 6.22 compares the fluorescence intensity, as a function of time and potential, at E2 detected from CoCrMo particles and 80 nm TF in both SBF and serum-SBF. The observed increase in intensity in the case of the TF was noticeably larger than that observed from the particles, illustrating the larger concentration of analyte attainable in the case of sputtered TF compared to a population of drop cast particles.

The presence of protein reduced the detected increase in absorbance intensity from both TF and particles, thus indicating a reduced Cr dissolution. Generally, in this work, the presence of protein has consistently inhibited metal dissolution. Proteins restrained Co dissolution as was evident by *in situ* X-ray spectroscopy on a population of CoCrMo particles (chapter 5, section 5.3.2), and by reduced nanoporosity on the surfaces of TFs, *bulk* (chapter 4, section 4.3.4), and particles (chapter 5, section 5.3.4). However, it is noted that these observations are in contrast to the enhanced dissolution of Mo, in the presence of protein, as observed recently in the literature.[102,132]

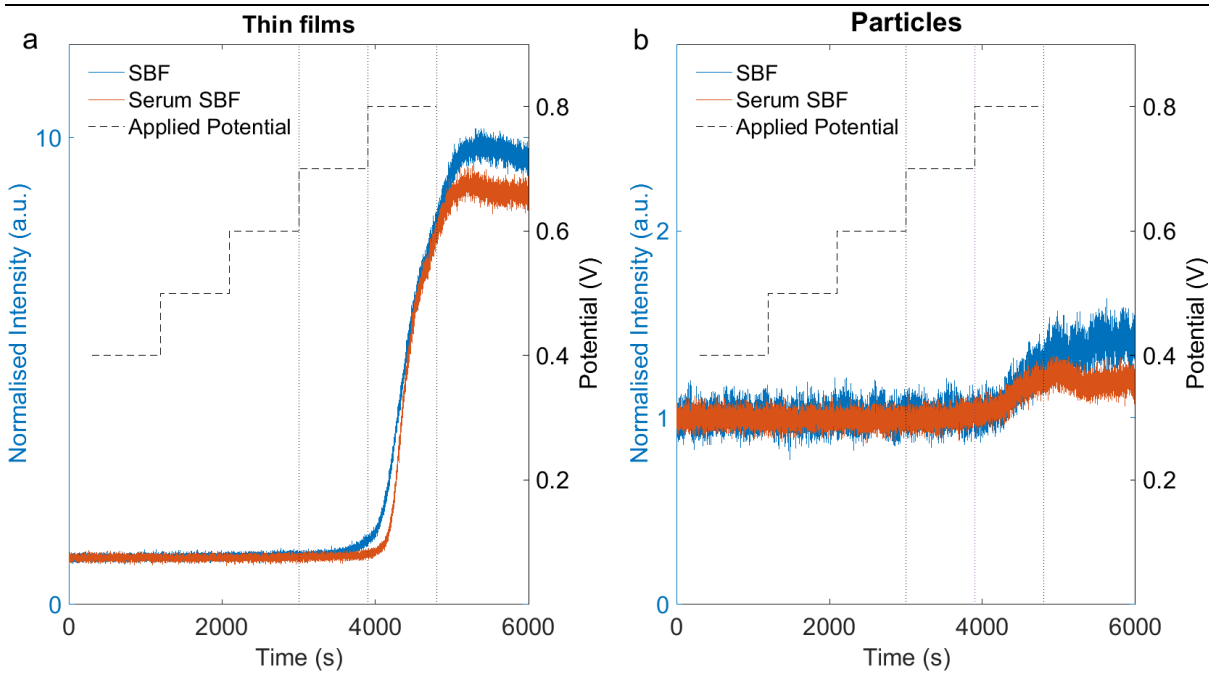


Fig. 6.22 In situ absorbance intensity (at E2) as a function of time and potential. A comparison of detected dissolution in SBF and Serum SBF from CoCrMo TF samples (a), and CoCrMo particles samples (b). The results indicate less detected dissolution in the presence of serum. The system was at OCP at the end of the 0.8 V step.

Overall, the increase in measured fluorescence intensity after transpassive polarisation marked the onset of Cr dissolution into the electrolyte. This is consistent with the onset of Cr loss observed during *in situ* measurements of Cr content in a population of particles reported in the study in chapter 5, section 5.3.2. Apart from a focus on the speciation of the dissolved Cr species examined here in this chapter, another difference between the two studies was the measurement geometry. Here, the sample window was fitted in the electrochemical cell downstream of the X-ray beam. The X-ray path was sufficiently large to ensure fluorescence signal was obtained from the electrolyte only. Thus, dissolution measurements are made based on the rise of Cr content in the electrolyte. However, in the earlier study reported in chapter 5, the sample window was fitted upstream of the X-ray beam and hence the signal was continuously obtained from the sample (the CoCrMo particles). Dissolution measurements were then made based on the loss of Cr content from the particles and its diffusion into the electrolyte away from the X-ray path. The results of both studies remained consistent revealing an onset of Cr dissolution above 700 mV polarisation. Moreover, the onset of Cr dissolution is consistent with the increase in Co dissolution kinetics as noticed in the Co speciation maps reported here in section 6.3.1.2. This is a direct illustration that the non-stoichiometric dissolution of the CoCrMo alloys is prompted by transpassive polarisation conditions; whereby a rapid increase in Co dissolution kinetics is facilitated by the perturbation of the alloy's Cr-rich passive film.

XANES spectra were recorded at the following conditions: i) dry cells (prior to the addition of the SBF electrolyte, thus representing the signal of the sample's original state), ii) wet cells at OCP (immediately after adding the electrolyte, representing the signal of the electrolyte only, prior to any applied potentials), iii) wet cell after the potential steps were applied (*i.e.* signal of electrolyte after electrochemical polarisation), and finally iv) the samples

were detached from the cells and XANES spectra of the dry samples after polarisation were recorded. All measurements were acquired in both SBF and serum SBF to study the effect of proteins. The XANES spectra (figure 6.23) show a signal corresponding to that of metallic Cr in TF dry cells (figure 6.23(a)) and no absorption signal after adding the electrolytes at open circuit condition (figure 6.23(c)). Therefore, this reveals no detectable dissolution of Cr at OCP and confirms that measurements in wet cell conditions are not sensitive to signal from the sample (which would have contributed a Cr metal signal). The XANES spectra collected after electrochemical polarisation reveal a Cr(III) signal from the electrolytes (figure 6.23(d)), and a 'mixed' XANES spectra from TFs (figure 6.23(b)) suggesting the presence of solid oxidised Cr deposits on the TF surfaces. These 'mixed' XANES of the post-polarisation TFs were fitted using a linear combination of the corresponding TF dry cell (representing the original state of the TF) and the post-polarisation signal from the relevant electrolyte (representing the oxidised species resulting from the polarisation of the TF). The fit results and weights are illustrated graphically in figure 6.24. Additionally, the fitting weights and R-factor are given in table 6.2. The fitting results indicate a greater percentage of oxidised species on the TF which reacted in SBF compared to the one reacted in Serum SBF; therefore, supporting suggestions that the presence of protein restricts the Cr reactivity. This comes in agreement with the results observed by fluorescence intensity time-scans (figure 6.22).

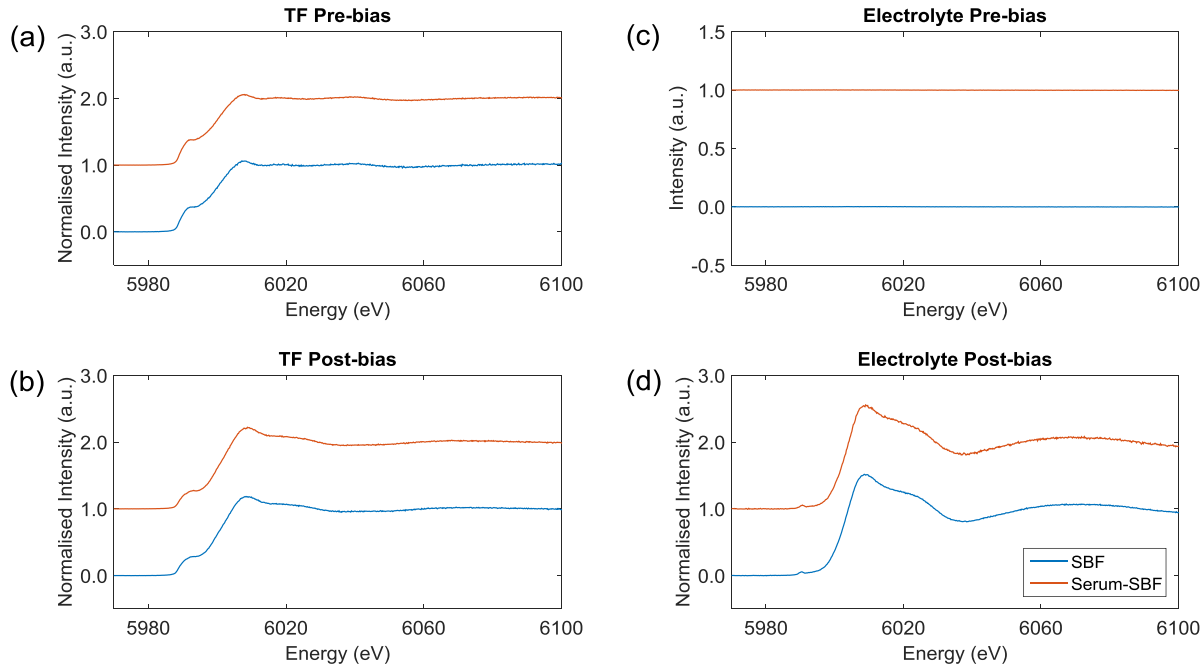


Fig. 6.23 XAS spectra of TF and electrolyte before and after potential application in both the SBF (blue) and Serum SBF (red).

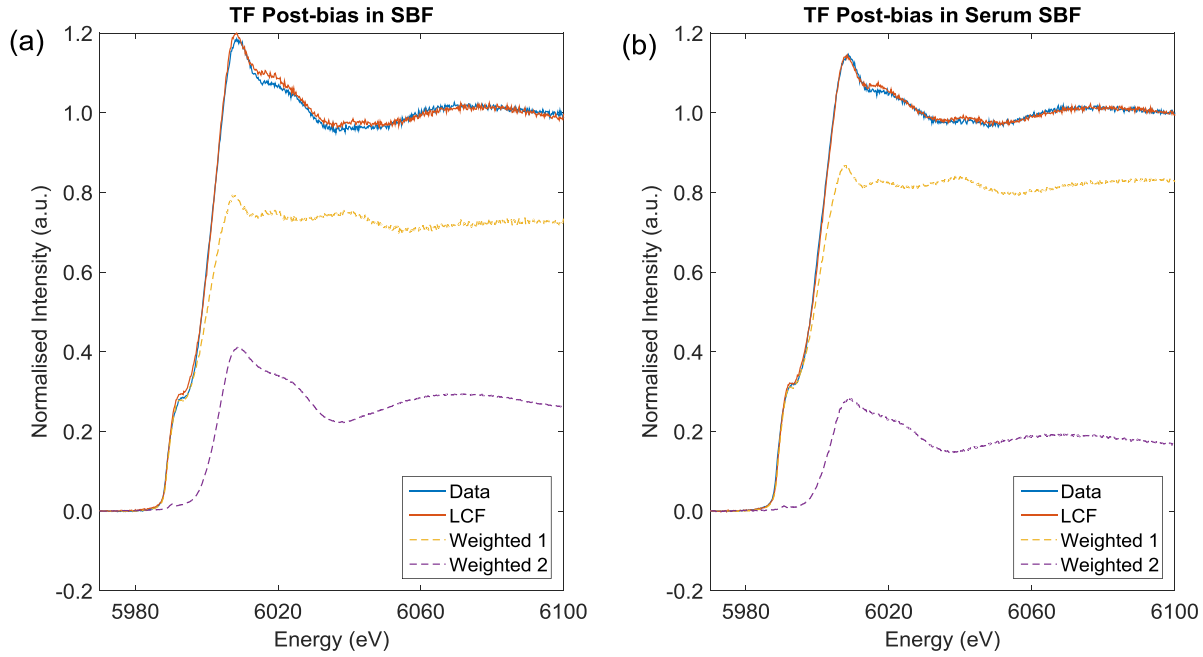


Fig. 6.24 XAS spectra of TF biased in SBF (a) and serum SBF (b) overlaid with fit results obtained by a linear combination of the TF pre-bias (original TF state, Weighted 1) and electrolyte post-bias (oxidised species, Weighted 2) spectra. The data shows a greater ratio of oxidised Cr (Weighted 2) on the surface of the TF biased in SBF compared to Serum SBF.

Table 6.2 LCF parameters for both TF biased in SBF and Serum SBF

	TF pre-bias	**Electrolyte post-bias**	**R-factor**
TF biased in SBF	0.725	0.275	0.000825
TF biased in Serum SBF	0.821	0.179	0.000369

6.3.3 *Ex situ* Co and Cr Speciation

Co and Cr speciation maps of 160 nm TFs had been obtained *ex situ* using X-ray fluorescence microscopy. Speciation maps were obtained of both as received and polarised (0.8 V in SBF for 30 minutes) films. X-ray fluorescence microscopy images were acquired at beamline 3-ID, NSLS-II, using an X-ray nanoprobe beam as described in chapter 4, section 4.2. For Co speciation, XFM images were collected at the same X-ray energies discussed in this chapter in section 6.3.1.2. Figure 6.25 shows XFM images of AR and polarised TFs at the selected post-Co-edge energies. Co speciation maps from two sites in each of the AR and polarised films are shown in figure 6.26. The results indicated an increase in Co(II) content from 1.6 % and 1.7 %, in the AR film, to 17.7 % and 5.8 % in the polarised films.

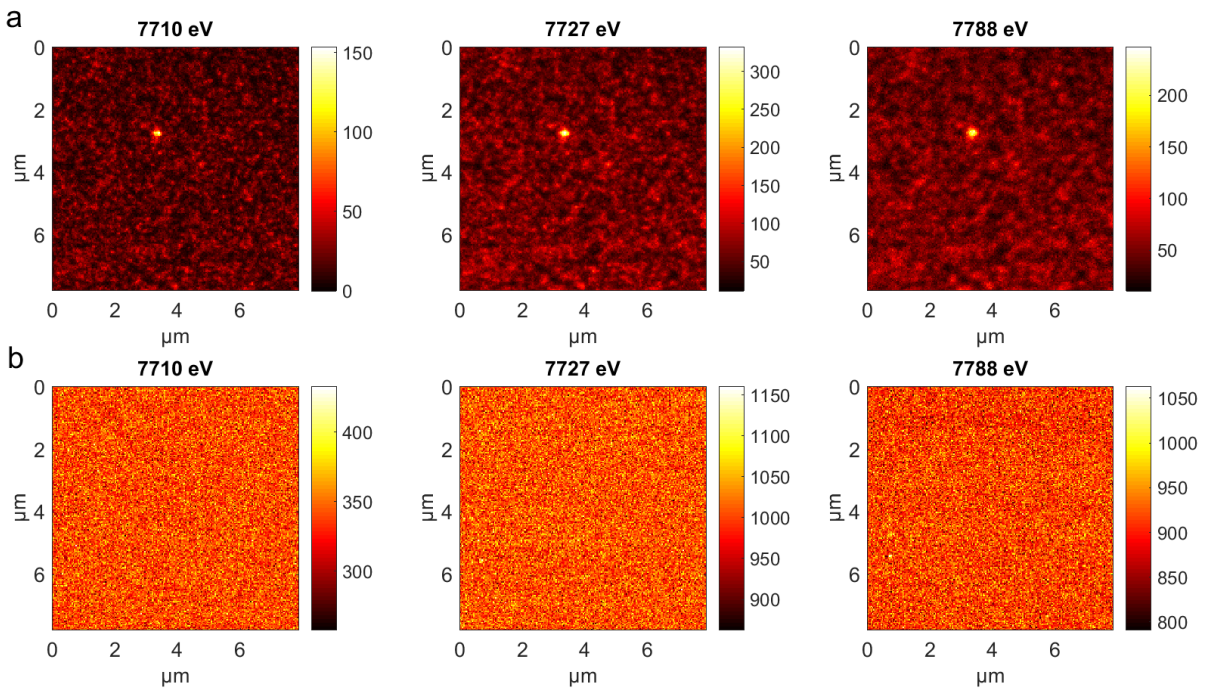


Fig. 6.25 XFM images of Co from (a) polarised, and (b) AR, CoCrMo TFs at the three selected energy points for speciation analysis. Colour bars indicate absorbance intensity (a.u.).

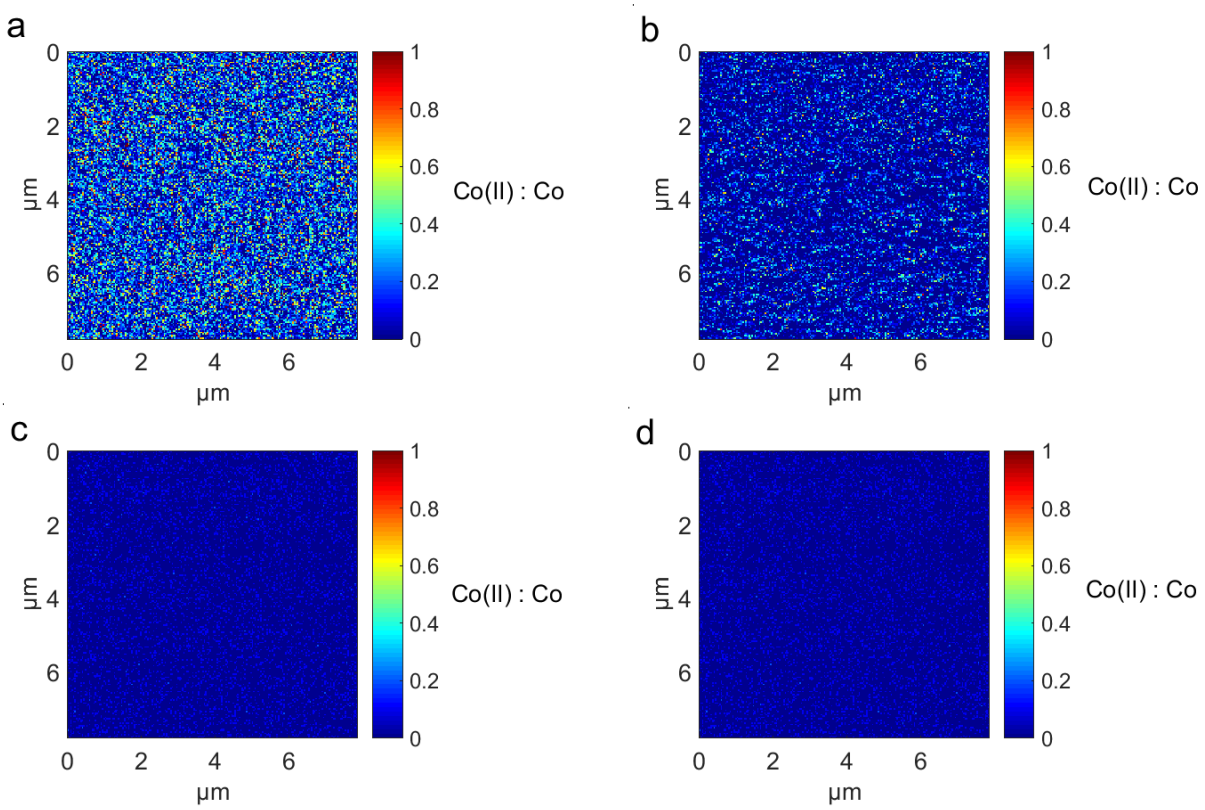


Fig. 6.26 Speciation maps representing the distribution of Co(II) composition fraction in (a-b) polarised, and (c-d) AR CoCrMo TFs. The overall Co(II) % was (a) 17.7 %, (b) 5.8 %, (c) 1.6 %, and (d) 1.7 %.

For Cr speciation, XFM images were collected at X-ray energies of 5992, 5993, 6009, 6038, and 6088 eV as indicated in figure 6.27. Figure 6.28 shows XFM images of AR and polarised TFs at selected post-Cr-edge energies. Cr speciation maps were obtained through the linear combination fitting using Cr metal and Cr(III) standards. Cr speciation maps from two sites in each of the AR and polarised films are shown in figure 6.29. The results revealed an increase in Cr(III) content from 30.3 % and 28.9 %, in the AR film, to 78.6 % and 83.8 % in the polarised film.

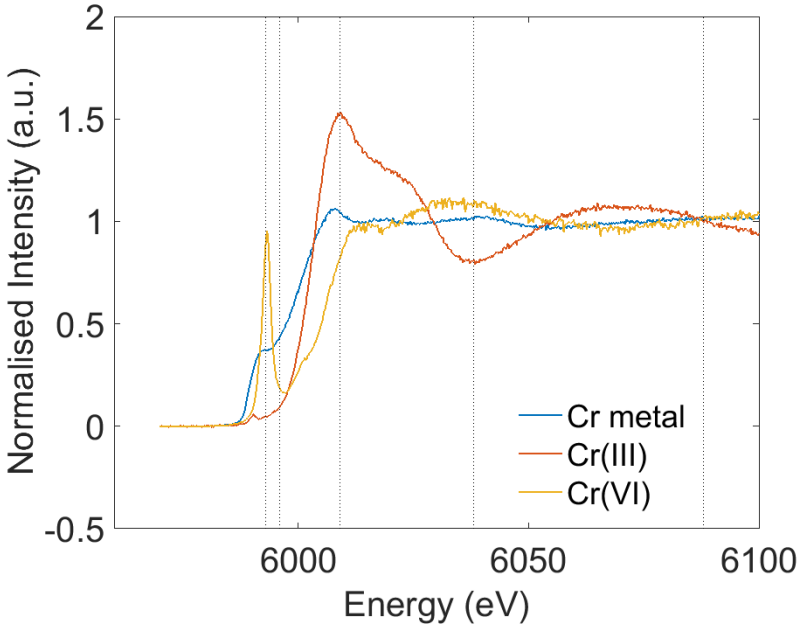


Fig. 6.27 Standard XAS spectra of Cr metal, obtained from a Cr foil, Cr(III), and Cr(VI), as obtained from boron nitride pellets containing 10 wt.% of $CrCl_3$ and $Na_2Cr_2O_7$ respectively. The vertical dotted lines indicate the energy points selected for speciation analysis

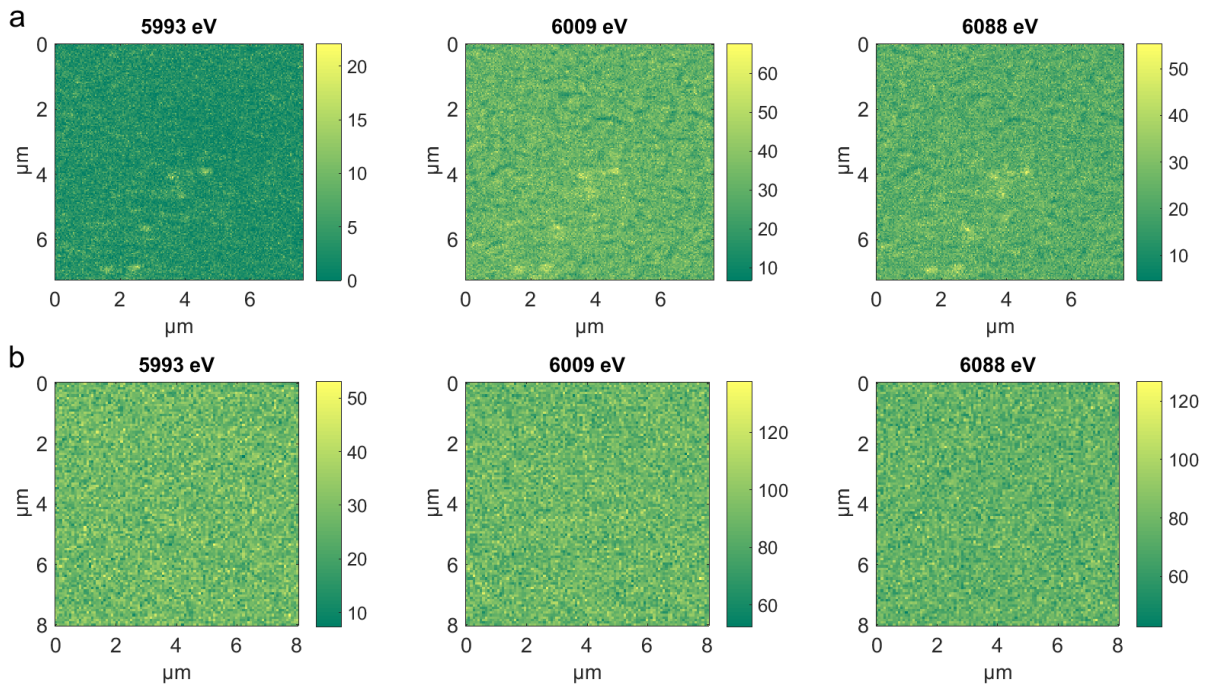


Fig. 6.28 XFM images of Cr from (a) polarised, and (b) AR, CoCrMo TFs at three of the selected energy points for speciation analysis. Colour bars indicate absorbance intensity (a.u.).Colour bars indicate absorbance intensity (a.u.)

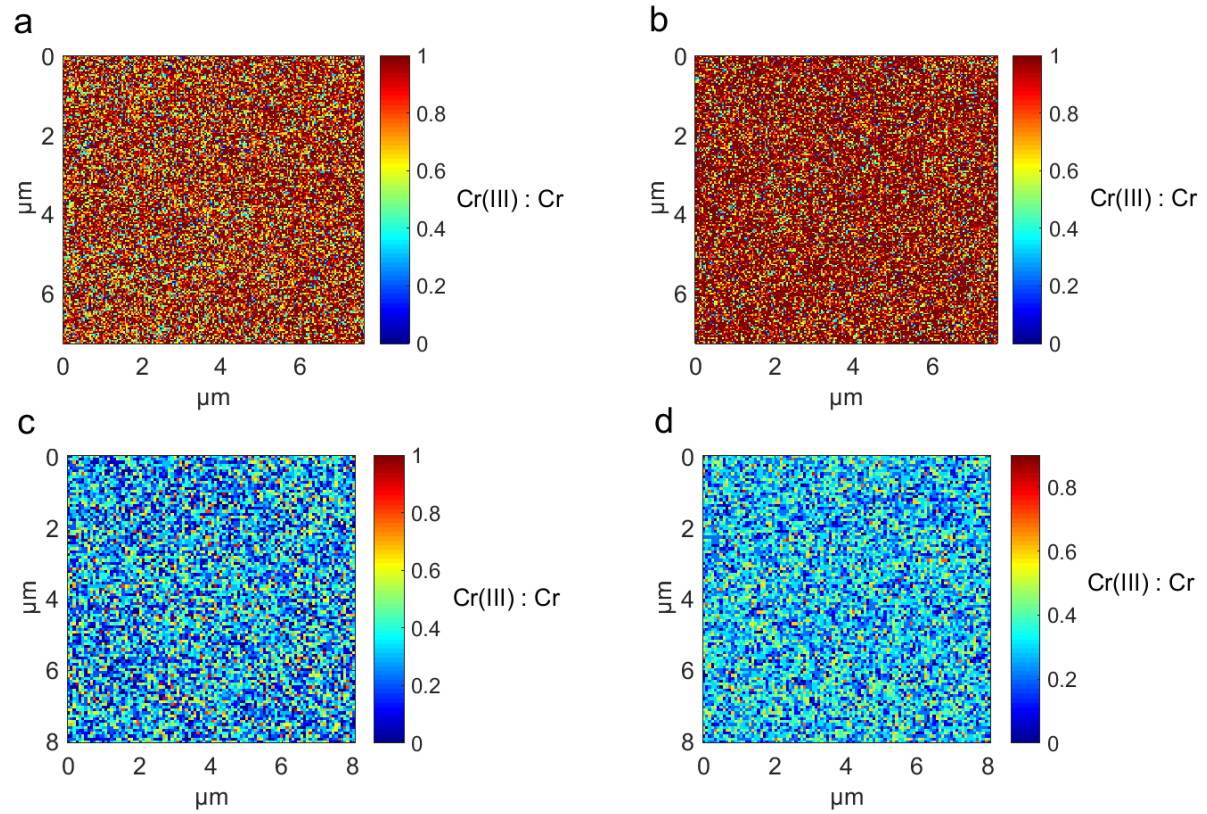


Fig. 6.29 Speciation maps representing the distribution of Cr(III) composition fraction in (a-b) polarised, and (c-d) AR CoCrMo TFs. The overall Cr(III) % was (a) 78.6 %, (b) 83.8 %, (c) 30.3 %, and (d) 28.8 %.

6.4 Summary

In situ TXM-XAS offered a powerful spectromicroscopy technique which enabled the measurement of spatially resolved chemical changes. Co speciation was mapped in CoCrMo particles dynamically as a function of applied electrochemical potential. The speciation mapping was obtained through fitting sample spectra with a linear combination of standard spectra. The accuracy of the spectral fitting process was virtually unaffected when using a total of six X-ray energy points compared to 101 points. This was demonstrated by the similar distribution of R-factor values, which were used to assess the goodness of fit, in both cases. Therefore, reducing the number of X-ray energy points enabled significant improvements in the temporal resolution of the process, without significant losses in the accuracy of the speciation analysis. Limited Co dissolution was observed at OCP and applied passive potentials compared to transpassive potentials. The increase in Co dissolution observed at 700 mV and 800 mV coincided with the onset of Cr dissolution at the same potentials. Therefore, the results demonstrate the increase in Co dissolution after the breakdown of the Cr-rich passive film at transpassive potentials.

Cr dissolution was initially detected using TXM-XAS from a CoCrMo TF sample. There was no dissolution signal detected from CoCrMo particles due to the low signal to noise ratio when using the micro-focused beam of TXM-XAS. The low signal to noise ratio and the need for using the featureless and uniform TF samples led to trading off spatial information for stronger signals using conventional, large-beam, XAS. In contrast to Co, no detectable Cr dissolution was observed at OCP or lower (passive) applied potentials. By monitoring the fluorescence signal from dissolved Cr species, as a function of time and potential, at two distinctive X-ray energies, the detected species was established to be Cr(III). This suggested that Cr(VI) is extremely transient in the conditions used here. However, this transient nature observed here is related to rapid diffusion away from the electrode surface, while in the case of Cr(VI) production *in vivo*, its subsequent reduction would be dependent on diffusion away from inflammatory conditions.

Although *ex situ* speciation mapping of both Co and Cr in CoCrMo TFs does not reveal spatial features (but a rather uniform speciation distribution), the results suggested that the composition of TFs polarised at 0.8 V may be analogous to that observed in periprosthetic CoCrMo implant wear debris (*i.e.* majorly Cr(III) species with only trace amount of Co).

In conclusion, the results showed a continuous dissolution of Co from CoCrMo particle, which dramatically increased in the transpassive regime. The results suggest that the *in vivo* dissolution of CoCrMo wear debris is an autocatalytic process, where extensive dissolution is only observed in strongly oxidising conditions, likely triggered by the inflammatory response to the particle. Although the initial dissolution of Co is small, given the large number of wear particles produced *in vivo*, this dissolution could activate the immune system response. The subsequent production of peroxy-like radicals leads to an increasingly oxidising environment and accelerated dissolution.

7 Conclusions and Future Work

The unexpected high failure rate of CoCrMo-based MOM implants steered extensive research on the behaviour of the alloy through both *in vivo* and *in vitro* studies. It was established that the most common reason for revision surgeries, and hence the failure of the implants, was the body's severe inflammatory response to CoCrMo wear debris. Despite the strong wear resistance of the alloy evident by its relatively low volumetric wear, large *numbers* of small wear particles were still produced *in vivo*. Additionally, despite nominally being a stable material with a strong Cr-rich passive film, chemical speciation studies on periprosthetic wear debris suggested a large extent of Co dissolution. The mechanism of this dissolution was unknown and in particular, its implication on Cr speciation has been a subject of concern. The aim of the present work was to elucidate the dissolution mechanism which leads to these implants' failure, and to determine whether or not Cr(VI) species are potentially produced *in vivo*. The studies involved the development of a correlative approach to examine both morphological and chemical changes to CoCrMo particles in a simulated biological environment. Furthermore*, in situ* approaches were developed based on synchrotron radiation studies, in order to follow the dissolution behaviour of the alloy as a function of both time and applied electrochemical potential.

In chapter 4, the electrochemical behaviour of CoCrMo was studied both in *bulk* discs and TFs form. Furthermore, *ex situ* analysis of surface morphology and elemental composition ratio were examined after exposure to the simulated biological environment by SEM and EDX. Interestingly, two different morphologies were observed on the *bulk* discs after transpassive polarisation. The inclusions had an advanced bi-continuous morphology compared to only surface nanoporosity in the surrounding matrix. This suggested that the process of dealloying was accelerated in inclusion sites, despite the higher percentage of Cr present in these regions. Further investigation is required to elucidate the mechanism behind an accelerated non-stoichiometric dissolution in inclusion sites. Possible galvanic coupling between inclusion sites and surrounding matrix could result in different rates of dissolution as both phases could be under a different overpotential during polarisation.

Chapter 5 focused on the morphological and chemical changes in CoCrMo particles revealing surface and subsurface morphology utilising FIB-SEM sectioning and TEM tomography. In addition, *in situ* studies (at synchrotron facilities) of morphological and chemical changes as a function of time and potential were introduced: firstly absolute Co and Cr content in a population of CoCrMo particles were monitored *via* XAS, and secondly *in situ* morphological development during particles' dissolution was revealed using TXM. This was the first time that a TXM based approach was used to follow local dissolution behaviour. However, TXM imaging of this dissolution was only performed above the Co-edge. In the future, following this dissolution at the Cr-edge could reveal further insights such as whether or not the observed released diffuse material contained any Cr content, or if Cr dissolution

occurs at a different onset potential. Subsequently, these results could be correlated with the *in situ* spectroscopy results.

In Chapter 6, a simultaneous combination of microscopy and spectroscopy, using TXM-XAS, enabled the spatially-resolved study of Co speciation *in situ*. Furthermore, an XAS-based study was developed to detect Cr dissolution, identify its chemical speciation and measure the kinetics of Cr(VI) reduction back to Cr(III).

Taken together, the data consistently showed the preferential dissolution of Co from CoCrMo discs, TFs, and particles in transpassive conditions. This was evident through the drop in the relative Co:Cr at. % composition ratio, the larger drop in absolute Co amounts measured dynamically *in situ* compared to Cr, and the development of nanoporosity on CoCrMo surfaces. These observations revealed the dissolution of CoCrMo through a dealloying mechanism, however, this did not occur at lower (passive) electrochemical potentials. It is strongly evident that the dealloying process requires the breakdown of the passive film through the transpassive oxidation of Cr(III) into soluble Cr(VI). During passive conditions, Co dissolution is restricted, possibly only to surface layers in contact with the electrolyte, as the passive film protects the alloy against further dissolution. However, after the transpassive breakdown of the alloy's surface film, the Co oxidation reaction to Co(II) is under a large overpotential and hence proceeds at a faster rate compared to Cr oxidation. Elemental distribution and speciation maps on TFs, which had been polarised at a transpassive potential, revealed the scarcity of Co and that Cr existed predominately as Cr(III) species. This composition is analogous to that of periprosthetic CoCrMo wear particles. Overall, it is believed that the large-scale Co dissolution observed in particles from the periprosthetic tissue is due to transpassive conditions being imposed *in vivo.* The dissolution of these particles is potentially an autocatalytic process; where the initially limited Co dissolution from a large *number* of wear particles may provoke the inflammatory immune response, which in turn leads to rise in local electrochemical potential and increase dissolution. Although transpassive dissolution is facilitated by the oxidation of Cr(III), from the passive film to Cr(VI); only dissolved Cr(III) species were detected *in situ* using high temporal and chemical resolution X-ray spectroscopy measurements. This revealed the extremely transient nature of Cr(VI) species in the simulated biological fluid which was instantly reduced back to Cr(III).

The effect of protein on the dissolution behaviour of CoCrMo has been a subject of debate; with theories suggesting that protein could either form a protective adsorbed film on the alloy surface or enhance dissolution through the formation of protein-metal complexes. However, these discrepancies may be related to differences in surface and solution properties which affect protein adsorption on the surface. Furthermore, the formation and detachment of metal-protein complexes is a relatively slow process and hence enhanced metal dissolution in the presence of protein may only be observed after prolonged periods. The present work consistently indicated a restricted Co dissolution in the presence of proteins. This was evident through reduced drops in X-ray fluorescence intensity (proportional to Co amount) during *in situ* polarisation of CoCrMo particles, and inhibited surface nanoporosity.

Additionally, X-ray spectroscopy indicated the reduced Cr dissolution in the presence of protein. However, proteins inhibit the dissolution of Co more than Cr as the relative Co:Cr at. % (measured by EDX) were consistently higher after polarisation in serum-SBF compared to polarisation in SBF. In the future, the stability of this positive effect of protein on CoCrMo dissolution should be examined through longer studies. Enhanced metal dissolution, in the presence of proteins, from a titanium-aluminium-vanadium alloy was only observed after 24 hours;[135] whether or not a similar trend would be observed in CoCrMo alloys remains unanswered.

CoCrMo alloys obtained regulatory approval based on volumetric wear examinations and general electrochemical behaviour. However, the behaviour of the material under the associated *in vivo* inflammatory conditions was not considered suggesting that these examinations were insufficiently discriminating.

The knowledge learnt from the failure of MOM implants was developed through multidisciplinary collaborations between surgeons, engineers, and scientists. The continuation of multidisciplinary research is essential for the development of future safe biomedical implants. Furthermore, new regulatory testing protocols must be developed for the assessment of future implant materials. Evaluation of wear resistance should not solely depend on measurements of volumetric wear. Characterisation of wear particles, from any future implant materials, is essential. Additionally, the general biocompatibility of the material is not sufficient, but the biological effects of wear in the human environment must also be evaluated. In general, wear particles are a common reason for the failure of MOM and MOP implants, albeit through different mechanisms and timescales. Therefore, for future materials, considerable emphasis must be directed towards reducing the release of wear-particles and evaluating their biological effects.

8 Appendix A: TXM-XAS Simulation

8.1 Introduction

This appendix covers the simulation study which was designed to evaluate the quantification process of elemental chemical speciation based on TXM-XAS measurements. In particular, the aim was to study the effect of reducing the number of energy points used for quantifying the Co(II) content of a *structure* of a known composition. Two structures of known Co metal to Co(II) composition fractions, with an added noise profile, were designed and the Co(II) contents were quantified using a different set of energy points. The quantification is based on identifying the Co(II) fraction in each region (pixel) in the structures through the fitting of XAS data spectra of each region with the linear combination of the standard spectra. The process is discussed in full details in chapter 6, section 6.2.1.

8.2 Simulated Structure Design

Two simulated structures were designed and consisted of concentric square shapes, with a different Co:Co(II) composition ratio each. The structures were constructed by assigning absorbance values to the individual image elements (pixels) based on the weighted summation of Co and Co(II) standard spectra. Design *A*, consisted of five squares with a core square composed purely of metallic Co and the outer (bordering) squares contained 30 %, 50 %, 70 %, and 100 % Co(II) respectively. This resulted in an overall composition of 50.3 % Co(II). Design *B*, consisted predominantly of metallic Co, in a large core square, and one outer border containing 10 % Co(II). The resulting overall composition of Design *B* was 1.3 % Co(II). In order to replicate the noise of a relevant TXM-XAS measurement, a random Gaussian noise was added to the absorbance values with a signal to noise ratio of 20. Figure 8.1 shows simulated TXM images, at the X-ray energy 7727 eV, of the two designs before and after noise addition. Examples of the XAS spectra, from the core squares and the outermost border of the designs, are shown in figure 8.2. The structures were uniform (no thickness variations included) therefore at the isosbestic X-ray energy 7788 eV (where Co and Co(II) absorptions are equal) the TXM images are uniform as shown in figure 8.3.

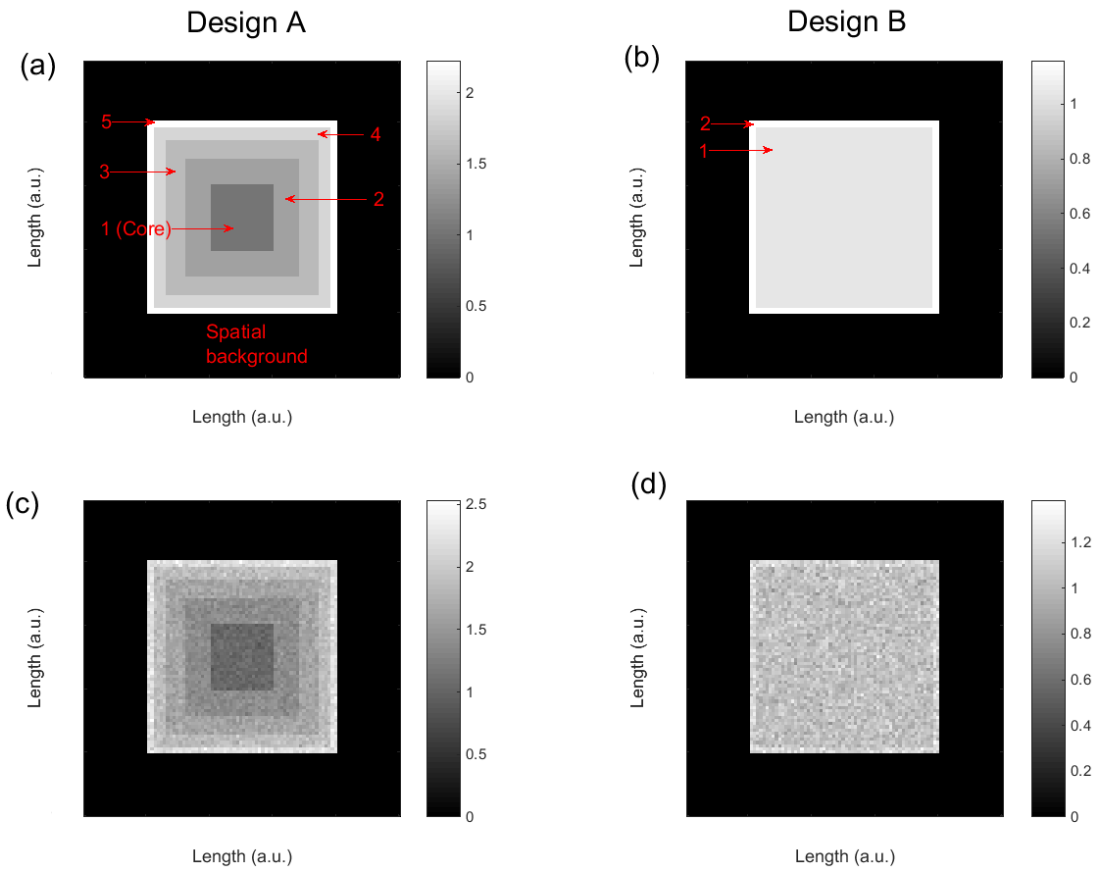


Fig. 8.1 Simulated TXM images of the two simulated designs, at energy 7727 eV (peak of absorption edge). (a-b) are the simulated images before addition of noise. (c-d) the images after the addition of random Gaussian noise. Colour bars indicate absorbance intensity (a.u.).

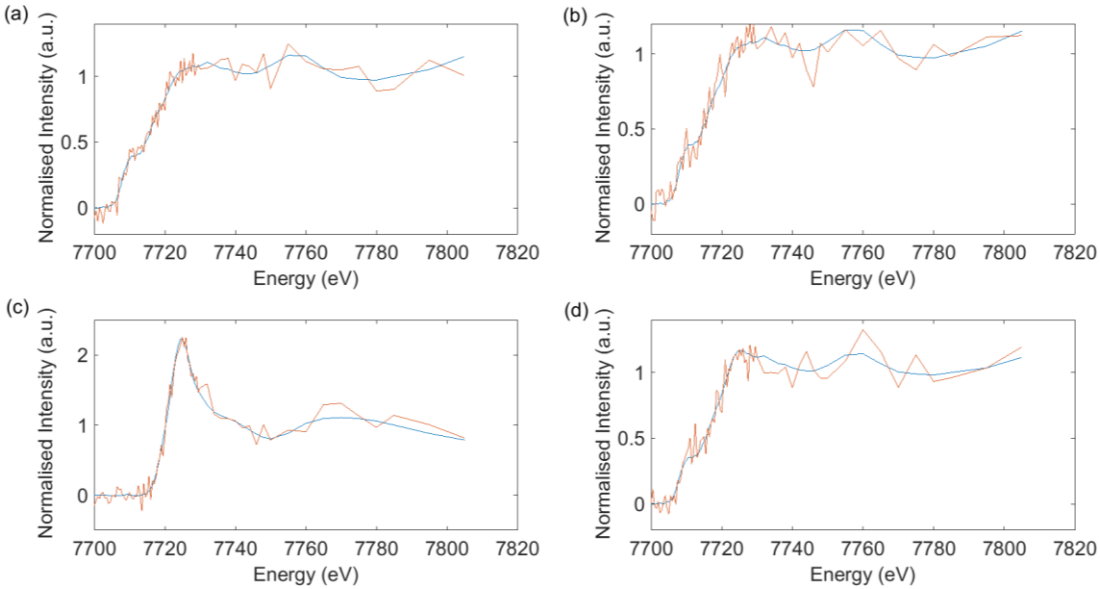


Fig. 8.2 Examples of simulated XAS spectra before (blue) and after (red) addition of noise. (a & c) spectra from the core and outer most squares of design A respectively. (b & d) spectra from the core and outer most squares of design B respectively.

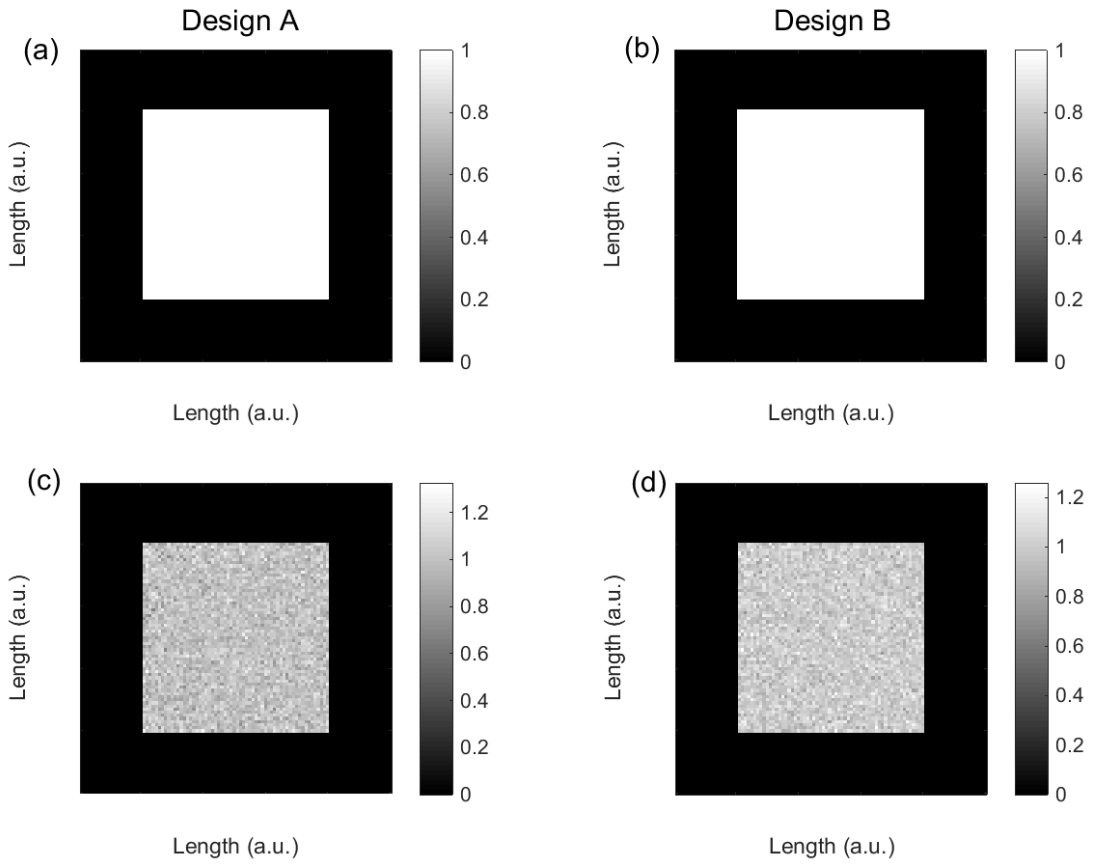


Fig. 8.3 Simulated TXM images of the two simulated designs, at energy 7788 eV (isosbestic point). (a-b) are the simulated images before addition of noise. (c-d) the images after the addition of random Gaussian noise. Colour bars indicate absorbance intensity (a.u.).

8.3 Speciation Mapping

Speciation maps, representing the Co(II) composition fraction per image element (pixel), were constructed by linear combination fitting and are shown in figure 8.4. These speciation maps were constructed based on fitting the complete simulated spectra which consisted of 80 energy points. The pre-known composition maps (constructed from the non-noisy data) were compared to the maps reconstructed using the noisy, more realistic, data. The distinctive *concentric squares* structure of both designs were preserved and the calculated overall Co(II) percentages were 50.3 % and 1.9 % compared to the designed compositions of 50.3 % and 1.3 % respectively. Although the Co(II) content of design *A* was accurately quantified, the results suggest a limitation in the specificity of this quantification process in low concentration cases such as that of the Co(II) content in design *B*.

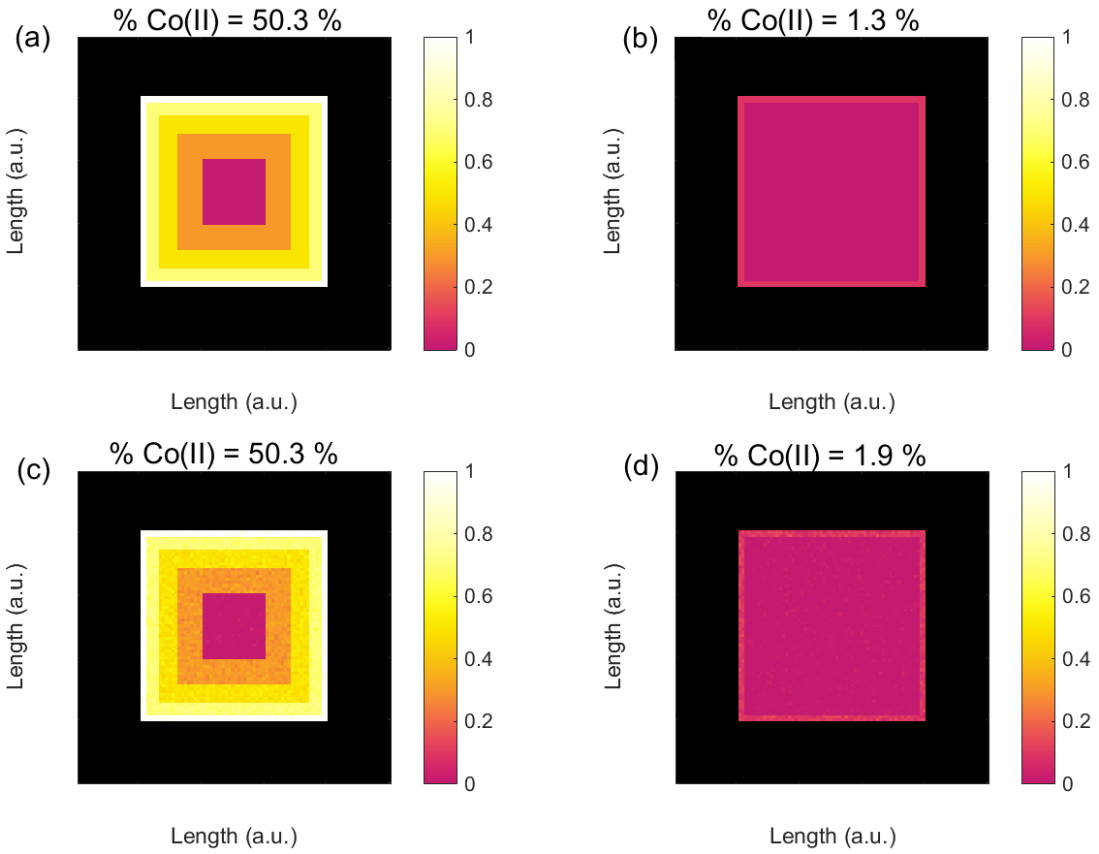


Fig. 8.4 Constructed speciation maps representing the distribution of the Co(II) composition fraction for both design A (a, c) and design B (b, d). (a-b) represent the speciation map of originally intended designs (i.e. before addition of noise). (c-d) represent the maps after the addition of random noise. Colour bars represent the Co(II):Co composition ratio.

In order to assess the accuracy of the quantification when using a fewer number of energy points, the speciation mapping and Co(II) quantification processes were repeated using different sets of selected energy points. Energy sets containing from three to nine energy points were used. Table 8.1 summarises the results showing the overall calculated % Co(II) content per each energy set for both simulated designs. The % Co(II) content of design A was always accurately calculated using the various energy lists containing three, five, or nine energy points. The % Co(II) content of design B was always overestimated. Furthermore, by comparing the results obtained from case 1 to case 2, and cases 3, 4 to case 5, it could be argued that imaging at double the number of energy points may have little improvement on the accuracy of the quantification. Therefore, it could be argued that using double the detection time per image may result in more accurate quantifications compared to obtaining images at more energy points. In both cases (whether doubling the collection time per image or using double the number of energy points) the X-ray dose is approximately doubled, but it is preferable to compromise the X-ray dose with a focus on achieving a higher signal to noise ratio than obtaining more data points for the fitting calculation. This could be examined in future studies by conducting this simulation experiment using improved signal to noise ratios, as opposed to the

value of 20 used here. Furthermore, future studies could also examine the results on structures of more varied compositions, as opposed to the 50.3 % and 1.3 % structures designed here.

Table 8.1 The calculated % Co(II) for both design A and B using different sets of energy points

Case no.	No. of selected post-edge energies	Selected energies eV	% Co(II) Design A	% Co(II) Design B
1	3	7710, 7727, 7788	50.2 %	3.3 %
2	5	7710, 7727, 7750, 7775, 7788	50.3 %	3.3 %
3	5	7710, 7715, 7724, 7727, 7788	50.2 %	2.4 %
4	5	7710, 7710.5, 7727, 7727.5, 7788	50.3 %	2.5 %
5	9	7710, 7715, 7724, 7727, 7750, 7755, 7775, 7780, 7788	50.2 %	2.3 %

9 References

1. Catelas, I. *et al.* Size, shape, and composition of wear particles from metal-metal hip simulator testing: effects of alloy and number of loading cycles. *J. Biomed. Mater. Res. A* **67,** 312–327 (2003).
2. Langton, D. J. *et al.* Adverse reaction to metal debris following hip resurfacing the influence of component type, orientation and volumetric wear. *J. Bone Jt. Surgery, Br. Vol.* **93,** 164–171 (2011).
3. Kwon, Y.-M. *et al.* Analysis of wear of retrieved metal-on-metal hip resurfacing implants revised due to pseudotumours. *J. Bone Jt. Surgery, Br. Vol.* **92,** 356–361 (2010).
4. Goode, A. E. *et al.* Chemical speciation of nanoparticles surrounding metal-on-metal hips. *Chem. Commun.* **48,** 8335 (2012).
5. Learmonth, I. D., Young, C. & Rorabeck, C. The operation of the century: total hip replacement. *Lancet* **370,** 1508–1519 (2007).
6. Iorio, R. *et al.* Orthopaedic Surgeon Workforce and Volume Assessment for Total Hip and Knee Replacement in the United States: Preparing for an Epidemic. *J. Bone Jt. Surgery-American Vol.* **90,** 1598–1605 (2008).
7. Kurtz, S. M. *et al.* Future young patient demand for primary and revision joint replacement: National projections from 2010 to 2030. in *Clinical Orthopaedics and Related Research* **467,** 2606–2612 (2009).
8. Wiles, P. The surgery of the osteo-arthritic hip. *Br. J. Surg.* **45,** 488–497 (1958).
9. Amstutz, H. C. & Grigoris, P. Metal on metal bearings in hip arthroplasty. *Clin. Orthop. Relat. Res.* **329,** S11--S34 (1996).
10. Charnley, J. The long-term results of low-friction arthroplasty of the hip performed as a primary intervention. *J. Bone Jt. Surgery, Br. Vol.* **54,** 61–76 (1972).
11. Willert, H. G., Bertram, H. & Buchhorn, G. H. Osteolysis in alloarthroplasty of the hip. The role of ultra-high molecular weight polyethylene wear particles. *Clin. Orthop. Relat. Res.* 95–107 (1990). doi:10.1097/00003086-199009000-00013
12. Kadoya, Y., Kobayashi, A. & Ohashi, H. Wear and osteolysis in total joint replacements. *Acta Orthop.* **69,** 435–436 (1998).
13. Mukka, S. S. *et al.* Osteoclasts in Periprosthetic Osteolysis: The Charnley Arthroplasty Revisited. *J. Arthroplasty* **32,** 3219–3227 (2017).
14. Anissian, H. L., Stark, A., Gustafson, A., Good, V. & Clarke, I. C. Metal-on-metal bearing in hip prosthesis generates 100-fold less wear debris than metal-on-polyethylene. *Acta Orthop.* **70,** 578–582 (1999).
15. Goldsmith, A. A. J., Dowson, D., Isaac, G. H. & Lancaster, J. G. A comparative joint simulator study of the wear of metal-on-metal and alternative material combinations in hip replacements. *Proc. Inst. Mech. Eng. Part H J. Eng. Med.* **214,** 39–47 (2000).
16. Jin, Z. M., Firkins, P., Farrar, R. & Fisher, J. Analysis and modelling of wear of cobalt-chrome alloys in a pin-on-plate test for a metal-on-metal total hip replacement. *Proc. Inst. Mech. Eng. Part H J. Eng. Med.* **214,** 559–568 (2000).
17. Scholes, S. C., Green, S. M. & Unsworth, A. The wear of metal-on-metal total hip prostheses measured in a hip simulator. in *Proceedings of the Institution of Mechanical Engineers, Part H: Journal of Engineering in Medicine* **215,** 523–530 (2001).
18. Smith, A. J., Dieppe, P., Vernon, K., Porter, M. & Blom, A. W. Failure rates of stemmed metal-on-metal hip replacements: Analysis of data from the National Joint Registry of England and Wales. *Lancet* **379,** 1199–1204 (2012).
19. Ong, K. L. *et al.* Economic burden of revision hip and knee arthroplasty in Medicare enrollees. *Clin. Orthop. Relat. Res.* **446,** 22–28 (2006).
20. Treacy, R. B. C., McBryde, C. W. & Pynsent, P. B. Birmingham hip resurfacing arthroplasty a minimum follow-up of five years. *J. Bone Jt. Surgery, Br. Vol.* **87,** 167–170 (2005).
21. National Joint Registry. National Joint Registry. *12th Annual progress report National Joint Registry Reports* (2015). Available at: http://www.njrreports.org.uk/hips-all-procedures-activity/H03v2NJR.
22. Hip implant patients sue manufacturer. *BBC* (2017). Available at: http://www.bbc.co.uk/news/health-41634354.
23. Meier, B. & Roberts, J. Hip implant complaints surge, even as the dangers are studied. *The New York*

Times (2011).

24. Hart, A. J. *et al.* Microfocus study of metal distribution and speciation in tissue extracted from revised metal on metal hip implants. *J. Phys. Conf. Ser.* **190,** 12208 (2009).

25. Konttinen, Y. T. & Pajarinen, J. Surgery: Adverse reactions to metal-on-metal implants. *Nat. Rev. Rheumatol.* **9,** 5–6 (2013).

26. Mahendra, G. *et al.* Necrotic and inflammatory changes in metal-on-metal resurfacing hip arthroplasties: relation to implant failure and pseudotumor formation. *Acta Orthop.* **80,** 653–659 (2009).

27. Gill, H. S., Grammatopoulos, G., Adshead, S., Tsialogiannis, E. & Tsiridis, E. Molecular and immune toxicity of CoCr nanoparticles in MoM hip arthroplasty. *Trends Mol. Med.* **18,** 145–155 (2012).

28. Bozic, K. J. *et al.* The Epidemiology of Revision Total Hip Arthroplasty in the United States. *J. Bone Jt. Surg.* **91,** 128–133 (2009).

29. Crook, P. in *ASM Handbook Vol. 2: Properties and selection: Nonferrous alloys and special-purpose materials* 446–454 (1990). doi:10.1361/asmhba000

30. Lee, S.-H., Nomura, N. & Chiba, A. Significant Improvement in Mechanical Properties of Biomedical Co-Cr-Mo Alloys with Combination of N Addition and Cr-Enrichment. *Mater. Trans.* **49,** 260–264 (2008).

31. ASTM F75-12. Standard Specification for Cobalt-28 Chromium-6 Molybdenum Alloy Castings and Casting Alloy for Surgical Implants (UNS R30075). (2012). doi:https://doi.org/10.1520/F0075-12

32. ASTM F1537-11. Standard Specification for Wrought Cobalt-28Chromium-6Molybdenum Alloys for Surgical Implants (UNS R31537, UNS R31538, and UNS R31539). (2011). doi:https://doi.org/10.1520/F1537-11

33. Vander Sande, J. B., Coke, J. R. & Wulff, J. A transmission electron microscopy study of the mechanisms of strengthening in heat-treated Co-Cr-Mo-C alloys. *Metall. Trans. A* **7,** 389–397 (1976).

34. Georgette, F. S. & Davidson, J. A. The effect of HIPing on the fatigue and tensile strength of a cast, porous-coated Co-Cr-Mo alloy. *J. Biomed. Mater. Res.* **20,** 1229–1248 (1986).

35. Adams, R. & Altstetter, C. Thermodynamics of the cobalt transformation. *TRANS MET SOC AIME* **242,** (1968).

36. López, H. F. & Saldivar-Garcia, A. J. Martensitic transformation in a cast Co-Cr-Mo-C alloy. *Metall. Mater. Trans. A Phys. Metall. Mater. Sci.* **39,** 8–18 (2008).

37. Salinas-Rodriguez, A. & Rodriguez-Galicia, J. L. Deformation behavior of low-carbon Co-Cr-Mo alloys for low-friction implant applications. *J. Biomed. Mater. Res. Part A* **31,** 409–419 (1996).

38. Chen, Y. *et al.* Effects of sigma phase and carbide on the wear behavior of CoCrMo alloys in Hanks' solution. *Wear* **310,** 51–62 (2014).

39. Huang, P. & Lopez, H. F. Strain induced E-martensite in a Co-Cr-Mo alloy: grain size effects. *Mater. Lett.* **39,** 244–248 (1999).

40. García, A. de J. S., Medrano, A. M. & Rodríguez, A. S. Formation of hcp martensite during the isothermal aging of an fcc Co-27Cr-5Mo-0.05 C orthopedic implant alloy. *Metall. Mater. Trans. A* **30,** 1177–1184 (1999).

41. Balagna, C., Spriano, S. & Faga, M. G. Characterization of Co-Cr-Mo alloys after a thermal treatment for high wear resistance. *Mater. Sci. Eng. C* **32,** 1868–1877 (2012).

42. Giacchi, J. V., Morando, C. N., Fornaro, O. & Palacio, H. A. Microstructural characterization of as-cast biocompatible Co-Cr-Mo alloys. *Mater. Charact.* **62,** 53–61 (2011).

43. Mineta, S., Namba, S., Yoneda, T., Ueda, K. & Narushima, T. Carbide formation and dissolution in biomedical CO-CR-MO alloys with different carbon contents during solution treatment. *Metall. Mater. Trans. A Phys. Metall. Mater. Sci.* **41,** 2129–2138 (2010).

44. Kilner, T., Pilliar, R. M., Weatherly, G. C. & Allibert, C. Phase identification and incipient melting in a cast Co-Cr surgical implant alloy. *J. Biomed. Mater. Res.* **16,** 63–79 (1982).

45. Caudillo, M. *et al.* On carbide dissolution in an as-cast ASTM F-75 alloy. *J. Biomed. Mater. Res.* **59,** 378–385 (2002).

46. Liao, Y. *et al.* New insights into hard phases of CoCrMo metal-on-metal hip replacements. *J. Mech. Behav. Biomed. Mater.* **12,** 39–49 (2012).

47. Salinas-Rodriguez, A., Aguilar, M. S. & López, H. F. The effect of carbon on the mechanical strength of heat treated cast Co sub 27 Cr sub 5 Mo alloys. *Process. Fabr. Adv. Mater. V* 69–79 (1996).

48. Walczak, M., Beer, K., Surowska, B. & Borowicz, J. The issue of using remelted cocrmo alloys in dental prosthetics. *Arch. Civ. Mech. Eng.* **12,** 171–177 (2012).

49. Placko, H. E., Brown, S. A. & Payer, J. H. Effects of microstructure on the corrosion behavior of CoCr porous coatings on orthopedic implants. *J. Biomed. Mater. Res.* **39,** 292–299 (1998).

50. Cawley, J., Metcalf, J. E. P., Jones, A. H., Band, T. J. & Skupien, D. S. A tribological study of cobalt chromium molybdenum alloys used in metal-on-metal resurfacing hip arthroplasty. *Wear* **255,** 999–1006 (2003).

51. Chen, Y., Li, Y., Koizumi, Y., Haider, H. & Chiba, A. Effects of carbon addition on wear mechanisms of CoCrMo metal-on-metal hip joint bearings. *Mater. Sci. Eng. C* **76,** 997–1004 (2017).

52. Wang, Z., Yan, Y., Xing, L., Su, Y. & Qiao, L. The role of hard phase carbides in tribocorrosion processes for a Co-based biomedical alloy. *Tribol. Int.* **113,** 370–376 (2017).

53. Clemow, A. J. T. & Daniell, B. L. Solution treatment behavior of Co-Cr-Mo alloy. *J. Biomed. Mater. Res.* **13,** 265–279 (1979).

54. Yan, Y., Dowson, D. & Neville, A. In-situ electrochemical study of interaction of tribology and corrosion in artificial hip prosthesis simulators. *J. Mech. Behav. Biomed. Mater.* **18,** 191–199 (2013).

55. Tipper, J. L. *et al.* Quantitative analysis of the wear and wear debris from low and high carbon content cobalt chrome alloys used in metal on metal total hip replacements. *J. Mater. Sci. Mater. Med.* **10,** 353–362 (1999).

56. Varano, R., Bobyn, J. D., Medley, J. B. & Yue, S. The effect of microstructure on the wear of cobalt-based alloys used in metal-on-metal hip implants. *Proc. Inst. Mech. Eng. Part H J. Eng. Med.* **220,** 145–159 (2006).

57. Kinbrum, A. & Unsworth, A. The wear of high-carbon metal-on-metal bearings after different heat treatments. *Proc. Inst. Mech. Eng. Part H J. Eng. Med.* **222,** 887–895 (2008).

58. Casabán Julián, L. & Igual Muñoz, A. Influence of microstructure of HC CoCrMo biomedical alloys on the corrosion and wear behaviour in simulated body fluids. *Tribol. Int.* **44,** 318–329 (2011).

59. Yan, Y., Neville, A., Dowson, D. & Williams, S. Tribocorrosion in implants-assessing high carbon and low carbon Co-Cr-Mo alloys by in situ electrochemical measurements. *Tribol. Int.* **39,** 1509–1517 (2006).

60. Bowsher, J. G., Nevelos, J., Williams, P. A. & Shelton, J. C. 'Severe' wear challenge to 'as-cast' and 'double heat-treated' large-diameter metal-on-metal hip bearings. *Proc. Inst. Mech. Eng. Part H J. Eng. Med.* **220,** 135–143 (2006).

61. Wimmer, M. A., Loos, J., Nassutt, R., Heitkemper, M. & Fischer, A. The acting wear mechanisms on metal-on-metal hip joint bearings: In vitro results. *Wear* **250–251,** 129–139 (2001).

62. Chiba, A., Kumagai, K., Nomura, N. & Miyakawa, S. Pin-on-disk wear behavior in a like-on-like configuration in a biological environment of high carbon cast and low carbon forged Co-29Cr-6Mo alloys. *Acta Mater.* **55,** 1309–1318 (2007).

63. Büscher, R. & Fischer, A. The pathways of dynamic recrystallization in all-metal hip joints. *Wear* **259,** 887–897 (2005).

64. Zeng, P., Rana, A., Thompson, R. & Rainforth, W. M. Subsurface characterisation of wear on mechanically polished and electro-polished biomedical grade CoCrMo. *Wear* **332–333,** 650–661 (2015).

65. Sun, D., Wharton, J. A., Wood, R. J. K., Ma, L. & Rainforth, W. M. Microabrasion-corrosion of cast CoCrMo alloy in simulated body fluids. *Tribol. Int.* **42,** 99–110 (2009).

66. Wang, Z., Yan, Y., Su, Y. & Qiao, L. Effect of proteins on the surface microstructure evolution of a CoCrMo alloy in bio-tribocorrosion processes. *Colloids Surfaces B Biointerfaces* **145,** 176–184 (2016).

67. Büscher, R. *et al.* Subsurface microstructure of metal-on-metal hip joints and its relationship to wear particle generation. *J. Biomed. Mater. Res. - Part B Appl. Biomater.* **72,** 206–214 (2005).

68. Pourzal, R. *et al.* Subsurface changes of a MoM hip implant below different contact zones. *J. Mech. Behav. Biomed. Mater.* **2,** 186–191 (2009).

69. Pourzal, R., Theissmann, R., Morlock, M. & Fischer, A. Micro-structural alterations within different areas of articulating surfaces of a metal-on-metal hip resurfacing system. *Wear* **267,** 689–694 (2009).

70. Liao, Y. *et al.* Graphitic tribological layers in metal-on-metal hip replacements. *Science (80-.).* **334,** 1687–1690 (2011).

71. Wimmer, M. A. *et al.* Wear mechanisms in metal-on-metal bearings: The importance of tribochemical reaction layers. *J. Orthop. Res.* **28,** 436–443 (2010).

72. Wimmer, M. A., Sprecher, C., Hauert, R., Täger, G. & Fischer, A. Tribochemical reaction on metal-on-metal hip joint bearings. *Wear* **255,** 1007–1014 (2003).

73. Yan, Y., Neville, A. & Dowson, D. Biotribocorrosion of CoCrMo orthopaedic implant materials-Assessing the formation and effect of the biofilm. *Tribol. Int.* **40,** 1492–1499 (2007).

74. Sadiq, K., Stack, M. M. & Black, R. A. Wear mapping of CoCrMo alloy in simulated bio-tribocorrosion conditions of a hip prosthesis bearing in calf serum solution. *Mater. Sci. Eng. C* **49,** 452–462 (2015).

75. Mathew, M. T. *et al.* Tribolayer formation in a metal-on-metal (MoM) hip joint: An electrochemical investigation. *J. Mech. Behav. Biomed. Mater.* **29,** 199–212 (2014).

76. Catelas, I. & Wimmer, M. A. New insights into wear and biological effects of metal-on-metal bearings. *Journal of Bone and Joint Surgery - Series A* **93,** 76–83 (2011).

77. Heuberger, M. P., Widmer, M. R., Zobeley, E., Glockshuber, R. & Spencer, N. D. Protein-mediated boundary lubrication in arthroplasty. *Biomaterials* **26,** 1165–1173 (2005).

78. Sun, D., Wharton, J. A. & Wood, R. J. K. Micro-abrasion mechanisms of cast CoCrMo in simulated body fluids. *Wear* **267,** 1845–1855 (2009).

79. Arenas, M. A., Conde, A., de Frutos, A. & de Damborenea, J. J. Electrochemical noise measurements of AISI 316L during wear in simulated physiological media. *Corros. Eng. Sci. Technol.* **49,** 656–660 (2014).

80. Codaro, E. N., Melnikov, P., Ramires, I. & Guastaldi, A. C. Corrosion behavior of a cobaltchromium-molybdenum alloy. *Russ. J. Electrochem.* **36,** 1117–1121 (2000).

81. Valero Vidal, C. & Igual Muñoz, A. Electrochemical characterisation of biomedical alloys for surgical implants in simulated body fluids. *Corros. Sci.* **50,** 1954–1961 (2008).

82. Rodríguez-Díaz, R. A. *et al.* Electrochemical corrosion behavior of a Co20Cr alloy in artificial saliva. *Int. J. Electrochem. Sci.* **10,** 7212–7226 (2015).

83. Foelske, A. & Strehblow, H. H. Passivity of cobalt in borate buffer at pH 9.3 studied by X-ray photoelectron spectroscopy. *Surf. Interface Anal.* **29,** 548–555 (2000).

84. Metikoš-Huković, M. & Ceraj-Ceric, M. p-Type and n-Type Behavior of Chromium Oxide as a Function of the Applied Potential. *J. Electrochem. Soc.* **134,** 2193 (1987).

85. Metikoš-Huković, M., Pilić, Z., Babić, R. & Omanović, D. Influence of alloying elements on the corrosion stability of CoCrMo implant alloy in Hank's solution. *Acta Biomater.* **2,** 693–700 (2006).

86. Li, Y.-S., Wang, K., He, P., Huang, B. X. & Kovacs, P. Surface-enhanced Raman spectroelectrochemical studies of corrosion films on implant Co--Cr--Mo alloy in biosimulating solutions. *J. Raman Spectrosc.* **30,** 97–103 (1999).

87. Hanawa, T., Hiromoto, S. & Asami, K. Characterization of the surface oxide film of a Co--Cr--Mo alloy after being located in quasi-biological environments using XPS. *Appl. Surf. Sci.* **183,** 68–75 (2001).

88. Milošev, I. & Strehblow, H. H. The composition of the surface passive film formed on CoCrMo alloy in simulated physiological solution. *Electrochim. Acta* **48,** 2767–2774 (2003).

89. Hodgson, A. W. E. *et al.* Passive and transpassive behaviour of CoCrMo in simulated biological solutions. *Electrochim. Acta* **49,** 2167–2178 (2004).

90. Lewis, A. C. & Heard, P. J. The effects of calcium phosphate deposition upon corrosion of CoCr alloys and the potential for implant failure. *J. Biomed. Mater. Res. - Part A* **75,** 365–373 (2005).

91. Milošev, I. The effect of biomolecules on the behaviour of CoCrMo alloy in various simulated physiological solutions. *Electrochim. Acta* **78,** 259–273 (2012).

92. Bettini, E., Eriksson, T., Boström, M., Leygraf, C. & Pan, J. Influence of metal carbides on dissolution behavior of biomedical CoCrMo alloy: SEM, TEM and AFM studies. *Electrochim. Acta* **56,** 9413–9419 (2011).

93. Hedberg, Y. S., Qian, B., Shen, Z., Virtanen, S. & Odnevall Wallinder, I. In vitro biocompatibility of CoCrMo dental alloys fabricated by selective laser melting. *Dent. Mater.* **30,** 525–534 (2014).

94. Ouerd, A., Alemany-Dumont, C., Normand, B. & Szunerits, S. Reactivity of CoCrMo alloy in physiological medium: Electrochemical characterization of the metal/protein interface. *Electrochim. Acta* **53,** 4461–4469 (2008).

95. Zhang, X., Li, Y., Tang, N., Onodera, E. & Chiba, A. Corrosion behaviour of CoCrMo alloys in 2 wt% sulphuric acid solution. *Electrochim. Acta* **125,** 543–555 (2014).

96. Bettini, E., Leygraf, C. & Pan, J. Nature of current increase for a CoCrMo alloy: 'transpassive' dissolution vs. water oxidation. *Int. J. Electrochem. Sci.* **8,** 11791–11804 (2013).

97. Kanan, M. W. & Nocera, D. G. In situ formation of an oxygen-evolving catalyst in neutral water containing phosphate and Co2+. *Science (80-.).* **321,** 1072–1075 (2008).

98. Zhong, D. K. & Gamelin, D. R. Photoelectrochemical Water Oxidation by Cobalt Catalyst ('Co - Pi') r -Fe 2 O 3 Composite Photoanodes Oxygen Evolution and Resolution of a Kinetic Bottleneck.pdf. *J. Am. Chem. Soc.* **132,** 4202–4207 (2010).

99. Nikoloski, A. N. & Nicol, M. J. Addition of cobalt to lead anodes used for oxygen evolutiona literature review. *Mineral Processing and Extractive Metallurgy Review* **31,** 30–57 (2010).

100. Lewis, A. C., Kilburn, M. R., Papageorgiou, I., Allen, G. C. & Case, C. P. Effect of synovial fluid, phosphate-buffered saline solution, and water on the dissolution and corrosion properties of CoCrMo alloys as used in orthopedic implants. *J. Biomed. Mater. Res. - Part A* **73,** 456–467 (2005).

101. Okazaki, Y. & Gotoh, E. Comparison of metal release from various metallic biomaterials in vitro. *Biomaterials* **26,** 11–21 (2005).

102. Espallargas, N., Torres, C. & Muñoz, A. I. A metal ion release study of CoCrMo exposed to corrosion and tribocorrosion conditions in simulated body fluids. *Wear* **333,** 669–678 (2014).

103. Hedberg, Y. & Odnevall Wallinder, I. Metal release and speciation of released chromium from a biomedical CoCrMo alloy into simulated physiologically relevant solutions. *J. Biomed. Mater. Res. - Part B Appl. Biomater.* **102,** 693–699 (2014).

104. Badawy, W. A. & Al-Kharafi, F. M. Corrosion and passivation behaviors of molybdenum in aqueous solutions of different pH. *Electrochim. Acta* **44,** 693–702 (1998).

105. Hodgson, A. W., Mischler, S., Von Rechenberg, B. & Virtanen, S. An analysis of the in vivo deterioration of Co-Cr-Mo implants through wear and corrosion. *Proc. Inst. Mech. Eng. Part H J. Eng. Med.* **221,** 291–303 (2007).

106. Toh, W. Q., Tan, X., Bhowmik, A., Liu, E. & Tor, S. B. Tribochemical characterization and tribocorrosive behavior of CoCrMo alloys: A review. *Materials (Basel).* **11,** (2017).

107. Mischler, S. Triboelectrochemical techniques and interpretation methods in tribocorrosion: A comparative evaluation. *Tribol. Int.* **41,** 573–583 (2008).

108. Mathew, M. T., Jacobs, J. J. & Wimmer, M. A. Wear-corrosion synergism in a cocrmo hip bearing alloy is influenced by proteins. *Clin. Orthop. Relat. Res.* **470,** 3109–3117 (2012).

109. Neville, A. & Hu, X. Mechanical and electrochemical interactions during liquid--solid impingement on high-alloy stainless steels. *Wear* **251,** 1284–1294 (2001).

110. Igual Muñoz, A. & Casabán Julián, L. Influence of electrochemical potential on the tribocorrosion behaviour of high carbon CoCrMo biomedical alloy in simulated body fluids by electrochemical impedance spectroscopy. *Electrochim. Acta* **55,** 5428–5439 (2010).

111. Mischler, S. & Muñoz, A. I. Wear of CoCrMo alloys used in metal-on-metal hip joints: A tribocorrosion appraisal. *Wear* **297,** 1081–1094 (2013).

112. Igual Muñoz, A. & Mischler, S. Effect of the environment on wear ranking and corrosion of biomedical CoCrMo alloys. *J. Mater. Sci. Mater. Med.* **22,** 437–450 (2011).

113. Watson, S. W., Friedersdorf, F. J., Madsen, B. W. & Cramer, S. D. Methods of measuring wear-corrosion synergism. *Wear* **181–183,** 476–484 (1995).

114. Landolt, D., Mischler, S. & Stemp, M. Electrochemical methods in tribocorrosion: A critical appraisal. *Electrochim. Acta* **46,** 3913–3929 (2001).

115. Yan, Y., Neville, A. & Dowson, D. Tribo-corrosion properties of cobalt-based medical implant alloys in simulated biological environments. *Wear* **263,** 1105–1111 (2007).

116. Yan, Y., Neville, A., Hesketh, J. & Dowson, D. Real-time corrosion measurements to assess biotribocorrosion mechanisms with a hip simulator. *Tribol. Int.* **63,** 115–122 (2013).

117. Uhlig, H. H. Mechanism of fretting corrosion. *Trans. Am. Soc. Mech. Eng. - J. Appl. Mech.* **21,** 401–407 (1954).

118. Wang, Y., Yan, Y., Su, Y. & Qiao, L. Release of metal ions from nano CoCrMo wear debris generated from tribo-corrosion processes in artificial hip implants. *J. Mech. Behav. Biomed. Mater.* **68,** 124–133 (2017).

119. Muñoz, A. I. & Mischler, S. Interactive Effects of Albumin and Phosphate Ions on the Corrosion of CoCrMo Implant Alloy. *J. Electrochem. Soc.* **154,** C562 (2007).

120. Kocijan, A., Milošev, I., Merl, D. K. & Pihlar, B. Electrochemical study of Co-based alloys in simulated physiological solution. *J. Appl. Electrochem.* **34,** 517–524 (2004).

121. Valero Vidal, C. & Igual Muñoz, A. Study of the adsorption process of bovine serum albumin on passivated surfaces of CoCrMo biomedical alloy. *Electrochim. Acta* **55,** 8445–8452 (2010).

122. Silva-Bermudez, P. & Rodil, S. E. An overview of protein adsorption on metal oxide coatings for biomedical implants. *Surf. Coatings Technol.* **233,** 147–158 (2013).

123. Hedberg, Y., Karlsson, M. E., Blomberg, E., Odnevall Wallinder, I. & Hedberg, J. Correlation between surface physicochemical properties and the release of iron from stainless steel AISI 304 in biological media. *Colloids Surfaces B Biointerfaces* **122,** 216–222 (2014).

124. Hedberg, Y. *et al.* Interaction of Albumin and Fibrinogen with Stainless Steel: Influence of Sequential Exposure and Protein Aggregation on Metal Release and Corrosion Resistance. *Corrosion* **73,** 1423–1436 (2017).

125. Muñoz, A. I. & Mischler, S. Electrochemical Quartz Crystal Microbalance and X-Ray Photoelectron Spectroscopy study of cathodic reactions in Bovine Serum Albumin containing solutions on a Physical Vapour Deposition-CoCrMo biomedical alloy. *Electrochim. Acta* **180,** 96–103 (2015).

126. Hedberg, Y. S. Role of proteins in the degradation of relatively inert alloys in the human body. *npj Mater. Degrad.* **2,** 26 (2018).

127. Khan, M. A., Williams, R. L. & Williams, D. F. The corrosion behaviour of Ti-6Al-4V, Ti-6Al-7Nb and Ti-13Nb-13Zr in protein solutions. *Biomaterials* **20,** 631–637 (1999).

128. Contu, F., Elsener, B. & Böhni, H. Serum effect on the electrochemical behaviour of titanium, Ti6Al4V and Ti6Al7Nb alloys in sulphuric acid and sodium hydroxide. *Corros. Sci.* **46,** 2241–2254 (2004).

129. Valero-Vidal, C., Igual-Munoz, A., Olsson, C.-O. A. & Mischler, S. Adsorption of BSA on Passivated CoCrMo PVD Alloy: An EQCM and XPS Investigation. *J. Electrochem. Soc.* **161,** C294–C301 (2014).

130. Virtanen, S. *et al.* Special modes of corrosion under physiological and simulated physiological conditions. *Acta Biomater.* **4,** 468–476 (2008).

131. Yan, Y., Dowson, D. & Neville, A. In-situ electrochemical study of interaction of tribology and corrosion in artificial hip prosthesis simulators. *J. Mech. Behav. Biomed. Mater.* **18,** 191–199 (2013).

132. Simoes, T. A. *et al.* Evidence for the dissolution of molybdenum during tribocorrosion of CoCrMo hip implants in the presence of serum protein. *Acta Biomater.* **45,** 410–418 (2016).

133. Contu, F., Elsener, B. & Böhni, H. Corrosion behaviour of CoCrMo implant alloy during fretting in bovine serum. *Corros. Sci.* **47,** 1863–1875 (2005).

134. Karimi, S., Nickchi, T. & Alfantazi, A. Effects of bovine serum albumin on the corrosion behaviour of AISI 316L , Co – 28Cr – 6Mo , and Ti – 6Al – 4V alloys in phosphate buffered saline solutions. *Corros. Sci.* **53,** 3262–3272 (2011).

135. Zhang, Y. *et al.* Time-dependent Enhanced Corrosion of Ti6Al4V in the Presence of H2O2and Albumin. *Sci. Rep.* **8,** (2018).

136. Hedberg, Y. S., Žnidaršič, M., Herting, G., Milošev, I. & Odnevall Wallinder, I. Mechanistic insight on the combined effect of albumin and hydrogen peroxide on surface oxide composition and extent of metal release from Ti6Al4V. *J. Biomed. Mater. Res. Part B Appl. Biomater.* (2018). doi:10.1002/jbm.b.34182

137. Liu, Y. & Gilbert, J. L. Effect of simulated inflammatory conditions and potential on dissolution and surface oxide of CoCrMo alloy: In situ electrochemical atomic force microscopy study. *Electrochim. Acta* **262,** 252–263 (2018).

138. Liu, Y. & Gilbert, J. L. The effect of simulated inflammatory conditions and Fenton chemistry on the electrochemistry of CoCrMo alloy. *J. Biomed. Mater. Res. - Part B Appl. Biomater.* **106,** 209–220 (2018).

139. Yan, Y., Neville, a & Dowson, D. Understanding the role of corrosion in the degradation of metal-on-metal implants. *Proc. Inst. Mech. Eng. H.* **220,** 173–181 (2006).

140. Montero-Ocampo, C. & Salinas Rodriguez, A. Effect of carbon content on the resistance to localized corrosion of as-cast cobalt-based alloys in an aqueous chloride solution. *J. Biomed. Mater. Res.* **29,** 441–453 (1995).

141. Montero-Ocampo, C., Juarez, R. & Rodriguez, A. S. Effect of Fcc-Hcp Phase Transformation Produced by Isothermal Aging on the Corrosion Resistance of a Co-27-Cr-5Mo-0.05C. *Metall. Mater. Trans. A* **33 A,** 2229–2235 (2002).

142. Placko, H. E., Brown, S. A. & Payer, J. H. Effects of microstructure on the corrosion behaviour of CoCr porous coatings on orthopedic implants. *J. Biomed. Mater. Res.* **39,** 292–299 (1998).

143. Vidal, C. V. & Muñoz, A. I. Effect of thermal treatment and applied potential on the electrochemical behaviour of CoCrMo biomedical alloy. *Electrochim. Acta* **54,** 1798–1809 (2009).

144. Bettini, E., Leygraf, C., Lin, C., Liu, P. & Pan, J. Influence of Grain Boundaries on Dissolution Behavior of a Biomedical CoCrMo Alloy: In-Situ Electrochemical-Optical, AFM and SEM/TEM Studies. *J. Electrochem. Soc.* **159,** C422–C427 (2012).

145. Hoffman, E. E., Lin, A., Liao, Y. & Marks, L. D. Grain Boundary Assisted Crevice Corrosion in CoCrMo Alloys. *CORROSION* **72,** 1445–1461 (2016).

146. Lin, A., Hoffman, E. E. & Marks, L. D. Effects of Grain Boundary Misorientation and Chromium Segregation on Corrosion of CoCrMo Alloys. *CORROSION* **73,** 256–267 (2016).

147. Hiromoto, S., Onodera, E., Chiba, A., Asami, K. & Hanawa, T. Microstructure and corrosion behaviour in biological environments of the new forged low-Ni Co-Cr-Mo alloys. *Biomaterials* **26,** 4912–4923 (2005).

148. Varano, R., Bobyn, J. D., Medley, J. B. & Yue, S. Effect of microstructure on the dry sliding friction behavior of CoCrMo alloys used in metal-on-metal hip implants. *J. Biomed. Mater. Res. - Part B Appl. Biomater.* **76,** 281–286 (2006).

149. Kurosu, S., Nomura, N. & Chiba, A. Effect of Sigma Phase in Co-29Cr-6Mo Alloy on Corrosion and Mechanical Properties. *Adv. Mater. Res.* **26–28,** 777–780 (2007).

150. Wang, Z., Yan, Y., Su, Y. & Qiao, L. Effect of electrochemical corrosion on the subsurface microstructure evolution of a CoCrMo alloy in albumin containing environment. *Appl. Surf. Sci.* **406,** 319–329 (2017).

151. McKee, G. . Total hip replacement — past, present and future. *Biomaterials* **3,** 130–135 (1982).

152. Ulrich, S. D. *et al.* Total hip arthroplasties: What are the reasons for revision? *Int. Orthop.* **32,** 597–604 (2008).

153. Ingham, E. & Fisher, J. The role of macrophages in osteolysis of total joint replacement. *Biomaterials* **26,** 1271–1286 (2005).

154. Abu-Amer, Y., Darwech, I. & Clohisy, J. C. Aseptic loosening of total joint replacements: Mechanisms underlying osteolysis and potential therapies. *Arthritis Res. Ther.* **9,** 1–7 (2007).

155. Dyskova, T., Gallo, J. & Kriegova, E. The role of the chemokine system in tissue response to prosthetic by-products leading to periprosthetic osteolysis and aseptic loosening. *Front. Immunol.* **8,** (2017).

156. Veronesi, F., Tschon, M. & Fini, M. Gene expression in osteolysis: Review on the identification of altered molecular pathways in preclinical and clinical studies. *Int. J. Mol. Sci.* **18,** (2017).

157. Goodman, S. B., Gibon, E. & Yao, Z. The basic science of periprosthetic osteolysis. *Instr. Course Lect.* **62,** 201 (2013).

158. Zhu, Y., Chiu, K. & Tang, W. Review Article: Polyethylene Wear and Osteolysis in Total Hip Arthroplasty. *J. Orthop. Surg.* **9,** 91–99 (2001).

159. Amirhosseini, M., Andersson, G., Aspenberg, P. & Fahlgren, A. Mechanical instability and titanium particles induce similar transcriptomic changes in a rat model for periprosthetic osteolysis and aseptic loosening. *Bone Reports* **7,** 17–25 (2017).

160. Milosev, I. *et al.* Hip Replacements at a Mean of Seven Years Survivorship and Retrieval Analysis of Sikomet Metal-on-Metal Total Survivorship and Retrieval Analysis of Sikomet Metal-on- Metal Total Hip Replacements at a Mean of Seven Years. *J. Bone Jt. Surg. Am. Copyr. © BY J. BONE Jt. Surg.* 1173–1182 (2006). doi:10.2106/JBJS.E.00604

161. Huber, M., Reinisch, G., Zenz, P., Zweymüller, K. & Lintner, F. Postmortem study of femoral osteolysis associated with metal-on-metal articulation in total hip replacement: an analysis of nine cases. *J. Bone Joint Surg. Am.* **92,** 1720–1731 (2010).

162. Goodman, S. B. Wear particles, periprosthetic osteolysis and the immune system. *Biomaterials* **28,** 5044–5048 (2007).

163. Haynes, D. R., Rogers, S. D., Hay, S., Pearcy, M. J. & Howie, D. W. The differences in toxicity and release of bone-resorbing mediators induced by titanium and cobalt-chromium-alloy wear particles. *J. Bone Joint Surg. Am.* **75,** 825–34 (1993).

164. Toms, A. P. *et al.* MRI of early symptomatic metal-on-metal total hip arthroplasty: a retrospective review of radiological findings in 20 hips. *Clin. Radiol.* **63,** 49–58 (2008).

165. Willert, H.-G. *et al.* Metal-on-metal bearings and hypersensitivity in patients with artificial hip joints. *J. Bone Jt. Surg.* **87,** 28–36 (2005).

166. Samelko, L. *et al.* Cobalt-Alloy Implant Debris Induce HIF-1α Hypoxia Associated Responses: A Mechanism for Metal-Specific Orthopedic Implant Failure. *PLoS One* **8,** 1–7 (2013).

167. Doorn, P. F., Mirra, J. M., Campbell, P. a & Amstutz, H. C. Tissue reaction to metal on metal total hip prostheses. *Clin. Orthop. Relat. Res.* S187–S205 (1996). doi:8769334

168. Delaunay, C., Petit, I., Learmonth, I. D., Oger, P. & Vendittoli, P. A. Metal-on-metal bearings total hip arthroplasty: The cobalt and chromium ions release concern. *Orthop. Traumatol. Surg. Res.* **96,** 894–904 (2010).

169. Medley, J. B., Chan, F. W., Krygier, J. J. & Bobyn, J. D. Comparison of alloys and designs in a hip simulator study of metal on metal implants. *Clin. Orthop. Relat. Res.* S148–S159 (1996). doi:54

170. Medley, J. B., Dowling, J. M., Poggie, R. A., Krygier, J. J. & Bobyn, J. D. Simulator wear of some commercially available metal-on-metal hip implants. *ASTM STP 1346* 92–110 (1999).

171. Chan, F. W., Bobyn, J. D., Medley, J. B., Krygier, J. J. & Tanzer, M. Wear and Lubrication of {Metal-on-Metal} Hip Implants. *Clin. Orthop. Relat. Res.* **369,** 10 (1999).

172. McKellop, H. *et al.* In vivo wear of three types of metal on metal hip prostheses during two decades of use. *Clin Orthop Relat Res* S128-40 (1996). doi:64

173. Rieker, C. B., Kottig, P., Schon, R., Windler, M. & Wyss, U. P. in *Alternative Bearing Surfaces in Total Joint Replacement* **1346,** 144–156 (1998).

174. Campbell, P. *et al.* Metal-on-metal hip replacements: Wear performance and cellular response to wear particles. in *ASTM Special Technical Publication* (1999).

175. Willert, H. G., Semlitsch, M. & Peltier, L. F. Tissue reactions to plastic and metallic wear products of joint endoprostheses. *Clin. Orthop. Relat. Res.* **333,** 4–14 (1996).

176. Doorn, P. F. *et al.* Metal wear particle characterization from metal-on-metal total hip replacements: transmission electron microscopy study of periprosthetic tissues and isolated particles. *J. Biomed. Mater. Res.* **42,** 103–111 (1998).

177. Donaldson, K. *et al.* The pulmonary toxicology of ultrafine particles. *J. aerosol Med.* **15,** 213–220 (2002).

178. Oberdörster, G., Oberdörster, E. & Oberdörster, J. Nanotoxicology: an emerging discipline evolving from studies of ultrafine particles. *Environ. Health Perspect.* 823–839 (2005).

179. Gelb, H., Ralph Schumacher, H., Cuckler, J. & Baker, D. G. In vivo inflammatory response to polymethylmethacrylate particulate debris: Effect of size, morphology, and surface area. *J. Orthop. Res.* **12,** 83–92 (1994).

180. González, O., Smith, R. L. & Goodman, S. B. Effect of size, concentration, surface area, and volume of polymethylmethacrylate particles on human macrophages in vitro. *J. Biomed. Mater. Res.* **30,** 463–473 (1996).

181. Sabokbar, A., Pandey, R. & Athanasou, N. A. The effect of particle size and electrical charge on macrophage-osteoclast differentiation and bone resorption. *J. Mater. Sci. Mater. Med.* **14,** 731–738 (2003).

182. Papageorgiou, I. *et al.* The effect of nano- and micron-sized particles of cobalt-chromium alloy on human fibroblasts in vitro. *Biomaterials* **28,** 2946–2958 (2007).

183. Yue, H. *et al.* Particle size affects the cellular response in macrophages. *Eur. J. Pharm. Sci.* **41,** 650–657 (2010).

184. Shah, K. M., Quinn, P. D., Gartland, A. & Wilkinson, J. M. Understanding the tissue effects of tribo-corrosion: Uptake, distribution, and speciation of cobalt and chromium in human bone cells. *J. Orthop. Res.* **33,** 114–121 (2015).

185. Caicedo, M. S., Pennekamp, P. H., Mcallister, K., Jacobs, J. J. & Hallab, N. J. Soluble ions more than particulate cobalt-alloy implant debris induce monocyte costimulatory molecule expression and release of proinflammatory cytokines critical to metal-induced lymphocyte reactivity. 22–26 (2009). doi:10.1002/jbm.a.32627

186. Urban, R. M., Tomlinson, M. J., Hall, D. J. & Jacobs, J. J. Accumulation in liver and spleen of metal particles generated at nonbearing surfaces in hip arthroplasty. *J. Arthroplasty* **19,** 94–101 (2004).

187. Swiatkowska, I. *et al.* Synchrotron analysis of human organ tissue exposed to implant material. *J. Trace Elem. Med. Biol.* **46,** 128–137 (2018).

188. Case, C. P. *et al.* Widespread dissemination of metal debris from implants. *J. Bone Joint Surg. Br.* **76,** 701–12 (1994).

189. De Smet, K. *et al.* Metal ion measurement as a diagnostic tool to identify problems with metal-on-metal hip resurfacing. *J. Bone Jt. Surg.* **90,** 202–208 (2008).

190. Hart, A. J. *et al.* Sensitivity and specificity of blood cobalt and chromium metal ions for predicting failure of metal-on-metal hip replacement. *J. Bone Jt. Surgery, Br. Vol.* **93,** 1308–1313 (2011).

191. Jacobs, J. J., Hallab, N. J., Skipor, A. K. & Urban, R. M. Metal degradation products: a cause for concern in metal-metal bearings? *Clin. Orthop. Relat. Res.* **417,** 139–147 (2003).

192. Davda, K., Lali, F. V, Sampson, B., Skinner, J. A. & Hart, A. J. An analysis of metal ion levels in the joint fluid of symptomatic patients with metal-onmetal hip replacements. *J. Bone Jt. Surgery-British Vol.* **93B,** 738–745 (2011).

193. Hosman, A. H., van der Mei, H. C., Bulstra, S. K., Busscher, H. J. & Neut, D. Effects of metal-on-metal wear on the host immune system and infection in hip arthroplasty. *Acta Orthop.* **81,** 526–534 (2010).

194. Behl, B. *et al.* Biological effects of cobalt-chromium nanoparticles and ions on dural fibroblasts and dural epithelial cells. *Biomaterials* **34,** 3547–3558 (2013).

195. Gilbert, J. L. *et al.* Direct in vivo inflammatory cell-induced corrosion of CoCrMo alloy orthopedic implant surfaces. *J. Biomed. Mater. Res. - Part A* **103,** 211–223 (2015).

196. Laura, A. Di *et al.* Clinical relevance of corrosion patterns attributed to inflammatory cell-induced corrosion : A retrieval study. 155–164 (2015). doi:10.1002/jbm.b.33540

197. Anderson, R. G. A view of acidic intracellular compartments. *J. Cell Biol.* **106,** 539–543 (1988).

198. Cooper, G. M. & Hausman, R. E. The Cell: A Molecular Approach 2nd Edition. *Sinauer Associates* 1–820 (2000).

199. Eskelinen, E.-L. & Saftig, P. Autophagy: A lysosomal degradation pathway with a central role in health and disease. *Biochim. Biophys. Acta - Mol. Cell Res.* **1793,** 664–673 (2009).

200. Catelas, I., Petit, A., Zukor, D. J., Antoniou, J. & Huk, O. L. TNF-α secretion and macrophage mortality induced by cobalt and chromium ions in vitro - Qualitative analysis of apoptosis. *Biomaterials* **24,** 383–391 (2003).

201. Kwon, Y.-M. *et al.* Dose-dependent cytotoxicity of clinically relevant cobalt nanoparticles and ions on macrophages in vitro. *Biomed. Mater.* **4,** 25018 (2009).

202. Akbar, M., Brewer, J. M. & Grant, M. H. Effect of chromium and cobalt ions on primary human lymphocytes in vitro. *J. Immunotoxicol.* **8,** 140–149 (2011).

203. Dunstan, E., Ladon, D., Whittingham-Jones, P., Carrington, R. & Briggs, T. W. R. Chromosomal aberrations in the peripheral blood of patients with metal-on-metal hip bearings. *J. Bone Joint Surg. Am.* **90,** 517–22 (2008).

204. Hartwig, A. Current aspects in metal genotoxicity. *Biometals* **8,** 3–11 (1995).

205. El-Yamani, N., Zúñiga, L., Stoyanova, E., Creus, A. & Marcos, R. Chromium-induced genotoxicity and interference in human lymphoblastoid cell (TK6) repair processes. *J. Toxicol. Environ. Heal. Part A* **74,** 1030–1039 (2011).

206. Colognato, R. *et al.* Comparative genotoxicity of cobalt nanoparticles and ions on human peripheral leukocytes in vitro. *Mutagenesis* **23,** 377–382 (2008).

207. Papageorgiou, I. *et al.* Genotoxic effects of particles of surgical cobalt chrome alloy on human cells of different age in vitro. *Mutat. Res. - Fundam. Mol. Mech. Mutagen.* **619,** 45–58 (2007).

208. Chromium (VI) compounds. *IARC Monogr. Eval. Carcinog. Risks to Humans* **100 C,** 147–167 (2011).

209. Reynolds, M. F. *et al.* Rapid DNA double-strand breaks resulting from processing of Cr-DNA cross-links by both MutS dimers. *Cancer Res.* **69,** 1071–1079 (2009).

210. Zhitkovich, A. Importance of chromium-DNA adducts in mutagenicity and toxicity of chromium (VI). *Chem. Res. Toxicol.* **18,** 3–11 (2005).

211. Ladon, D. *et al.* Changes in metal levels and chromosome aberrations in the peripheral blood of patients after metal-on-metal hip arthroplasty. *J. Arthroplasty* **19,** 78–83 (2004).

212. Bhabra, G. *et al.* Nanoparticles can cause DNA damage across a cellular barrier. *Nat. Nanotechnol.* **4,** 876–883 (2009).

213. Visuri, T. I., Pukkala, E., Pulkkinen, P. & Paavolainen, P. Cancer incidence and causes of death among total hip replacement patients: a review based on Nordic cohorts with a special emphasis on metal-on-metal bearings. *Proc. Inst. Mech. Eng. Part H J. Eng. Med.* **220,** 399–407 (2006).

214. Visuri, T., Pukkala, E., Paavolainen, P., Pulkkinen, P. & Riska, E. B. Cancer risk after metal on metal and polyethylene on metal total hip arthroplasty. *Clin. Orthop. Relat. Res.* **329,** S280--S289 (1996).

215. Yang, M. A current global view of environmental and occupational cancers. *J. Environ. Sci. Heal. Part C* **29,** 223–249 (2011).

216. Simoes, T. a *et al.* Microstructural characterization of low and high carbon CoCrMo alloy nanoparticles produced by mechanical milling. *J. Phys. Conf. Ser.* **522,** 12059 (2014).

217. Huber, M., Reinisch, G., Trettenhahn, G., Zweymüller, K. & Lintner, F. Presence of corrosion products and

hypersensitivity-associated reactions in periprosthetic tissue after aseptic loosening of total hip replacements with metal bearing surfaces. *Acta Biomater.* **5,** 172–180 (2009).

218. Catelas, I., Campbell, P. A., Bobyn, J. D., Medley, J. B. & Huk, O. L. Wear particles from metal-on-metal total hip replacements: effects of implant design and implantation time. *Proc. Inst. Mech. Eng. Part H J. Eng. Med.* **220,** 195–208 (2006).

219. De Flora, S. *et al.* Estimates of the chromium(VI) reducing capacity in human body compartments as a mechanism for attenuating its potential toxicity and carcinogenicity. *Carcinogenesis* **18,** 531–537 (1997).

220. Niedowicz, D. M. & Daleke, D. L. The role of oxidative stress in diabetic complications. *Cell Biochem. Biophys.* **43,** 289–330 (2005).

221. Mulyani, I., Levina, A. & Lay, P. A. Biomimetic oxidation of chromium(III): Does the antidiabetic activity of chromium(III) involve carcinogenic chromium(VI)? *Angew. Chemie - Int. Ed.* **43,** 4504–4507 (2004).

222. Egerton, R. F. Limits to the spatial, energy and momentum resolution of electron energy-loss spectroscopy. *Ultramicroscopy* **107,** 575–586 (2007).

223. Schneider, N. M. *et al.* Electron–Water Interactions and Implications for Liquid Cell Electron Microscopy. *J. Phys. Chem. C* **118,** 22373–22382 (2014).

224. Kaznatcheev, K. V. *et al.* Soft X-ray spectromicroscopy beamline at the CLS: Commissioning results. *Nucl. Instruments Methods Phys. Res. Sect. A Accel. Spectrometers, Detect. Assoc. Equip.* **582,** 96–99 (2007).

225. Yan, H. *et al.* Multimodality hard-x-ray imaging of a chromosome with nanoscale spatial resolution. *Sci. Rep.* **6,** 1–7 (2016).

226. Kerkar, M., Robinson, J. & Forty, a J. In situ structural studies of the passive film on iron and iron/chromium alloys using X-ray absorption spectroscopy. *Faraday Discuss. Chem. Soc* **89,** 31–40 (1990).

227. Oblonsky, L. J., Ryan, M. P. & Isaacs, H. S. In Situ Determination of the Composition of Surface Films Formed on Fe-Cr Alloys. *J. Electrochem. Soc.* **145,** 1922 (1998).

228. Oblonsky, L. J. & Ryan, M. P. In situ XANES study on the active and transpassive dissolution of Ni and Ni-Cr alloys in 0.1 M H2SO4. *Proc. - Electrochem. Soc.* **2000–4,** 198–209 (2000).

229. Schmuki, P. *et al.* Electrochemical behavior of Cr2O3/Fe2O3 artificial passive films studied by in situ XANES. *J. Electrochem. Soc.* **145,** (1998).

230. Wang, J., Chen-Wiegart, Y. K. & Wang, J. In situ chemical mapping of a lithium-ion battery using full-field hard X-ray spectroscopic imaging. *Chem. Commun.* **49,** 6480 (2013).

231. Weker, J. N. *et al.* Insitu nanotomography and operando transmission X-ray microscopy of micron-sized Ge particles. *Energy Environ. Sci.* **7,** 2771–2777 (2014).

232. Tay, S. E. R. *et al.* Direct in situ observation of ZnO nucleation and growth via transmission X-ray microscopy. *Nanoscale* **8,** 1849–1853 (2016).

233. Liu, J. *et al.* Tribocorrosion behavior of DLC-coated CoCrMo alloy in simulated biological environment. *Vacuum* **92,** 39–43 (2013).

234. Lutz, J. & Mändl, S. Reduced tribocorrosion of CoCr alloys in simulated body fluid after nitrogen insertion. *Surf. Coatings Technol.* **204,** 3043–3046 (2010).

235. Lutz, J., Díaz, C., García, J. A., Blawert, C. & Mändl, S. Corrosion behaviour of medical CoCr alloy after nitrogen plasma immersion ion implantation. *Surf. Coatings Technol.* **205,** 3043–3049 (2011).

236. Murr, L. E. *et al.* Metal Fabrication by Additive Manufacturing Using Laser and Electron Beam Melting Technologies. *J. Mater. Sci. Technol.* **28,** 1–14 (2012).

237. Laura, A. Di *et al.* The Chemical Form of Metal Species Released from Corroded Taper Junctions of Hip Implants : Synchrotron Analysis of Patient Tissue. *Sci. Rep.* 1–13 (2017). doi:10.1038/s41598-017-11225-w

238. Hart, A. J., Sabah, S. A., Henckel, J., Lloyd, G. & Skinner, J. A. Lessons Learnt from Metal-On-Metal Hip Arthroplasties will Lead to Safer Innovation for all Medical Devices. *HIP Int.* **25,** 347–354 (2015).

239. Bao, Q. B. & Yuan, H. A. Artificial disc technology. *Neurosurg. Focus* **9,** e14 (2000).

240. Cook, R. B. *et al.* Pseudotumour formation due to tribocorrosion at the taper interface of large diameter metal on polymer modular total hip replacements. *J. Arthroplasty* **28,** 1430–1436 (2013).

241. Ice, G. E. in *Characterization of Materials* (John Wiley & Sons, Inc., 2002). doi:10.1002/0471266965.com076.pub2

242. Australian Microscopy and Microanalysis Research Facility. Available at: http://www.ammrf.org.au/myscope/tem/background/concepts/lenses/poleandcoil.php. (Accessed: 10th

June 2010)

243. Williams, D. B. & Carter, C. B. *Transmission Electron Microscopy*. (Springer US, 2009). doi:10.1007/978-0-387-76501-3

244. Howe, J. M., Fultz, B. & Miao, S. in *Characterization of Materials* (John Wiley & Sons, Inc., 2002). doi:10.1002/0471266965.com082.pub2

245. Leonard, D. N., Chandler, G. W. & Seraphin, S. in *Characterization of Materials* (John Wiley & Sons, Inc., 2002). doi:10.1002/0471266965.com081.pub2

246. Pennycook, S. J. & Ardenne, B. M. Von. Scanning Transmission Electron Microscopy. 1736–1763 (2011). doi:10.1007/978-1-4419-7200-2

247. Newbury, D. E. in *Characterization of Materials* (John Wiley & Sons, Inc., 2002). doi:10.1002/0471266965.com087.pub2

248. Bell, D. C. & Erdman, N. in *Low Voltage Electron Microscopy* (eds. Bell, D. C. & Erdman, N.) 1–30 (John Wiley & Sons, Ltd, 2012). doi:10.1002/9781118498514.ch1

249. Stock, S. In situ X-ray Measurement Methods. *Charact. Mater.* 1652–1671 (2012).

250. Margaritondo, G. *INTRODUCTION TO SYNCHROTRON RADIATION*. *NEW YORK, USA: OXFORD UNIV. PR. (1988) 280p* (1988).

251. Kelly, S. D., Hesterberg, D. & Ravel, B. Analysis of soils and minerals using X-ray absorption spectroscopy. *Methods soil Anal. Part 5. Mineral. methods* **5,** 387–464 (2008).

252. Heald, S. XAFS Spectroscopy. *Charact. Mater.* 1–15 (2012). doi:10.1002/0471266965.com072.pub2

253. Sakdinawat, A. & Attwood, D. Nanoscale X-ray imaging. *Nat. Photonics* **4,** 840–848 (2010).

254. Vila-Comamala, J. *et al.* Dense high aspect ratio hydrogen silsesquioxane nanostructures by 100keV electron beam lithography. *Nanotechnology* **21,** (2010).

255. Wang, Y. in *Characterization of Materials* (John Wiley & Sons, Inc., 2002). doi:10.1002/0471266965.com133

256. Kang, H. C. *et al.* Focusing of hard x-rays to 16 nanometers with a multilayer Laue lens. *Appl. Phys. Lett.* **92,** 3–5 (2008).

257. Huang, X. *et al.* 11 nm hard X-ray focus from a large-aperture multilayer Laue lens. *Sci. Rep.* **3,** (2013).

258. Penner-Hahn, J. E. in *Comprehensive Coordination Chemistry II* **2,** 159–186 (Elsevier, 2003).

259. Chao, W., Harteneck, B. D., Liddle, J. A., Anderson, E. H. & Attwood, D. T. Soft X-ray microscopy at a spatial resolution better than 15 nm. *Nature* **435,** 1210–1213 (2005).

260. Vila-Comamala, J. *et al.* Advanced thin film technology for ultrahigh resolution X-ray microscopy. *Ultramicroscopy* **109,** 1360–1364 (2009).

261. Wang, Y. High-Resolution 3D Imaging and Material Analysis with Transmission X-ray Microscopy and Nano-CT. *Charact. Mater.* 1–10 (2012). doi:10.1002/0471266965.com133

262. Guttmann, P. *et al.* Nanoscale spectroscopy with polarized X-rays by NEXAFS-TXM. *Nat. Photonics* **6,** 25–29 (2012).

263. Futamoto, M., Honda, Y., Kakibayashi, H., Shimotsu, T. & Uesaka, Y. Microstructure of cocr thin films prepared by sputtering. *Jpn. J. Appl. Phys.* **24,** L460–L462 (1985).

264. Maeda, Y., Asahi, M. & Seki, M. TEM Observation of Segregated Microstructure in Sputtered Co-Cr Film. *Jpn. J. Appl. Phys.* **25,** L668–L670 (1986).

265. Nalwa, H. S. *Handbook of Thin Film Materials: Characterization and spectroscopy of thin films*. (Academic Press, 2002).

266. Erlebacher, J., Aziz, M. J., Karma, a, Dimitrov, N. & Sieradzki, K. Evolution of nanoporosity in dealloying. *Nature* **410,** 450–453 (2001).

267. Schofield, E. J., Ingham, B., Turnbull, A., Toney, M. F. & Ryan, M. P. Strain development in nanoporous metallic foils formed by dealloying. *Appl. Phys. Lett.* **92,** 1–4 (2008).

268. Friedrich, R., Radons, G., Ditzinger, T. & Henning, A. Ripple Formation through an Interface Instability from Moving Growth and Erosion Sources. *Phys. Rev. Lett.* **85,** 4884–4887 (2000).

269. Chen, Q. & Sieradzki, K. Mechanisms and Morphology Evolution in Dealloying. *J. Electrochem. Soc.* **160,** C226–C231 (2013).

270. Pugh, D. V., Dursun, A. & Corcoran, S. G. Electrochemical and Morphological Characterization of Pt–Cu

Dealloying. *J. Electrochem. Soc.* **152,** B455 (2005).

271. Tay, S. E. R. *et al.* Direct in situ observation of ZnO nucleation and growth via transmission X-ray microscopy. *Nanoscale* **8,** 1849–1853 (2016).

272. Koronfel, M. A. *et al.* Understanding the reactivity of CoCrMo-implant wear particles. *npj Mater. Degrad.* **2,** 8 (2018).

273. Lerotic, M., Jacobsen, C., Schäfer, T. & Vogt, S. Cluster analysis of soft X-ray spectromicroscopy data. *Ultramicroscopy* **100,** 35–57 (2004).

274. Ravel, B. & Newville, M. ATHENA , ARTEMIS , HEPHAESTUS : data analysis for X-ray absorption spectroscopy using IFEFFIT. *J. Synchrotron Radiat.* **12,** 537–541 (2005).

275. Geissbuehler, M. & Lasser, T. How to display data by color schemes compatible with red-green color perception deficiencies. *Opt. Express* **21,** 9862 (2013).